

Hierarchical Deep Research with Local–Web RAG: Toward Automated System-Level Materials Discovery

Rui Ding^{1,2,*} Rodrigo Pires Ferreira^{1,2,*} Yuxin Chen^{3,†}
 Junhong Chen^{1,2,†}

¹Pritzker School of Molecular Engineering, University of Chicago

²Chemical Sciences and Engineering Division, Argonne National Laboratory

³Department of Computer Science, University of Chicago

Abstract

We present a long-horizon, hierarchical deep research (DR) agent designed for complex materials and device discovery problems that exceed the scope of existing Machine Learning (ML) surrogates and closed-source commercial agents. Our framework instantiates a locally deployable DR instance that integrates local retrieval-augmented generation with large language model reasoners, enhanced by a Deep Tree of Research (DToR) mechanism that adaptively expands and prunes research branches to maximize coverage, depth, and coherence. We systematically evaluate across 27 nanomaterials/device topics using a large language model (LLM)-as-judge rubric with five web-enabled state-of-the-art models as jurors. In addition, we conduct dry-lab validations on five representative tasks, where human experts use domain simulations (e.g., density functional theory, DFT) to verify whether DR-agent proposals are actionable. Results show that our DR agent produces reports with quality comparable to—and often exceeding—those of commercial systems (ChatGPT-5-thinking/o3/o4-mini-high Deep Research) at a substantially lower cost, while enabling on-prem integration with local data and tools.

Keywords: deep research, hierarchical reasoning, materials discovery, retrieval-augmented generation, large language models, computational materials science, autonomous agents

1 Introduction

Machine learning (ML) for nanomaterials and device discovery has advanced from tractable single-entity predictions to increasingly complex, system-level challenges. At the molecular or crystal level (S1), modern surrogates routinely predict intrinsic properties [1]. Small assemblies (S2)—interfaces, heterostructures, or simple 2–3-component devices—introduce coupling effects yet remain manageable. Real-world nano-devices, however, operate at system scope (S3): multi-layer perovskite stacks with interdependent layers, core-shell-doped catalysts with engineered interfaces, or nano-architected battery electrodes where transport across length scales governs performance [2]. The ultimate challenge lies in cross-domain integration (S4): platforms that span material families, recognition chemistries, and transduction modalities—for example, engineering 2D-material field-effect transistor (FET) sensors with aptamer functionalization for environmental detection [3, 4].

Meeting this escalation in scope requires a matching escalation in depth. We frame depth from single-pass prediction/forward screening (D1), to multi-stage pipelines with structured outputs (D2), to long-horizon synthesis with iterative planning (D3), and ultimately hierarchical, breadth–depth exploration (D4). While recent agentic frameworks have successfully demonstrated hierarchical orchestration for complex scientific workflows [5, 6, 7], ensuring robust execution and simulation management, device/system-level optimization and design (S3–S4) presents a distinct challenge. The governing laws for device integration are not fully encoded in standard simulation packages, requiring long-horizon hierarchical autonomous discovery (D3–D4) with potential to navigate the combinatorial explosion of processing parameters sparsely

¹These authors contributed equally to this work.

²Corresponding authors: cheniyuxin@uchicago.edu, junhongchen@uchicago.edu

distributed across heterogeneous knowledge sources. Existing approaches typically face limitations in this unstructured knowledge regime [8, 9, 10, 11] (Detailed in Appendix A).

To address this gap, we introduce a hierarchical deep-research (DR) agent¹ purpose-built for long-horizon scientific inquiry. Given a natural-language inquiry, the system instantiates a locally deployable DR instance that iterates between local and web retrieval-augmented generation (RAG) and large language model (LLM) reasoners (summarizers, reflectors). We further expand the DR instance into a Deep Tree of Research (DToR) where each instance is treated as a node in a tree-structured workflow. DToR adaptively expands/prunes branches to improve coverage, depth, and coherence. The agent is self-directed/navigated (plans its own research path), runs locally for controllability and privacy, and targets S3-S4 hypotheses. At a glance, our goal is to measure synthesis quality by a programmatic evaluation harness (anchored rubric, A/B preferences) plus dry-lab checks. We then show that orchestration via DToR consistently improves synthesis quality over single-instance DR across model backbones and local-corpus budgets at comparable compute.

Contributions. (1) A democratized, locally deployable framework for scientific deep research, enabling materials researchers to exercise fine-grained control over cost and preferences using open-source LLMs while achieving performance that surpasses commercial state-of-the-art solutions in most cases (§3). (2) A hierarchical orchestration (DToR) that yields robust gains over single-instance DR across LLM backbones and local data budgets, supported by comprehensive factorial and targeted component ablations. (3) An evaluation program combining anchored rubric scores, repeated A/B duels, and dry-lab validation to assess synthesis quality.

1.1 Related work

Recent work on structured reasoning for LLMs has moved beyond linear prompting toward explicit search structures. Tree-of-Thoughts (ToT) frames inference as a branching search over intermediate ‘thoughts’, while Graph-of-Thoughts (GoT) generalizes this to arbitrary graphs to model non-linear dependencies and subproblem coordination [12, 13, 14]. In parallel, reason-act and self-improvement paradigms—ReAct, Reflexion, and Self-Refine—provide strong baselines for multi-step decision-making and revision ([15, 16, 17]). Foundational web-agent environments/benchmarks—BrowseComp, WebLINX, WebArena, and BrowserGym—formalize browsing/navigation competencies and support reproducible evaluation [18, 19, 20, 21]. Work on retrieval is also moving toward more adaptive strategies: Self-RAG [22] learns when to retrieve and critique outputs, CRAG [23] evaluates retrieval quality and escalates to web search when evidence is weak, and GraphRAG [24] uses graph-structured knowledge for non-flat retrieval. Despite this progress, there is no framework that unifies structured branching and adaptive retrieval in a way that scales under practical compute and data limits for domain-specific research settings.

2 Method

D4 requires structured and budget-aware planning beyond short-term queries. We introduce DToR, a breadth-then-depth controller for DR that starts from multiple parallel perspectives, selectively expands or prunes based on explicit gap checks, runs evidence-first research steps (local RAG with adapted web search), and produces source-grounded reports.

2.1 Single DR Instance

As shown in Fig. S1² (with comparison against common standard DR agent [25]), each DR instance is an evidence-first loop that (1) generates a search query; (2) performs local RAG; (3) summarizes local evidence; (4) generates a complementary query to induce topical diversity; (5) conducts web research for both queries; (6) integrates/updates previous retrieved segments in a running summary; (7) reflects to propose follow-up query. The process would loop until a set maximum round before (8) finalizing. Three design choices distinguish this instance from common local DR agents[25] which only conduct (1)-(5)-(6)-(7): local-first retrieval (before web) to reduce drift, hallucination, and surface domain priors; diversity-aware query generation (local summary derived complementary query) to guarantee comprehensiveness;

¹We use *Deep Research (DR)* to denote a single-threaded, iterative retrieval-reasoning-writing loop run by one agent. *Deep Tree of Research (DToR)* denotes a tree-structured orchestration that spawns and selects among multiple DR branches with hierarchical planning and merge. Throughout, "hierarchical deep research" is synonymous with DToR; we henceforth use only DR and DToR for clarity.

²Supporting figures (S1-S13) illustrating detailed experimental results and supplementary analyses are presented in Appendix B.

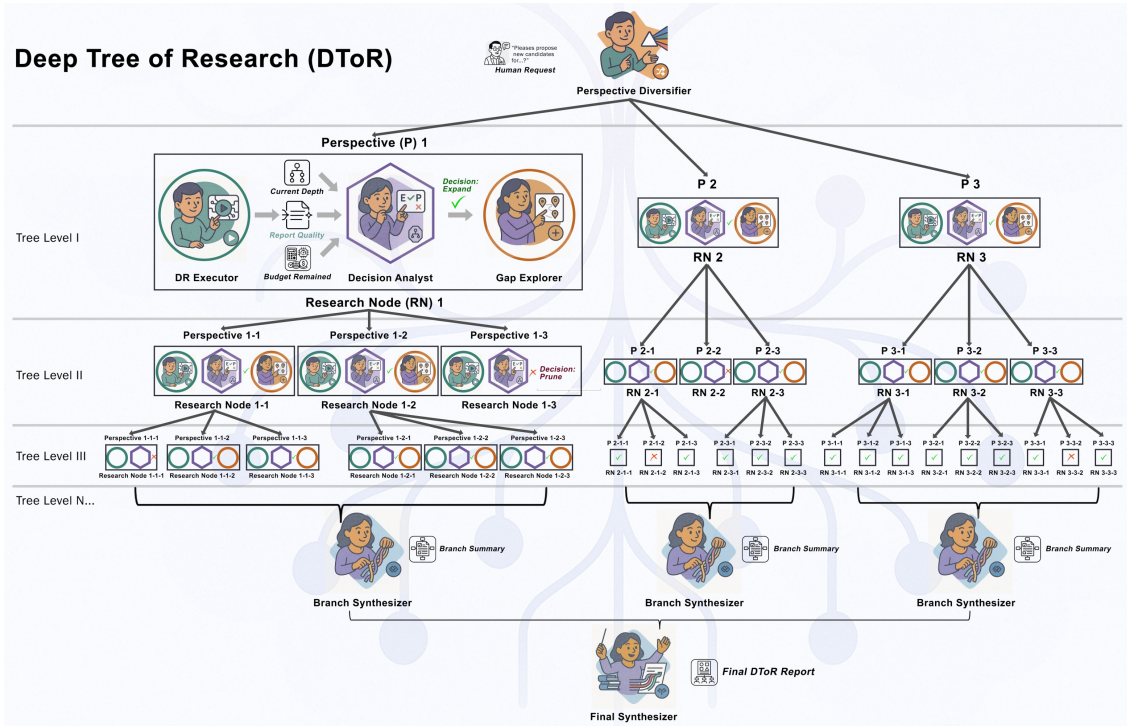


Figure 1: The DToR Depth-Breadth Workflow

and robust I/O discipline to prevent controller stalls on local-hosted LLMs. Compared with classic ReAct/Reflexion-style linear loops, this instance adds an explicit breadth mechanism and escalation policy akin to adaptive/corrective-RAG, while remaining compatible with the drop-in alternative RAG methods.

2.2 DToR: from perspectives to gap-driven expansion

Based on the single DR instance, we treat each DR instance as a Research Node (RN) inside a branch-and-bound controller (Fig. 1). Starting from a user query, a diversifier proposes several orthogonal Perspectives (P1, P2...)—each seeds one branch with a budget: maximum depth, nodes per branch, and total branches. For the active branch, the router (i) runs the next pending RN (the single DR instance), producing a RN summary; (ii) invokes analyst based on remaining depth/budget/current RN report quality to give a decision EXPAND, PRUNE; and, if EXPAND with budget remaining, (iii) invokes knowledge gap explorer to materializes new RNs from this RN targeted to those gaps (depth+1) and updates remaining budget. Branches that stagnate are pruned; (iv) branches that reach depth or converge are synthesized into a perspective report. When all branches reach synthesis, a final synthesizer reconciles cross-branch evidence, resolves conflicts, and outputs a provenance-rich, consolidated report. Conceptually, this is a tree-of-search over (query, evidence, summary) states rather than over purely symbolic "thoughts," inheriting the benefits of structured exploration/backtracking from tree/graph-based reasoning while remaining tailored to information-seeking and citation fidelity under explicit resource budgets.

3 Experiments

3.1 Experimental setup

We evaluate across 27 expert-crafted topics spanning materials and devices (e.g., per- and polyfluoroalkyl substances (PFAS) FET probes, CO₂ sensing in 2D materials, Li/Na-selective membranes, CO₂-reduction catalysts); full topic prompts are provided in Appendix C. For each topic, we consider 41 agents—11 commercial and 30 local (split evenly between single DR-instance and DToR-mode)—on consumer-level hardware. We evaluate local agents across LLM backbones (gpt-oss120B, gpt-oss20B, QwQ32B) and local RAG budgets (local0/local100/local500), holding orchestration fixed and varying only backbone

and corpus size; full agent configurations in Appendix D. Using an LLM-as-judge protocol (Appendix E), we generate 41 distinct report variants per topic and have five web-enabled SOTA judges—Claude 4 Opus (thinking), Gemini 2.5 Pro, Grok-3 (thinking), ChatGPT-o3, and ChatGPT-o4-mini-high—score each report under a fixed, double-blind rubric (judges are blinded to agent identities) with five equally weighted dimensions—(1) relevance, (2) depth, (3) clarity, (4) applicability, and (5) novelty—whose concise definitions are provided in Appendix E.

Judge view and anonymization: LLM judges see only the final report text—no agent/model identifiers, tool logs, or token/count metadata—and assign numeric scores on five anchored dimensions (relevance, depth/rigor, clarity/reproducibility, applicability, novelty) under a fixed instruction to “act as an experienced materials scientist” (Appendix E). The rubric provides positive/negative exemplars per dimension; unresolved contradictions or failure to reconcile conflicts between local and web evidence are penalized under Depth/Rigor and Clarity/Reproducibility, while reports that explicitly compare sources and justify a resolution are rewarded. Access to local vs. web contexts is controlled at generation time (agents run in local-only or web-enabled modes), whereas judges never see those contexts—only the synthesized report—so the evaluation targets synthesis/reasoning quality rather than retrieval exposure. Judges assign 0–10 per dimension with one-sentence justifications; numeric ratings are extracted by a deterministic parser. We repeat the evaluation three times per topic–report–judge combination, yielding $27 \times 41 \times 5 \times 3 = 16,605$ rubric-based judgments. Inter-judge agreement (Pearson correlation on scores and Spearman rank correlation) remains high across all dimensions.

We then run A/B dueling preferences using the same setup. For each topic, we form three pools: commercial, local gpt-oss, and local non-gpt-oss. Within each pool we rank reports by rubric average and select the top-3; the resulting 9 reports then enter all pairwise duels ($\binom{9}{2} = 36$ pairs per topic). Duels are double-blind and order-randomized, guided by a concise “experienced materials scientist” prompt emphasizing clarity, gap prioritization, and actionable next steps. Each duel is repeated three times, yielding $27 \times 36 \times 3 = 2916A/B$ trials and 14,580 individual judge decisions.

Finally, we conduct dry-lab validation on five representative tasks—PFAS sensor probe, PFAS degradation catalysts, battery binder selection, oxygen evolution reaction (OER) catalyst stability, and CO₂ sensor probe—by sending anonymized best-local and best-commercial reports to domain experts who extract candidates and build simulation environments (Appendix F). We score ten simulation metrics per task with domain-standard protocols (e.g., explicit-solvent ab initio molecular dynamics, AIMD, when necessary) and aggregate per-task and overall performance; full simulation setups and metric definitions are in Appendix F. We also run a full-factorial ablation across Method \times LLM backbone \times local-corpus budget (27 topics, 41 agents) to isolate main effects and interactions (Fig. 2b), and conduct targeted component ablations on the best-performing configuration across three representative topics to further dissect orchestration contributions (Appendix G). To characterize the benchmark itself, we compute per-topic difficulty (mean performance across agents) and discrimination power (standard deviation of agent scores), revealing which topics best separate strong from weak systems; full topic-level analysis is in Appendix H. All runs were executed on a workstation with 4 \times NVIDIA RTX A5500 (Ubuntu); completion-time statistics and energy estimates are reported in Appendix I. The DToR framework source code is publicly available at https://github.com/ruiding-uchicago/DToR_deep_research.

3.2 Experimental results

Across the five LLM-as-judge dimensions on 27 topics \times 41 agents (Fig. 2a), DToR_gpt-oss120B_local500 (running DToR with gpt-oss120B and all 500 volumes of local corpus for RAG; see details in Appendix D) achieves an average score of 8.57/10, ranking 1st overall. When the local RAG budget is reduced to local100 and local0, the scores remain 8.53/10 and 8.37/10, both still top-3. Even without the DToR controller (i.e., a single DR instance), gpt-oss120B reaches 8.33/10 (local100) and 8.32/10 (local500), ranking 4th and 5th. Under the same setup with gpt-oss20B, DToR yields 8.15/10, 8.12/10, and 8.08/10 for local500/local100/local0, respectively. All of the above surpass commercial baselines including ChatGPT-o4-mini-high (7.96/10), ChatGPT-o3 (7.95/10), and ChatGPT-5-thinking (7.85/10), as well as other widely used systems such as Gemini 2.5 Pro (7.81/10), Claude Opus 4 (7.78/10), Grok 3 (7.51/10), and Perplexity (7.51/10). Notably, DToR_QwQ32B_local500 driven by laptop compatible lightweight LLM also attains 7.80/10, outperforming roughly half of the commercial systems.

A closer look at the five dimensions (Fig. S2) shows that clarity and depth are the most challenging, with the lowest means and the largest dispersion. Even so, DToR yields the largest gains over a single-DR instance precisely on these two dimensions, with average improvements of +0.69 and +0.72, respectively. Excluding relevance—which exhibits a ceiling effect and thus limited separability—DToR delivers clear improvements on the remaining four dimensions. For example, on novelty and applicability, DToR

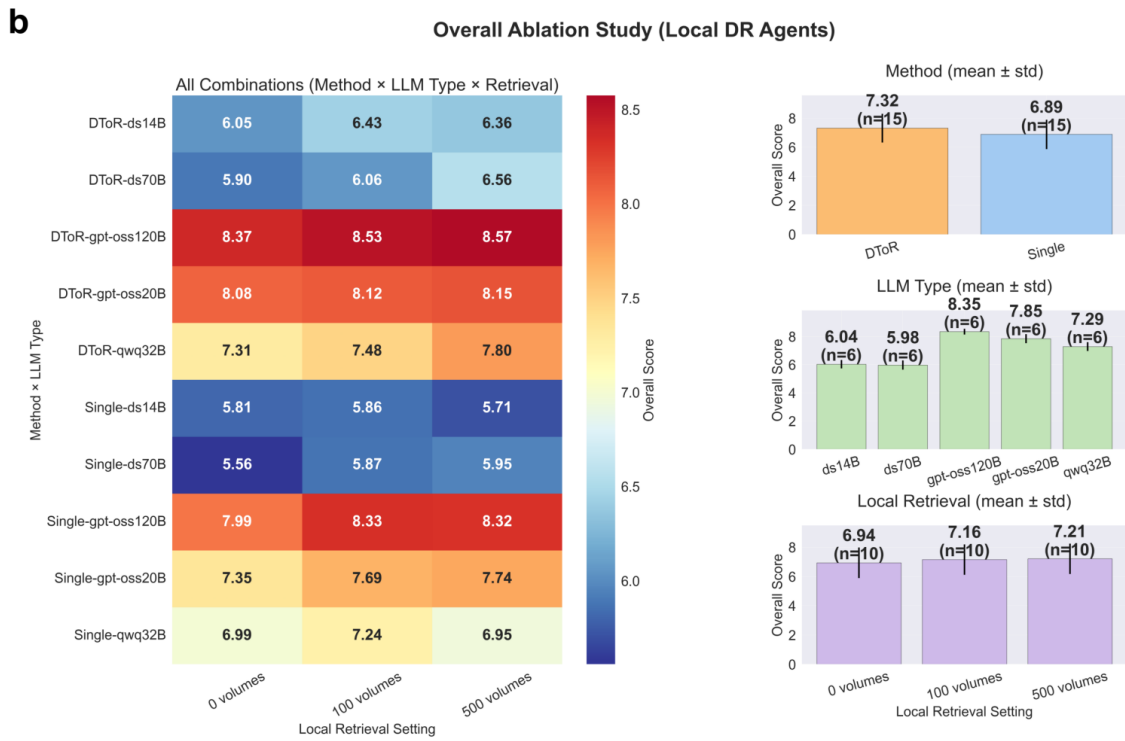
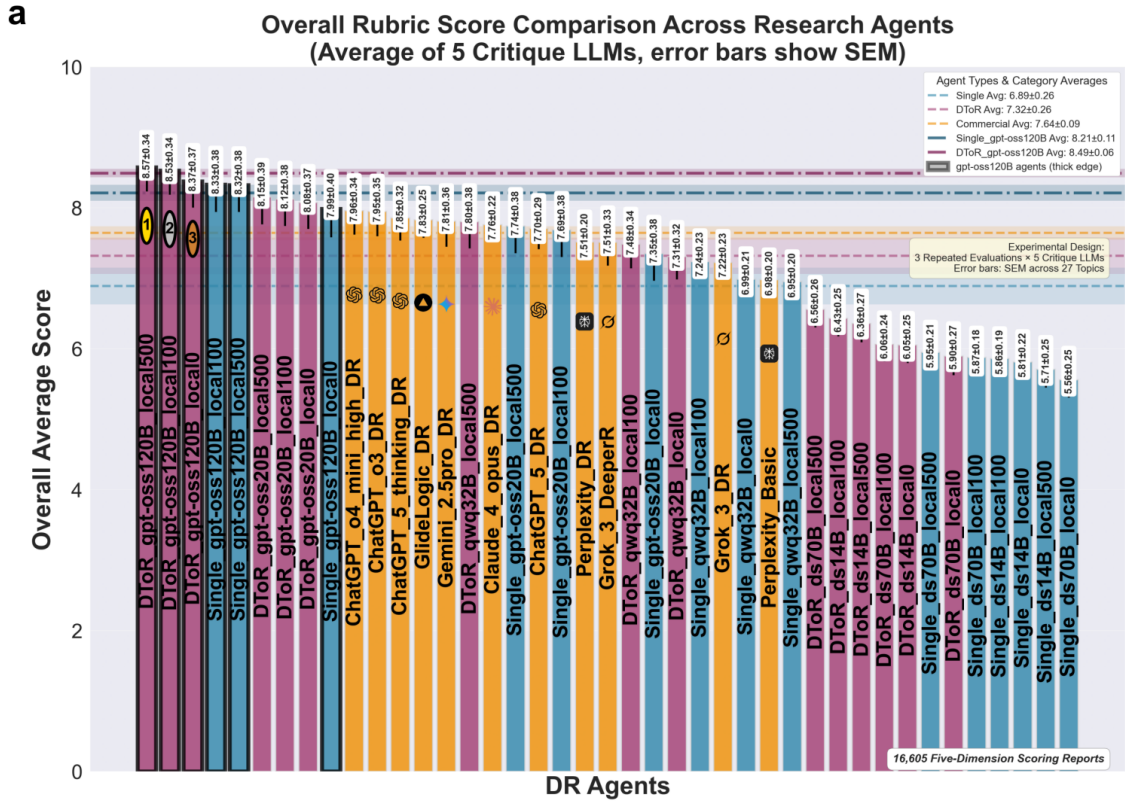


Figure 2: (a) Overall five-dimension rubric scores across 41 agents (27 topics; 5 judges; 3 trials). (b) Full-factorial ablation (Method × LLM × Local retrieval); heatmap shows overall means; side bars show each factor impact.

improves Single_gpt-oss120B_local500 by +0.43 and +0.42 points on average, pushing it above the leading commercial baseline. Inter-rater consistency across the five LLM critics was high: average Pearson correlation $p = 0.97$ on raw scores and Spearman $\rho = 0.97$ on rank orders (Fig. S3).

Reliability is further supported by agent-specific and inter-trial consistency (Fig. S4, Fig. S5). From an ablation study perspective (Fig. 2b), enabling local RAG (7.21/10) and especially DToR mode (7.32/10) increases the average score. Across all 27 topics and 41 agents, Method \times Backbone \times Local-corpus budget factorial analysis shows that the dominant effect is orchestration: DToR consistently outperforms single-instance DR once a non-trivial local corpus is present (local100/local500), whereas at local0 the gap narrows and a strong backbone (gpt-oss120B) can close it. To further isolate orchestration components, we conducted targeted component ablations on the best-performing configuration (DToR_gpt-oss120B_local500) across three representative topics: systematically degrading tree depth (3 \rightarrow 2 perspectives), reflection loops (3 \rightarrow 0 iterations), and retrieval counts (5 \rightarrow 1 papers per query) all reduce performance, with reflection proving most critical; removing web search (local-only or LLM-only modes) similarly degrades quality, confirming gap-triggered web complement adds value; driving the same orchestration with API models (gpt-5-mini/nano) maintains relative orderings but at materially higher cost (Fig. S6, Fig. S7, Fig. S8; full details in Appendix G). Per-topic analysis reveals a clear difficulty spectrum: sensing/characterization tasks (in-situ TEM, printed FET arrays) are easiest, while battery electrochemistry topics (lithium ion battery: LIB binders, fluoroether anion receptors) are hardest; discrimination power shows environmental sensing topics (microplastics, antibiotics detection) separate agents weakly ($\sigma \approx 0.7$), whereas battery/materials synthesis challenges (LIB fluoroether receptor, ambient-pressure diamond growth) sharply distinguish strong from weak systems ($\sigma > 1.1$). Notably, topic difficulty and discrimination are decoupled: LIB_Fluoroether_Anion_Receptor exhibits both the highest difficulty ($\mu = 6.93$) and the largest discrimination ($\sigma = 1.24$), sharply separating strong and weak agents; conversely, Microplastics_Sensing_2D shows the lowest discrimination ($\sigma = 0.69$) at mid-pack difficulty ($\mu = 7.19$); Catalytic_Mineralization_of_Microplastics is relatively easy ($\mu = 7.49$) yet still discriminates well ($\sigma = 1.03$), while Wastewater_Resource_Recovery_Cats is hard ($\mu = 7.04$) but offers weak separation ($\sigma = 0.93$). Critically, DToR agents maintain consistent performance advantages across both high- σ and low- σ topics, confirming that orchestration benefits are robust to topic characteristics rather than prompt-specific artifacts; full per-topic difficulty rankings and discrimination analysis are in Appendix H.

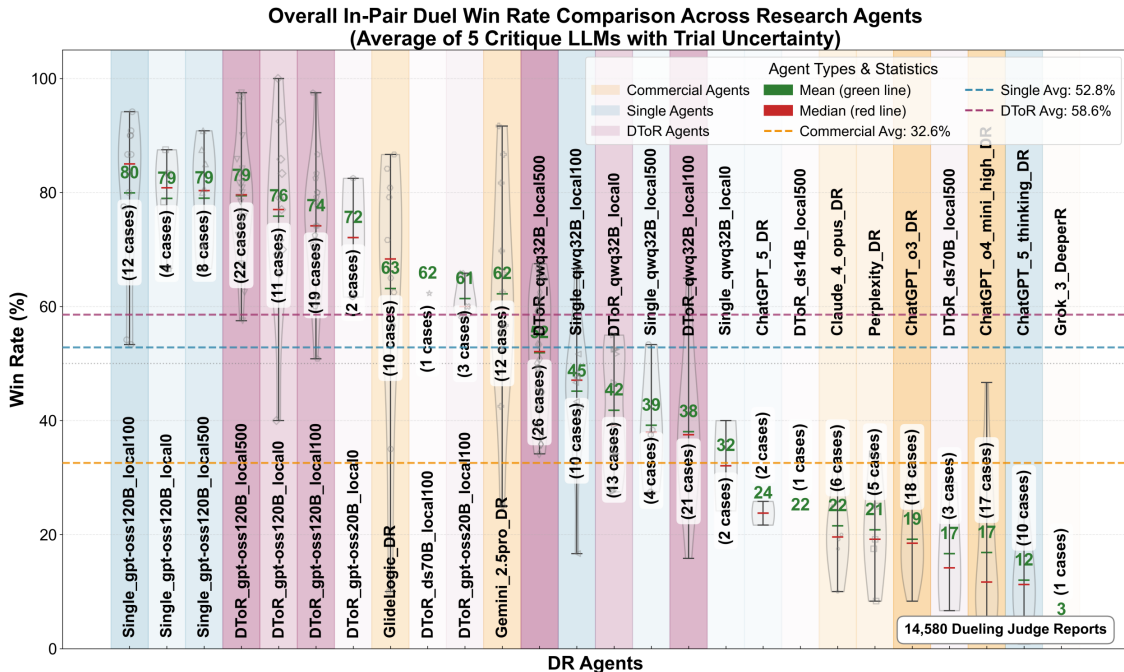


Figure 3: Win Rate Violin Plot - Shows the distribution of win rates across different agents and topics with detailed statistical information and performance variations

To mitigate potential bias inherent in numerical rubric scoring, we further complement these results with pairwise dueling—a side-by-side comparison that directly elicits preferences from LLM judges without

imposing a rigid numerical scale. Pairwise dueling (Fig. 3) confirms these findings across all 27 topics (Fig. S9) with strong experimental consistency (Fig. S10): (1) DToR agents show a higher average win rate (58.6%) than Single DR agents (52.8%) in head-to-head comparisons; (2) DToR_gpt-oss120B_local500 achieves an impressive 79% mean win rate; (3) gpt-oss-driven DToR and Single agents both exhibit similarly high win rates above 74%, demonstrating a clear advantage. These outcomes further support the previous rubric scoring results, confirming that our locally hosted DToR agents generate superior DR reports.

Dry-Lab Validation: Agent Performance Across 5 Representative Applications (Candidate Average - 10 Simulation Metrics - Log Scale)

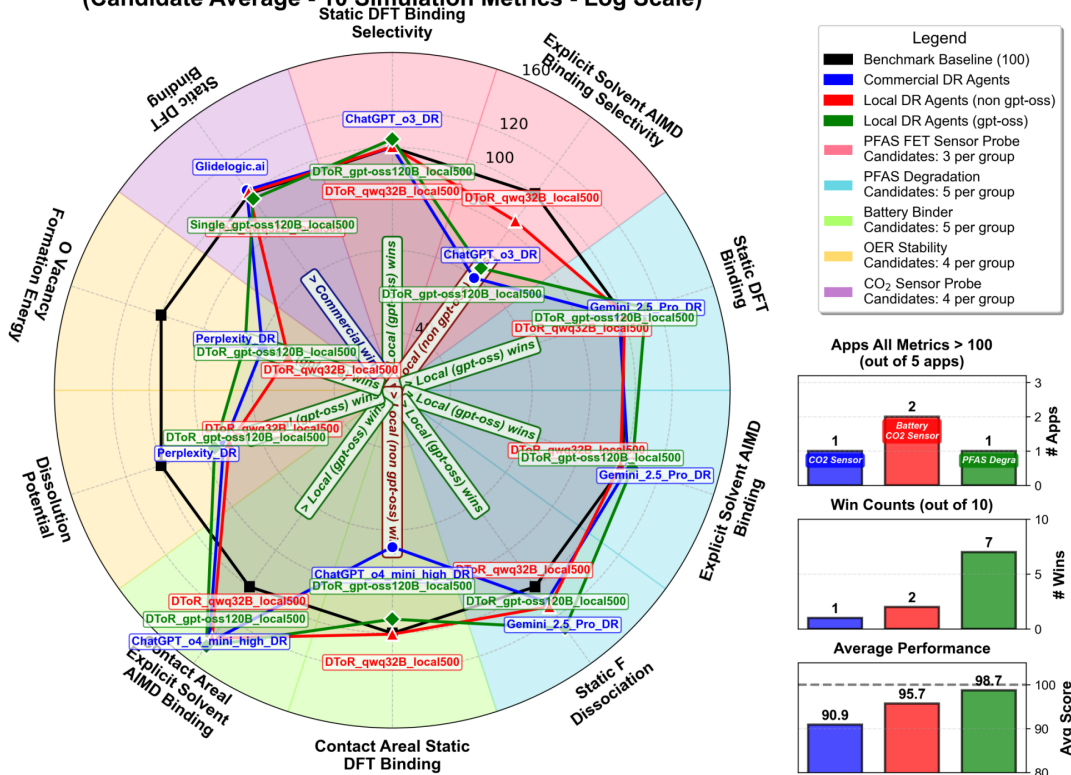
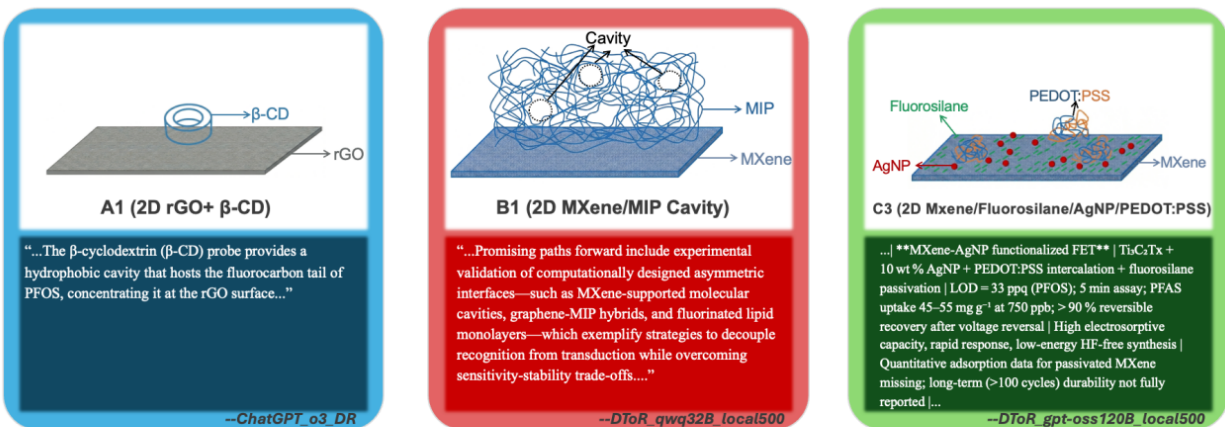


Figure 4: Dry-lab validation on five tasks: radar of 10 simulation metrics comparing best local vs. best commercial DR Agents. The bar plots located at bottom right indicate respectively: the time of agent proposed candidates obtain score surpassed domain prior (>100); the time of agent proposed candidates obtain the highest score among three groups; the overall 10 metrics average score.

In dry-lab validation spanning 10 metrics over five application scenarios (Fig. 4), we comprehensively validate across domain benchmarks with DFT and explicit-solvent AIMD, scoring each task against a well-recognized baseline normalized to 100. The tasks and metrics are: (i) PFAS sensor binding—static-DFT binding energies ΔE_{bind} for PFAS vs. interferents and explicit-solvent end-state potential-energy gaps from short AIMD, with selectivity scored as $\Delta\Delta E$ (PFAS minus interferent) and anchored to β -cyclodextrin[26] (Score=100); (ii) PFAS degradation catalysis—C–F bond dissociation energies from constrained scans and solvated binding stability proxies, normalized to Ti_4O_7 (Magnéli)[27] as the domain benchmark (100); (iii) battery binder adhesion (on NCM811)—areal-normalized $\Delta E_{\text{bind}}/A$ (static DFT, contact area via convex-hull atoms within 3.5 \AA) and explicit-solvent end-state gap (AIMD) to capture electrolyte competition, anchored to polyvinylidene fluoride (PVDF)[28] (100); (iv) OER catalyst stability—dissolution potential U_{diss} (tendency for surface metal leaching) and oxygen-vacancy formation energy V_{O} (lattice robustness), normalized to IrO_2 [29] (100); and (v) CO_2 sensor binding—grid-sampled static-DFT binding energies on candidate surfaces, linearly transformed and anchored to g- C_3N_4 [30] (100). Across these five applications, we observe four all-metrics > 100 events (i.e., every metric for a task exceeds its baseline): commercial once on CO_2 sensor; local DR (non-gpt-oss) twice on CO_2 sensor and battery binder; and local DR (gpt-oss) once on PFAS degradation. In these cases, the DR-proposed candidates point to concrete,

PFAS FET Sensor Probe Candidates



PFAS Degradation Candidates

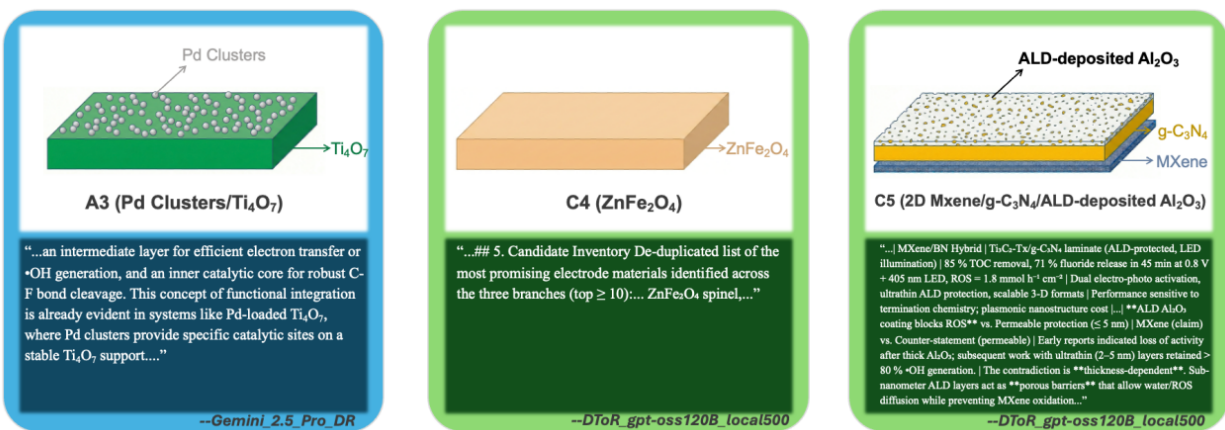


Figure 5: Visual representations of selected candidates drawn based on specific descriptions from the DR reports. The top panel illustrates candidates for PFAS sensing (A1, B1, C3), while the bottom panel shows candidates for PFAS degradation (A3, C4, C5), accompanied by the original text excerpts generated by the agents. Dry lab qualitative studies are available in Appendix F.2 and Appendix F.3

testable improvements over their domain baselines in terms of qualitative dry lab trials: for CO₂ sensing, stronger and more uniform adsorption than g-C₃N₄ (reduced site-to-site dispersion); for battery binders, higher areal-normalized adhesion than PVDF under dry interfaces and competitive performance under explicit electrolyte; and for PFAS degradation, lower C–F dissociation energies relative to Ti₄O₇ while maintaining adequate adsorption stability. Notably, explicit-solvent AIMD often reorders static-DFT rankings, revealing candidates that look promising in vacuum but lose ground when solvation/competition is included—an effect we quantify in the AIMD score panels. The gpt-oss-based local DR agent leads on 7 out of 10 metrics when judged by per-metric averages and also achieves a higher overall score aggregating across metrics (98.7). Related details are available in Appendix F.

While dry-lab simulations provide an initial filter, looking more closely at the candidates proposed by the DR agents reveals a feasibility gap in current LLM–RAG orchestration (Fig. 5). In PFAS sensing, the agents successfully identified rational designs like B1 and A1, yet DToR agent also produced “kitchen-sink” failures like C3, which stacks four mutually incompatible phases (hydrophobic fluorosilane, hydrophilic MXene, Ag nanoparticles, acidic PEDOT:PSS). In practice, synthesis of such a complex system would be infeasible, because the agents ignored likely colloidal incompatibilities (e.g., phase separation and acid-induced etching) that would render the device chemically unstable [31, 32]. Similarly, for PFAS degradation, cost-effective and chemically robust candidates like C4 and A3 stand in contrast to C5, a triple heterostructure (MXene/g-C₃N₄/Al₂O₃) that neglects potential challenges in interfacial charge-transfer resistance and

fabrication complexity[33, 34]. These over-engineered failures stem from a fundamental limitation in current agent architectures: without intrinsic wet-lab feasibility priors, cost models, or external physics validators, LLMs are prone to “inverse-design hallucinations” [35, 36] that assume functional additivity where physical incompatibility exists. This underscores that future AI4Science frameworks must integrate dedicated domain-validator modules (e.g., synthesis-aware ReAct loops) to ground theoretical generation in experimental reality³.

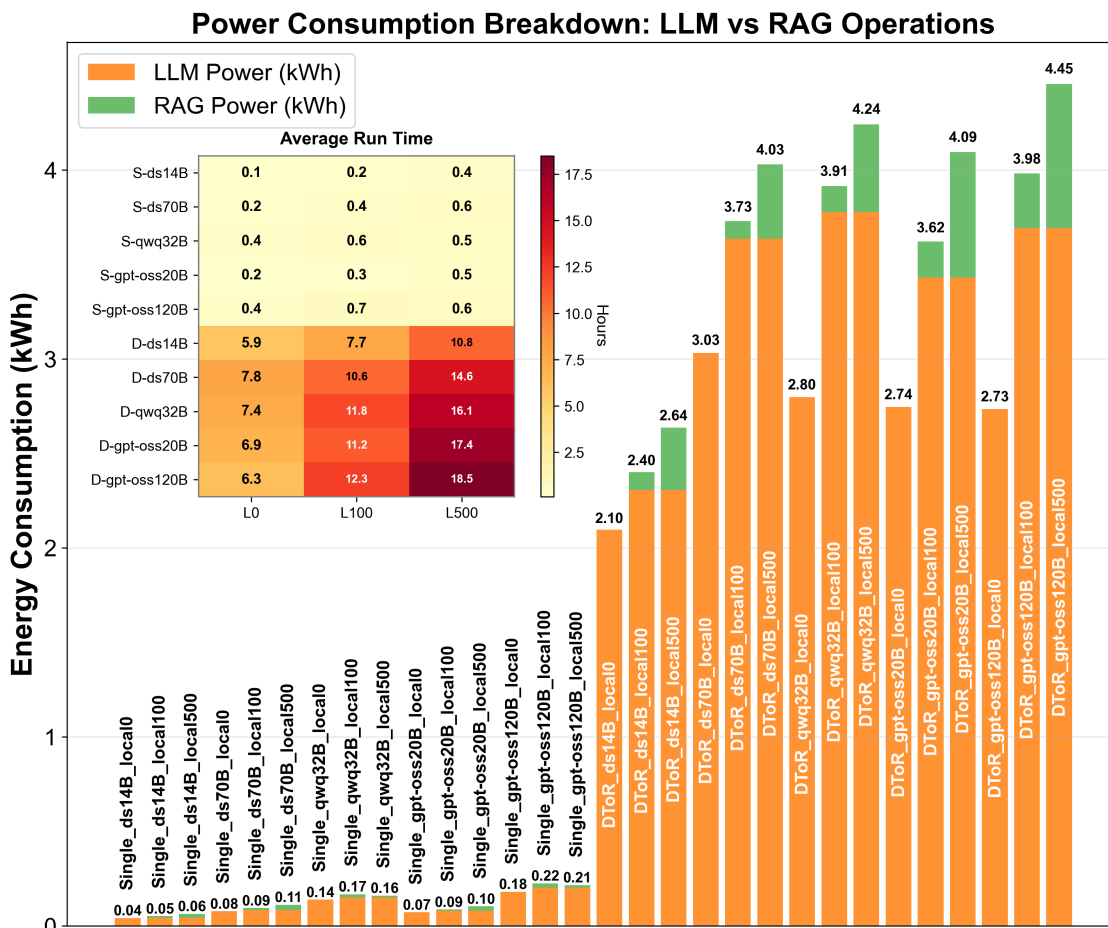


Figure 6: Local deployment cost: stacked energy (kWh) split into LLM vs. RAG; inset = average runtime (hour).

All timings reflect a single-machine setup with serialized agent scheduling (energy estimation methodology in Appendix I); under this controlled setting, DToR with gpt-oss120B averages 19.6 h (Fig. 6, Fig. S11). This should be viewed as an upper bound of orchestration cost, not a requirement for quality: a low-resource profile that disables local-corpus RAG finishes in < 6 h (an overnight run), and a single-instance DR pipeline with gpt-oss120B typically completes within ~30 min—on the same order as commercial solutions yet, as shown earlier, with higher rubric and duel scores. Overall, our gains arise from orchestration and information coverage rather than “model pile-up”: users can explicitly tune for quality (DToR + corpus) or for cost/latency (DR/no-RAG) depending on resources. Without high subscription fees (Fig. S12) for commercial solutions, this framework offers flexible deployment from lightweight laptops to multi-node clusters⁴, enabling democratized, transparent, and open access to advanced research agents adaptable to diverse computational budgets of materials researchers.

³Extended discussion with further citations is available in Appendix F.7

⁴DToR branches can run in parallel; see https://github.com/ruiding-uchicago/DToR_deep_research for implementation details.

4 Conclusion

We introduced DToR, a locally deployable DR agent with a resource-bounded tree controller that unifies local-first RAG, diversity-aware query generation, and gap-driven branching into provenance-rich, long-horizon information seeking. Across 27 topics and 41 agents, under 16,605 rubric judgments from 5 web-enabled judges, our best local model (DToR_gpt-oss120B_local500) ranked 1st (8.57/10) with a 79% mean duel win rate (14,580 dueling judgement) while using only 4.37 kWh/report on consumer devices. In dry-lab validation across five applications, its candidates matched or surpassed the best commercial solutions. This work highlights a practical path toward open, secure, and scalable on-prem DR agents for automated, accelerated scientific discovery at the S3–S4 level.

Acknowledgements

This project is supported in part by the Eric and Wendy Schmidt AI in Science Fellowship, a program of Schmidt Sciences. This project is also supported in part by the National Science Foundation Research Traineeship in AI-enabled Molecular Engineering of Materials and Systems for Sustainability (NRT-AIMEMS). Additional support came from the University of Chicago Data Science Institute through the 2024 AI+Science Research Initiative. This work was also supported in part by the National Science Foundation under the Future Manufacturing program (award 2037026) and the Robust Intelligence program (award 2313131 and 2332475). Computational resources were provided by the Carbon high-performance computing cluster at the Center for Nanoscale Materials, Argonne National Laboratory, a U.S. Department of Energy Office of Science user facility (Contract No. DE-AC02-06CH11357); the Argonne Leadership Computing Facility, a U.S. Department of Energy Office of Science user facility at Argonne National Laboratory, under the DOE Office of Science Advanced Scientific Computing Research program (Contract No. DE-AC02-06CH11357) via an ALCF Discretionary award “BRAINIAC” (Allocation ID 14368); the University of Chicago Research Computing Center (proposal #68909) and the University of Chicago Data Science Institute high-performance computing cluster; and the Delta system and advanced computing resources at Texas A&M High Performance Research Computing, both accessed through the Advanced Cyberinfrastructure Coordination Ecosystem: Services & Support (ACCESS) program under allocation MAT240097 and supported by U.S. National Science Foundation awards 2138259, 2138286, 2138307, 2137603, 2138296.

References

- [1] Tian Xie and Jeffrey C. Grossman. Crystal graph convolutional neural networks for an accurate and interpretable prediction of material properties. *Physical Review Letters*, 120(14):145301, 2018.
- [2] Kristen A. Severson, Peter M. Attia, Norman Jin, Nicholas Perkins, Benben Jiang, Zi Yang, Michael H. Chen, Muratahan Aykol, Patrick K. Herring, Dimitrios Fragedakis, Martin Z. Bazant, Stephen J. Harris, William C. Chueh, and Richard D. Braatz. Data-driven prediction of battery cycle life before capacity degradation. *Nature Energy*, 4(5):383–391, 2019.
- [3] Nathan J. Szymanski, Bernardus Rendy, Yuxing Fei, Rishi E. Kumar, Tanjin He, David Milsted, Matthew J. McDermott, Max Gallant, Ekin D. Cubuk, Amil Merchant, Haegyeom Kim, Anubhav Jain, Christopher J. Bartel, Kristin Persson, Yan Zeng, and Gerbrand Ceder. An autonomous laboratory for the accelerated synthesis of novel materials. *Nature*, 624:86–91, 2023.
- [4] Shun Wang, Mingyuan Sun, Yunhong Zhang, Hao Ji, Jianwei Gao, Shuai Song, Jun Sun, Hong Liu, Yu Zhang, and Lin Han. Ultrasensitive antibiotic perceiving based on aptamer-functionalized ultraclean graphene field-effect transistor biosensor. *Analytical Chemistry*, 94(42):14785–14793, 2022.
- [5] Juraj Gottweis, Wei-Hung Weng, Alexander Daryin, Tao Tu, Anil Palepu, Petar Sirkovic, Artiom Myaskovsky, Felix Weissenberger, Keran Rong, Ryutaro Tanno, Khaled Saab, Dan Popovici, Jacob Blum, Fan Zhang, Katherine Chou, Avinatan Hassidim, Burak Gokturk, Amin Vahdat, Pushmeet Kohli, Yossi Matias, Andrew Carroll, Kavita Kulkarni, Nenad Tomasev, Yuan Guan, Vikram Dhillon, Eeshit Dhaval Vaishnav, Byron Lee, Tiago R D Costa, José R Penadés, Gary Peltz, Yunhan Xu, Annalisa Pawlosky, Alan Karthikesalingam, and Vivek Natarajan. Towards an ai co-scientist. *arXiv preprint arXiv:2502.18864*, 2025.
- [6] Alireza Ghafarollahi and Markus J. Buehler. Sciagents: Automating scientific discovery through bioinspired multi-agent intelligent graph reasoning. *Advanced Materials*, 37:2413523, 2025.

- [7] Yunheng Zou, Austin H. Cheng, Abdulrahman Aldossary, Jiaru Bai, Shi Xuan Leong, Jorge Arturo Campos-Gonzalez-Angulo, Changhyeok Choi, Cher Tian Ser, Gary Tom, Andrew Wang, Zijian Zhang, Ilya Yakavets, Han Hao, Chris Crebolder, Varinia Bernales, and Alán Aspuru-Guzik. El agente: An autonomous agent for quantum chemistry. *Matter*, 8:102263, 2025.
- [8] Joseph H. Montoya, Kirsten T. Winther, Raul A. Flores, Thomas Bligaard, Jens S. Hummelshøj, and Muratahan Aykol. Autonomous intelligent agents for accelerated materials discovery. *Chemical Science*, 11(32):8517–8532, 2020.
- [9] Amil Merchant, Simon Batzner, Samuel S. Schoenholz, Muratahan Aykol, Gowoon Cheon, Ekin Dogus Cubuk, et al. Scaling deep learning for materials discovery. *Nature*, 624:80–85, 2023.
- [10] Lowik Chanussot, Abhishek Das, Siddharth Goyal, Thibaut Lavril, Muhammed Shuaibi, Morgane Riviere, Kevin Tran, Javier Heras-Domingo, Caleb Ho, Weihua Hu, Aini Palizhati, Anuroop Sriram, Brandon M. Wood, Junwoong Yoon, Devi Parikh, C. Lawrence Zitnick, and Zachary W. Ulissi. Open catalyst 2020 (oc20) dataset and community challenges. *ACS Catalysis*, 11:6059–6072, 2021.
- [11] Daniel S. Levine, Muhammed Shuaibi, Evan Walter Clark Spotte-Smith, Michael G. Taylor, Muhammad R. Hasyim, Kyle Michel, Ilyes Batatia, Gábor Csányi, Misko Dzamba, Peter Eastman, Nathan C. Frey, Xiang Fu, Vahe Gharakhanyan, Aditi S. Krishnapriyan, Joshua A. Rackers, Sanjeev Raja, Ammar Rizvi, Andrew S. Rosen, Zachary Ulissi, Santiago Vargas, C. Lawrence Zitnick, Samuel M. Blau, and Brandon M. Wood. The open molecules 2025 (omol25) dataset, evaluations, and models. *arXiv preprint arXiv:2505.08762*, 2025.
- [12] Shunyu Yao, Dian Yu, Jeffrey Zhao, Izhak Shafran, Tom Griffiths, Yuan Cao, and Karthik Narasimhan. Tree of thoughts: Deliberate problem solving with large language models. *Advances in neural information processing systems*, 36:11809–11822, 2023.
- [13] Michał Besta et al. Graph of thoughts: Solving elaborate problems with large language models. In *Proceedings of the AAAI Conference on Artificial Intelligence*, volume 38, pages 17682–17690, 2024.
- [14] Yao Yao, Zuchao Li, and Hai Zhao. Beyond chain-of-thought: Effective graph-of-thought reasoning in language models. In *Findings of the Association for Computational Linguistics: NAACL 2024*, pages 2901–2921, Mexico City, Mexico, 2024. Association for Computational Linguistics.
- [15] Shunyu Yao, Jeffrey Zhao, Dian Yu, Nan Du, Izhak Shafran, and Karthik Narasimhan. React: Synergizing reasoning and acting in language models. *arXiv preprint arXiv:2210.03629*, 2022.
- [16] Noah Shinn, Federico Cassano, Edward Berman, Ashwin Gopinath, Karthik Narasimhan, and Shunyu Yao. Reflexion: Language agents with verbal reinforcement learning. *arXiv preprint arXiv:2303.11366*, 2023.
- [17] Aman Madaan, Niket Tandon, Prakhar Gupta, Skyler Hallinan, Luyu Gao, Sarah Wiegrefe, Uri Alon, Nouha Dziri, Shrimai Prabhumoye, Yiming Yang, Shashank Gupta, Bodhisattwa Prasad Majumder, Katherine Hermann, Sean Welleck, Amir Yazdanbakhsh, and Peter Clark. Self-refine: Iterative refinement with self-feedback. *arXiv preprint arXiv:2303.17651*, 2023.
- [18] J. Wei et al. Browsecomp: A simple yet challenging benchmark for browsing agents. *arXiv preprint arXiv:2504.12516*, 2025.
- [19] Y. Pan et al. Weblinx: Real-world website navigation with multi-turn dialogue. *arXiv preprint arXiv:2402.05930*, 2024.
- [20] S. Zhou et al. Webarena: A realistic web environment for building autonomous agents. *arXiv preprint arXiv:2307.13854*, 2023.
- [21] Thibault Le Sellier De Chezelles et al. The browsergym ecosystem for web agent research. *arXiv preprint arXiv:2412.05467*, 2024.
- [22] Akari Asai et al. Self-rag: Learning to retrieve, generate, and critique through self-reflection. In *Proceedings of the Twelfth International Conference on Learning Representations (ICLR)*, 2024.
- [23] S.-Q. Yan et al. Corrective retrieval augmented generation. *arXiv preprint arXiv:2401.15884*, 2024.
- [24] B. Peng et al. Graph retrieval-augmented generation: A survey. *arXiv preprint arXiv:2408.08921*, 2024.
- [25] LangChain. Local deep researcher. <https://github.com/langchain-ai/local-deep-researcher>, 2025. GitHub repository. Version pinned at commit 8a5e220 (2025-08-08).

- [26] Yuqin Wang, Hyun-June Jang, Max Topel, Siva Dasetty, Yining Liu, Mohamed Ateia, Aaron Tam, Vepa Rozyyev, Ellie Ouyang, Wen Zhuang, Haihui Pu, Sang Soo Lee, Jeffrey Elam, Andrew Ferguson, Seth Darling, and Junhong Chen. Reversible ppt-level detection of perfluorooctane sulfonic acid in tap water using field-effect transistor sensors. *Nature Water*, 3:1187–1197, 2025.
- [27] Hui Lin, Junfeng Niu, Shangtao Liang, Chong Wang, Yujuan Wang, Fangyuan Jin, Qi Luo, Szu-Yin Chiang, and Qingguo Huang. Development of macroporous magnéli phase Ti_4O_7 ceramic materials: As an efficient anode for mineralization of poly- and perfluoroalkyl substances. *Chemical Engineering Journal*, 354:1058–1067, 2018.
- [28] Xuehu Zhong, Junwei Han, Lingling Chen, Wei Liu, Fei Jiao, Hong Zhu, and Wenqing Qin. Binding mechanisms of pvdf in lithium ion batteries. *Applied Surface Science*, 553:149564, 2021.
- [29] Rui Ding, Jianguo Liu, Kang Hua, Xuebin Wang, Xiaoben Zhang, Minhua Shao, Yuxin Chen, and Junhong Chen. Leveraging data mining, active learning, and domain adaptation for efficient discovery of advanced oxygen evolution electrocatalysts. *Science Advances*, 11(14):eadr9038, 2025.
- [30] T. V. K. Karthik, H. Martínez-García, F. Ortiz-Chi, C. G. Espinosa-González, J. G. Torres-Torres, A. G. Hernandez, S. Godavarthi, and M. K. Kesarla. CO_2 gas sensing properties of graphitic carbon nitride ($\text{g-c}_3\text{n}_4$) thin films. *Diamond and Related Materials*, 133:109736, 2023.
- [31] Joseph Cameron and Peter J. Skabara. The damaging effects of the acidity in pedot:pss on semiconductor device performance and solutions based on non-acidic alternatives. *Materials Horizons*, 7:1759–1772, 2020.
- [32] Sunil Kumar, Hyun Min Park, Tej Singh, Manjeet Kumar, and Yongho Seo. Long-term stability studies and applications of $\text{Ti}_3\text{C}_2\text{Tx}$ mxene. *International Journal of Energy Research*, 2023:5275439, 2023.
- [33] Kotesch Kumar Mandari and Misook Kang. $\text{g-c}_3\text{n}_4/\text{mxene}$ -based heterostructures: advanced catalysts for efficient and sustainable renewable energy production. *Advances in Industrial and Engineering Chemistry*, 1:14, 2025.
- [34] Andrew J. Bagnall, Ziwen Zhao, Mun Hon Cheah, and Alina Sekretareva. Re-evaluating the stability of Al_2O_3 barriers prepared by atomic layer deposition under electrochemical conditions. *ACS Applied Materials & Interfaces*, 17:48320–48333, 2025.
- [35] Santiago Miret, N. M. Anoop Krishnan, et al. Are llms ready for real-world materials discovery? *Nature Machine Intelligence*, 2025.
- [36] Adam Tauman Kalai, Ofir Nachum, Santosh S. Vempala, and Edwin Zhang. Why language models hallucinate. *arXiv preprint arXiv:2509.04664*, 2025.
- [37] Richard Tran, Janice Lan, Muhammed Shuaibi, Brandon M. Wood, Siddharth Goyal, Abhishek Das, Javier Heras-Domingo, Adeesh Kolluru, Ammar Rizvi, Nima Shoghi, Anuroop Sriram, Felix Therrien, Jehad Abed, Oleksandr Voznyy, Edward H. Sargent, Zachary Ulissi, and C. Lawrence Zitnick. The open catalyst 2022 (oc22) dataset and challenges for oxide electrocatalysts. *ACS Catalysis*, 13:3066–3084, 2023.
- [38] Luis Barroso-Luque, Muhammed Shuaibi, Xiang Fu, Brandon M. Wood, Misko Dzamba, Meng Gao, Ammar Rizvi, C. Lawrence Zitnick, and Zachary W. Ulissi. Open materials 2024 (omat24) inorganic materials dataset and models. *arXiv preprint arXiv:2410.12771*, 2024.
- [39] Brandon M. Wood, Misko Dzamba, Xiang Fu, Meng Gao, Muhammed Shuaibi, Luis Barroso-Luque, Kareem Abdelmaqsoud, Vahe Gharakhanyan, John R. Kitchin, Daniel S. Levine, Kyle Michel, Anuroop Sriram, Taco Cohen, Abhishek Das, Ammar Rizvi, Sushree Jagriti Sahoo, Zachary W. Ulissi, and C. Lawrence Zitnick. Uma: A family of universal models for atoms. *arXiv preprint arXiv:2506.23971*, 2025.
- [40] Orbital Materials. Orb, 2025. Research page.
- [41] Tanishq Gupta, Mohd Zaki, N. M. Anoop Krishnan, and Mausam. MatSciBERT: A materials domain language model for text mining and information extraction. *npj Computational Materials*, 8:102, 2022.
- [42] Amalie Trewartha, Nicholas Walker, Haoyan Huo, Sanghoon Lee, Kevin Cruse, John Dagdelen, Alexander Dunn, Kristin A. Persson, Gerbrand Ceder, and Anubhav Jain. Quantifying the advantage of domain-specific pre-training on named entity recognition tasks in materials science. *Patterns*, 3:100488, 2022.

- [43] Michiko Yoshitake, Fumitaka Sato, Hiroyuki Kawano, and Hiroshi Teraoka. Materialbert for natural language processing of materials science texts. *Science and Technology of Advanced Materials: Methods*, 2:372–380, 2022.
- [44] InternLM. Intern-s1, 2025. Model card.
- [45] Seyone Chithrananda, Gabriel Grand, and Bharath Ramsundar. Chemberta: Large-scale self-supervised pretraining for molecular property prediction. *arXiv preprint arXiv:2010.09885*, 2020.
- [46] Walid Ahmad, Elana Simon, Seyone Chithrananda, Gabriel Grand, and Bharath Ramsundar. Chemberta-2: Towards chemical foundation models. *arXiv preprint arXiv:2209.01712*, 2022.
- [47] Riya Singh, Aryan Amit Barsainyan, Rida Irfan, Connor Joseph Amorin, Stewart He, Tony Davis, Arun Thiagarajan, Shiva Sankaran, Seyone Chithrananda, Walid Ahmad, Derek Jones, Kevin McLoughlin, Hyojin Kim, Anoushka Bhutani, Shreyas Vinaya Sathyanarayana, Venkat Viswanathan, Jonathan E. Allen, and Bharath Ramsundar. Chemberta-3: An open source training framework for chemical foundation models. *ChemRxiv preprint ChemRxiv: 10.26434/chemrxiv-2025-4glrl*, 2025.
- [48] NVIDIA. Megamolbart, 2022. GitHub repository. Release: Aug 30, 2022. Accessed: 2025-08-19.
- [49] Jingjing Hu, Dan Guo, Zhan Si, Deguang Liu, Yunfeng Diao, Jing Zhang, Jinxing Zhou, and Meng Wang. Mol-mamba: Enhancing molecular representation with structural & electronic insights. *arXiv preprint arXiv:2412.16483*, 2025.
- [50] Nathan C. Frey, Ryan Soklaski, Simon Axelrod, Siddharth Samsi, Rafael Gómez-Bombarelli, Connor W. Coley, and Vijay Gadepally. Neural scaling of deep chemical models. *Nature Machine Intelligence*, 5:1297–1305, 2023.
- [51] Changwen Xu, Yuyang Wang, and Amir Barati Farimani. Transpolymer: a transformer-based language model for polymer property predictions. *npj Computational Materials*, 9:64, 2023.
- [52] Christopher Kuenneth and Rampi Ramprasad. polybert: a chemical language model to enable fully machine-driven ultrafast polymer informatics. *Nature Communications*, 14:4099, 2023.
- [53] Haoke Qiu, Lunyang Liu, Xuepeng Qiu, Xuemin Dai, Xiangling Ji, and Zhao-Yan Sun. Polync: a natural and chemical language model for the prediction of unified polymer properties. *Chemical Science*, 15:534–544, 2024.
- [54] Yeonghun Kang and Jihan Kim. Chatmof: an artificial intelligence system for predicting and generating metal–organic frameworks using large language models. *Nature Communications*, 15:4705, 2024.
- [55] Zhiling Zheng, Zichao Rong, Nakul Rampal, Christian Borgs, Jennifer T. Chayes, and Omar M. Yaghi. A gpt-4 reticular chemist for guiding mof discovery. *Angewandte Chemie International Edition*, 62(46):e202311983, 2023.
- [56] Ludi Wang, Xueqing Chen, Yi Du, Yuanchun Zhou, Yang Gao, and Wenjuan Cui. CataLM: Empowering catalyst design through large language models. *arXiv preprint arXiv:2405.17440*, 2024.
- [57] Luis M. Antunes, Keith T. Butler, and Ricardo Grau-Crespo. Crystal structure generation with autoregressive large language modeling. *Nature Communications*, 15:10570, 2024.
- [58] Claudio Zeni, Robert Pinsler, Daniel Zügner, Andrew Fowler, Matthew Horton, Xiang Fu, Zilong Wang, Aliaksandra Shysheya, Jonathan Crabbé, Shoko Ueda, Roberto Sordillo, Lixin Sun, Jake Smith, Bichlien Nguyen, Hannes Schulz, Sarah Lewis, Chin-Wei Huang, Ziheng Lu, Yichi Zhou, Han Yang, Hongxia Hao, Jielan Li, Chunlei Yang, Wenjie Li, Ryota Tomioka, and Tian Xie. A generative model for inorganic materials design. *Nature*, 639:624–632, 2025.
- [59] Merck KGaA. Synthia® retrosynthesis software. <https://www.synthiaonline.com/>, 2025. Accessed 2025-08-19.
- [60] Andres M. Bran, Sam Cox, Oliver Schilter, Carlo Baldassari, Andrew D. White, and Philippe Schwaller. Augmenting large language models with chemistry tools. *Nature Machine Intelligence*, 6:525–535, 2024.
- [61] Huan Zhang, Yu Song, Ziyu Hou, Santiago Miret, and Bang Liu. Honeycomb: A flexible llm-based agent system for materials science. *Findings of the Association for Computational Linguistics: EMNLP 2024*, pages 3369–3382, 2024.
- [62] Mengsong Wu, YaFei Wang, Yidong Ming, Yuqi An, Yuwei Wan, Wenliang Chen, Binbin Lin, Yuqiang Li, Tong Xie, and Dongzhan Zhou. Chematagent: Enhancing llms for chemistry and materials science through tree-search based tool learning. *arXiv preprint arXiv:2506.07551*, 2025.

- [63] Xiangru Tang, Tianyu Hu, Muyang Ye, Yanjun Shao, Xunjian Yin, Siru Ouyang, Wangchunshu Zhou, Pan Lu, Zhuosheng Zhang, Yilun Zhao, Arman Cohan, and Mark Gerstein. Chemagent: Self-updating library in large language models improves chemical reasoning. *arXiv preprint arXiv:2501.06590*, 2025.
- [64] Adib Bazgir, Rama Chandra Praneeth Madugula, and Yuwen Zhang. Matagent: A human-in-the-loop multi-agent llm framework for accelerating the material science discovery cycle. *AI4MAT-ICLR-2025 Poster*, 2025.
- [65] Zhucong Li, Bowei Zhang, Jin Xiao, Zhijian Zhou, Fenglei Cao, Jiaqing Liang, and Yuan Qi. Chemhas: Hierarchical agent stacking for enhancing chemistry tools. *arXiv preprint arXiv:2505.21569*, 2025.
- [66] Tonghui Wang, Ruipeng Li, Hossein Ardekani, Lucía Serrano-Luján, Jiantao Wang, Mahdi Ramezani, Ryan Wilmington, Mihirsinh Chauhan, Robert W. Epps, Kasra Darabi, Boyu Guo, Dali Sun, Milad Abolhasani, Kenan Gundogdu, and Aram Amassian. Sustainable materials acceleration platform reveals stable and efficient wide-bandgap metal halide perovskite alloys. *Matter*, 6:2963–2986, 2023.
- [67] IBM Research. Ibm roborxn for chemistry. <https://rxn.res.ibm.com/rxn/robo-rxn/>, 2020.
- [68] Wen Jie Ong, Piero Altoè, Justin S. Smith, Dallas Foster, Melisa Alkan, and Harry Petty. Revolutionizing ai-driven material discovery using nvidia ALCHEMI. *AI4AM 2025*, 2025.
- [69] Dario Lacalamita, Chiara Mongiovi, Grégorio Crini, and Nadia Morin-Crini. Cyclodextrins for the removal of per- and polyfluoroalkyl substances: a review. *Environmental Chemistry Letters*, 23:1713–1743, 2025.
- [70] Xiaoyu Zhu, Chen Cheng, Xingao Qin, and Ying Wang. β -cyclodextrin imprinted film embedded with methylene blue: A host-guest sensitive electrochemical strategy for pfas detection. *Journal of Hazardous Materials*, 485:136870, 2025.
- [71] Ri Wang, Zhi-Wei Lin, Max J. Klemes, Mohamed Ateia, Brittany Trang, Jieyuan Wang, Casey Ching, Damian E. Helbling, and William R. Dichtel. A tunable porous β -cyclodextrin polymer platform to understand and improve anionic pfas removal. *ACS Central Science*, 8:663–669, 2022.
- [72] Rosalba Pitruzzella, Alessandro Chiodi, Riccardo Rovida, Francesco Arcadio, Giovanni Porto, Simone Moretti, Gianfranco Brambilla, Luigi Zeni, and Nunzio Cennamo. An mip-based pfas sensor exploiting nanolayers on plastic optical fibers for ultra-wide and ultra-low detection ranges—a case study of pfas detection in river water. *Nanomaterials*, 14:1764, 2024.
- [73] Ting Liu, Chunyan Sang, Bolu Sun, Hua Cai, Hong Liu, Yuwei Liu, and Gengsheng He. Highly sensitive determination of perfluorooctanoic acid in food and river samples with an electrochemical platform based on mip and modified mwcnts. *Microchemical Journal*, 208:112328, 2025.
- [74] ChemicalBook. 1h,1h,2h,2h-perfluorooctyltriethoxysilane. https://www.chemicalbook.com/ChemicalProductProperty_EN_CB9474048.htm, 2025. CAS No. 51851-37-7. Accessed: 2025-11-21.
- [75] Junpeng Liu, Zaid A. Janjua, Martin Roe, Fang Xu, Barbara Turnbull, Kwing-So Choi, and Xianghui Hou. Super-hydrophobic/icephobic coatings based on silica nanoparticles modified by self-assembled monolayers. *Nanomaterials*, 6(12):232, 2016.
- [76] Yunlong Luo, Ashkan Khoshyan, Md. Al Amin, Annette L. Nolan, Fiona Robinson, Jim Fenstermacher, Junfeng Niu, Mallavarapu Megharaj, Ravi Naidu, and Cheng Fang. Ultrasound-enhanced magnéli phase Ti_4O_7 anodic oxidation of per- and polyfluoroalkyl substances (pfas) towards remediation of aqueous film forming foams (aff). *Science of the Total Environment*, 862:160836, 2023.
- [77] Chaimaa Gomri, Elissa Makhoul, Fatou Niang Koundia, Eddy Petit, Stephane Raffy, Mikhael Bechelany, Mona Semsarilar, and Marc Cretin. Electrochemical advanced oxidation combined to electro-fenton for effective treatment of perfluoroalkyl substances “pfas” in water using a magnéli phase-based anode. *Nanoscale Advances*, 7:261–268, 2025.
- [78] Rabid Ullah. Semiconductor ZnFe_2O_4 as efficient photocatalyst for the degradation of organic dyes: An update. *Journal of Chemical Reviews*, 5(4):466–476, 2023.
- [79] Ryan Goul, Jamie Wilt, Jagaran Acharya, Bo Liu, Dan Ewing, Matthew Casper, Alex Stramel, Alan Elliot, and Judy Z. Wu. Electron tunneling properties of Al_2O_3 tunnel barrier made using atomic layer deposition in multilayer devices. *AIP Advances*, 9:025018, 2019.

Table of Contents

Contents

1	Introduction	1
1.1	Related work	2
2	Method	2
2.1	Single DR Instance	2
2.2	DTorR: from perspectives to gap-driven expansion	3
3	Experiments	3
3.1	Experimental setup	3
3.2	Experimental results	4
4	Conclusion	10
A	Related Work in Physics ML Surrogates, Domain LLMs, and Agentic Systems	17
A.1	Physics-aligned surrogates and classical ML	17
A.2	Domain LLMs (non-agent)	17
A.3	Agentic systems for scientific inquiry	17
A.4	Gap to deep research at S3-S4/D4	18
B	Supplementary Figures	19
C	Nanomaterials and Device Topics	30
C.1	PFAS_2D_FET_Probes	30
C.2	LIB_Advanced_Binders	30
C.3	S_aureus_FET_Commercial_Probes	30
C.4	Wastewater_Resource_Recovery_Cats	30
C.5	OER_Wastewater_Resistant_Cats	30
C.6	Solar_Evap_Wastewater_Photothermal	30
C.7	Nutrient_Sensors_Anti_Interference	30
C.8	CO2_Sensing_2D_Materials	30
C.9	Printed_FET_Array_Process_Window	31
C.10	2D_Synaptic_Transistors_Practical	31
C.11	Microplastics_Sensing_2D	31
C.12	Antibiotics_Sensing_2D_Probes	31
C.13	Li_over_Na_Selectivity_Membranes	31
C.14	PFAS_Electro_Degradation	31
C.15	LiCoNi_Selective_Membranes	31
C.16	InSitu_Liquid_TEM_MoS2_Sensing	32
C.17	CO2RR_SOTA_and_Emerging_Cats	32
C.18	NextGen_Solar_Unconventional	32
C.19	Ambient_Pressure_Diamond_Growth	32
C.20	Diamane_Bandgap_Functionalization	32
C.21	LIB_Fluoroether_Anion_Receptor	32
C.22	ML_e_Tongue_for_Water	32
C.23	Batteryless_Stretchable_Biosensors	32
C.24	Mixed_Dimensional_Low_Noise_Transducers	33
C.25	Electro_Photo_Gated_Smart_Membranes	33
C.26	Transient_Biodegradable_Sensor_Nodes	33
C.27	Catalytic_Mineralization_of_Microplastics	33
D	Local DR Experimental Settings	34
D.1	Open-source LLMs and local RAG corpus	34
D.1.1	Corpus construction	34
D.2	Domain-Scoping Query Templates	35
D.2.1	Sensor Domain Template	35

	D.2.2	Energy and Environment Domain Template	36
	D.2.3	Semiconductor and Device Domain Template	38
	D.2.4	Catalysis Domain Template	39
E		LLM-as-Judge Rubric and Templates	40
	E.1	LLM-as-Judge Rubric Prompt (applied to DR Report)	40
	E.1.1	Definitions of the Five Dimensions (equal weights)	40
	E.1.2	Example raw response (DToR_gpt-oss120B_local500; Topic: PFAS FET sensor probe) — Claude 4 Opus (thinking)	40
	E.1.3	Example raw response (DToR_gpt-oss120B_local500; Topic: PFAS FET sensor probe) — Gemini 2.5 Pro	41
	E.1.4	Example raw response (DToR_gpt-oss120B_local500; Topic: PFAS FET sensor probe) — Grok 3 (thinking)	42
	E.1.5	Example raw response (DToR_gpt-oss120B_local500; Topic: PFAS FET sensor probe) — ChatGPT o3	42
	E.1.6	Example raw response (DToR_gpt-oss120B_local500; Topic: PFAS FET sensor probe) — ChatGPT o4 mini high	43
	E.2	A/B Dueling Prompt (DR Report A vs. DR Report B)	43
	E.2.1	Raw dueling response (DToR_gpt-oss120B_local500; Topic: PFAS FET sensor probe) — Claude 4 Opus (thinking)	44
	E.2.2	Raw dueling response (DToR_gpt-oss120B_local500; Topic: PFAS FET sensor probe) — Gemini 2.5 Pro	45
	E.2.3	Raw dueling response (DToR_gpt-oss120B_local500; Topic: PFAS FET sensor probe) — Grok 3 (thinking)	45
	E.2.4	Raw dueling response — ChatGPT o4 mini high	45
	E.2.5	Raw dueling response (DToR_gpt-oss120B_local500; Topic: PFAS FET sensor probe) — ChatGPT o3	46
F		Dry-Lab Validation Details	47
	F.1	DFT simulation settings	47
	F.2	PFAS FET Sensor Probe	50
	F.2.1	PFAS_2D_FET_Probes	50
	F.2.2	Selectivity Scoring for PFAS Sensor Performance	51
	F.3	PFAS Degradation	60
	F.3.1	PFAS_Electro_Degradation	60
	F.3.2	Multi-Metric Evaluation of PFAS Degradation Catalysts	63
	F.4	Battery Binder	76
	F.4.1	LIB_Advanced_Binders	76
	F.4.2	Battery Binder Adhesion Performance	78
	F.5	OER Stability	85
	F.5.1	OER_Wastewater_Resistant_Cats	85
	F.5.2	OER Catalyst Stability Assessment	90
	F.6	CO ₂ Sensor Probe	96
	F.6.1	CO ₂ _Sensing_2D_Materials	96
	F.6.2	CO ₂ Sensor Performance Evaluation	99
	F.7	Candidate Feasibility Discussions	104
G		Targeted Component Ablations	105
	G.1	Experimental setup	105
	G.2	Results and interpretation	105
H		Topic Analysis	106
I		Power Consumption Estimation	111
	I.1	Power estimation and LLM/RAG time decomposition.	111
	I.2	Empirical split of runtime into LLM vs. RAG.	111
	I.3	Energy calculation.	112

Appendix A Related Work in Physics ML Surrogates, Domain LLMs, and Agentic Systems

A.1 Physics-aligned surrogates and classical ML

Physics-guided predictive surrogates now operate at web-scale, with graph networks and equivariant models trained on massive curated corpora. For crystalline stability, GNoME trains large graph models and active-learning pipelines to propose millions of candidate structures and flag hundreds of thousands as likely stable—establishing that data+scale can systematically widen the known inorganic universe [9]. In catalysis, the Open Catalyst efforts formalized realistic workloads: OC20 introduced 1.28M DFT relaxations and 265M single-point evaluations for adsorbate-surface energetics and created standardized tasks (IS2RE/IS2RS/S2EF) with stringent generalization splits; OC22 extended to oxide electrocatalysts relevant to OER with more realistic catalysts and targets [10, 37]. New foundation-style datasets push further: OMat24 aggregates >110M DFT entries and releases strong baselines (e.g., Equiformer-V2) that achieve near-chemical-accuracy on multiple targets [38]; OMol25 analogously scales molecular DFT data to >100M calculations spanning tens of millions of unique molecules, enabling broad pretraining for small-molecule physics [11]. Complementing datasets, foundation models like the universal model of atoms (UMA) and Orb explore single architectures that transfer across chemistry and tasks, aiming for cross-domain generalization with shared tokenization/featurization of atoms and local environments [39, 40]. These surrogates excel at S1–S2 targets (bulk stability, adsorption energies, local structural relaxations) but are largely D1–D2 in operation: fixed-form predictors trained on equilibrium data, with limited capacity to reason about kinetics, synthesis windows, or device-level constraints that emerge at S3–S4. The net effect is that they remain superb "atoms-to-properties" engines, yet they do not autonomously help solve the long-horizon, multi-paper evidence assembly and process-aware planning needed, from atomic scale to device scale rationales [9, 10, 37, 38, 11, 39].

A.2 Domain LLMs (non-agent)

Domain LLMs span three useful roles. (i) Materials-text models (MatSciBERT/MatBERT/MaterialBERT) are trained on materials corpora to power entity/relation extraction, document classification, and graph building; MatSciBERT outperforms SciBERT on named entity recognition (NER) and relation tasks across curated benchmarks, while MatBERT shows that domain-specific pretraining significantly lifts NER F1 and sample efficiency in materials texts; MaterialBERT introduces a domain tokenizer/vocabulary tuned to materials literature, while Intern-S1 scales domain-specific reasoning capabilities [41, 42, 43, 44]. (ii) Chemical/polymer LLMs target sequence-level prediction/generation: ChemBERTa established transformer baselines and scaling trends for SMILES; ChemBERTa-2 pushed to 77M SMILES and showed consistent gains (and that multi-task regression pretraining can beat MLM (Masked Language Modeling) in transfer); ChemBERTa-3 contributes to open, end-to-end training infrastructure for chemical foundation models; MegaMolBART provides a large-scale generative sequence model optimized for molecular design, with MOL-Mamba introducing state-space models for efficient representation [45, 46, 47, 48, 49]. ChemGPT demonstrates generative scaling to >1B parameters with clear neural-scaling laws for chemical LLMs, clarifying how model/data scale trade off in practice [50]. In polymers, TransPolymer introduces a chemically-aware tokenizer and MLM pretraining that improves regression performances across ten benchmarks; polyBERT builds an end-to-end, ultrafast pipeline and screens 100M hypothetical polymers; PolyNC fuses natural-language and chemical-sequence inputs to improve unified polymer property prediction [51, 52, 53]. (iii) Generative/design LLMs for materials include ChatMOF and the GPT-4 Reticular Chemist for MOF proposals [54, 55], CataLM for catalyst design [56]; Crystal-LLM (autoregressive) generates crystal structures from composition, and MatterGen scales inorganic structure generation with validated discoveries and robust property control [54, 57, 58]. Collectively these models deliver flexible text/code/structure interfaces and strong S1–S2 performance—ideal for curation, candidate suggestion, or surrogate-assisted screening—but they are typically short-horizon (D1–D2): they answer prompts, not conduct hours-long, tool-grounded, hierarchical inquiry across conflicting literature [43, 42, 41, 53, 52, 51, 45, 46, 47, 50, 48, 54, 58, 57].

A.3 Agentic systems for scientific inquiry

Agent frameworks aim to orchestrate end-to-end inquiry: decompose goals, retrieve and reconcile evidence, use domain tools/simulators, and iteratively critique/plan. Early exemplars used rule/graph planning and Bayesian loops within constrained scopes—Chematica/SYNTHIA operationalized expert retrosynthesis

rules and heuristic search; CAMD framed autonomous design/make/test/learn for materials screening [59, 8]. LLM-based agents extend this with language-native decomposition and tool-use: ChemCrow connects models to chemistry tools (e.g., RDKit, databases) to complete realistic tasks [60]; HoneyComb provides a flexible materials-agent stack with retrieval/tooling and HPC hooks [61]; SciAgents formalizes multi-agent graph reasoning for scientific planning [6]. Recent hierarchical frameworks like El Agente introduce orchestration for complex quantum chemistry workflows [7], while systems such as CheMatAgent, ChemAgent, MatAgent, and ChemHAS further specialize in tool learning and human-in-the-loop coordination [62, 63, 64, 65]. Finally, "AI co-scientist" frameworks couple planning with web/code tools and emphasize evaluation and provenance [5]. Execution back-ends close the loop: A-Lab and RoboMapper demonstrate self-driving labs discovering and characterizing new materials [3, 66]; IBM RXN/RoboRXN links digital retrosynthesis with automated synthesis [67]; and NVIDIA ALCHEMI targets scaled infrastructure (data, models, and accelerated simulation) for materials discovery [68]. Despite progress, most agents today operate at D2–D3 depth and S1–S3 scope; they rarely sustain thousand-query retrieval runs, explicit topic-tree governance, or tight coupling to cross-domain process constraints that S3–S4 device problems demand. This is precisely the niche for deep-research agents: to deliver hierarchical planning, multi-stage local+web retrieval at scale, targeted tool/simulator calls, and systematic self-critique with dense provenance until a decision-ready synthesis emerges [59, 8, 60, 61, 6, 5, 3, 67, 68].

A.4 Gap to deep research at S3–S4/D4

Despite existing progress, the transition to S3–S4 nano-device complexity poses a fundamental barrier. The combinatorial explosion across materials, interfaces, processing parameters, and operational constraints creates hypothesis spaces where decisive insights lie at the intersections of disparate literature, conflicting reports, and cross-domain phenomena. Crucially, long-horizon, hierarchical evidence accumulation (D4) remains under-documented: many agents cap at D2–D3, with limited iterative loops, shallow coordination, and no explicit topic-tree control for breadth-then-depth synthesis. Commercial deep-research offerings introduced in 2025 enable multi-step inquiry but remain closed-source with limited controllability and local integration, reinforcing the need for open, on-prem frameworks tailored to proprietary materials workflows. DToR addresses this by treating each research node as an evidence-grounded state in a resource-bounded tree search, bridging the symbolic reasoning of ToT/GoT with the domain knowledge grounding required for scientific discovery. To our knowledge, DToR is the first open, on-prem framework that explicitly couples local domain RAG with gap-triggered web expansion within a resource-bounded tree to address S3–S4 materials discovery—a regime where neither pure surrogates nor closed commercial DR agents operate reliably.

Appendix B Supplementary Figures

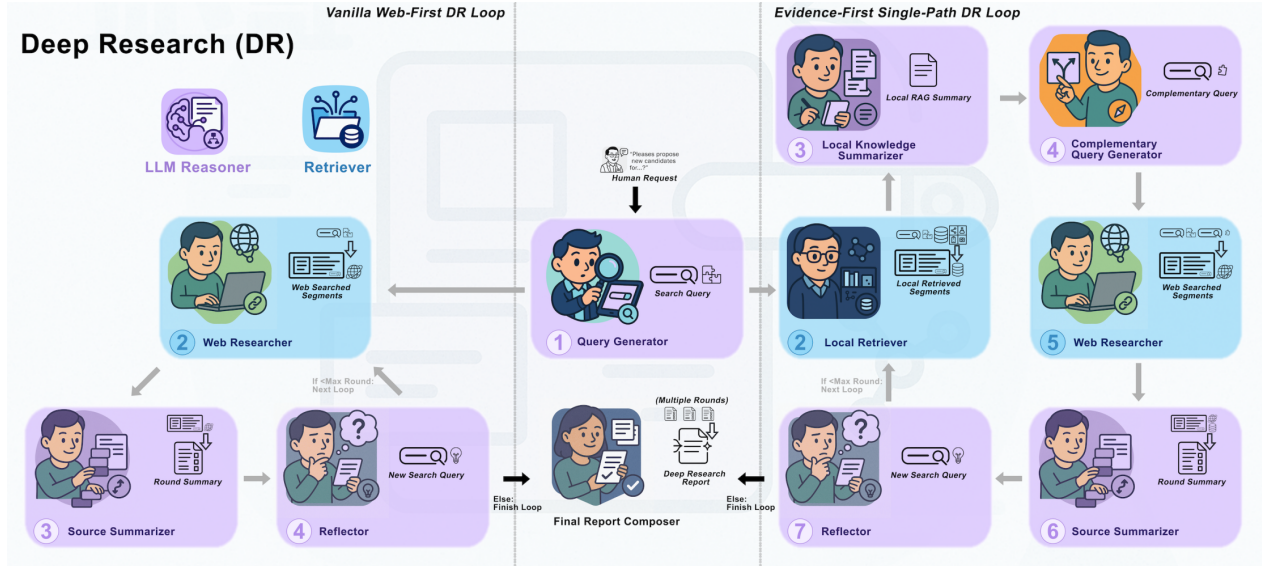


Figure S1: Schematic of the local evidence-first single DR instance in comparison with common web-first DR (Adapted from [25])

Inter-Critic Correlation Matrices: Pearson vs Spearman Comparison
Top: Linear relationships (Pearson r) | Bottom: Rank relationships (Spearman ρ)

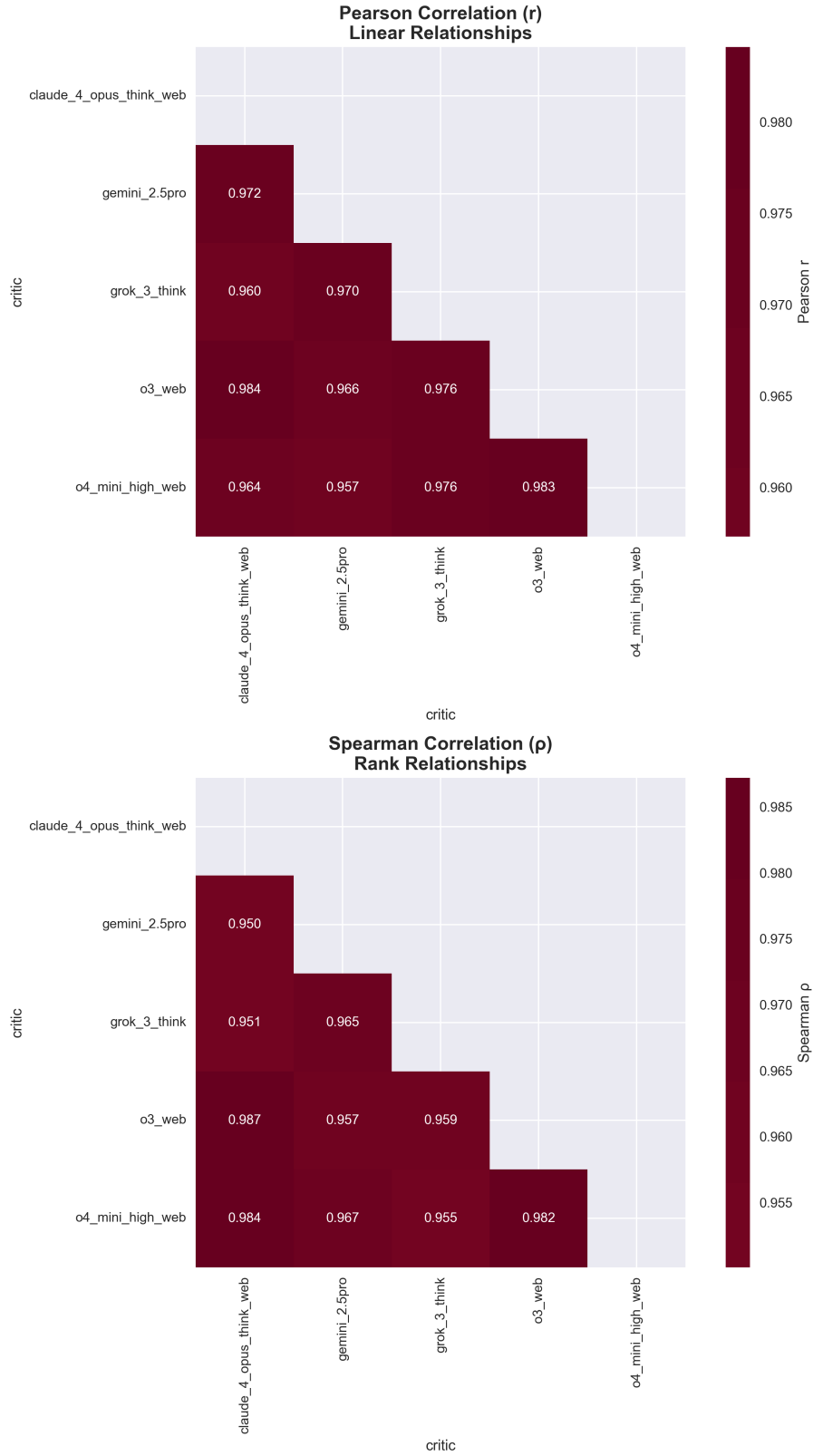


Figure S3: Rubric score agent agreement level over the five critic LLMs, computed by correlation factors. The average Pearson correlation is $p = 0.968$ on raw scores and Spearman correlation is $\rho = 0.967$ on rank orders.

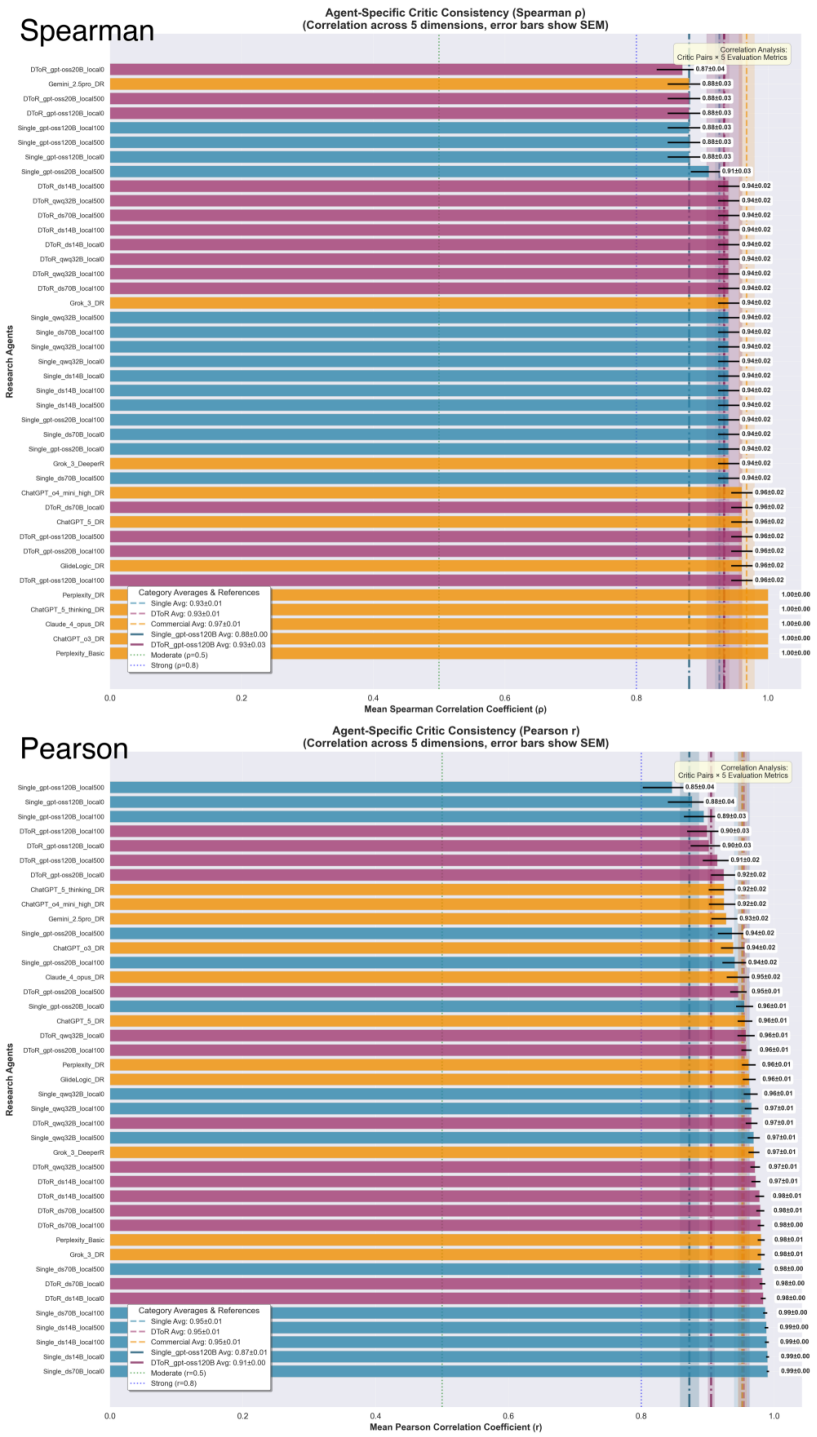


Figure S4: Agent-Specific Critic Consistency Analysis. Pearson correlation coefficients measuring linear agreement between critique LLMs across 5 evaluation dimensions (Relevance, Depth, Clarity, Applicability, Novelty) for each research agent. Spearman rank correlation coefficients measuring ordinal agreement between critics. Higher values indicate greater consensus among the 5 critique LLMs (Claude, Gemini, Grok, O3, O4) about each agent’s relative performance strengths and weaknesses. Data aggregated from 27 research topics \times 3 trials per agent. Perfect correlation ($\rho = 1.00$) indicates all critics completely agree on the ranking of an agent’s performance across the 5 dimensions.

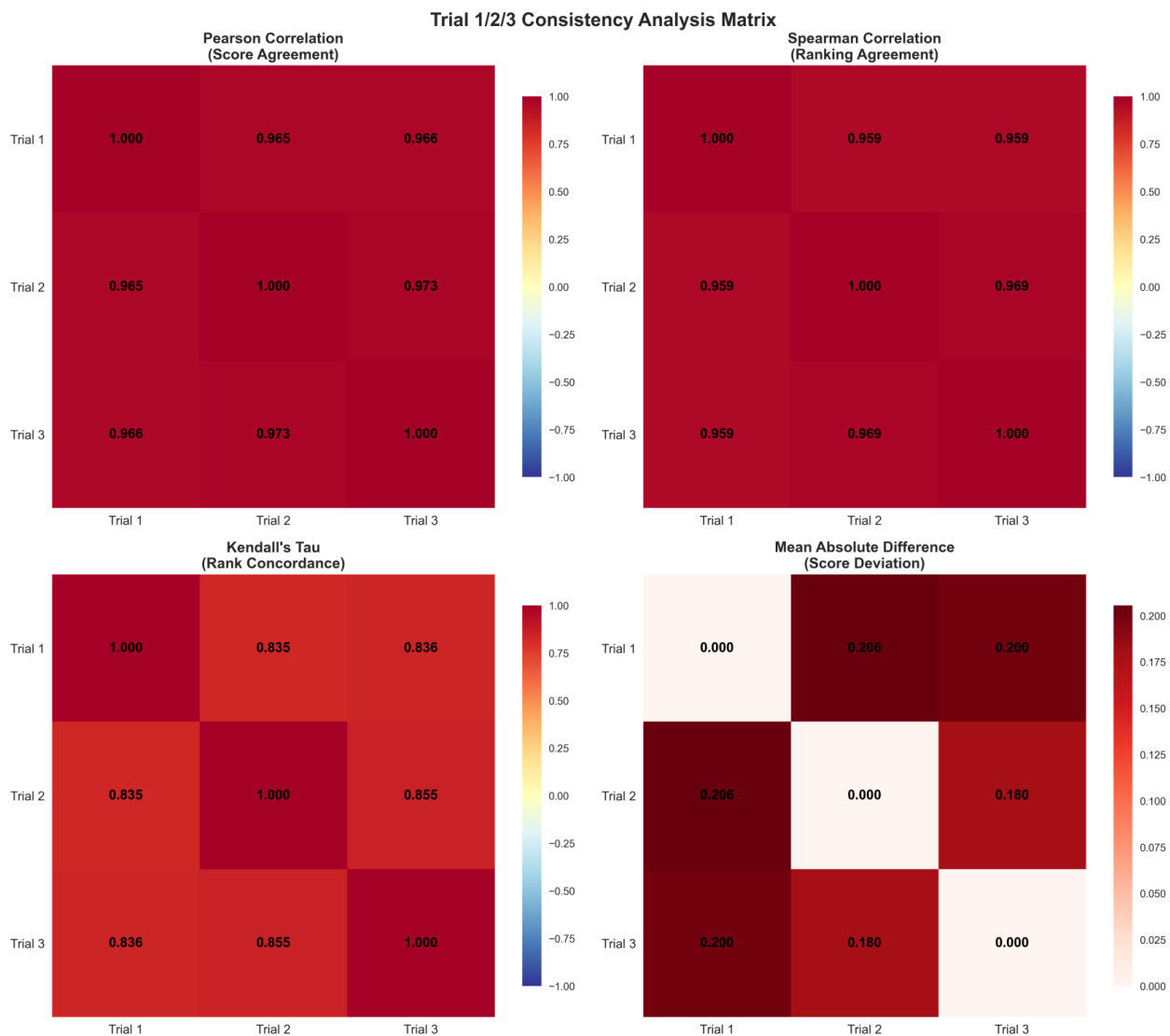
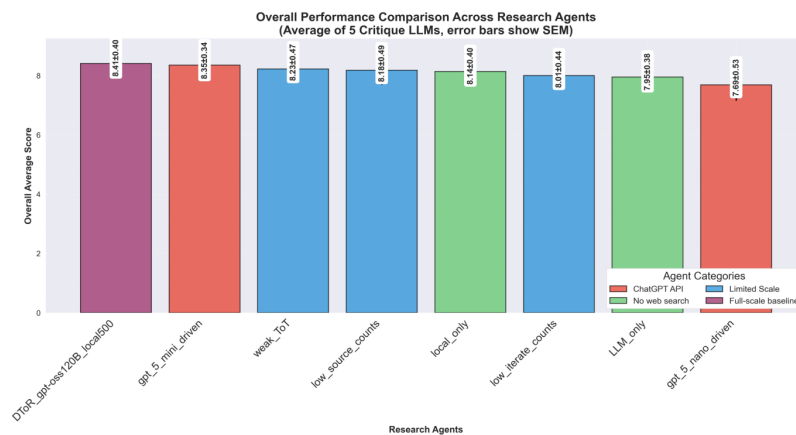
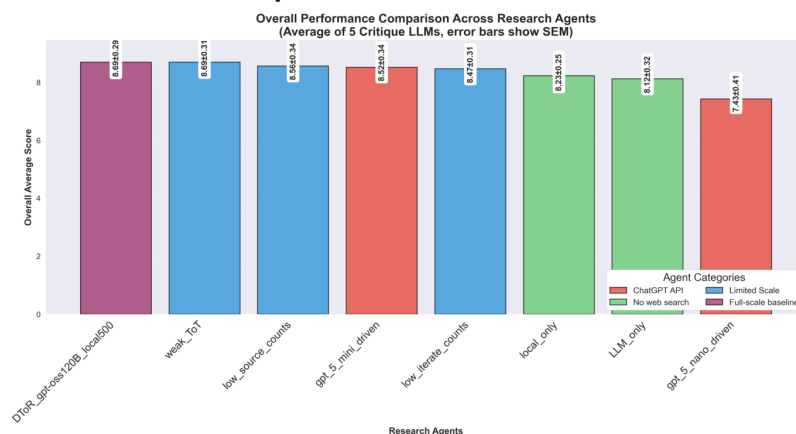


Figure S5: Trial-to-Trial Consistency Analysis Matrix. Four metrics assess reproducibility across three independent trials: (A) Pearson correlation measures score agreement, (B) Spearman correlation evaluates ranking consistency, (C) Kendall's tau provides alternative rank concordance, and (D) Mean absolute difference quantifies score deviations. Data aggregated across 27 topics, 41 agents, and 5 LLM critics. Higher correlations (>0.8) and lower deviations (<0.5) indicate excellent experimental reproducibility.

PFAS 2D FET Probes



LIB Fluoroether Anion Receptor



Microplastics Sensing 2D

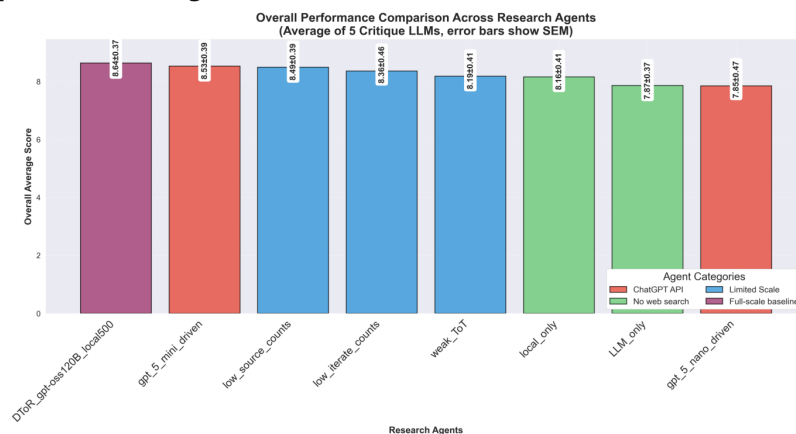
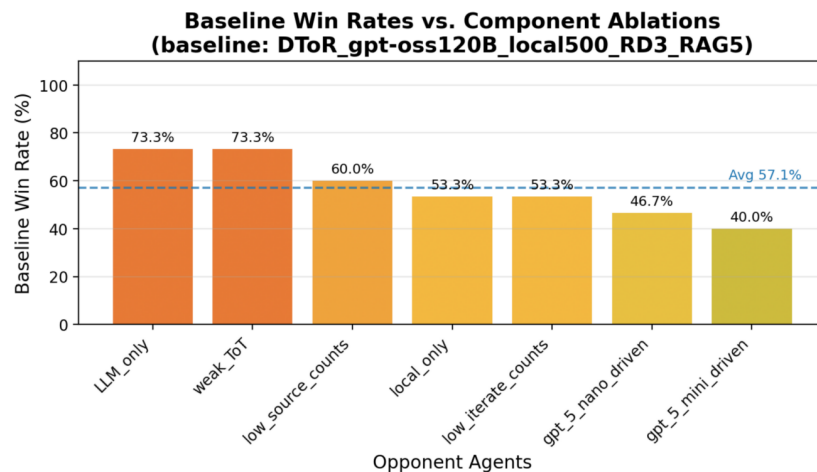
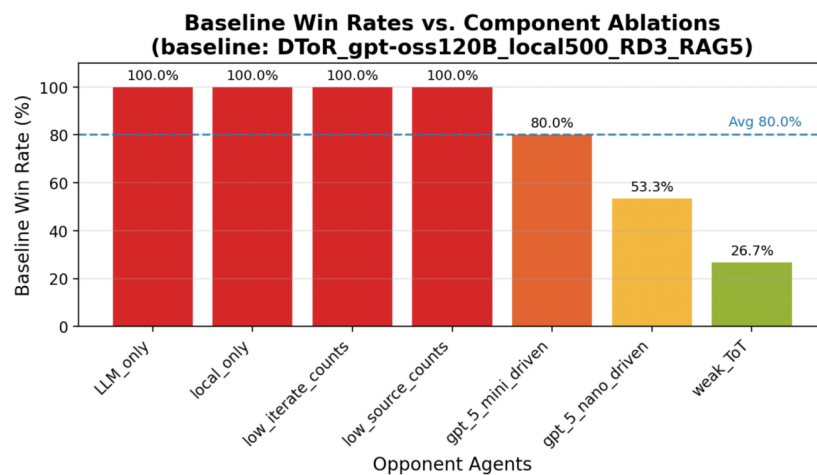


Figure S6: Targeted component ablations: Overall average scores (0-10 scale) for different research agent configurations across three scientific topics (LIB_Fluoroether_Anion_Receptor, Microplastics_Sensing_2D, PFAS_2D_FET_Probes), averaged over five critique LLMs with error bars showing SEM. Agent categories are distinguished by color: ChatGPT API (red), Full-scale baseline (purple), No web search (orange), and Limited Scale (blue/green). Dashed lines indicate baseline performance levels.

PFAS 2D FET Probes



LIB Fluoroether Anion Receptor



Microplastics Sensing 2D

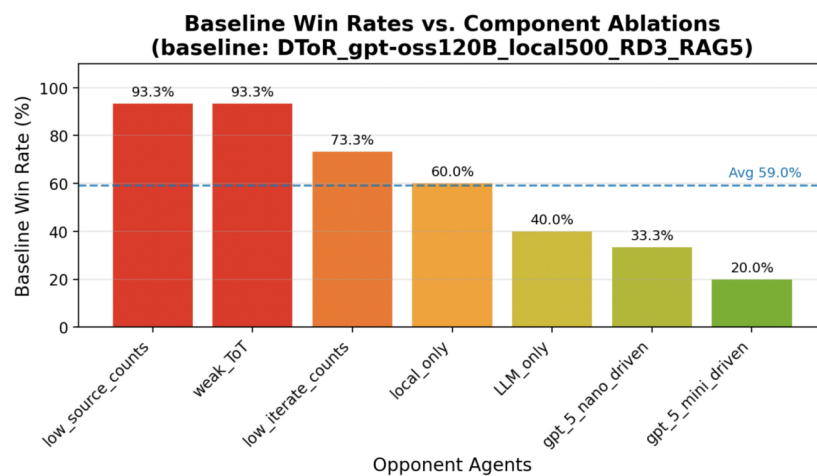
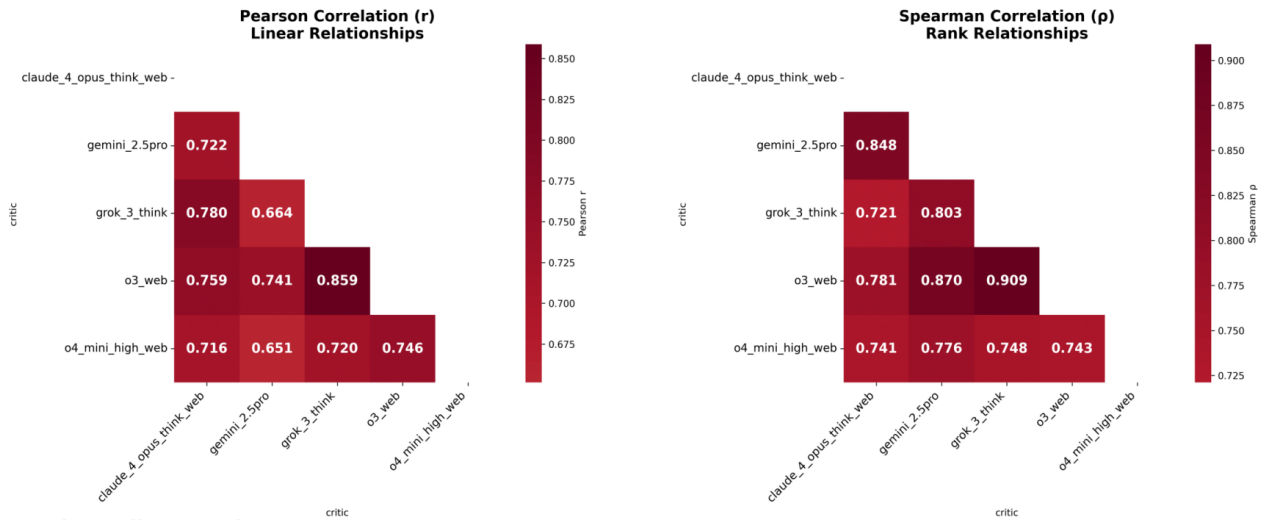


Figure S7: Targeted component ablations: Win rates of the full-scale baseline agent (DToR_gpt-oss120B_local500) competing against ablated opponents across three research topics. Dashed lines indicate average win rates for each topic.

5-Dimensional Rubric Consistency

Inter-Critic Correlation Matrices: Pearson vs Spearman Comparison
 Final Ablation DR (3 Topics Combined)
 Left: Linear relationships (Pearson r) | Right: Rank relationships (Spearman ρ)



In-pair Dueling Consistency

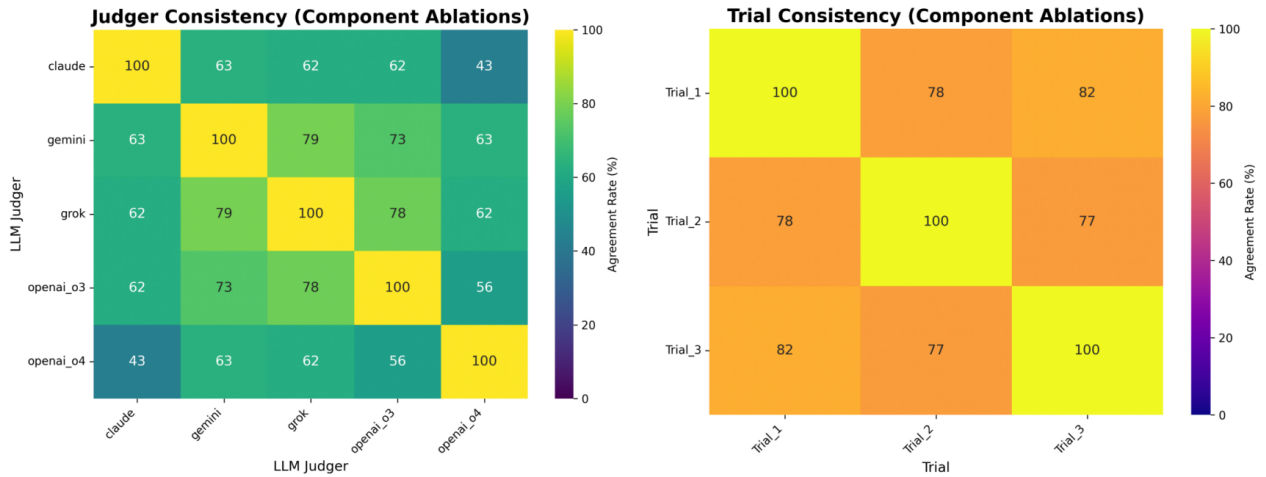


Figure S8: Targeted component ablations: Top: Inter-critic correlation matrices (Pearson and Spearman) showing agreement across five critique LLMs when evaluating research proposals on a 5-dimensional rubric across three topics. Bottom: In-pair dueling consistency heatmaps showing agreement rates across different LLM judges (left) and experimental trials (right) in binary comparison decisions.

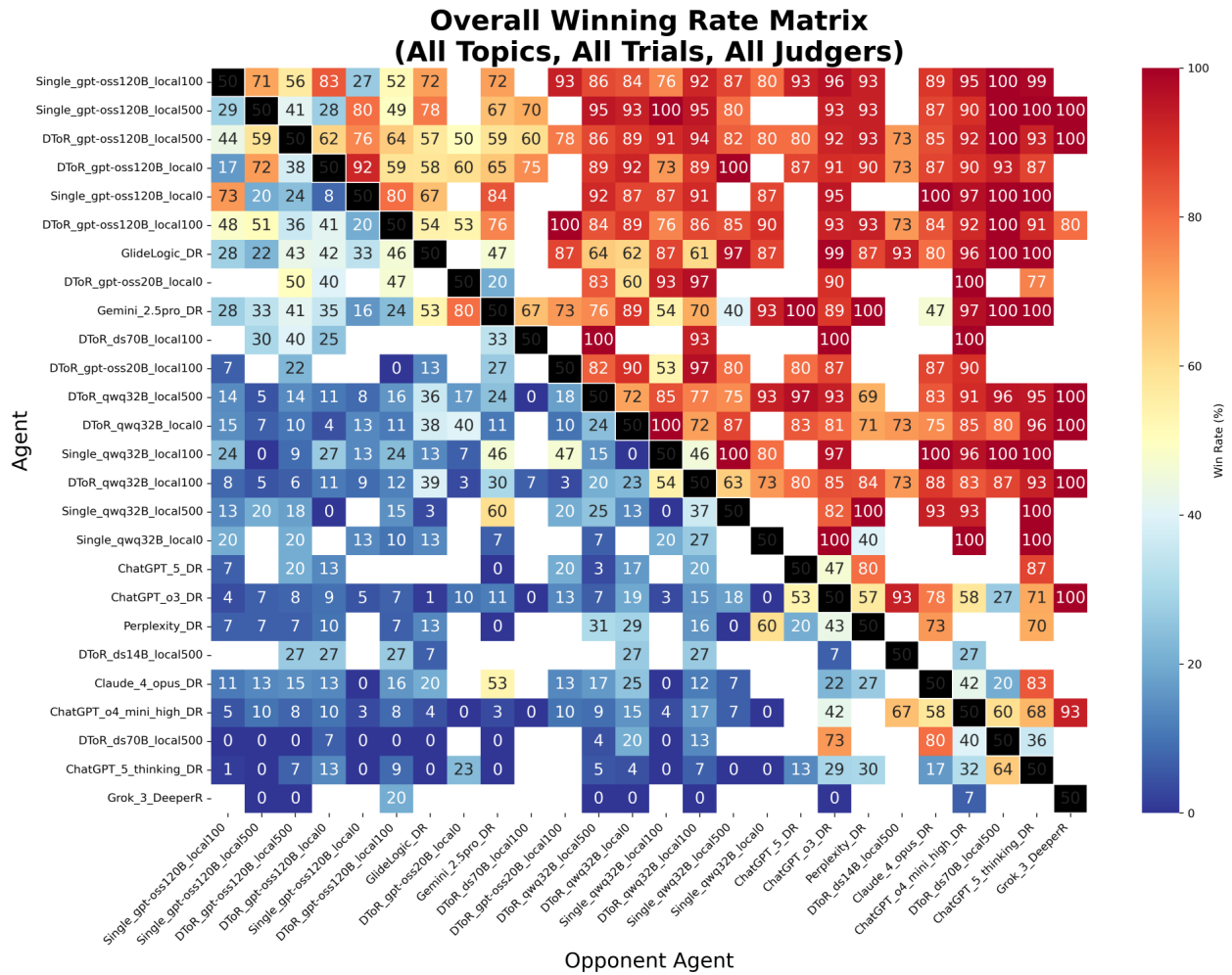


Figure S9: Overall Winning Matrix All Topics - Displays the comprehensive winning matrix with head-to-head performance comparisons between all agents across all research topics.

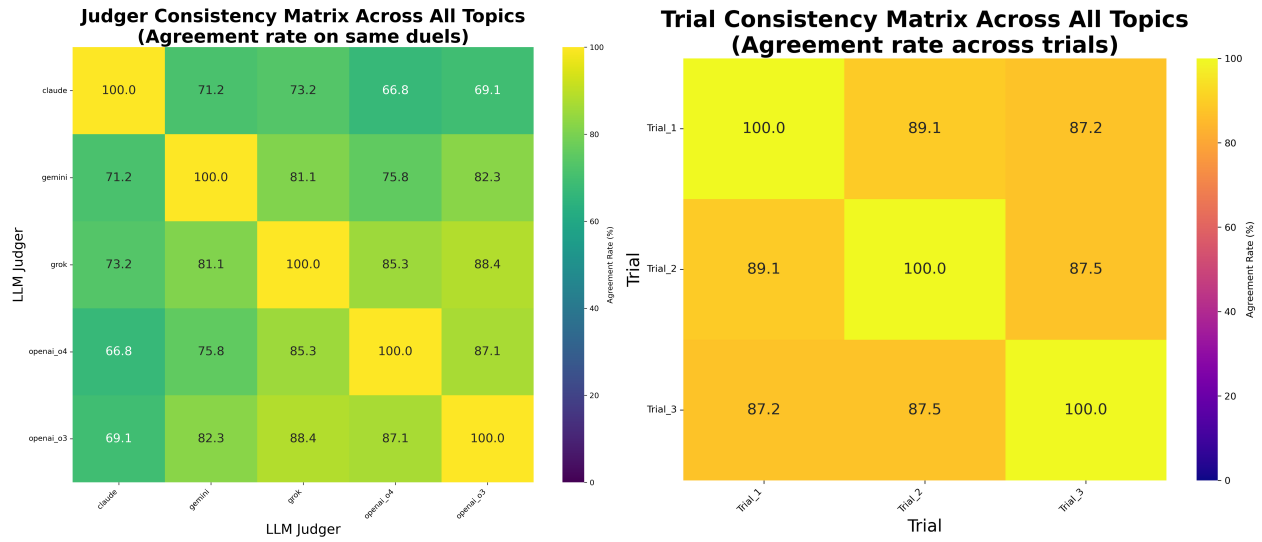


Figure S10: Consistency of in pair dueling. Left: Judge Consistency All Topics - Shows the consistency of judgment patterns across different research topics and agents, indicating how reliable the evaluation criteria are. Right: Trial Consistency All Topics - Displays the consistency of performance across multiple trials for each agent-topic combination, revealing the stability and reproducibility of results.

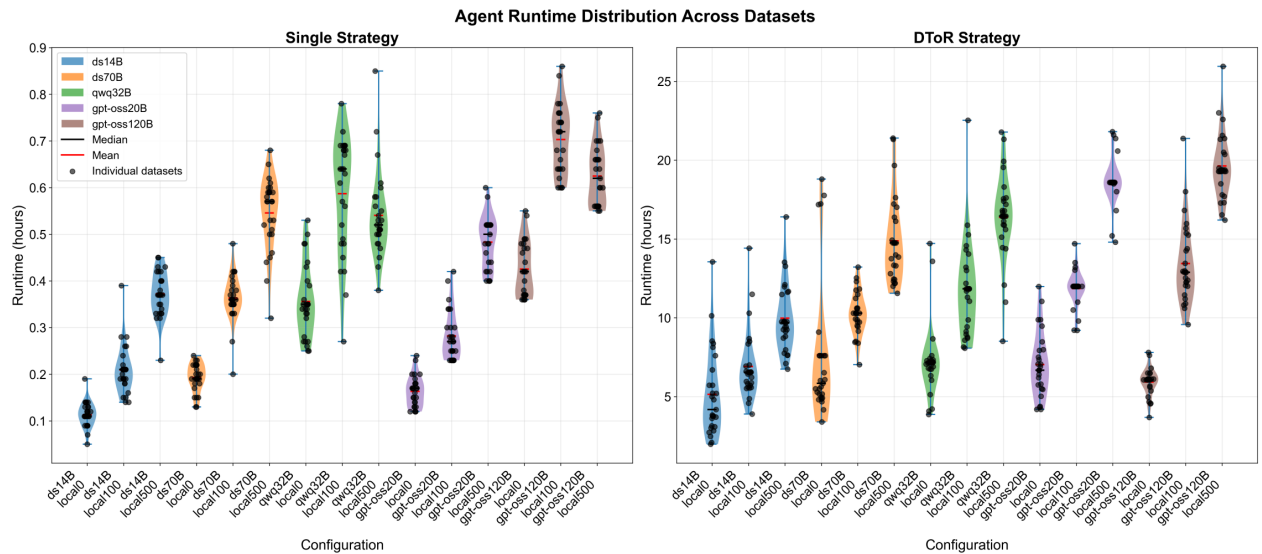


Figure S11: Violin plot visualizing the distribution of local DR agents runtime under different settings.

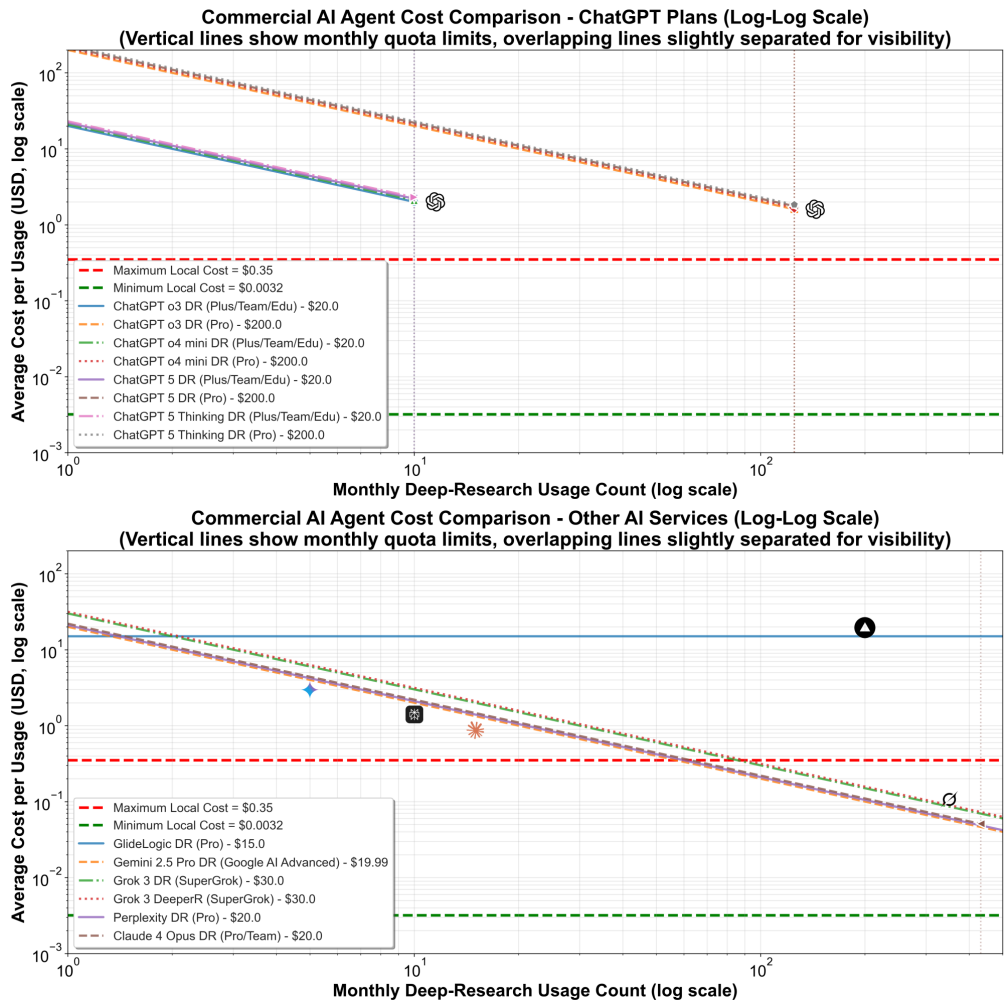


Figure S12: Comparison of cost over commercial DR agent solution with our local solution based on Chicago area electricity price October 2025.

Appendix C Nanomaterials and Device Topics

C.1 PFAS_2D_FET_Probes

Which two-dimensional (2D) nanomaterials or molecular probes—including novel, underexplored candidates—offer the greatest potential to achieve highly sensitive and selective detection of per- and polyfluoroalkyl substances (PFAS), or more broadly chemical and biological analytes, when integrated into a field-effect transistor (FET)-based sensor platform?

C.2 LIB_Advanced_Binders

Which advanced binder technologies are being developed to improve the performance and longevity of lithium-ion batteries?

C.3 S_aureus_FET_Commercial_Probes

How can emerging probe chemistries that are commercially available, cost-effective, and exhibit minimal batch-to-batch variability be used to develop a novel FET-based biosensor for detecting *Staphylococcus aureus*?

C.4 Wastewater_Resource_Recovery_Cats

Which nanostructured electrocatalyst materials demonstrate the highest selectivity and efficiency for electrochemical detection and recovery of critical resources (e.g., Li^+ , PO_4^{3-} , NH_4^+) from complex wastewater matrices, and what key performance metrics—such as selectivity, sensitivity, recovery rate, energy consumption, and operational stability—distinguish them?

C.5 OER_Wastewater_Resistant_Cats

Identify the top nanostructured electrocatalyst materials for driving the oxygen evolution reaction (OER) in complex wastewater matrices—such as high-chloride, high-organic-load, or multi-ion streams—, for each the material class/composition, comprehensively consider key performance metrics (overpotential at 10 mA cm^{-2} , Faradaic efficiency, stability), and the surface-engineering strategies that confer corrosion resistance and sustained activity in real effluent conditions.

C.6 Solar_Evap_Wastewater_Photothermal

What photothermal materials and system designs are most effective for solar-driven water evaporation in complex wastewater matrices—such as high-organic-load or multi-ion streams—and how do they compare in terms of material composition, solar-to-vapor conversion efficiency under one-sun illumination, evaporation rate, fouling resistance, and integrated resource-recovery functionalities?

C.7 Nutrient_Sensors_Anti_Interference

Which sensor probe materials/chemicals and designs offer the best performance in minimizing interference factors—such as competing ions, dissolved organic matter, pH fluctuations, and temperature variations—for accurate and selective detection of nutrients (e.g., nitrate, phosphate, ammonium) in complex water matrices, and what mitigation strategies do they employ?

C.8 CO2_Sensing_2D_Materials

Which two-dimensional materials—such as graphene derivatives, transition metal dichalcogenides, or MXenes—offer the highest CO_2 sensing performance in complex gas or aqueous environments, and how do they compare in terms of detection limit (ppm), selectivity against common interferents (e.g., O_2 , H_2O), response/recovery time, and long-term stability, including any functionalization or structural modifications that enhance these metrics? Think of novel candidates.

C.9 Printed_FET_Array_Process_Window

Which printed-electronics fabrication parameters and post-processing strategies—such as ink viscosity, printing speed and resolution, substrate surface energy, annealing temperature profiles, and in-line calibration methods—have been shown to minimize device-to-device variability in FET sensor arrays, and what specific process windows achieve low variation in threshold voltage and field-effect mobility?

C.10 2D_Synaptic_Transistors_Practical

Which two-dimensional material platforms (e.g., MoS₂, WSe₂, black phosphorus, h-BN), device architectures (e.g., floating-gate, ionic-gated, dual-gate), and fabrication protocols (e.g., channel thickness control, dielectric engineering, contact metallurgy) have been shown to optimize synaptic transistor performance—specifically in terms of energy per event, weight-update linearity, retention time, and cycling endurance—for neuromorphic sensing applications? Think of most practical and promising candidates.

C.11 Microplastics_Sensing_2D

Which two-dimensional material platforms (e.g., graphene derivatives, transition metal dichalcogenides, MXenes), molecular recognition elements (e.g., molecularly imprinted polymers, aptamers, peptide receptors), and device integration strategies (e.g., FET, electrochemical impedance, photonic transduction) have demonstrated the highest sensitivity, selectivity against organic matter and ionic interferents, and rapid response times for detecting micro- and nanoplastic particles in complex water matrices? Think of novel candidates.

C.12 Antibiotics_Sensing_2D_Probes

Which commercially available, cost-effective probe chemistries (e.g., thiolated DNA aptamers, antibody mimetics, conductive MIPs) combined with two-dimensional nanomaterial transducer platforms (e.g., WS₂ FETs, graphene field-effect sensors, nanotube-extended gate FETs) deliver the lowest detection limits, minimal batch variability, and robust performance for sensing trace levels of pharmaceutical antibiotics in diverse aqueous waterbody.

C.13 Li_over_Na_Selectivity_Membranes

What material or membrane exhibits the highest selectivity for Li⁺ over Na⁺ in aqueous systems, given their nearly identical hydrated ionic radii and solvation environments? Beyond crown-ether-functionalized polymers, what novel or unexpected materials—such as bioinspired ultrahigh-selectivity membranes or covalent organic framework nanochannels—might provide breakthrough Li⁺ discrimination over Na⁺? Find novel and promising candidates.

C.14 PFAS_Electro_Degradation

Which novel electrode materials can achieve efficient PFAS degradation under ambient aqueous electrochemical conditions, delivering both high mineralization and defluorination rates? What intrinsic properties—such as PFAS adsorption affinity, reactive oxygen species generation capacity, and C–F bond activation energy—should be optimized to guide their discovery?

C.15 LiCoNi_Selective_Membranes

Which membrane materials can effectively separate Li⁺, Co²⁺, and Ni²⁺ ions from aqueous solutions by leveraging selective transport properties—such as tailored pore sizes, specific surface functionalizations, and charge affinities—and what membrane design principles optimize both selectivity and permeability? Think of potential novel, effective, and practical candidates.

C.16 InSitu_Liquid_TEM_MoS2_Sensing

How can in situ liquid cell TEM be employed to directly visualize the real-time adsorption and structural changes of 2D MoS₂ nanosheets used in aqueous FET sensors during analyte binding? What fluid cell configurations and electron dose parameters are necessary to preserve native water-material interfaces while capturing high-resolution sensing events without beam-induced artifacts?

C.17 CO2RR_SOTA_and_Emerging_Cats

Given the current landscape of CO₂ electroreduction, which state-of-the-art catalyst platforms—such as oxide-derived copper, single-atom catalysts on nitrogen-doped carbon supports, or metal-organic framework-derived materials—demonstrate the highest activity and selectivity? Moreover, what emerging catalytic systems or novel heterostructures beyond these examples could feasibly outperform today's leading electrocatalysts in terms of faradaic efficiency and stability?

C.18 NextGen_Solar_Unconventional

Perovskite-silicon tandem cells, organic photovoltaics, and quantum-dot solar cells currently represent the forefront of next-generation solar technologies. Beyond these established platforms, which unconventional material classes or innovative device architectures—such as chalcogenide perovskites, 2D semiconductor heterostructures, or ferroelectric photovoltaic systems—offer the most unexpected promise for achieving breakthroughs in efficiency, stability, and scalability?

C.19 Ambient_Pressure_Diamond_Growth

How can ambient-pressure diamond synthesis using a Ga-Ni-Fe-Si liquid-metal alloy at 1 atm and 1025 °C be adapted to produce larger-area diamond films or oriented single crystals, and what key mechanistic steps govern nucleation and growth kinetics under these mild-pressure conditions?

C.20 Diamane_Bandgap_Functionalization

What chemical functionalizations or reaction pathways are most promising for tuning the electronic bandgap and mechanical stability of diamane-like 2D diamond films formed via sp²-to-sp³ conversion, and how might those modifications influence their integration into nanoelectronic devices?

C.21 LIB_Fluoroether_Anion_Receptor

Search for novel fluorinated ether-based electrolyte candidates that incorporate covalently bound anion-receptor motifs (e.g. boron- or phosphorus-centered groups) to deliver oxidative stability beyond 5.6 V, Li⁺ transference numbers above 0.8, and minimal interfacial impedance on lithium-metal anodes.

C.22 ML_e_Tongue_for_Water

Which mixed-material (e.g., graphene/2D) multi-sensor arrays with on-chip QA/QC and pattern-recognition deliver robust mixture fingerprinting (metals + microbes + organics) in flowing water, with automated drift/fault handling for field deployment?

C.23 Batteryless_Stretchable_Biosensors

Which tribo/piezo-powered, skin-conformal platforms (CNT/graphene networks, ionic gels) sustain continuous metabolite/ion monitoring without batteries—what power densities and duty-cycled readouts are practical for week-scale operation?

C.24 Mixed_Dimensional_Low_Noise_Transducers

Which 2D-0D/2D-1D/2D-3D vdW stacks (e.g., MoS₂-QD, CNT-graphene) best combine strong capture/absorption with high-mobility transport to push FET/photodetector responsivity and baseline stability in real media?

C.25 Electro_Photo_Gated_Smart_Membranes

Which electrically gated or photo-responsive nanochannels (MXene/COF/polymer hybrids) deliver on-demand selectivity and anti-fouling for ion separations and resource recovery in wastewater, and what gating “on/off” ratios and cycling lifetimes are state-of-the-art?

C.26 Transient_Biodegradable_Sensor_Nodes

Which dissolvable conductors, dielectrics, and encapsulants enable time-programmed water/soil sensors that operate stably for weeks then resorb without e-waste—what degradation kinetics and wireless/data-retention strategies are most practical?

C.27 Catalytic_Mineralization_of_Microplastics

Which ROS-generating photocatalysts and micromotor architectures achieve verifiable depolymerization/mineralization of common MPs (PE, PP, PET) in real waters—what mineralization fractions, spectra, and by-product toxicology benchmarks define “true cleanup”?

Appendix D Local DR Experimental Settings

D.1 Open-source LLMs and local RAG corpus

We implement the framework in LangGraph and deploy three low-deployment-cost, open-source LLMs—DeepSeek-R1-14B, DeepSeek-R1-70B, QwQ-32B, gpt-oss-20B, and gpt-oss-120B—served locally via Ollama. All agent prompts and tool I/O use a JSON/tool-calling discipline for determinism and easy parsing, and the same research node (RN) described in Algorithm 2 is the unit of work in the controller (Algorithm 3 DToR). To provision representative, application-driven knowledge for nanomaterials and devices, we build a standardized Chroma vector store spanning 1,136,297 full-text papers organized around four pillars: sensors, batteries, catalysis, and semiconductors. The corpus is queried first under a local-first RAG policy; complementary web retrieval is invoked only when Algorithm 2 (local evidence-first)’s reflection detects unresolved knowledge gaps. Consistent with our emphasis on report-level usefulness rather than information retrieval (IR) benchmarking, the local-first RAG layer is treated as a routine, swappable component; DToR only triggers complementary web evidence upon explicit knowledge gaps and resolves cross-source conflicts by evidence majority \rightarrow recency \rightarrow domain authority. To make domain coverage portable and auditable without exposing any local texts or indices, we release the exact domain-scoping query templates corresponding to these four pillars. In practice we provide templates for sensors, energy/environment (covering batteries), semiconductors, and catalysis so others can target the same scope with their own holdings while keeping the orchestration identical.

D.1.1 Corpus construction

Raw full texts are normalized with a cleaning pipeline designed for scientific documents at scale. The cleaner (i) preserves section structure and headers, (ii) retains LaTeX/MathJax equations and common math environments via stable markers, (iii) standardizes tables into a compact textual schema, (iv) normalizes URLs/DOIs and citation markers instead of stripping them, and (v) removes XML/HTML artifacts and noisy back matter conservatively. For long inputs, we apply sliding-window tokenization (default window 8192 tokens, stride 4096) or a section-aware variant that respects detected boundaries, yielding JSONL suitable for downstream training or indexing. As our focus is on the DToR orchestration, we adhere to widely used, off-the-shelf preparation and vector-indexing practices; the corpus layer functions as a routine, swappable component rather than a methodological contribution. To enable scope-equivalent replication across different holdings, we release the exact domain-scoping query templates for sensors, energy/environment (including batteries), semiconductors, and catalysis; users may instantiate a local store with their customary institutional pipelines and preferred indexers.

Indexing and retrieval Cleaned texts are split with a recursive character splitter (default chunk size 2500, overlap 500) and embedded using BAAI/bge-m3. Each chunk carries rich metadata (paper id, DOI, chunk id/index, source path, shard id) to support provenance and de-duplication. Embeddings are persisted in Chroma, enabling fast k-NN retrieval and incremental persistence during large ingestions. For robustness across machines, the store is partitioned into 500 volumes (shards). This organization serves two purposes: (1) controllable breadth—DToR can expand to additional volumes when the analyst decides to broaden coverage—and (2) bounded depth/latency—branches can be pruned once depth or evidence sufficiency is reached, without touching unrelated volumes. To mitigate licensing and privacy risk, our local corpus is restricted to institutionally licensed or open sources, and we release only the domain-scoping query templates—not texts or indices—so others can replicate scope without redistributing copyrighted content or PII.

Policy integration In each research node, local retrieval is attempted first; summaries are synthesized from local evidence. Only when reflection surfaces concrete gaps does the controller expand (selecting additional volumes and spawning new RNs) or prune (stopping further growth of a branch). This strategy couples breadth (multi-volume exploration across pillars) with depth (iterative drilling within a volume) while keeping costs predictable on commodity hardware and avoiding external dependencies during the main research loop.

Agent Configuration By default, we run all agents in a local-first configuration with cost-aware web fallback. Concretely, both single-agent DR and DToR branches use a research depth of 3 iterations, each RN queries the local Chroma first with top-k = 5, and only then invokes web search—by default DuckDuckGo—to avoid API fees. In DToR mode, breadth-depth is bounded with max branches = 3,

max branch depth = 3, nodes per branch = 100, and a global cap of 500 nodes per experiment, ensuring predictable latency and compute. Models are served locally via Ollama; RAG is enabled by default with BAAI/bge-m3 embeddings, and we preserve document fidelity via full-page fetch and safe output hygiene. All parameters remain user-tunable through the configuration/RunnableConfig to trade off coverage, latency, and cost—for example, increasing depth or top-k for harder queries, or switching web backends when budgets permit.

D.2 Domain-Scoping Query Templates

The templates below define the *domain coverage* used by our local-first pipeline (sensors, energy/environment, semiconductors, catalysis). They are released to enable others to target the same topic scope with their own collections and entitlements.

D.2.1 Sensor Domain Template

```
(
  TITLE-ABS-KEY(
    (
      "Optical" OR "Gas" OR "Pressure" OR "Thermal" OR "Magnetic" OR "Acoustic" OR
      "Humidity" OR "Strain" OR
      "Flexible" OR "Wearable" OR "Piezoelectric" OR "Photoelectric" OR "Biosensing" OR
      "Nanofiber" OR
      "Electrochemical" OR "RFID" OR "Environmental monitoring" OR "Photonics" OR
      "Nanowire" OR "Quantum" OR
      "Water quality" OR "Environmental" OR "Pollution detection" OR "Biological" OR
      "Biomarker" OR "VOC" OR
      "Medical" OR "Health monitoring" OR "Diagnostic" OR "Smart" OR "IoT" OR
      "Graphene-based" OR "Nano" OR
      "Agricultural" OR "Industrial" OR "Mercury ion" OR "Heavy metal ion" OR
      "Low-concentration gas" OR
      "CO" OR "H2" OR "NO2" OR "NH3" OR "Protein" OR "DNA" OR "Bacteria" OR
      "Nanocomposite" OR
      "Flexible electronic" OR "Food safety" OR "Air quality"
    )
    AND ("detector" OR "sensor")
  )
)

OR TITLE-ABS-KEY(
  (
    "biosensor" OR "chemical sensor" OR "gas sensor" OR "humidity sensor" OR "pressure
    sensor" OR
    "strain gauge" OR "photodetector" OR "phototransistor" OR "chemiresistive" OR
    "chemiresistor" OR
    "field-effect transistor" OR FET OR ISFET OR EGFET OR OFET OR GFET OR BioFET OR
    "electrolyte-gated transistor" OR "lab-on-a-chip" OR "microfluidic*" OR "surface
    acoustic wave" OR SAW OR
    "quartz crystal microbalance" OR QCM OR "surface plasmon resonance" OR SPR OR SERS
  )
  OR
  "electrochemical impedance spectroscopy" OR EIS OR "potentiometric" OR
  "amperometric" OR "voltammetric"
)
AND ("sensor*" OR "detector*" OR "transducer*" OR "FET" OR "transistor")
)

OR TITLE-ABS-KEY(
  (
    "H2S" OR "SO2" OR "NO" OR "O3" OR "CO2" OR "CH4" OR "ethanol" OR "methanol" OR
    "acetone" OR "toluene" OR
  )
)
```

```

    "benzene" OR "formaldehyde" OR "isopropanol" OR "xylene" OR "hydrogen peroxide" OR
    "glucose" OR "urea" OR
    "lactate"
  )
  AND ("sensor*" OR "detector*" OR "biosensing" OR "chemosensing")
)

OR TITLE-ABS-KEY(
  "graphene oxide" OR "reduced graphene oxide" OR rGO OR "carbon nanotube" OR CNT OR
  "nanoribbon" OR "nanotube" OR
  MXene OR "Ti3C2Tx" OR MoS2 OR WS2 OR WSe2 OR "transition metal dichalcogenide*" OR
  TMD
)

OR TITLE-ABS-KEY(
  "advanced sensor network" OR "real-time monitoring" OR "smart sensor network" OR
  "integrated sensor network" OR "biosensing platform"
)

OR TITLE-ABS-KEY(
  "wireless sensor network" OR WSN OR "edge sensing" OR "edge computing" OR "digital
  twin"
)

OR TITLE-ABS-KEY(
  "selective binding" OR "molecular recognition" OR "binding affinity" OR "synthetic
  receptor" OR
  "probe design" OR "molecular docking" OR "computational probe design" OR "artificial
  binding site"
)

OR TITLE-ABS-KEY(
  "host-guest" OR "supramolecular" OR "molecular imprint*" OR MIP OR "affinity sensor"
  OR "bioprobe"
)

OR TITLE-ABS-KEY(
  "hydrocarbon binding" OR "non-polar molecule" OR "hydrocarbon adsorption" OR
  "pi-pi interaction" OR "van der Waals"
)

OR TITLE-ABS-KEY(
  "drug discovery" AND (
    "ligand receptor" OR "structure-based design" OR "biochemical assay" OR
    "high-throughput screening" OR "aptamer" OR "peptide probe"
  )
)

AND ( LIMIT-TO ( DOCTYPE , "ar" ) )
AND ( LIMIT-TO ( LANGUAGE , "English" ) )

```

D.2.2 Energy and Environment Domain Template

```

(
  TITLE-ABS-KEY(
    (
      "Lithium-ion battery" OR "Supercapacitor" OR "Fuel cell" OR "Flow battery" OR
      "Graphene battery" OR
      "Sodium-ion battery" OR "Flexible battery" OR "Fast charging technology" OR
      "Next-generation battery technologies" OR "Quantum batteries" OR "Redox flow
      batteries" OR "Metal-air batteries" OR
    )
  )
)

```

"Thermal batteries" OR "Biodegradable batteries" OR "Ultrafast charging batteries"
 OR
 "Solar rechargeable batteries" OR "Lithium-sulfur battery" OR "Potassium-ion
 battery" OR "Solid-state battery" OR
 "Green energy storage" OR "CO2 capture" OR "Graphene-Sn hybrids" OR
 "Vertically-oriented graphene" OR
 "Graphene-SnO2 nanoparticle structures" OR "High-porosity graphene" OR "Graphene
 nanoparticle hybrids" OR
 "Energy density" OR "Cycle life" OR "Safety" OR "Sustainability" OR "Electrolyte
 innovation" OR
 "Anode materials" OR "Cathode materials"
)
 AND ("battery" OR "storage")
)

OR TITLE-ABS-KEY(
 "Li-ion" OR "Li metal" OR "Na-ion" OR "K-ion" OR "Li-S" OR "solid electrolyte" OR
 SEI OR
 "solid-state electrolyte" OR "polymer electrolyte" OR "ionic liquid electrolyte" OR
 "supercapacit*" OR "ultracapacitor"
)

OR TITLE-ABS-KEY(
 "selective ion separation" OR "PFAS removal" OR "phosphate removal" OR "nitrate
 removal" OR
 "ion exchange" OR "chelation strategy" OR "selective extraction" OR "water
 purification"
)

OR TITLE-ABS-KEY(
 "advanced materials" AND (
 "selective membrane" OR "nanofiltration" OR "adsorption membrane" OR
 "responsive polymer" OR "smart polymer" OR "nanostructured adsorbent"
)
)

OR TITLE-ABS-KEY(
 "water treatment" OR "water recovery" OR "wastewater treatment" OR "resource
 recovery" OR
 "water processing" OR "sustainable water management" OR "water reuse"
)

OR TITLE-ABS-KEY(
 "environmental remediation" AND ("sustainable recovery" OR "circular economy" OR
 "contaminant removal")
)

OR TITLE-ABS-KEY(
 "mineral processing" OR "critical mineral extraction" OR "hydrometallurgy" OR
 "separation technology" OR "selective separation"
)

OR TITLE-ABS-KEY(
 PFAS OR "per- and polyfluoroalkyl" OR "perfluorinated" OR PFOA OR PFOS OR
 "reverse osmosis" OR RO OR "membrane distillation" OR MD OR "adsorption" OR
 "ion-selective" OR
 "direct air capture" OR DAC
)

```

/* critical minerals detail */
OR TITLE-ABS-KEY(
  "rare earth*" OR REE OR "lithium extraction" OR "lithium brine" OR cobalt OR nickel
  OR manganese OR
  "solvent extraction" OR SX OR "electrowinning" OR EW OR "adsorptive separation" OR
  "resin"
)
)
AND ( LIMIT-TO ( DOCTYPE , "ar" ) )
AND ( LIMIT-TO ( LANGUAGE , "English" ) )

```

D.2.3 Semiconductor and Device Domain Template

```

(
  TITLE-ABS-KEY(
    (
      "Quantum dots" OR "Thin film" OR "Organic" OR "Inorganic" OR "Flexible" OR
      "Optoelectronic" OR "Power" OR
      "High-frequency" OR "2D materials" OR "Nanostructured" OR "Spintronics" OR
      "Photovoltaic" OR "Thermoelectric" OR
      "Piezoelectric" OR "Memory" OR "Quantum computing" OR "Perovskite" OR
      "Nanocrystals" OR
      "Light-emitting diodes" OR "Solar cell" OR "Environmental monitoring" OR
      "Graphene-based" OR "Nanoelectronic" OR
      "Inkjet printing" OR "Printable" OR "Flexible electronics" OR "Wearable
      electronics" OR "Energy harvesting" OR
      "Silicon-based" OR "Gallium nitride" OR "High mobility" OR "Low-dimensional" OR
      "Transition metal dichalcogenides" OR "Black phosphorus" OR "Quantum well" OR
      "Heterojunctions" OR
      "Stretchable electronics" OR "High-efficiency solar cells" OR "Low-power" OR "High
      thermal conductivity"
    )
    AND ("semiconductor" OR "device")
  )
)

OR TITLE-ABS-KEY(
  (
    transistor* OR MOSFET OR JFET OR HEMT OR CMOS OR "integrated circuit" OR IC OR
    diode* OR LED OR OLED OR QLED OR
    "photodetector*" OR "phototransistor*" OR "optoelectronic device*" OR "memory
    device*" OR "spintronic device*"
  )
  AND ("device*" OR "semiconductor*")
)

OR TITLE-ABS-KEY(
  "III-V" OR "SiC" OR "Ga2O3" OR "GaN" OR "InP" OR "InGaAs" OR "AlGaN" OR MoS2 OR WS2
  OR WSe2 OR MoSe2 OR MoTe2 OR
  "black phosphorus" OR "perovskite" OR "graphene" OR MXene OR CNT OR "carbon
  nanotube" OR "nanoribbon"
)

OR TITLE-ABS-KEY(
  "Schottky" OR "p-n junction" OR "heterostructure" OR "bandgap" OR "carrier mobility"
  OR "on/off ratio"
)
)
)
AND ( LIMIT-TO ( DOCTYPE , "ar" ) )

```

AND (LIMIT-TO (LANGUAGE , "English"))

D.2.4 Catalysis Domain Template

```
(
  TITLE-ABS-KEY(
    (
      "Catalysis" OR "Heterogeneous" OR "Homogeneous" OR "Bio-" OR "Green" OR
      "Photoelectro" OR
      "Thermal" OR "Organocatalysis" OR "Asymmetric" OR "Nanozyme" OR "Photocatalytic
      water splitting" OR
      "CO2 reduction" OR "Electrochemical" OR "Plasmonic" OR "Enzyme immobilization" OR
      "Molecular" OR
      "Chiral" OR "Single atom" OR "Energy conversion" OR "Selective oxidation" OR
      "Environmental remediation" OR
      "Green energy" OR "hydrogen evolution" OR "hydrogen oxidation" OR "Oxygen
      reduction" OR "Oxygen evolution" OR
      "Metal-organic framework" OR "Bimetallic" OR "Fuel cell" OR "Biomass conversion"
      OR "high entropy"
    )
    AND ("catalyst" OR "catalysis")
  )

  OR TITLE-ABS-KEY(
    "photocatalysis" OR "electrocatalysis" OR "thermocatalysis" OR HER OR HOR OR ORR OR
    OER OR CO2RR OR "CO2 RR" OR
    "oxygen evolution reaction" OR "oxygen reduction reaction" OR "hydrogen evolution
    reaction"
  )

  OR TITLE-ABS-KEY(
    "single-atom catalyst" OR "defect engineering" OR "heterojunction" OR "perovskite
    oxide" OR spinel OR
    MXene OR MOF OR "metal-organic framework" OR COF OR "covalent organic framework" OR
    "g-C3N4" OR
    "graphitic carbon nitride" OR "NiFe LDH" OR "layered double hydroxide" OR
    "high-entropy alloy"
  )

  OR TITLE-ABS-KEY(
    "advanced catalysis" AND ("water purification" OR "photocatalytic degradation" OR
    "catalytic oxidation" OR "green catalysis")
  )

  OR TITLE-ABS-KEY(
    "advanced oxidation process*" OR AOP OR Fenton OR "photo-Fenton" OR "persulfate
    activation"
  )
)
AND ( LIMIT-TO ( DOCTYPE , "ar" ) )
AND ( LIMIT-TO ( LANGUAGE , "English" ) )
```

Appendix E LLM-as-Judge Rubric and Templates

E.1 LLM-as-Judge Rubric Prompt (applied to DR Report)

{Anonymous DR Report content}

Now please analyze and evaluate the Report above on five equally weighted dimensions:

1. Relevance to the stated objective,
2. Depth and rigor of validation and benchmarking protocols,
3. Clarity and reproducibility of methodology,
4. Practical applicability and implementation readiness,
5. Novelty and breadth of candidate coverage.

For each dimension, assign a score from 0–10 and supply a one-sentence justification. This rubric places equal emphasis on procedural rigor and clear implementation steps alongside overall alignment, ensuring that reports with well-defined benchmarks and actionable guidance receive full credit. The five-dimensional rubric was specifically designed to reward not just information retrieval but true research utility—prioritizing actionable insights with clear provenance over mere comprehensiveness.

Inter-rater reliability. We compute Pearson and Spearman correlations across judges over repeated topic-report evaluations; these correlations quantify *consistency among judges* and are *not* used as evidence of factual correctness. While the rubric emphasizes objective dimensions like novelty and applicability, potential LLM judge biases—such as favoring outputs from similar architectures—were mitigated by averaging across diverse models.

E.1.1 Definitions of the Five Dimensions (equal weights)

Relevance = Alignment to the stated objective and scope, including coverage of key subcomponents rather than topic keywords alone.

Depth = Rigor of analysis and validation (e.g., explicit assumptions, benchmarking or ablations, uncertainty/limitations stated).

Clarity = Structure and reproducibility of the methodology, with traceable provenance (citations, data/sources, steps) and unambiguous claims.

Applicability = Actionability of the outputs (materials/candidates, parameters/protocols, resource requirements) enabling near-term implementation.

Novelty = Non-trivial ideas or candidate combinations beyond canonical baselines, with rationale, plus *breadth* of candidate coverage across the design space.

E.1.2 Example raw response (DToR_gpt-oss120B_local500; Topic: PFAS FET sensor probe) — Claude 4 Opus (thinking)

```
## Evaluation of Final ToT Synthesis Report
```

```
### Dimension 1: Relevance to the Stated Objective
```

```
**Score: 9/10**
```

```
The report directly addresses the core question about which 2D nanomaterials and molecular probes offer greatest potential for PFAS detection in FET-based sensors, providing comprehensive analysis of three distinct material approaches (COF-MIP monolayers, hybrid graphene/MoS2 heterostructures, and MXene-based platforms) with specific performance metrics and clear recommendations.
```

```
### Dimension 2: Depth and Rigor of Validation and Benchmarking Protocols
```

```
**Score: 7/10**
```

```
While the report presents impressive performance metrics (LODs down to 0.12 fg L-1, selectivity factors >20), it acknowledges critical gaps in long-term validation data (>100 cycles, >12 months field testing) and relies heavily on theoretical projections rather than comprehensive experimental validation across all three branches.
```

Dimension 3: Clarity and Reproducibility of Methodology

Score: 8/10

The report provides detailed material specifications, synthesis parameters (e.g., HF-free MXene delamination <5 MJ kg⁻¹, roll-to-roll coating at >200 fibers h⁻¹), and clear fabrication steps, though some advanced integration procedures (monolithic FET architecture combining all components) lack sufficient procedural detail for immediate reproduction.

Dimension 4: Practical Applicability and Implementation Readiness

Score: 6/10

Despite promising scalable manufacturing claims and cost projections (\$0.35-1.00 per sensor), the report reveals significant implementation barriers including limited PFAS aptamer libraries, incomplete life-cycle assessments, and lack of demonstrated monolithic integration of the most promising hybrid approaches.

Dimension 5: Novelty and Breadth of Candidate Coverage

Score: 9/10

The report demonstrates exceptional breadth with 40+ distinct materials and methodologies spanning multiple 2D material classes (COFs, graphene heterostructures, MXenes), innovative functionalization strategies (molecular imprinting, aptamer conjugation, plasmonic enhancement), and creative integration approaches (dual-mode detection, on-chip preconcentration).

Overall Score: 7.8/10

The report excels in comprehensively addressing the research question with innovative material combinations and demonstrates strong theoretical foundation, but implementation readiness is limited by acknowledged validation gaps and incomplete experimental verification of the most promising integrated approaches.

E.1.3 Example raw response (DToR_gpt-oss120B_local500; Topic: PFAS FET sensor probe) — Gemini 2.5 Pro

An analysis and evaluation of the Final ToT Synthesis Report is provided below.

1. Relevance to the stated objective

Score: 10/10

Justification: The report directly and comprehensively addresses the core research question, culminating in a clear, prioritized list of candidate materials and sensor architectures tailored to the FET platform.

2. Depth and rigor of validation and benchmarking protocols

Score: 10/10

Justification: The report consistently uses quantitative performance metrics (LOD, sensitivity, cost) and includes a dedicated contradiction analysis section that critically evaluates and resolves conflicting claims from different research branches.

3. Clarity and reproducibility of methodology

Score: 9/10

Justification: The report outlines a clear, actionable design framework in its conclusion and uses well-structured tables to transparently present complex

information, though specific synthesis protocols are understandably beyond its high-level scope.

****4. Practical applicability and implementation readiness****

Score: 10/10

Justification: The analysis consistently emphasizes real-world implementation factors such as scalable manufacturing, cost-per-sensor, anti-fouling strategies, and sensor lifetime, providing a clear roadmap from lab to field.

****5. Novelty and Breadth of Candidate Coverage****

Score: 10/10

Justification: The report synthesizes findings from three distinct and advanced material classes (COFs, heterostructures, MXenes) and covers a comprehensive inventory of novel probes, functionalization chemistries, and signal amplification techniques.

E.1.4 Example raw response (DToR_gpt-oss120B_local500; Topic: PFAS FET sensor probe) — Grok 3 (thinking)

Evaluation of the Report

1. ****Relevance to the stated objective****: Score 10/10 - The report directly synthesizes and evaluates 2D nanomaterials and molecular probes for PFAS detection in FET sensors, identifying top candidates like COF monolayers, graphene/MoS2 heterostructures, and MXenes while addressing sensitivity, selectivity, and broader analyte potential.
2. ****Depth and rigor of validation and benchmarking protocols****: Score 7/10 - While the report benchmarks performance metrics like LODs and sensitivities against techniques such as EIS, QCM-D, and SERS, it relies on synthesized branch data without detailing original experimental protocols or statistical rigor, leaving some validation gaps unresolved.
3. ****Clarity and reproducibility of methodology****: Score 8/10 - Methodologies for material synthesis, functionalization (e.g., MIP imprinting, fluorosilane passivation), and integration (e.g., roll-to-roll coating) are described with specific parameters and performance data, enabling reasonable reproducibility, though some steps like aptamer generation lack step-by-step instructions.
4. ****Practical applicability and implementation readiness****: Score 8/10 - The report emphasizes scalable manufacturing, cost estimates (e.g., \$0.35 per sensor), regeneration strategies, and real-world challenges like anti-fouling, indicating strong readiness for field deployment, but notes gaps in long-term validation that could hinder immediate implementation.
5. ****Novelty and Breadth of Candidate Coverage****: Score 9/10 - The report covers a broad inventory of established (e.g., graphene) and underexplored candidates (e.g., Nb4C3Tx MXenes, PFAS-specific aptamers) with innovative hybrids like MXene-AgNP composites, highlighting novel integrations while synthesizing unique perspectives from multiple branches.

E.1.5 Example raw response (DToR_gpt-oss120B_local500; Topic: PFAS FET sensor probe) — ChatGPT o3

Expert Evaluation of the "Final ToT Synthesis Report"

Dimension 1 - Relevance to the stated objective: 9/10

The report stays tightly focused on identifying 2-D materials and molecular probes for PFAS-targeted FET sensing, continuously mapping every finding back to sensitivity, selectivity and scalability goals.

Dimension 2 - Depth and rigor of validation and benchmarking protocols: 7/10

It cites quantitative LODs, mobility values, cost metrics and comparative tables, yet long-term cycling data, full life-cycle assessments and multi-lab benchmarking remain largely prospective rather than experimentally demonstrated.

Dimension 3 - Clarity and reproducibility of methodology: 8/10

Process flows (e.g., roll-to-roll coating, HF-free MXene synthesis, dual-mode FET construction) are described with sufficient detail and metrics to guide replication, though specific experimental parameters (e.g., polymerisation currents, imprinting times) are occasionally omitted.

Dimension 4 - Practical applicability and implementation readiness: 8/10

The report highlights scalable manufacturing routes and <\$1 per-sensor costs, but real-world field trials, regulatory certification pathways and integration with portable electronics are only touched on, indicating TRL 4-5 rather than deployment-ready status.

Dimension 5 - Novelty and breadth of candidate coverage: 9/10

It spans COF monolayers, graphene/MoS2 heterostructures, multiple MXenes, nano-MIPs, aptamers and plasmonic enhancers--introducing several under-explored pairings--while articulating how each uniquely advances PFAS sensing.

E.1.6 Example raw response (DToR_gpt-oss120B_local500; Topic: PFAS FET sensor probe) — ChatGPT o4 mini high

1. Relevance to the stated objective - Score: 10

The report directly addresses PFAS-focused FET sensor design by comparing 2D nanomaterial platforms, functionalization strategies, and performance metrics tailored to ultra-sensitive, selective detection.

2. Depth and rigor of validation and benchmarking protocols - Score: 8

It presents quantitative LODs, binding constants, and comparative deviations versus LC-MS/MS, but lacks standardized cross-laboratory protocols and detailed statistical analyses.

3. Clarity and reproducibility of methodology - Score: 6

While the report outlines material choices, functionalization chemistries, and device architectures, it omits step-by-step experimental procedures and specific process parameters needed for exact replication.

4. Practical applicability and implementation readiness - Score: 9

The discussion of scalable roll-to-roll/printing methods, cost estimates (< \$1 per sensor), and anti-fouling/regeneration strategies demonstrates strong real-world deployment potential.

5. Novelty and breadth of candidate coverage - Score: 9

By surveying COFs, graphene/MoS2 heterostructures, and diverse MXene compositions alongside a wide array of molecular probes, the report offers a comprehensive and innovative candidate inventory.

E.2 A/B Dueling Prompt (DR Report A vs. DR Report B)

Report A: {Anonymous DR Report content}

Report B: {Anonymous DR Report content}

Table S1: Example raw response (DToR_gpt-oss120B_local500; Topic: PFAS FET sensor probe; Trial #1) — cross-model score matrix (0–10).

Model	Relevance	Depth	Clarity	Applicability	Novelty	Overall (mean)
Claude 4 Opus (thinking)	9	7	8	6	9	7.8
Gemini 2.5 Pro	10	10	9	10	10	9.8
Grok 3 (thinking)	10	7	8	8	9	8.4
ChatGPT o3	9	7	8	8	9	8.2
ChatGPT o4 mini high	10	8	6	9	9	8.4
Average across models	9.6	7.8	7.8	8.2	9.2	8.5

As an experienced materials scientist who bridges the gap between research and pilot lines, please review these two reports. I need your professional judgment: which one offers the clearer high-level strategic roadmap for our team’s R&D over the next six months? We are especially interested in the report that presents a well-structured narrative, systematically identifies and prioritizes knowledge gaps, and synthesizes actionable next steps—beyond performance metrics. Please give me your recommendation in a brief, plain-language note—straight to the point—ending with a clear verdict on which report to back and the single most decisive reason why.

```
A/B Duel: Metadata
agent_a: ChatGPT_o3_DR
agent_b: DToR_gpt-oss120B_local500
trial: trial_1
```

E.2.1 Raw dueling response (DToR_gpt-oss120B_local500; Topic: PFAS FET sensor probe) — Claude 4 Opus (thinking)

****Materials Scientist Assessment****

****Report A**** provides a comprehensive academic survey but reads more like a literature review than a strategic roadmap. While thorough, it spreads across too many materials without clear prioritization and lacks concrete next steps for R&D planning.

****Report B**** delivers exactly what you need for strategic planning. It systematically identifies the top-performing candidates (MXene with fluorinated brushes for sensitivity, COF nanosheets for durability), resolves key technical contradictions through specific architectural solutions, and maps out clear manufacturing pathways with roll-to-roll processing. Most importantly, it explicitly identifies remaining knowledge gaps and provides actionable timelines.

Report B’s “Contradiction Analysis & Resolution” section alone is worth its weight in gold--it tackles the real engineering trade-offs your team will face (sensitivity vs. durability, manufacturing speed vs. quality) and provides specific solutions rather than just flagging issues.

The device architecture recommendation is concrete and implementable: MXene channel + sub-5nm fluorinated COF dielectric + MIP-COF overlayer. This gives your team a clear target to work toward with defined performance metrics and manufacturing constraints.

****Verdict: Back Report B****

****Decisive reason:**** Report B transforms scattered research into a concrete R&D roadmap with prioritized materials, specific architectures, and identified next steps--exactly what you need to allocate resources and set milestones for the next six months.

E.2.2 Raw dueling response (DToR_gpt-oss120B_local500; Topic: PFAS FET sensor probe) — Gemini 2.5 Pro

Here is my recommendation, straight to the point.

Team,

After reviewing both documents, my recommendation is clear. Report A is an excellent, comprehensive library of the entire field--a valuable resource for onboarding a new researcher. Report B, however, is a strategic plan.

Report B provides the roadmap. It doesn't just list materials and their performance; it synthesizes the data into two competing but complementary perspectives. It then systematically resolves the conflicts between them, which is where the real strategic value lies. The report directly answers \"what should we do next?\" by providing a specific, multi-layered device architecture to target and a prioritized list of knowledge gaps that can be converted directly into our Q3/Q4 milestones. It gives us a strong, defensible point of view to build our project around.

****Verdict:** We back Report B.**

The single most decisive reason is its ****Contradiction Analysis section.**** This transforms the document from a passive review into an active strategy, showing us not just what the challenges are, but how to resolve the technical trade-offs to build a superior device.

E.2.3 Raw dueling response (DToR_gpt-oss120B_local500; Topic: PFAS FET sensor probe) — Grok 3 (thinking)

After reviewing both reports as a materials scientist with pilot-line experience, Report B stands out for its integrated synthesis of perspectives, clear resolution of contradictions, and explicit focus on practical trade-offs like manufacturing scalability and device architectures. It provides a more actionable framework by prioritizing real-world deployment challenges (e.g., wear validation in sweat) and recommending specific hybrid designs that balance sensitivity with durability.

****Verdict:** Back Report B.** The single most decisive reason is its systematic identification and prioritization of knowledge gaps, paired with synthesized next steps (e.g., multilayer heterostructures and process optimizations), which directly guide targeted R&D over the next six months beyond just metrics.

E.2.4 Raw dueling response — ChatGPT o4 mini high

Between the two, Report B gives you the sharper six-month R&D playbook. It lays out two complementary design perspectives, reconciles trade-offs, pinpoints exact knowledge gaps (wear-test validation, complex-matrix studies, environmental impact), and closes with a concrete, multilayer device architecture and prioritized material-probe combinations.

Verdict: Back Report B--because it distills the review into a clear, structured roadmap of what to build, test, and refine next.

E.2.5 Raw dueling response (DToR_gpt-oss120B_local500; Topic: PFAS FET sensor probe) — ChatGPT o3

Team,

Both reports give strong technical overviews, but only one reads like a playbook you can hand to an R&D scrum tomorrow.

* Report A is an encyclopedic review: rich detail, many examples, but it stops at describing what exists. You'd still need to distill priorities, rank open questions, and map experiments yourself.

* Report B is written as a roadmap: it organizes findings into themed "perspectives," lists candidate stacks, flags contradictions, clarifies trade-offs, and--critically--spells out the remaining knowledge gaps (long-term wear tests, matrix interference, environmental impact) as discrete to-dos. The table of device architectures with drift/noise targets and the hybrid-stack recommendation give an immediate six-month experiment sequence.

Verdict: Back Report B--because it converts the literature into a prioritized action plan, not just a survey.

Appendix F Dry-Lab Validation Details

This appendix presents the complete first-principles validation for the agent’s top-performing candidates, translating textual hypotheses into actionable, physically-grounded simulations. Across the five representative tasks, we used DFT and AIMD to move beyond textual scores and test real-world viability. A critical, recurring insight emerged: computationally demanding explicit-solvent AIMD simulations revealed performance reversals and candidate failures that were invisible to simpler static DFT calculations, particularly for the battery binder and PFAS sensor tasks. This successful dry-lab verification confirms that the DToR framework can generate novel hypotheses that are robust to complex, real-world operational conditions⁵. The following sections detail the full computational methodology and results for each of the five validation tasks.

F.1 DFT simulation settings

Static Simulation

To simulate the binding interactions of diverse combinations under periodic boundary conditions, we employed ab initio calculations employing parameters optimized for precision and computational efficiency. The plane-wave energy cutoff was set to 400 eV, and spin-polarized density functional theory DFT with the Perdew-Burke-Ernzerhof (PBE) functional was utilized to describe exchange-correlation interactions. The Brillouin zone integration employed a Gamma-centered $1 \times 1 \times 1$ k-point grid and van der Waals corrections were incorporated using the DFT-D3 method to capture dispersion effects. Ionic relaxations were conducted with a convergence criterion of 0.02 eV/Å for the forces, and the electronic structure iterations were set to converge to an energy difference of 10^{-4} eV. Implicit solvent field is added for static simulations by setting the dielectric constant at 78.4 if applicable (namely excluding the ab initio molecular dynamics (AIMD) with explicit solvent molecules, and the CO₂ sensor probe binding scenarios). The modeling of the slabs is directly conducted by human expert based on anonymously reading the DR report. To ensure fair comparison, we asked the expert to create same number of candidates from each report (e.g. 4 from DR report A, and 4 from DR report B), and also pick one domain commonly chosen benchmark material/chemical for each of the 5 applications. To prevent interactions between periodic images, we also include >20 Å vacuum gap along the z-, ensuring a reliable comparison between adsorbed and separated configurations.

To be noted, To manage the configurational complexity of these diverse heterostructures and ensure consistent high-throughput benchmarking, we adopted standardized initial adsorption geometries tailored to the dominant interaction mechanism of each application. For PFAS sensing, which relies on host-guest recognition, linear perfluorinated chains were initialized inserting vertically into the target cavities (e.g., MIP pores or β -cyclodextrin rings) to mimic inclusion complex formation. Conversely, for PFAS degradation and battery binder applications, where maximizing interfacial contact area is critical for catalysis and adhesion, adsorbates were positioned in a planar configuration parallel to the inorganic substrate. Similarly, for CO₂ sensing, the molecule was initialized in a parallel orientation relative to the surface to facilitate interaction with active sites. While we acknowledge that exhaustive conformational sampling might reveal subtle secondary minima, focusing on these chemically dominant interaction modes provides a consistent and unbiased baseline across all systems. This approach is sufficient to validate the physical plausibility of the agent’s proposals and establish a robust relative ranking for high-throughput screening without the prohibitive cost of global optimization.

Binding Energy Convention.

Following a standard DFT convention (Phys. Rev. B, 2008, 77, 12) for adsorption on typical studied 2D material systems like graphene, we report the binding energy ΔE_{bind} of an adsorbate at a given coverage as

$$\Delta E_{\text{bind}} = (E_{\text{clean_slab}} + E_{\text{adsorbate}}) - E_{\text{adsorbed}} \tag{1}$$

where E_{adsorbed} is the total energy of the fully relaxed adsorbate–slab complex (for certain applications, bottom atoms of bulk crystals are frozen and surface area are free to mimic realistic surface interactions),

⁵Dry-lab simulations are interpreted as relative ranking proxies under fixed protocols (system sizes/constraints and scoring transforms listed here) rather than definitive materials predictions; experimental validation remains necessary. Although dry-lab simulations validate the physical plausibility of agent proposals, these remain approximations; transitioning to wet-lab would involve synthesizing top candidates like aptamer-functionalized graphene FETs for PFAS detection, potentially using robotic platforms for high-throughput testing to close the discovery loop.

$E_{\text{clean_slab}}$ is the energy of the corresponding pristine clean slab supercell, and $E_{\text{adsorbate}}$ is the energy of the isolated adsorbate in the same supercell. All terms are computed with identical exchange–correlation functional, plane-wave cutoff, and k-point mesh. Unless stated specifically (like for battery binder normalized to be contact areal), we report ΔE_{bind} for only one adsorbate in the slab super cell for qualitative comparison. This definition mirrors the adsorption–energy convention widely used for molecules on typical substrates like graphene or MXene (we adopt the term “binding energy” throughout). By this convention, a more positive ΔE_{bind} indicates an exothermic, favorable adsorption (energy released upon binding).

Ab Initio Molecular Dynamics (AIMD) Simulation

To improve the physical realism of our calculations and especially considering solvent effect for surface events, we embedded explicit water molecules in the supercell according to conformations identified in preceding static simulations (Mol. Syst. Des. Eng. 2025, 10, 345–356; Sci. Adv. 2025, 11, eadr9038) using an end-state protocol. Specifically, the optimized adsorbed configuration corresponding to E_{adsorbed} was used as the initial snapshot for the solvated *adsorbed* state, with explicit water molecules added thereafter. For the *pulled* state, the adsorbate was translated by at least 15 Å away from the relaxed slab (e.g., graphene)—without additional geometry optimization—and then solvated under identical conditions. These two equilibrated states form the basis for directly comparing adsorption energetics in explicit solvent, consistent with end-state comparisons commonly applied in MD umbrella-sampling studies (J. Phys. Chem. C 2023, 127, 5920–5930; ChemPhysChem 2018, 19, 690–702), and in line with benchmark explicit-solvent AIMD treatments of metal/water interfacial solvation (J. Chem. Phys. 2020, 152, 144703) and first-principles determinations of interfacial hydration free energies for adsorbates on Pt (J. Chem. Phys. 2021, 154, 094107).

The water density was maintained at 1 g cm⁻³ (for battery binder, solvent composition is different as described in corresponding section). Our goal was to compare the evolution of the system’s potential (electronic) energy upon equilibration (Electrocatalysis 2017, 8, 577–586; Commun. Chem. 2022, 5, 76; J. Chem. Phys. 2020, 152, 144703; J. Chem. Phys. 2021, 155, 134703).

To ensure that the solvent adopted physically meaningful configurations, each system was first equilibrated for 2 ps at 300 K with a 0.5 fs time step. Temperature was regulated via a Langevin thermostat to suppress extraneous inertial effects while preserving canonical sampling. After equilibrium, we further performed a 3 ps production run, from which we extracted time-averaged electronic potential energies.

We therefore report an explicit-solvent end-state potential-energy gap, denoted $\Delta E_{\text{pot}}^{\text{ES}}$ (AIMD), defined as the difference between the time-averaged electronic potential energies of the solvated *adsorbed* and *pulled* basins in identical cells:

$$\Delta E_{\text{pot}}^{\text{ES}} \equiv \langle E_{\text{pot}} \rangle_{\text{pulled}} - \langle E_{\text{pot}} \rangle_{\text{ads}}. \quad (2)$$

Unless otherwise noted, all comparisons use the same supercell, water count, ion composition, thermostatting, and slab-electrostatics settings. Hence, the more positive $\Delta E_{\text{pot}}^{\text{ES}}$ (AIMD), the more energetically favorable the adsorbed state—i.e., a potential-energy analogue of the binding energy—whereas a negative $\Delta E_{\text{pot}}^{\text{ES}}$ indicates that explicit solvation stabilizes the pulled state and adsorption is disfavored.

Scope and limitations of $\Delta E_{\text{pot}}^{\text{ES}}$:

$\Delta E_{\text{pot}}^{\text{ES}}$ is not a rigorously converged adsorption free energy. By construction it (i) neglects configurational and translational entropy; (ii) folds solvent reorganization and water (or other solvent)–surface exchange energetics into the potential-energy baseline; and (iii) depends on finite-time sampling of each basin rather than a reversible pathway or an alchemical thermodynamic cycle. Consequently, its absolute magnitudes can reflect not only adsorbate–surface interactions but also large-scale differences in hydrogen-bond networks and long-range electrostatics associated with hundreds of explicit waters. Nonetheless, because all systems are treated consistently within the same AIMD framework, $\Delta E_{\text{pot}}^{\text{ES}}$ serves as a heuristic yet informative comparative descriptor for explicit-solvent binding trends across molecules and candidate surfaces, revealing solvent-mediated, surface-dependent effects that are not captured in vacuum or implicit-solvent calculations. Formal free-energy methods (umbrella sampling/PMF, metadynamics, and double-decoupling/TI with standard-state and slab-electrostatics corrections) are acknowledged as the rigorous routes to ΔG , as exemplified for interfacial adsorbates at water–Pt interfaces (J. Chem. Phys. 2021, 154, 094107).

Computational feasibility rationale:

Rigorous free-energy calculations become computationally prohibitive for our systems, which routinely exceed 500 atoms and include numerous transition-metal centers in addition to light elements; fully converged interfacial free-energy landscapes are beyond feasible AIMD timescales under such conditions.

Extensive explicit-solvent AIMD benchmarks of metal/water interfaces have likewise highlighted the costliness of such simulations (J. Chem. Phys. 2020, 152, 144703). In this context, the explicit-solvent end-state potential-energy gap provides a practical dynamic compromise: it captures key solvent-mediated effects absent from static DFT binding energies while remaining tractable for large, chemically realistic slabs. Thus, although approximate, $\Delta E_{\text{pot}}^{\text{ES}}$ offers higher fidelity and greater interpretive value than purely static vacuum or implicit-solvent descriptions for the screening-level comparisons emphasized in this work.

F.2 PFAS FET Sensor Probe

F.2.1 PFAS_2D_FET_Probes

For the first application: PFAS FET Sensor Probe. The query as shown in C is:

Which two-dimensional (2D) nanomaterials or molecular probes--including novel, underexplored candidates--offer the greatest potential to achieve highly sensitive and selective detection of per- and polyfluoroalkyl substances (PFAS), or more broadly chemical and biological analytes, when integrated into a field-effect transistor (FET)-based sensor platform?

The best commercial solution is: **ChatGPT_o3_DR**.

The best local non gpt-oss solution is: **DToR_qwq32B_local500**.

The best local gpt-oss solution is: **DToR_gpt-oss120B_local500**.

The expert based on the three reports, provided 3 commercial DR report derived candidates (A1-A3), and 3 local DR non gpt-oss report derived candidates (B1-B3), and 3 local DR gpt-oss report derived candidates (C1-C3), visualized in Fig. S13:

A1 — 2D rGO + β -Cyclodextrin (β -CD) Hexagonal P1 slab with $a = b = 36.90 \text{ \AA}$, $\gamma = 120^\circ$, $c = 45.00 \text{ \AA}$ (in-plane area $\approx 1179.19 \text{ \AA}^2$). Atom counts (C/H/O = 483/102/94) indicate a 2D graphene-derived sheet with oxygenated defects (epoxy/hydroxyl) on one face and a carbohydrate torus consistent with β -CD mounted above it. The populated thickness is $\approx 15.02 \text{ \AA}$ (vacuum $\approx 29.98 \text{ \AA}$); the 2D carbon plane sits near $z \approx 7.5 \text{ \AA}$. The β -CD presents a toroidal pocket with a projected mouth $\sim 15.3 \text{ \AA}$ diameter, oriented normal to the basal plane for PFOS capture. Oxygen sites on rGO act as plausible anchoring points while the underlying 2D lattice remains largely sp^2 and planar.

A2 — 2D MoS₂/2D hBN heterojunction + methacrylic-acid (MIP-like) cavity, pyrene-linked Hexagonal P1 with $a = b = 28.44 \text{ \AA}$, $\gamma = 120^\circ$, $c = 46.13 \text{ \AA}$ (area $\approx 700.47 \text{ \AA}^2$). Composition shows a **2D MoS₂/2D hBN heterojunction** stack capped by an aromatic (pyrene-type) tether and a **methacrylic-acid cluster forming a β -CD-like cavity** on one side (organics C/H/O sit above the dielectric). The populated thickness is $\approx 18.68 \text{ \AA}$ (vacuum $\approx 27.45 \text{ \AA}$). The cavity's projected mouth is $\sim 13.6 \text{ \AA}$ in diameter, positioned above hBN so PFOS can approach without perturbing the MoS₂ channel. The pyrene linker bridges π - π to the 2D cap while keeping the cavity axis roughly perpendicular to the surface, preserving electronic decoupling from the channel.

A3 — 2D Fluorographene (CF) slab Hexagonal P1 with $a = b = 36.90 \text{ \AA}$, $\gamma = 120^\circ$, $c = 45.00 \text{ \AA}$ (area $\approx 1179.19 \text{ \AA}^2$). Stoichiometry C₄₅₀F₄₅₀ yields a single-layer **2D CF** sheet with chair-like alternating C-F buckling; the "solid" thickness is $\approx 3.26 \text{ \AA}$ and vacuum $\approx 41.74 \text{ \AA}$. The surface is uniform and free of additional adsorbates, providing a continuous fluorinated interface. Fluorine is arranged on both sides of the 2D carbon lattice, giving a symmetric fluorophilic environment. The wide lateral extent minimizes edge effects, making it suitable for baseline PFOS adsorption comparisons.

B1 — 2D Ti₃C₂O₂ MXene + methacrylic-acid (MIP-like) cavity Hexagonal P1 with $a = b = 30.67 \text{ \AA}$, $\gamma = 120^\circ$, $c = 46.70 \text{ \AA}$ (area $\approx 814.63 \text{ \AA}^2$). The slab is an O-terminated **2D Ti₃C₂ MXene** bearing, on one side, a **methacrylic-acid cluster organized as a β -CD-like cavity** (additional C/H/O located at higher z). Populated thickness $\approx 16.14 \text{ \AA}$ (vacuum $\approx 30.56 \text{ \AA}$). The cavity mouth projects $\sim 13.5 \text{ \AA}$ in diameter, perched above the O-terminated surface while the bottom MXene layer serves as a rigid support. The one-sided functionalization creates an asymmetric interface—electronegative terminations and the cavity's polar rim cooperate to stabilize PFOS headgroup interactions.

B2 — 2D Graphene + methacrylic-acid (MIP-like) cavity Hexagonal P1 with $a = b = 36.90 \text{ \AA}$, $\gamma = 120^\circ$, $c = 45.00 \text{ \AA}$ (area $\approx 1179.19 \text{ \AA}^2$). A 15×15 **2D graphene** sheet supports, on one face, a **methacrylic-acid cluster arranged into a β -CD-like cavity** (C/H/O entirely above the carbon plane). The populated thickness is $\approx 9.58 \text{ \AA}$ with $\approx 35.42 \text{ \AA}$ vacuum. The cavity presents a projected $\sim 13.6 \text{ \AA}$ diameter single-sided pocket aligned normal to the basal plane for PFOS engagement. The 2D sp^2 lattice remains flat and conductive, making this a clean platform for decoupling recognition from transduction.

B3 — 2D Graphene + fluorinated phospholipid monolayer Hexagonal P1 with $a = b = 36.90 \text{ \AA}$, $\gamma = 120^\circ$, $c = 45.00 \text{ \AA}$ (area $\approx 1179.19 \text{ \AA}^2$). Elemental makeup (C/F/H/O with trace N and P) is consistent with phosphatidylcholine headgroups near the **2D** graphene plane and perfluorinated tails extending outward to form a dense brush. The populated thickness is $\approx 14.84 \text{ \AA}$ (vacuum $\approx 30.16 \text{ \AA}$), with F spanning roughly $z \approx 9.21\text{--}22.34 \text{ \AA}$ above the basal plane. The assembly yields a hydrophilic-to-fluorophilic gradient, presenting a fluorinated outer surface for PFOS tail affinity. Lipid tails show a collective tilt relative to the surface normal, producing a compact, low-defect fluorinated interface on one side while the opposite side remains bare graphene.

C1 — 2D $\text{Ti}_3\text{C}_2\text{O}_2$ MXene + C12-PFOTS Hexagonal P1 with $a = b = 30.67 \text{ \AA}$, $\gamma = 120^\circ$, $c = 46.70 \text{ \AA}$ (area $\approx 814.63 \text{ \AA}^2$). The slab is an O-terminated **2D Ti_3C_2 MXene** bearing, on one side, a single **perfluorododecyltrimethoxysilane (C12-PFOTS)** molecule lying flat on the surface. The longer perfluorocarbon chain ($-(\text{CF}_2)_9\text{CF}_3$) extends $\sim 17 \text{ \AA}$ above the surface, providing an elongated fluorophilic domain. Populated thickness $\approx 17.36 \text{ \AA}$ (vacuum $\approx 29.34 \text{ \AA}$). Compared to shorter PFOTS variants, the C12 tail offers greater van der Waals contact area, potentially favoring binding of longer-chain PFAS (PFOS, PFNA) over shorter ones (PFHxS). The Si–O–C(Me)₃ anchor affords compact attachment while preserving the extended fluorinated interface.

C2 — β -Ketoenamine-Linked 2D COF + MIP Cavity (In-Plane) Hexagonal P1 with $a = b = 58.18 \text{ \AA}$, $\gamma = 120^\circ$, $c = 48.02 \text{ \AA}$ (area $\approx 2931.40 \text{ \AA}^2$). Substrate is a $2 \times 2 \times 1$ supercell of a **β -ketoenamine linked covalent organic framework (COF)** bearing the same **methacrylic-acid MIP cavity** as in A2, now integrated **within the COF plane at the same z-height**. The COF layer and MIP cluster coexist laterally ($z \approx 4\text{--}12 \text{ \AA}$), creating a heterogeneous 2D surface where the cavity functions as an **in-plane defect/pore modification**. Populated thickness $\approx 8.14 \text{ \AA}$ (vacuum $\approx 39.88 \text{ \AA}$). This geometry promotes **lateral diffusion** of PFAS along the COF to the embedded site, restricting purely vertical access; the shallower rim may enhance **size/shape selectivity** by guiding linear PFAS into the cavity while disfavoring bulky interferents (e.g., humic substances).

C3 — 2D $\text{Ti}_3\text{C}_2\text{O}_2$ MXene + C12-PFOTS + AgNP + PEDOT:PSS Hexagonal P1 with $a = b = 30.67 \text{ \AA}$, $\gamma = 120^\circ$, $c = 46.70 \text{ \AA}$ (area $\approx 814.63 \text{ \AA}^2$). Derived from C1, the O-terminated **2D Ti_3C_2 MXene** supports a single **C12-PFOTS** chain and is augmented by (i) a $\sim 1 \text{ nm Ag}_{43}$ **nanoparticle cluster** positioned near the extended fluorocarbon tail, generating **plasmonic hotspots** along the chain, and (ii) **PEDOT** and **PSS** monomers as conductive spacers to maintain openness. Populated thickness $\approx 17.36 \text{ \AA}$ (vacuum $\approx 29.34 \text{ \AA}$). The extended C12 chain, coupled with the AgNP near-field, creates a more expansive **electromagnetic enhancement zone** tailored to longer-chain PFAS (PFOS, PFNA). **PEDOT:PSS** discourages MXene restacking and introduces **sulfonate sites (from PSS)** that may modulate selectivity via electrostatic interactions with PFAS sulfonate headgroups.

F.2.2 Selectivity Scoring for PFAS Sensor Performance

The practical deployment of PFAS sensors demands not only strong binding to target per- and polyfluoroalkyl substances but also selective discrimination against common environmental interferents. To quantitatively evaluate this selectivity, we developed a unified scoring framework applicable to both static DFT calculations and explicit-solvent AIMD simulations, enabling direct comparison between computational methodologies while maintaining thermodynamic rigor. **Selectivity Metric Derivation:** The fundamental selectivity metric $\Delta\Delta E$ quantifies the differential binding preference between PFAS compounds and interferent molecules:

$$\Delta\Delta E = \overline{\Delta E}_{\text{PFAS}} - \overline{\Delta E}_{\text{Interf}} \quad (3)$$

where $\overline{\Delta E}_{\text{PFAS}}$ represents the average binding energy across four representative PFAS compounds (PFOA, PFOS, PFNA, and PFHxS), and $\overline{\Delta E}_{\text{Interf}}$ denotes the average binding energy for interferent species (humic acid and SDS), as illustrated in Figure S14. A larger positive $\Delta\Delta E$ value indicates superior selectivity, signifying stronger preferential binding to PFAS over interferents. For static DFT calculations, ΔE values correspond to the conventional binding energies ΔE_{bind} computed under implicit solvent conditions (Figure S15). In explicit-solvent AIMD simulations, these are replaced by the time-averaged end-state potential energy gaps $\Delta E_{\text{pot}}^{\text{ES}}$, which capture solvent reorganization effects and hydrogen-bonding network rearrangements absent from static calculations (Figures S16 and S17). **Linear Selectivity Scoring Framework:** To enable meaningful comparison across candidate systems and computational methods, we normalize the selectivity metrics to a common scoring scale:

$$\text{Score} = 100 \times (1 + \beta(\Delta\Delta E - \Delta\Delta E_{\beta\text{-CD}})) \quad (4)$$

where $\Delta\Delta E_{\beta\text{-CD}}$ represents the selectivity of β -cyclodextrin, our domain benchmark reference with established PFAS binding capability [26]. The sensitivity parameter $\beta = 0.2$ was selected to provide appropriate score discrimination while maintaining numerical stability across both DFT and AIMD datasets. This linear transformation preserves the physical meaning of energy differences while establishing β -CD as the baseline reference (Score = 100). **Comparative Analysis of Selectivity Under Different Solvation Models:** The application of this unified scoring framework reveals striking differences between implicit and explicit solvation treatments. In static DFT calculations with implicit solvent, system A1 achieves the highest selectivity score of 102.4, outstandingly exceeding the β -CD baseline (Figure S18). The B-series candidates also prove competitive as B2 and B3 also showed slightly passing 100 score.

However, the inclusion of explicit water molecules and dynamic sampling in AIMD simulations dramatically alters the selectivity landscape (Figure S19). Most notably, the majority of the candidate systems' scores are below the β -CD baseline in explicit solvent, with only B1 achieving the highest relative performance at 102.0. This systematic reduction in scores reflects the critical role of solvent-mediated effects: competitive water adsorption at binding sites, strong hydration of anionic PFAS headgroups, and the entropic penalties associated with constraining flexible molecules in adsorbed configurations. The reversal of relative rankings between static DFT and AIMD calculations—particularly the superior performance of B-series candidates under explicit solvation—underscores the importance of including solvent dynamics in sensor design evaluation. While static calculations provide valuable initial screening, the explicit-solvent AIMD results more accurately capture the complex interplay between adsorbate–surface interactions and solvent reorganization that governs selectivity under realistic aqueous conditions. **Implications for Sensor Design:** The divergence between implicit and explicit solvent results carries significant implications for PFAS sensor development. Systems optimized solely based on static DFT calculations may exhibit diminished selectivity in aqueous environments due to unforeseen solvent competition effects. Conversely, candidates that appear suboptimal in vacuum or implicit solvent calculations may benefit from favorable solvent-mediated interactions that enhance their practical selectivity. This highlights the necessity of multi-scale computational approaches that progress from efficient static screening to rigorous explicit-solvent validation for promising candidates.

The linear selectivity scoring framework presented here provides a quantitative, thermodynamically grounded metric for evaluating sensor performance across computational methodologies. By maintaining consistent notation and normalization across static and dynamic simulations, this approach enables systematic comparison of candidate materials while preserving the physical interpretability of the underlying energy differences.

PFAS Sensing Candidate Structures

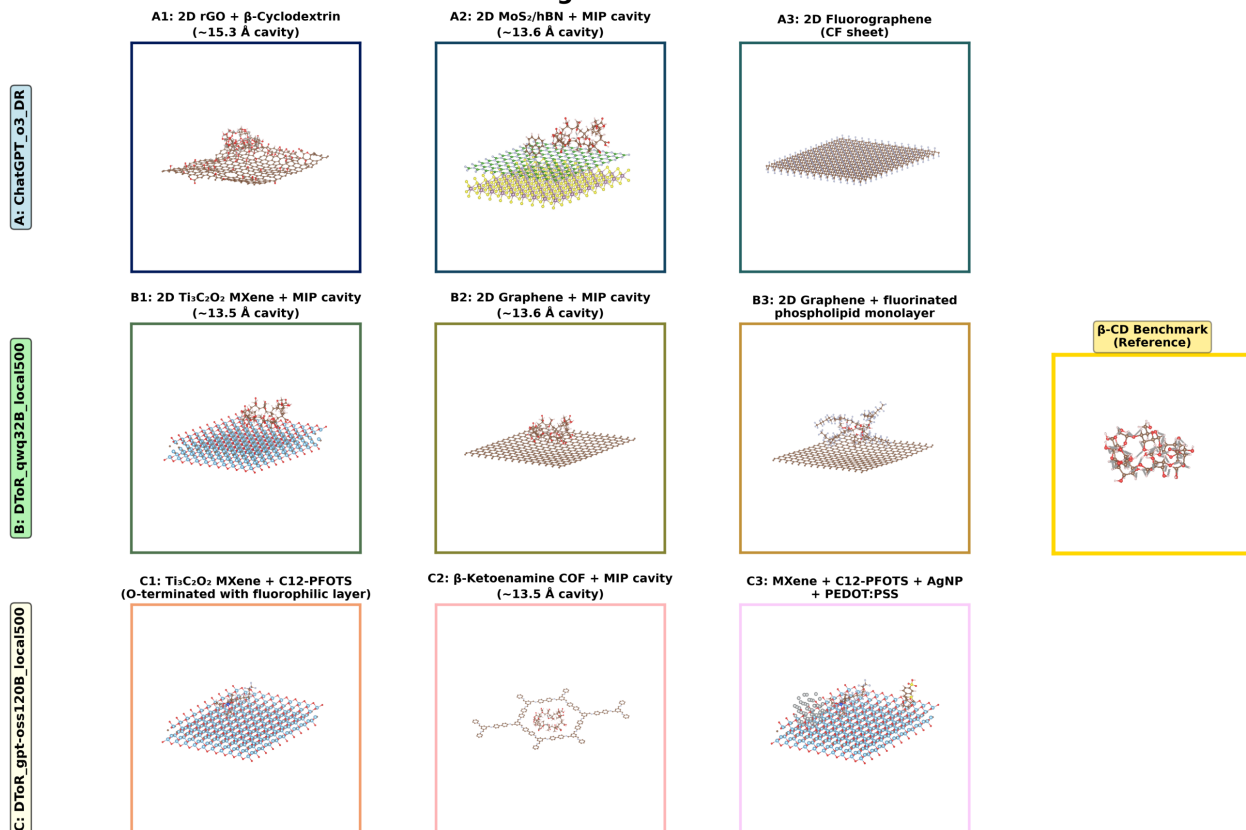


Figure S13: Structural configurations of candidates proposed by DR agents for selective PFAS binding, with β -cyclodextrin [26] included as the domain benchmark reference.

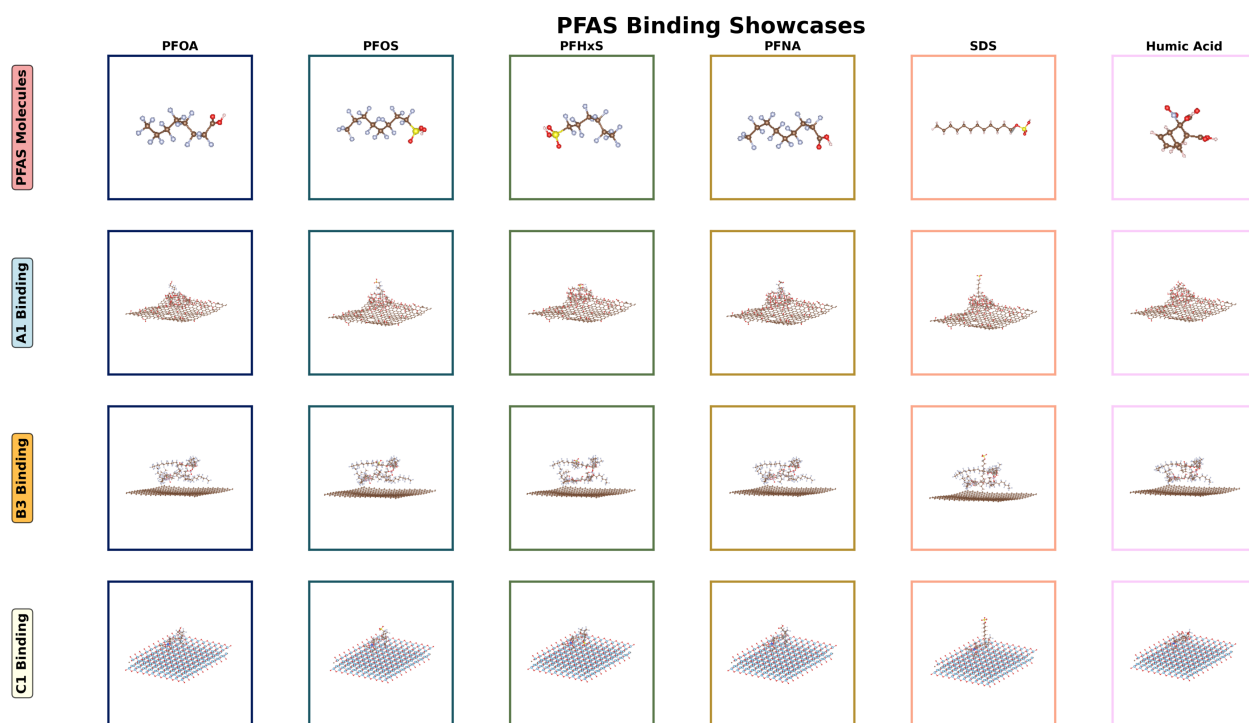


Figure S14: Representative PFAS compounds (PFOA, PFOS, PFNA, PFHxS) and interferent molecules (SDS and humic acid) employed in selectivity assessment, with corresponding optimized binding configurations. A number of candidates' relaxed structures (proposed by different DR agents) are shown.

PFAS Binding Energy (eV) Radar Chart

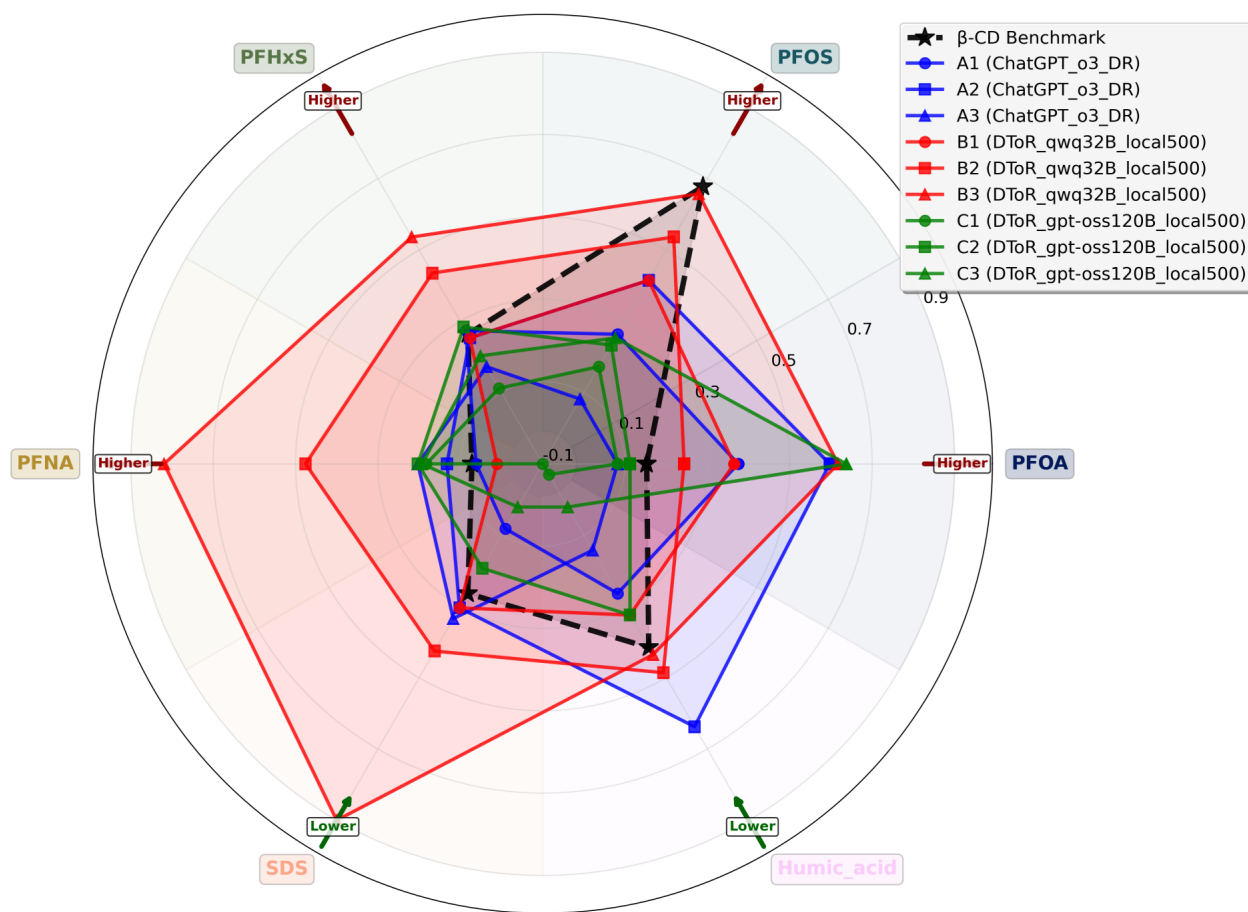


Figure S15: Radar plot comparing binding energies (ΔE_{bind}) across all candidate systems and benchmark β -CD obtained from static DFT calculations with implicit solvent.

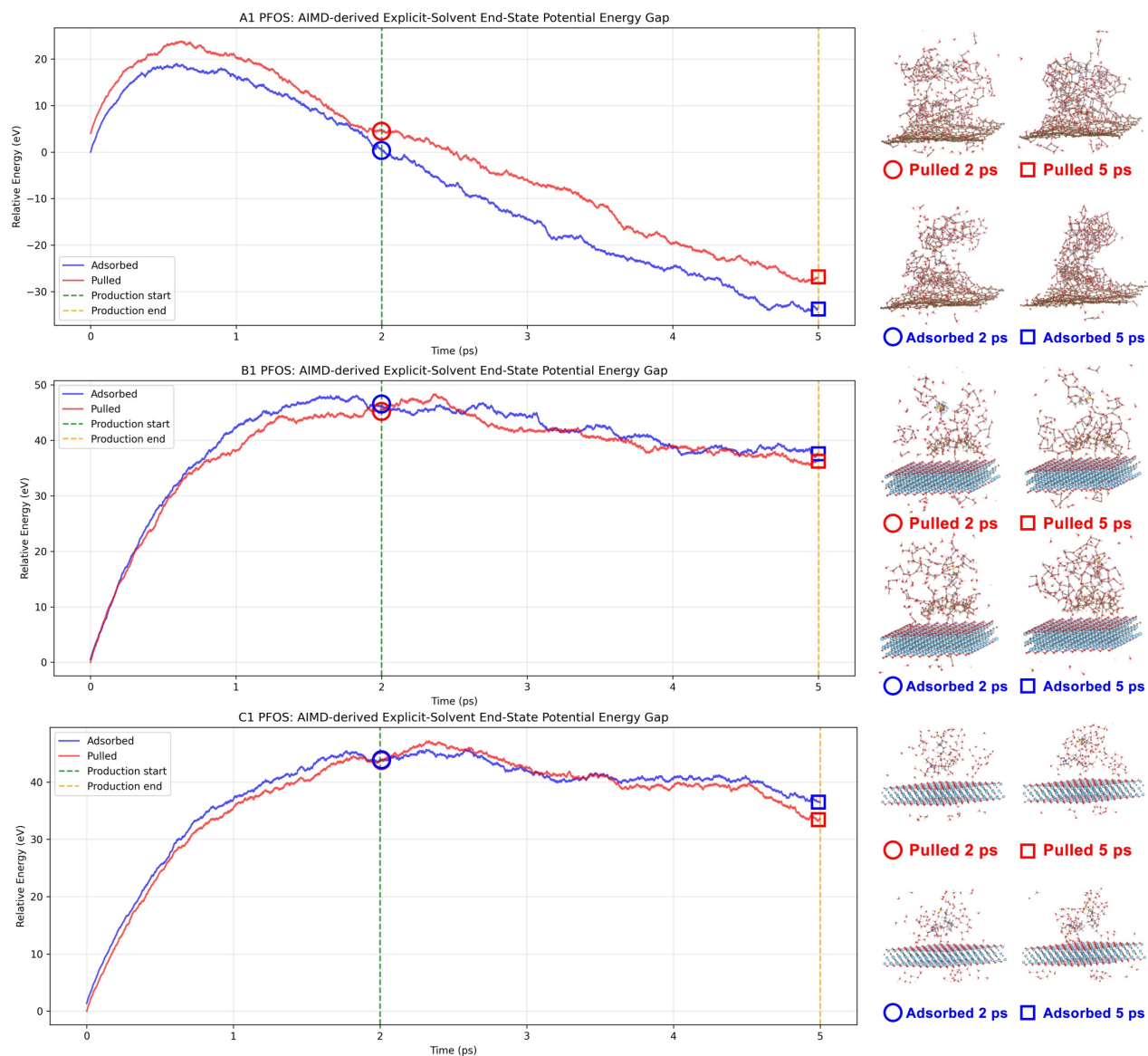


Figure S16: Representative AIMD trajectory showing relative energy evolution under explicit solvent conditions. The green dashed line denotes the 2 ps equilibration period. Right panels display system configurations at highlighted time points along the production trajectory.

**AIMD-derived Explicit-Solvent End-State Potential Energy Gap (eV) Radar Chart
(All Compounds)**

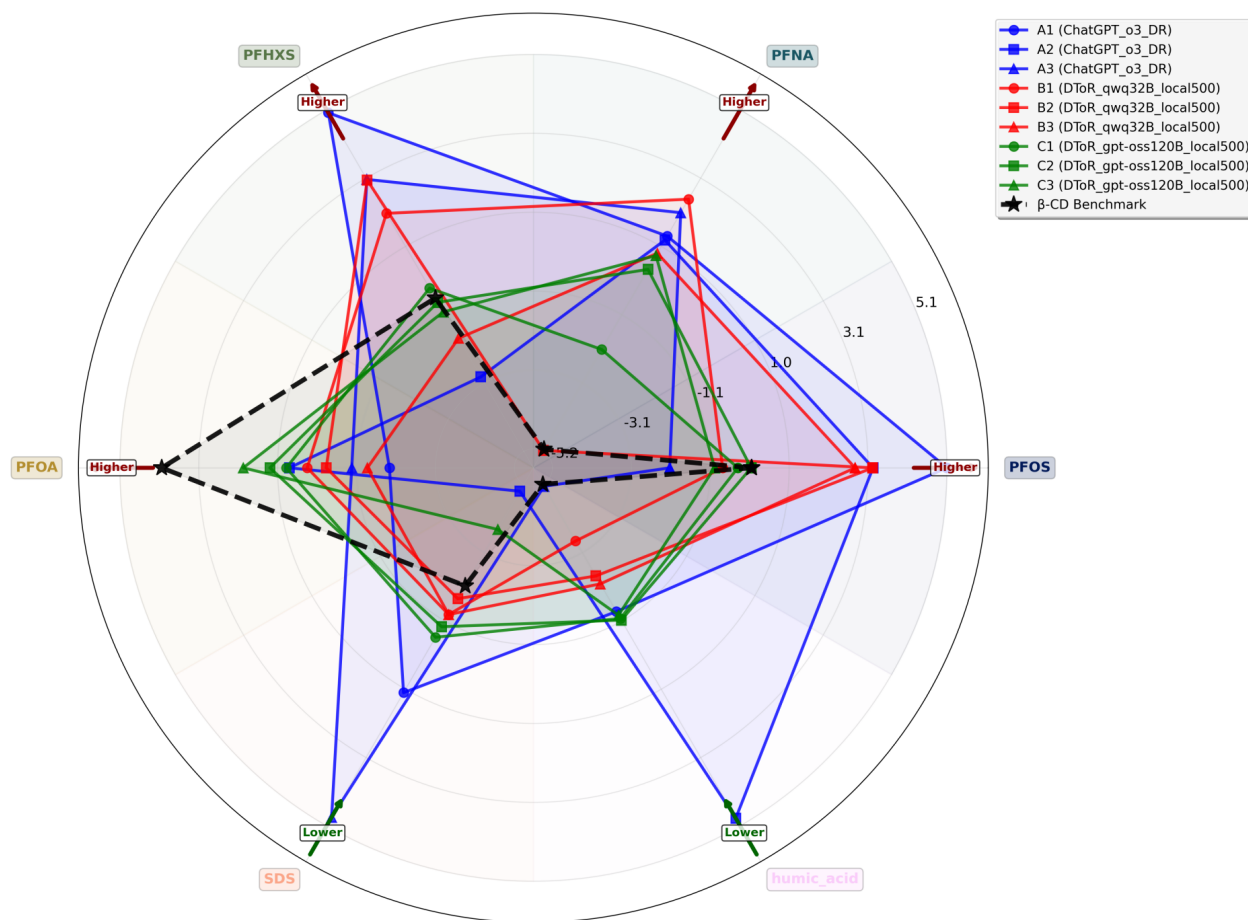


Figure S17: Radar plot comparing explicit-solvent end-state potential energy gaps ($\Delta E_{\text{pot}}^{\text{ES}}$) averaged over the 3 ps production period for all candidate systems and benchmark β -CD from AIMD simulations.

DFT Static: PFAS Sensor Selectivity Scores

Implicit solvent, linear selectivity metric

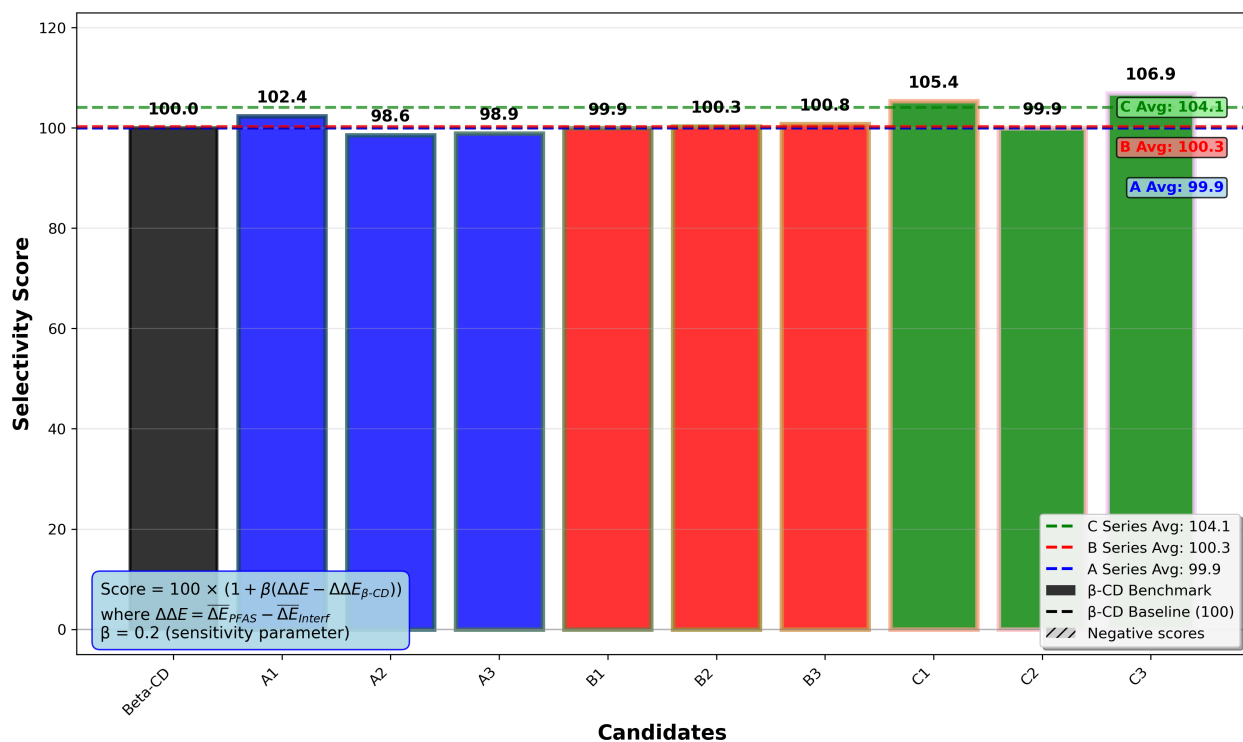


Figure S18: Selectivity scores for all candidate systems from static DFT calculations, normalized to β -CD baseline (100). Scores are calculated using the linear selectivity metric with sensitivity parameter $\beta = 0.2$, where $\Delta\Delta E = \overline{\Delta E}_{PFAS} - \overline{\Delta E}_{Interf}$ represents the difference between average PFAS and interferent binding energies.

AIMD Explicit Solvent: PFAS Sensor Selectivity Scores

Explicit water molecules, captures solvent reorganization effects

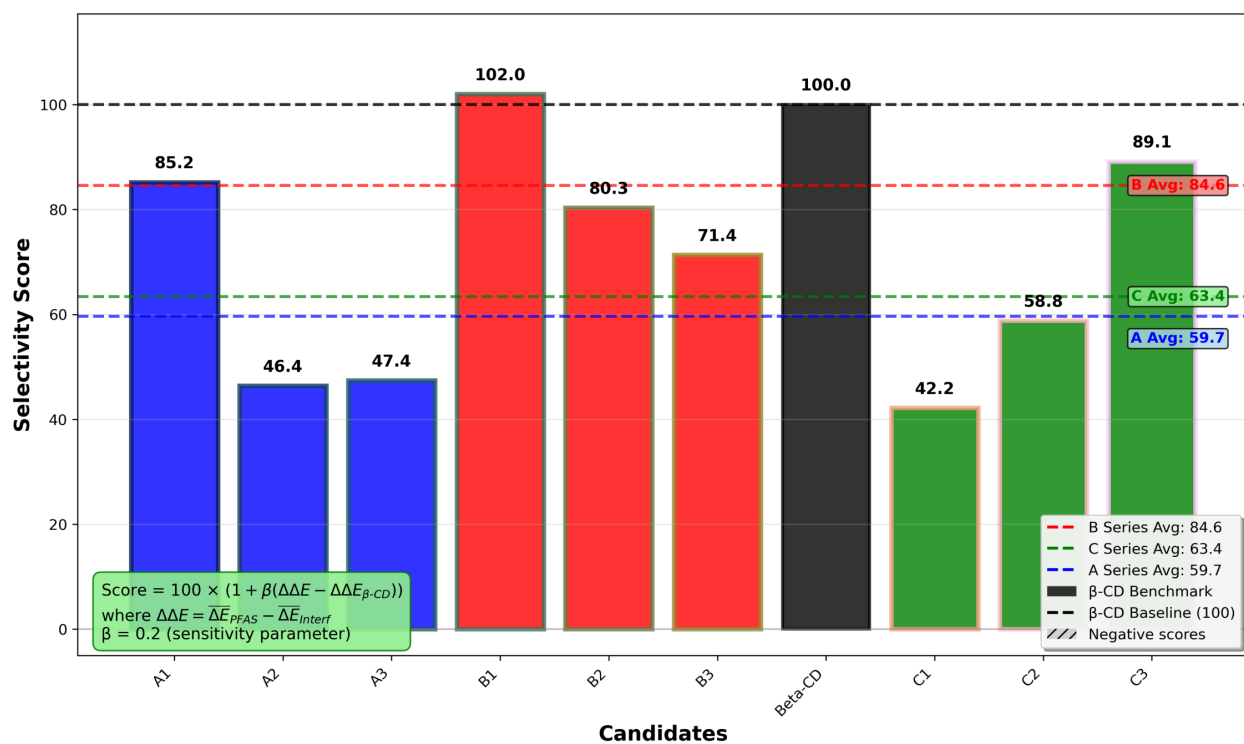


Figure S19: Selectivity scores for all candidate systems from explicit-solvent AIMD simulations, normalized to β -CD baseline (100). The scoring methodology remains identical to static DFT, except ΔE values are replaced by ΔE_{pot}^{ES} , the time-averaged potential energy gaps from the 3 ps production period.

F.3 PFAS Degradation

F.3.1 PFAS_Electro_Degradation

For the second application: PFAS Degradation. The query as shown in C is:

Which novel electrode materials can achieve efficient PFAS degradation under ambient aqueous electrochemical conditions, delivering both high mineralization and defluorination rates? What intrinsic properties--such as PFAS adsorption affinity, reactive oxygen species generation capacity, and C-F bond activation energy--should be optimized to guide their discovery?

The best commercial solution is: **Gemini_2.5_Pro_DR**.

The best local non gpt-oss solution is: **DToR_qwq32B_local500**.

The best local gpt-oss solution is: **DToR_gpt-oss120B_local500**.

The expert based on the two reports, provided 5 commercial DR report derived candidates (A1-A5), and 5 local non gpt-oss DR report derived candidates (B1-B5), and 5 local gpt-oss DR report derived candidates (C1-C5), visualized in Fig. S20:

Ti₄O₇ — Pristine Magnéli (001) bench slab Triclinic P1 slab with $a = 22.376 \text{ \AA}$, $b = 27.651 \text{ \AA}$, $\gamma = 75.306^\circ$, $c = 42.208 \text{ \AA}$ (in-plane area $\approx 598.50 \text{ \AA}^2$). Atom counts (Ti/O = 256/448; 704 total) match a Ti₄O₇ (001) termination. The populated thickness spans $\approx 12.13 \text{ \AA}$ ($z \approx 3.41\text{--}15.53 \text{ \AA}$), leaving $\approx 30.08 \text{ \AA}$ vacuum; the slab mid-plane lies near $z \approx 9.47 \text{ \AA}$. Surfaces are stoichiometric and flat, preserving Magnéli shear-plane connectivity and metallic conduction pathways—our baseline conductive-oxide reference for PFAS tests. Build/relax notes: 4 atomic layers; bottom two constrained. (Adsorbates for subsequent runs were seeded $\approx 3 \text{ \AA}$ above the most protruding Ti site, tail parallel to the surface.)

A1 — Ti₄O₇ (001) with through-pore + rim O-vacancies Triclinic P1 cell with $a = 22.376 \text{ \AA}$, $b = 27.651 \text{ \AA}$, $\gamma = 75.306^\circ$, $c = 42.208 \text{ \AA}$ (in-plane area $\approx 598.50 \text{ \AA}^2$). Atom counts (Ti/O = 249/437; 686 total) reflect removal of a top-side cluster and additional rim O-vacancies relative to the bench ($\Delta = -7 \text{ Ti}, -11 \text{ O}$). The populated thickness is $\approx 13.44 \text{ \AA}$ ($z \approx 3.00\text{--}16.45 \text{ \AA}$), leaving $\approx 28.77 \text{ \AA}$ vacuum; the slab mid-plane sits near $z \approx 9.73 \text{ \AA}$. A circular through-pore was introduced by deleting atoms within a $\sim 5 \text{ \AA}$ -radius cylinder from the upper layers, yielding an effective mouth $\sim 1.0 \text{ nm}$ diameter; the rim exposes under-coordinated Ti with a locally reduced O environment, while the surrounding lattice retains Magnéli shear-plane connectivity. Relaxation protocol used: bottom half constrained; top region (and any adsorbates) relaxed so the pore edge dominates binding/activation. Connection to the Ti₄O₇ bench: same lattice, cell vectors, and basal (001) termination as the pristine Ti₄O₇ bench slab; bottom region unchanged. All edits are localized to the top surface (pore machining + rim O-vacancies). Away from the pore, Ti/O stoichiometry per layer and shear-plane topology match the bench reference.

A2 — Pd-overlayer/Ti₄O₇ (001) composite (amorphous Pd on the bench slab) Triclinic P1 cell with $a = 22.376 \text{ \AA}$, $b = 27.651 \text{ \AA}$, $\gamma = 75.306^\circ$, $c = 42.21 \text{ \AA}$ (in-plane area $\approx 598.50 \text{ \AA}^2$). Atom counts (Ti/O/Pd = 256/448/94; 798 total) indicate a stoichiometric Ti₄O₇ substrate capped by a Pd overlayer. The populated thickness spans $\approx 16.45 \text{ \AA}$ ($z \approx 3.14\text{--}19.59 \text{ \AA}$), leaving $\approx 25.76 \text{ \AA}$ vacuum; mid-plane at $z \approx 11.37 \text{ \AA}$. Pd atoms populate the top terrace broadly (no single island), forming a disordered sheet with Pd heights $\sim 16.12\text{--}19.59 \text{ \AA}$ (mean $\approx 17.71 \text{ \AA}$), i.e., $\sim 3.1 \text{ \AA}$ above the top oxide layer ($z_{\text{ox,max}} \approx 16.49 \text{ \AA}$). **Connection to the Ti₄O₇ bench:** identical lattice and Ti/O stoichiometry to the pristine Magnéli (001) slab; modifications are limited to a Pd overlayer on the top surface (bottom half retained as in the bench), with no pores or O-vacancies introduced.

A3 — Pd₅₅ cluster on Ti₄O₇ (001) (icosahedral-like nanoparticle on the bench slab) Triclinic P1 cell with $a = 22.376 \text{ \AA}$, $b = 27.651 \text{ \AA}$, $\gamma = 75.306^\circ$, $c = 42.21 \text{ \AA}$ (in-plane area $\approx 598.50 \text{ \AA}^2$). Atom counts (Ti/O/Pd = 256/448/55; 759 total) show a Ti₄O₇ substrate supporting a compact Pd nanoparticle. The populated thickness spans $\approx 22.65 \text{ \AA}$ ($z \approx 3.23\text{--}25.87 \text{ \AA}$), leaving $\approx 19.56 \text{ \AA}$ vacuum; mid-plane at $z \approx 14.55 \text{ \AA}$. The Pd cluster (initially icosahedral; allowed to relax) ($n = 55$) is localized on the top terrace with a projected footprint $\sim 9.2 \times 9.6 \text{ \AA}$ (max in-plane radius $\approx 5.33 \text{ \AA}$; projected diameter $\approx 10.65 \text{ \AA}$) and vertical extent placing the apex $\sim 9.7 \text{ \AA}$ above the top oxide layer ($z_{\text{ox,max}} \approx 16.15 \text{ \AA}$). **Connection to the Ti₄O₇ bench:** same lattice and stoichiometric oxide as the pristine (001) slab; the only alteration is a single Pd₅₅ nanoparticle anchored on the top surface (no pore machining or O-vacancies), with the bottom region kept as in the bench reference.

A4 — F-doped rutile SnO₂ (110) slab (FTO, O→F substitution near surface) Orthogonal P1 cell with $a = 26.8022 \text{ \AA}$, $b = 25.4880 \text{ \AA}$, $\gamma = 90.0^\circ$, $c = 42.1012 \text{ \AA}$; in-plane area $\approx 683.13 \text{ \AA}^2$. The metrics correspond to a 4×8 SnO₂(110) supercell ($a \approx 4 \times a_{(\text{rutile})} \sqrt{2}$, $b \approx 8 \times c_{(\text{rutile})}$). Atom counts (Sn/O/F = 256/497/15; 768 total) indicate $\sim 2.9\%$ O→F substitution on the anion sublattice (15/512), i.e., a lightly F-doped “FTO” slab. The populated thickness spans $\approx 14.28 \text{ \AA}$ ($z \approx 4.32\text{--}18.60 \text{ \AA}$), leaving $\approx 27.83 \text{ \AA}$ vacuum; Sn layers occupy $z \approx 4.38\text{--}15.29 \text{ \AA}$, while F sites are confined to a narrow band near the top ($z \approx 16.33\text{--}17.17 \text{ \AA}$; mean $\approx 16.75 \text{ \AA}$), just beneath the outermost O ridges ($O_{\text{max}} \approx 18.60 \text{ \AA}$). This places F primarily in near-surface O positions on (110), preserving the characteristic bridging-O/in-plane-O relief of rutile and providing a slightly more electron-rich, less hydroxylated top termination expected for FTO.

A5 — B-doped four-layer graphene Hexagonal P1; $a = b = 19.68 \text{ \AA}$, $\gamma = 120^\circ$, $c \approx 36.0 \text{ \AA}$. Four graphene sheets stacked with the standard **interlayer spacing $d(002) \approx 3.35 \pm 0.05 \text{ \AA}$** (three gaps $\rightarrow \sim 10.05 \text{ \AA}$ slab thickness). Substitutional B is confined to the **top layer** (≈ 10 at% within that plane; $\approx 2\text{--}3$ at% overall), preserving an sp^2 framework. The remaining $\sim 26 \text{ \AA}$ is vacuum along c to suppress image interactions. During relaxation, we fixed the bottom two layers; relax the top two (and any adsorbates).

B1 — F-grafted four-layer graphene (consensus spacing; A5-consistent) Hexagonal P1; keep A5’s in-plane metrics ($a = b$, $\gamma = 120^\circ$) unchanged and $c \approx 36.0 \text{ \AA}$. Stack **four graphene sheets with the standard interlayer spacing $d(002) = 3.35 \pm 0.05 \text{ \AA}$** (three gaps $\rightarrow \sim 10.05 \text{ \AA}$ slab thickness), with the **remaining $\sim 26 \text{ \AA}$ as vacuum** along c to decouple periodic images. **Chemistry/dopant pattern exactly as in A5** (no changes to which layer(s) are doped/functionalized); the carbon network remains predominantly sp^2 . **Same Relaxation protocol as A5:** fix the bottom two layers; relax the top two (and any adsorbates). **Connection to A5:** identical spacing convention and vacuum budget as A5 to ensure cross-comparable adsorption energies and electrostatics across the graphene series, while leaving only the dopant/functional differences to drive behavior.

B2 — 2D Ti₃C₂ MXene (O/OH-terminated) Hexagonal P1 slab with $a = b = 24.536 \text{ \AA}$, $\gamma = 120^\circ$, $c = 36.700 \text{ \AA}$ (in-plane area $\approx 521.36 \text{ \AA}^2$). Atom counts (Ti/C/O/H = 192/128/128/114; 562 total) correspond to **64 f.u. of Ti₃C₂** with full two-sided terminations (128/site total): $\approx 89\%$ **–OH** (114 H) and $\approx 11\%$ **=O** (14 O), distributed symmetrically per face (**57 –OH + 7 =O** each side). The vacuum layer is around **27.21 \AA**. The sheet preserves the characteristic **2D MXene** core (Ti–C–Ti trilayers) with mixed O/OH terminations pointing outward, yielding a hydrophilic, electronically conductive surface appropriate for adsorption tests (e.g., PFAS headgroup coordination via –OH domains).

B3 — 2D MnO₂-like (birnessite-style) nanosheet with sparse one-sided –OH Orthogonal P1 cell with $a = b = 29.3628 \text{ \AA}$, $\gamma = 90.0^\circ$, $c = 33.595 \text{ \AA}$ (in-plane area $\approx 862.17 \text{ \AA}^2$). Atom counts (Mn/O/H = 216/411/18; 645 total) are consistent with a near-stoichiometric MnO₂ layer carrying light hydroxylation (H:Mn ≈ 0.083). The populated thickness is $\approx 9.32 \text{ \AA}$ ($z \approx 0.82\text{--}10.14 \text{ \AA}$), leaving $\approx 24.28 \text{ \AA}$ vacuum. Element-resolved spans: Mn $\approx 1.52\text{--}9.59 \text{ \AA}$; O $\approx 0.82\text{--}9.61 \text{ \AA}$; H confined to $\approx 7.12\text{--}10.14 \text{ \AA}$ on the outer face, indicating **one-sided –OH/water terminations** on a **2D** octahedral sheet. Relaxation note: we kept the lower half constrained and relaxed the top half/adsorbates; head-group binding is expected at surface –OH/O sites with the basal Mn–O framework remaining robust.

B4 — 2D MnO₂-like (birnessite-style) nanosheet, smaller supercell; one-sided –OH Orthogonal P1 cell with $a = b = 22.000 \text{ \AA}$, $\gamma = 90.0^\circ$, $c = 33.610 \text{ \AA}$ (in-plane area = 484.00 \AA^2). Composition (Mn/O/H = 150/285/12; 447 total) again reflects a MnO₂ sheet with light hydroxylation (H:Mn ≈ 0.08). The populated thickness is $\approx 9.40 \text{ \AA}$ ($z \approx 1.77\text{--}11.17 \text{ \AA}$), leaving $\approx 24.21 \text{ \AA}$ vacuum. Element-resolved spans: Mn $\approx 2.12\text{--}10.48 \text{ \AA}$; O $\approx 1.77\text{--}10.99 \text{ \AA}$; H $\approx 8.43\text{--}11.17 \text{ \AA}$, i.e., **–OH/water groups localized on the top face** of the **2D** sheet. Relaxation matches B3 (bottom region constrained, top free) to keep comparisons clean across the MnO₂ series.

B5 — Graphene-capped 2D MXene (derived from B2) Derived directly from **B2** (same cell vectors and terminations), a **single-layer graphene** sheet is added parallel to the top face of the MXene and centered to span the full in-plane cell. The initial MXene↔graphene separation is set to $\sim 3.35 \text{ \AA}$ (graphite $d(002)$), with **no covalent links**—pure van der Waals contact. Graphene is pristine sp^2 and allowed to relax laterally/vertically; the MXene beneath follows B2’s relaxation protocol (bottom

constrained, top free). The **c-axis vacuum is kept as in B2** to avoid inter-image coupling. **Connection to B2:** identical substrate; the only modification is the graphene capping layer.

C1 — Multi-doped graphene (N,S,B co-doping with dual-layer defects) Hexagonal P1; layer count and supercell dimensions ($a = b = 19.68 \text{ \AA}$, $\gamma = 120^\circ$, $c \approx 36.0 \text{ \AA}$) kept consistent with A5 and B1. Four graphene sheets stacked with standard interlayer spacing $d(002) \approx 3.35 \text{ \AA}$ (three gaps $\rightarrow \sim 10.05 \text{ \AA}$ nominal slab thickness), modified by extensive heteroatom doping and defect engineering across the top two layers. The populated thickness spans $\sim 10.05 \text{ \AA}$ ($z \approx 4.00\text{--}14.05 \text{ \AA}$), with the structure deliberately positioned low in the supercell to leave $\sim 19 \text{ \AA}$ of vacuum above the top surface, providing ample space for PFAS adsorbate placement and subsequent geometry optimization. The multi-doping architecture combines B–N nearest-neighbor pairs ($\sim 2.5 \text{ \AA}$ separation for electron-deficient/rich adjacency) and N–S nearest-neighbor pairs ($\sim 2.5 \text{ \AA}$ separation for direct electron transfer and reactive oxygen species synergy), distributed across both the top layer (3 B–N pairs + 3 N–S pairs + 5 isolated dopants) and second layer (2 B–N pairs + 2 N–S pairs + 3 isolated dopants). A localized “hole” defect ($\sim 4 \text{ \AA}$ radius cluster, 8 atoms removed) is introduced at the supercell center in the top layer to expose under-coordinated edge sites and create a nano-pore for enhanced PFAS molecular access, complemented by scattered single-atom vacancies (3% in top layer, 5% in second layer). Total heteroatom loading reaches $\sim 20\text{--}25\%$ in the top two layers (13 N + 8 S + 7 B across 495 total atoms). This dual-layer functionalization strategy ensures multi-modal catalytic pathways: electron-transfer modulation via B–N pairs, oxidative radical generation via N–S pairs, and defect-mediated C–F bond polarization around the central nano-pore and distributed vacancy sites.

C2 — N-doped CuFe_2O_4 spinel (111) with oxygen vacancies Triclinic P1 slab with $a = 16.81 \text{ \AA}$, $b = 18.64 \text{ \AA}$, $\gamma \approx 120^\circ$ (hexagonal-like in-plane symmetry), $c = 47.58 \text{ \AA}$ (in-plane area $\approx 313.5 \text{ \AA}^2$), representing a 2×2 surface expansion of the CuFe_2O_4 (111) spinel termination. Atom counts (Cu/Fe/N/O = 64/128/11/240; 443 total) reflect nitrogen substitution in the surface oxygen sublattice ($\sim 11\%$ of surface O sites replaced by N) and controlled oxygen-vacancy formation (5 vacancies, $\sim 7\%$ of remaining surface O). The populated thickness spans $\approx 14.58 \text{ \AA}$ ($z \approx 4.00\text{--}18.58 \text{ \AA}$), leaving $\approx 29 \text{ \AA}$ of vacuum above the top surface for PFAS adsorbate placement and explicit-solvent AIMD simulations. The (111) orientation exposes a mixed-termination surface with both octahedral Fe^{3+} and tetrahedral Cu^{2+} coordination environments. N-doping is distributed on the surface oxygen sublattice, while the engineered O-vacancies create under-coordinated metal centers (exposed $\text{Fe}^{3+}/\text{Cu}^{2+}$ sites).

C3 — Co-doped Mn_3O_4 spinel (001) with oxygen vacancies Orthorhombic P1 slab with $a = 33.07 \text{ \AA}$, $b = 17.23 \text{ \AA}$, $c = 46.60 \text{ \AA}$ (in-plane area $\approx 569.6 \text{ \AA}^2$), representing a 3×3 surface expansion of the Mn_3O_4 (001) spinel termination. Atom counts (Co/Mn/O = 6/318/429; 753 total) reflect cobalt substitution in subsurface octahedral Mn sites ($\sim 5\%$ of subsurface Mn) and controlled oxygen-vacancy formation (3 vacancies, $\sim 2.5\%$ of surface O). The populated thickness spans $\approx 13.60 \text{ \AA}$ ($z \approx 4.00\text{--}17.60 \text{ \AA}$), leaving $\approx 29 \text{ \AA}$ of vacuum above the top surface for PFAS adsorbate placement and explicit-solvent AIMD simulations. The (001) orientation exposes a three-dimensional spinel framework with mixed-valence $\text{Mn}^{2+}/\text{Mn}^{3+}$ coordination environments, distinct from the layered birnessite- MnO_2 structures (B3, B4). Co-doping is localized in the subsurface layer (positioned between surface and core, $\sim 2.5\text{--}5.0 \text{ \AA}$ from the top surface), while the engineered O-vacancies are distributed on the surface.

C4 — ZnFe_2O_4 spinel (111) with oxygen vacancies Triclinic P1 slab with $a = 23.86 \text{ \AA}$, $b = 20.66 \text{ \AA}$, $\gamma \approx 120^\circ$ (hexagonal-like in-plane symmetry), $c = 50.33 \text{ \AA}$ (in-plane area $\approx 493.0 \text{ \AA}^2$), representing a 2×2 surface expansion of the ZnFe_2O_4 (111) spinel termination. Atom counts (Fe/O/Zn = 256/506/128; 890 total) reflect controlled oxygen-vacancy formation (6 vacancies, $\sim 5\%$ of surface O). The populated thickness spans $\approx 17.33 \text{ \AA}$ ($z \approx 4.00\text{--}21.33 \text{ \AA}$), leaving $\approx 29 \text{ \AA}$ of vacuum above the top surface for PFAS adsorbate placement and explicit-solvent AIMD simulations. The (111) orientation exposes a mixed-termination surface with tetrahedral Zn^{2+} and octahedral Fe^{3+} coordination environments. The engineered O-vacancies are distributed on the surface, creating under-coordinated metal centers (exposed $\text{Fe}^{3+}/\text{Zn}^{2+}$ sites).

C5 — Ti_3C_2 MXene/g- $\text{C}_3\text{N}_4/\text{Al}_2\text{O}_3$ cluster heterostructure Hexagonal P1 slab with $a = b = 30.67 \text{ \AA}$, $\gamma = 120^\circ$, $c = 51.70 \text{ \AA}$ (in-plane area $\approx 704.6 \text{ \AA}^2$), representing a three-layer heterostructure with distinct functional regions. Atom counts (Al/C/H/N/O/Ti = 55/347/60/196/254/300; 1212 total) reflect a Ti_3C_2 MXene base layer with mixed oxygen/hydroxyl termination ($\sim 70\% = \text{O}$, $\sim 30\% \text{--OH}$; 140

=O + 60 -OH groups distributed on both surfaces), a graphitic carbon nitride (g-C₃N₄) middle layer (343 atoms: 147 C + 196 N, derived from a 7×7 supercell expansion of the literature s-C₃N₄ structure and strained ~8.4% to match the MXene lattice, positioned ~3.35 Å above MXene), and an octahedral Al₂O₃ cluster (109 atoms: 55 Al + 54 O) centered on the top surface (positioned 7 Å above g-C₃N₄). The populated thickness spans ~26.6 Å ($z \approx 5.62\text{--}32.22$ Å), with the MXene core occupying $z \approx 5.62\text{--}16.92$ Å, the g-C₃N₄ layer at $z \approx 20.27$ Å, and the Al₂O₃ cluster centered at $z \approx 27.27$ Å.

F.3.2 Multi-Metric Evaluation of PFAS Degradation Catalysts

Effective catalytic degradation of PFAS compounds requires both strong surface adsorption to concentrate the pollutants and sufficient activation of the exceptionally stable C–F bonds. To comprehensively evaluate candidate catalysts for PFAS degradation, we employed a three-pronged computational assessment framework encompassing static binding energies, explicit-solvent dynamics, and C–F bond dissociation energetics, with Ti₄O₇ serving as the domain benchmark reference [27].

Integrated Performance Metrics

The degradation performance evaluation integrates three complementary metrics that capture distinct aspects of the catalytic process. First, the binding energy ΔE_{bind} from static DFT calculations quantifies the thermodynamic driving force for PFAS adsorption onto catalyst surfaces (Figure S22). Strong binding ensures sufficient surface coverage and residence time for subsequent degradation reactions. Second, the explicit-solvent potential energy gap $\Delta E_{\text{pot}}^{\text{ES}}$ from AIMD simulations reveals how aqueous solvation affects the adsorption thermodynamics (Figures S26 and S27), accounting for competitive water adsorption and hydrogen-bonding network reorganization that static calculations cannot capture. Third, the C–F bond dissociation energy quantifies the activation barrier for the rate-limiting defluorination step, computed by displacing fluorine atoms from adsorbed PFAS configurations to isolated positions within the supercell (Figure S23). **Scoring Framework for Degradation Performance**

To enable quantitative comparison across these diverse metrics, we applied a unified linear scoring framework:

$$\text{Score} = 100 \times (1 + \beta \cdot \Delta_{\text{metric}}) \quad (5)$$

where Δ_{metric} represents the performance differential relative to the Ti₄O₇ baseline, defined as $\Delta \bar{E} - \Delta \bar{E}_{\text{Ti}_4\text{O}_7}$ for binding metrics and $\Delta \bar{E}_{\text{Ti}_4\text{O}_7} - \Delta \bar{E}$ for C–F dissociation. Here $\Delta \bar{E}$ is the mean energy value averaged over four representative PFAS compounds (PFOA, PFOS, PFNA, PFHxS), and $\beta = 0.2$ serves as the sensitivity parameter. For binding metrics (both static DFT and AIMD), stronger adsorption (corresponding to larger magnitude binding energies) yields higher scores. For C–F dissociation, lower energy barriers yield higher scores, reflecting more facile bond activation. The distribution of C–F dissociation energies across different PFAS compounds and candidate surfaces exhibits substantial variability (Figure S24), with mean values ranging from approximately 2 to 6 eV (Figure S25). This variation underscores the importance of averaging over multiple PFAS species to obtain representative performance metrics, as individual compounds may exhibit preferential interactions with specific surface sites or crystallographic facets. **Performance Analysis Across Computational Methods**

Application of this scoring framework reveals distinct performance patterns across the three evaluation metrics. In static DFT calculations, several candidates demonstrate superior PFAS binding relative to the Ti₄O₇ benchmark (Figure S28), with C-series materials generally exhibiting stronger adsorption energies. However, the inclusion of explicit solvent effects in AIMD simulations significantly alters these rankings (Figure S30), with most candidates showing reduced binding scores due to solvent-mediated destabilization effects. This divergence highlights the critical importance of accounting for aqueous solvation in evaluating catalyst performance under realistic conditions. The C–F bond activation scores (Figure S29) provide complementary insights into degradation potential. Notably, candidates that excel in binding may not necessarily facilitate efficient C–F bond cleavage, as these properties depend on distinct electronic and geometric factors. However, C-series materials were proven in average level better with lower F dissociation energy barriers. Nonetheless, the ideal degradation catalyst must balance strong PFAS adsorption with effective bond activation—a trade-off that our multi-metric scoring framework quantitatively captures. **Implications for Catalyst Design**

The comprehensive evaluation framework presented here reveals that no single candidate uniformly excels across all performance metrics. Strong surface binding, while essential for PFAS capture, does not guarantee facile C–F bond activation. Similarly, materials optimized for bond dissociation may suffer from weak adsorption, particularly under aqueous conditions where solvent competition is significant. This multi-dimensional performance landscape emphasizes the need for balanced catalyst design that considers both thermodynamic (binding) and kinetic (bond activation) factors, evaluated under both implicit and

explicit solvation conditions to ensure robust performance predictions for practical applications. As indicated in this dry lab study, A3, B2, C3, and C4 could be promising candidates for further investigation in wet lab.

PFAS Degradation Catalyst Structures

A: Gemini_2.5pro_DR

C: DToR_gpt-oss120B_local500 DToR_qwq32B_local500

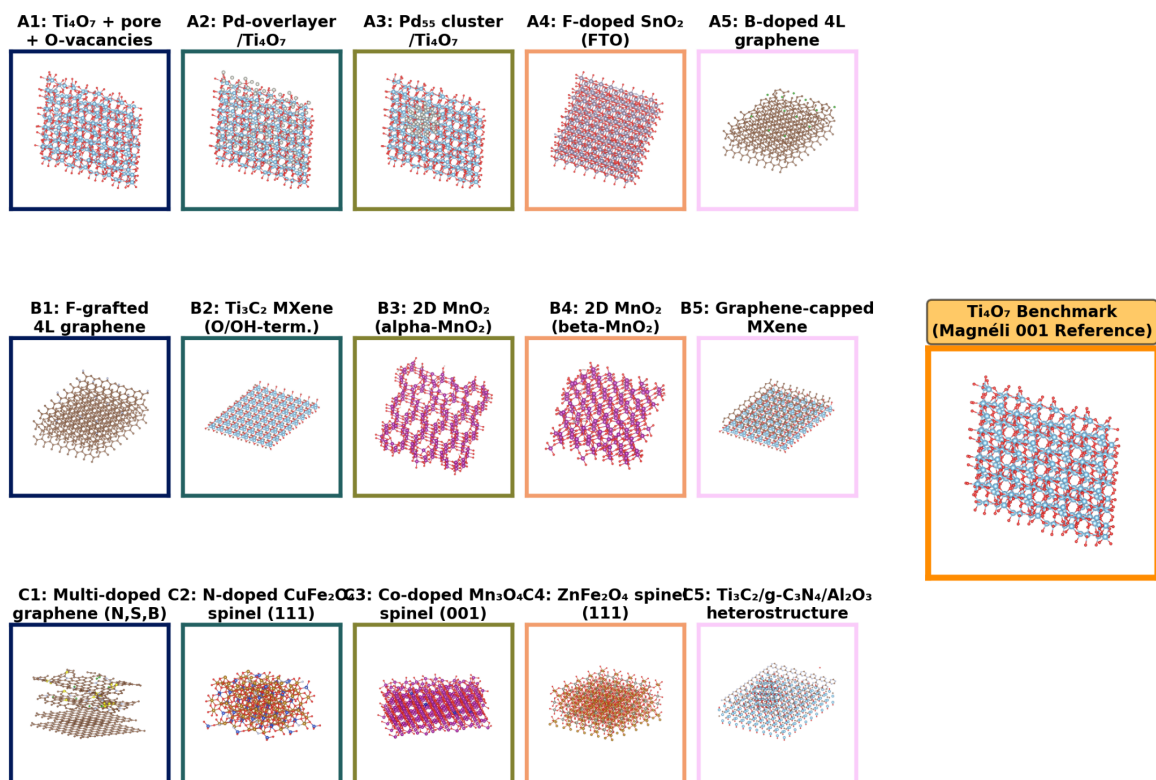


Figure S20: Structural configurations of candidate catalysts proposed by DR agents for PFAS degradation, with Ti₄O₇ [27] included as the domain benchmark reference.

PFAS Binding Showcases

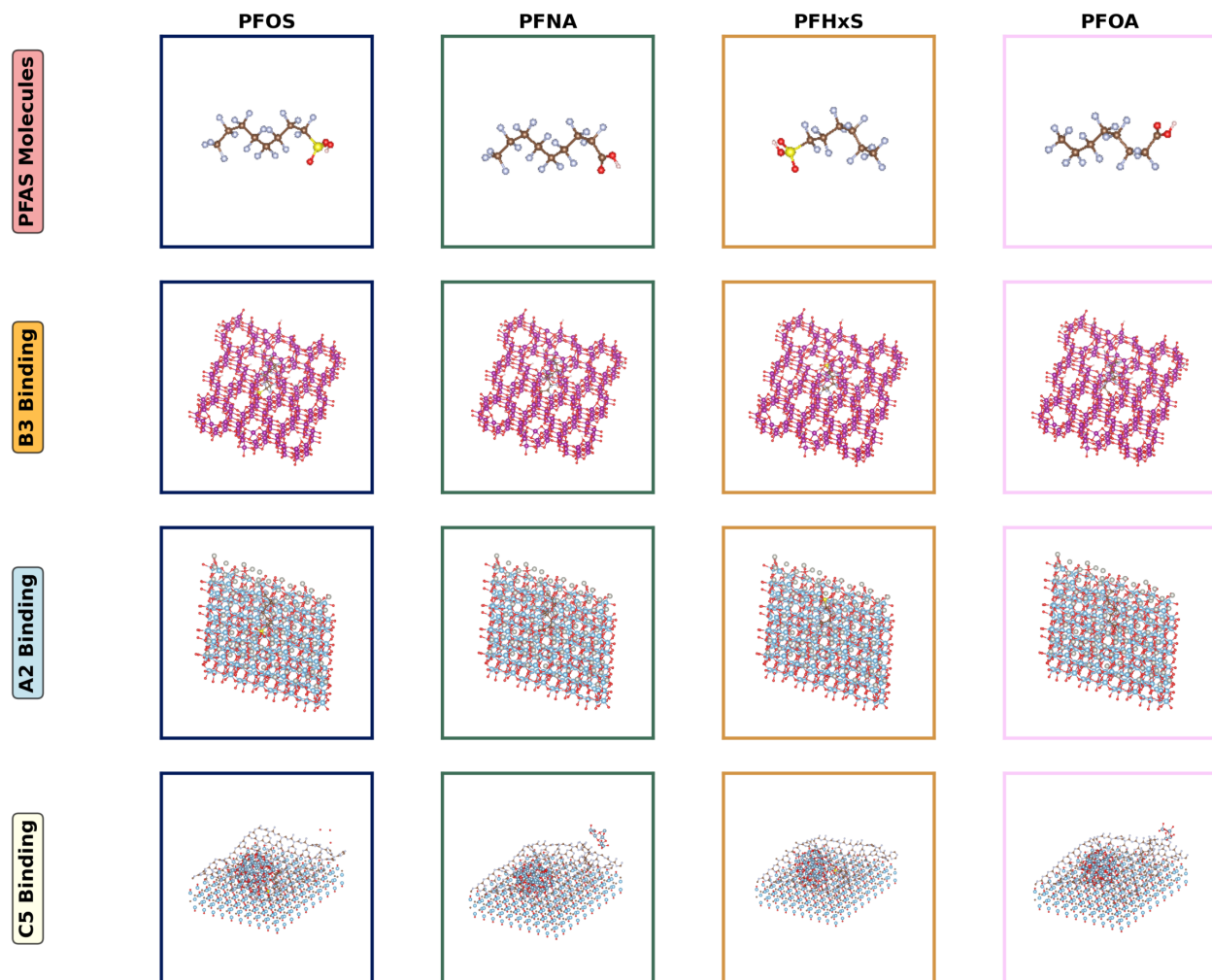


Figure S21: Representative PFAS compounds (PFOA, PFOS, PFNA, PFHxS) employed in degradation assessment, with corresponding optimized adsorption configurations on selected candidate surfaces.

PFAS Binding Energy (eV) Radar Chart

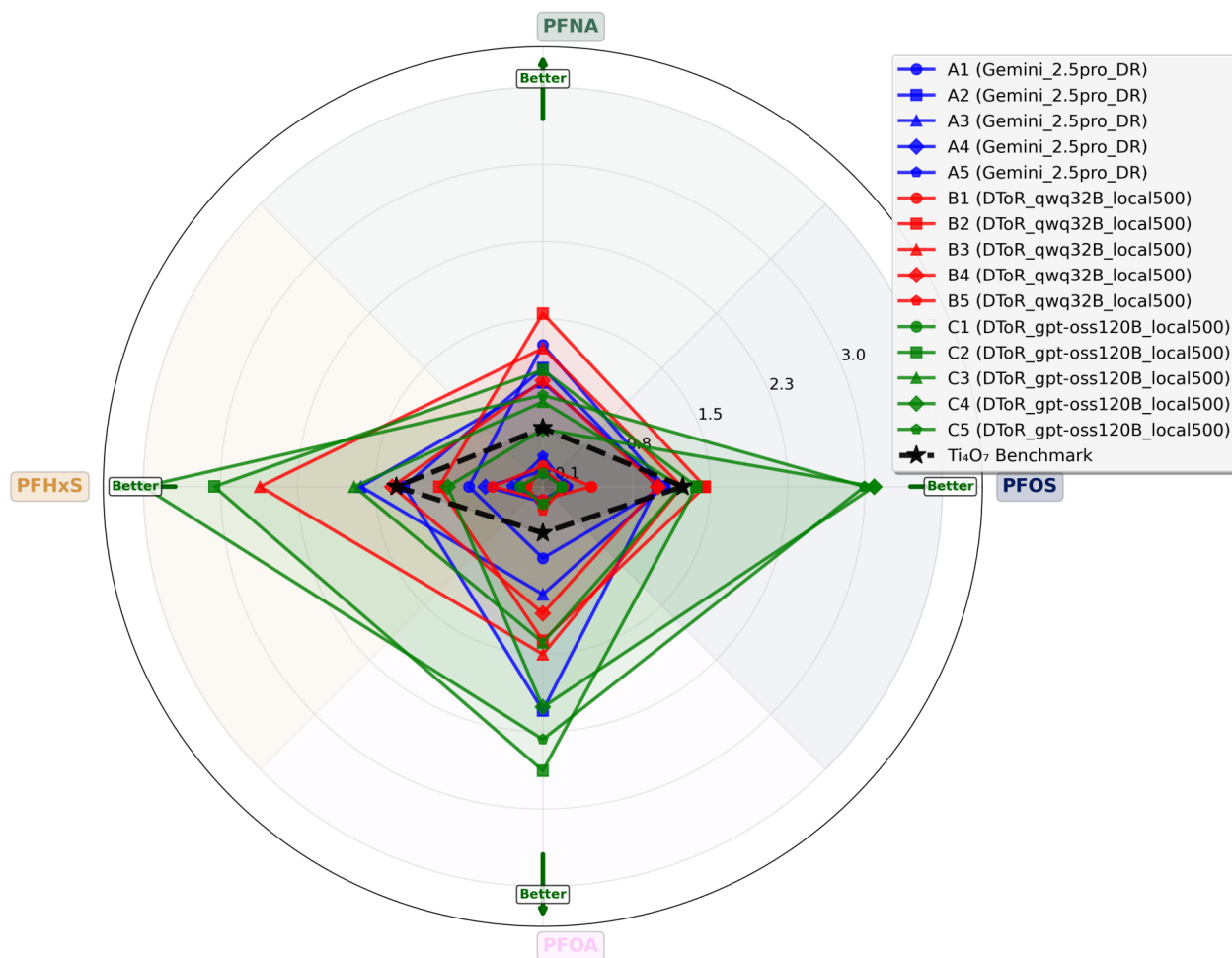
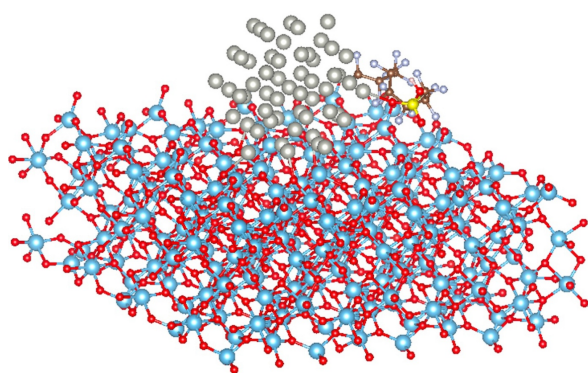
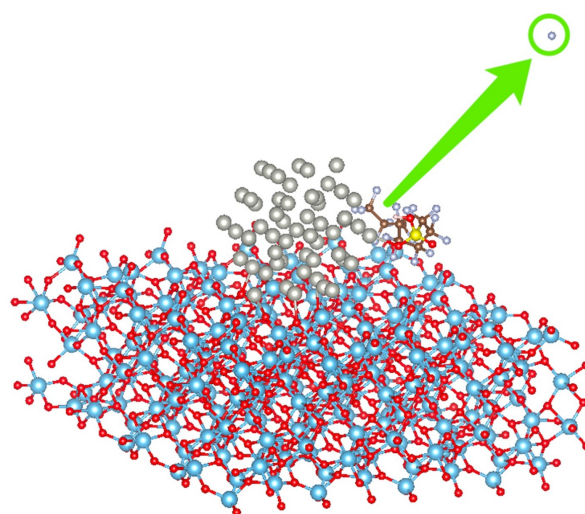


Figure S22: Radar plot comparing PFAS binding energies (ΔE_{bind}) across all candidate catalysts and benchmark Ti_4O_7 obtained from static DFT calculations with implicit solvent.



A3 PFOS Adsorbed



**A3 PFOS Adsorbed-
F dissociated**

Figure S23: Illustration of C–F bond dissociation simulation protocol. Left: Initial configuration with PFOS adsorbed on A3 surface. Right: Final configuration with fluorine atom displaced to corner position (5 Å from each boundary) of the supercell.

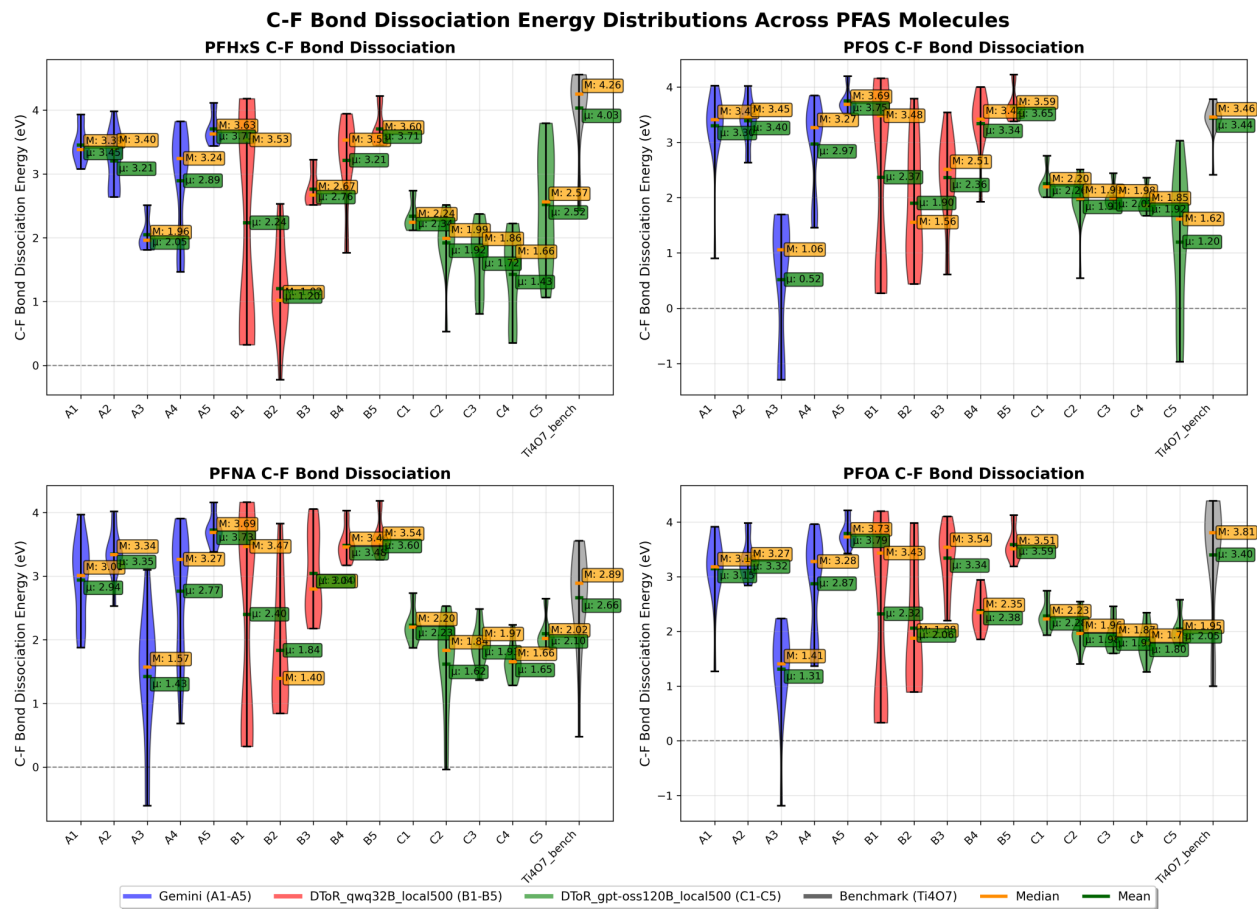


Figure S24: Violin plots showing distributions of C–F bond dissociation energies for different PFAS compounds (PFOA, PFOS, PFNA, PFHxS) across all candidate catalysts, with mean values indicated by horizontal bars.

PFAS Average C-F Bond Dissociation Energy (eV) Radar Chart

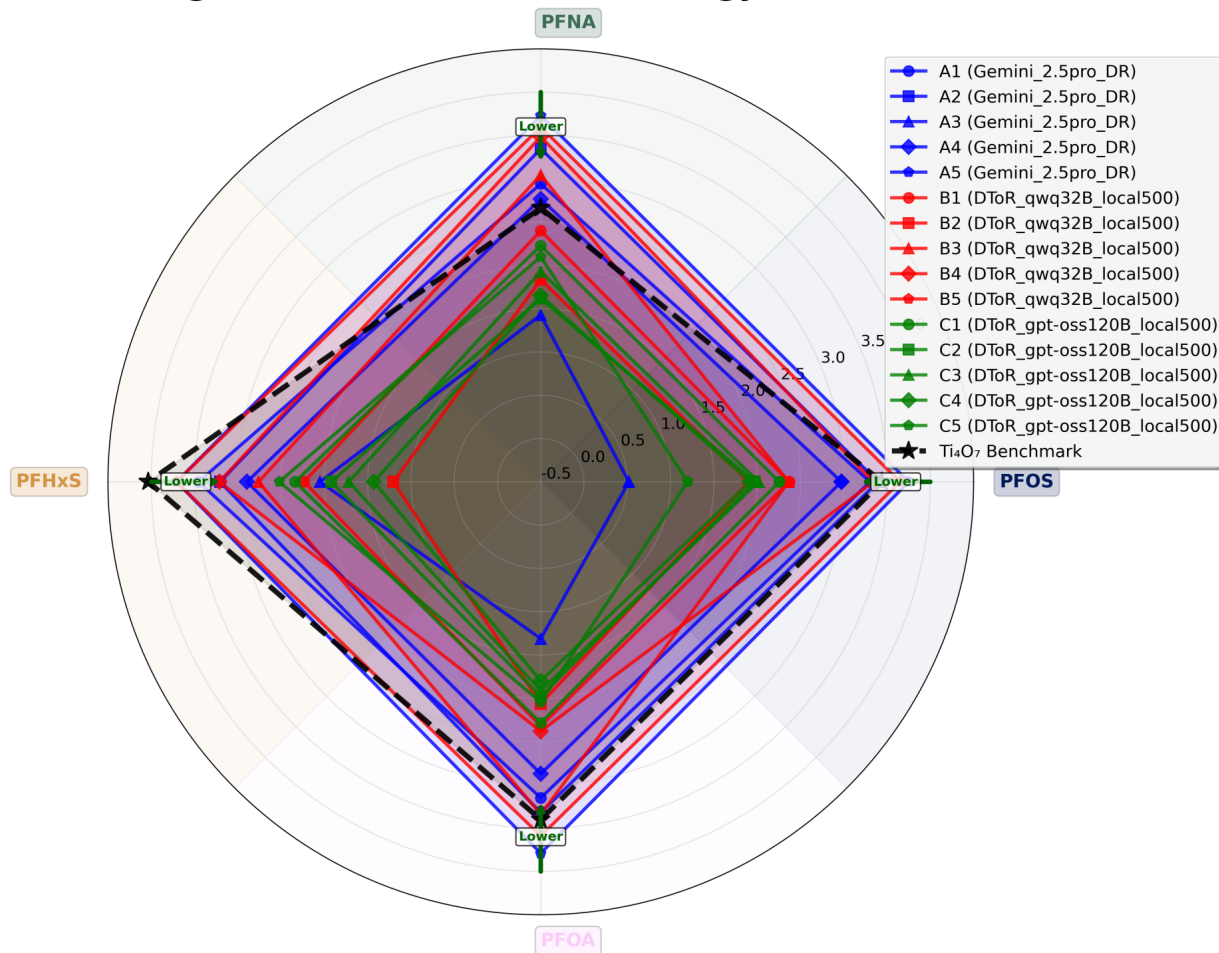


Figure S25: Radar plot comparing mean C-F bond dissociation energies across all candidate catalysts and benchmark Ti_4O_7 . Lower dissociation energies indicate more favorable C-F bond activation for degradation.

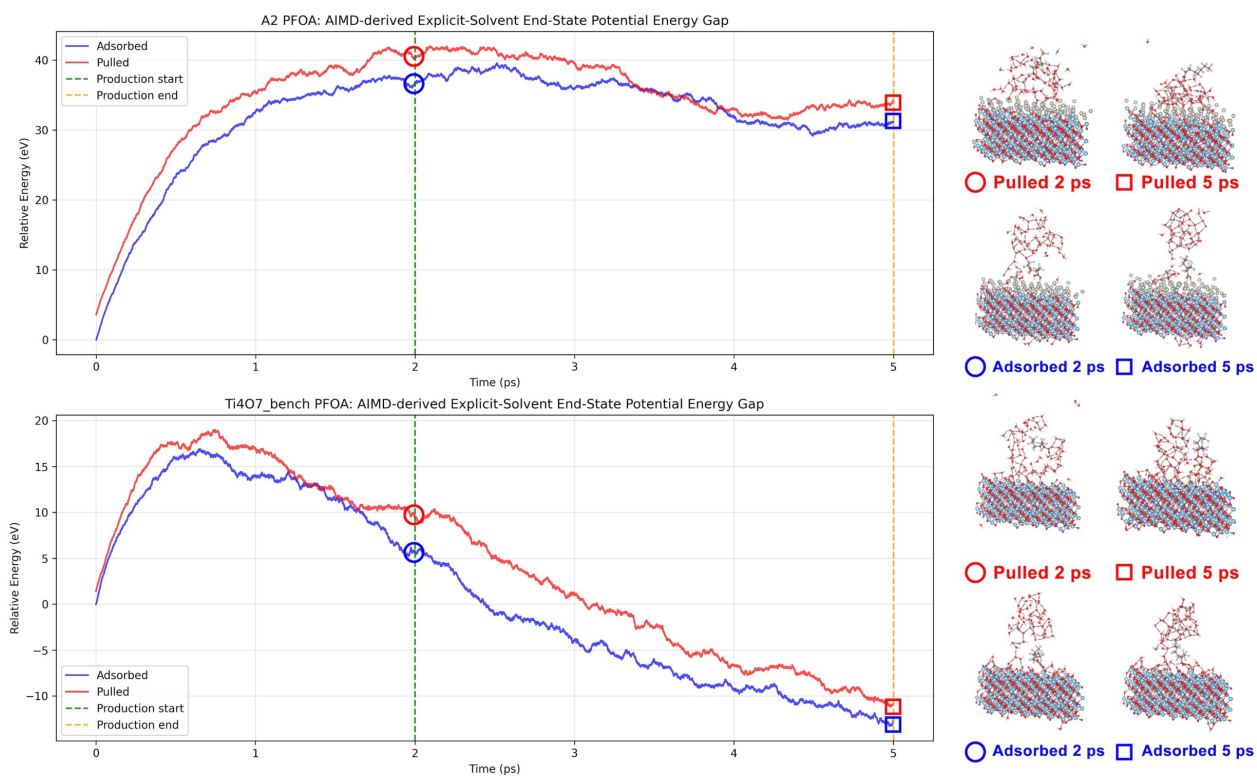


Figure S26: Representative AIMD trajectory showing system energy evolution under explicit solvent conditions. The green dashed line denotes the 2 ps equilibration period. Right panels display system configurations at highlighted time points along the 3 ps production trajectory.

AIMD-derived Explicit-Solvent End-State Potential Energy Gap (eV) Radar Chart

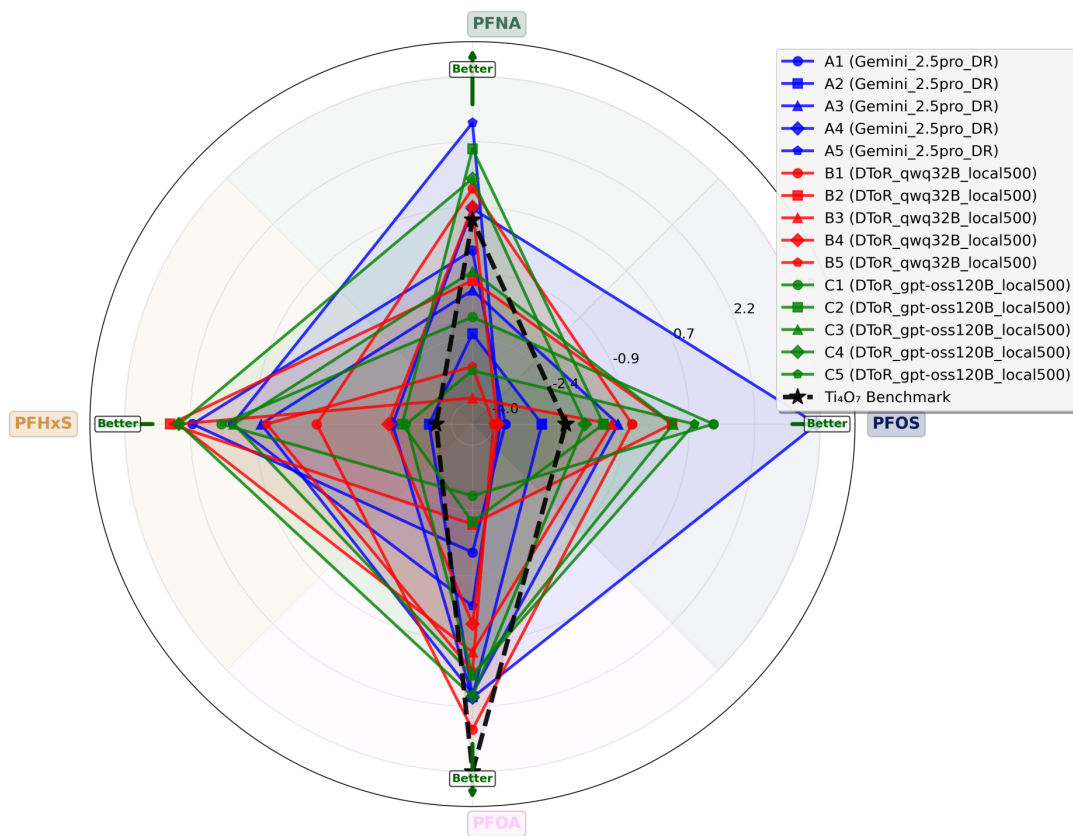


Figure S27: Radar plot comparing explicit-solvent end-state potential energy gaps ($\Delta E_{\text{pot}}^{\text{ES}}$) averaged over the 3 ps production period for all candidate catalysts and benchmark Ti_4O_7 from AIMD simulations.

DFT Static: PFAS Degradation Binding Scores

Implicit solvent, binding energy metric

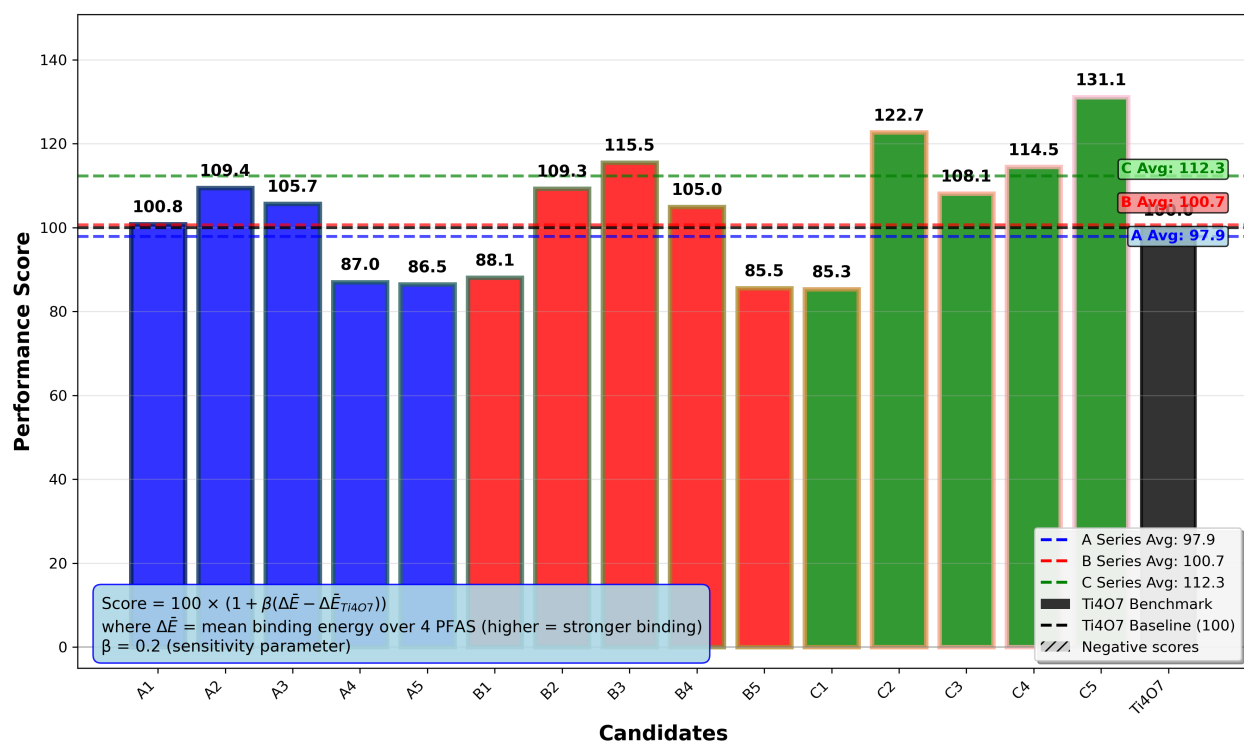


Figure S28: PFAS binding scores for all candidate catalysts from static DFT calculations, normalized to Ti_4O_7 baseline (100). Scores are calculated using the linear metric with sensitivity parameter $\beta = 0.2$, where $\Delta\bar{E} = \overline{\Delta E}_{PFAS}$ represents the mean binding energy averaged over four PFAS compounds.

F Dissociation: PFAS Degradation Performance Scores

F atom dissociation energy, higher values indicate more stable C-F bonds

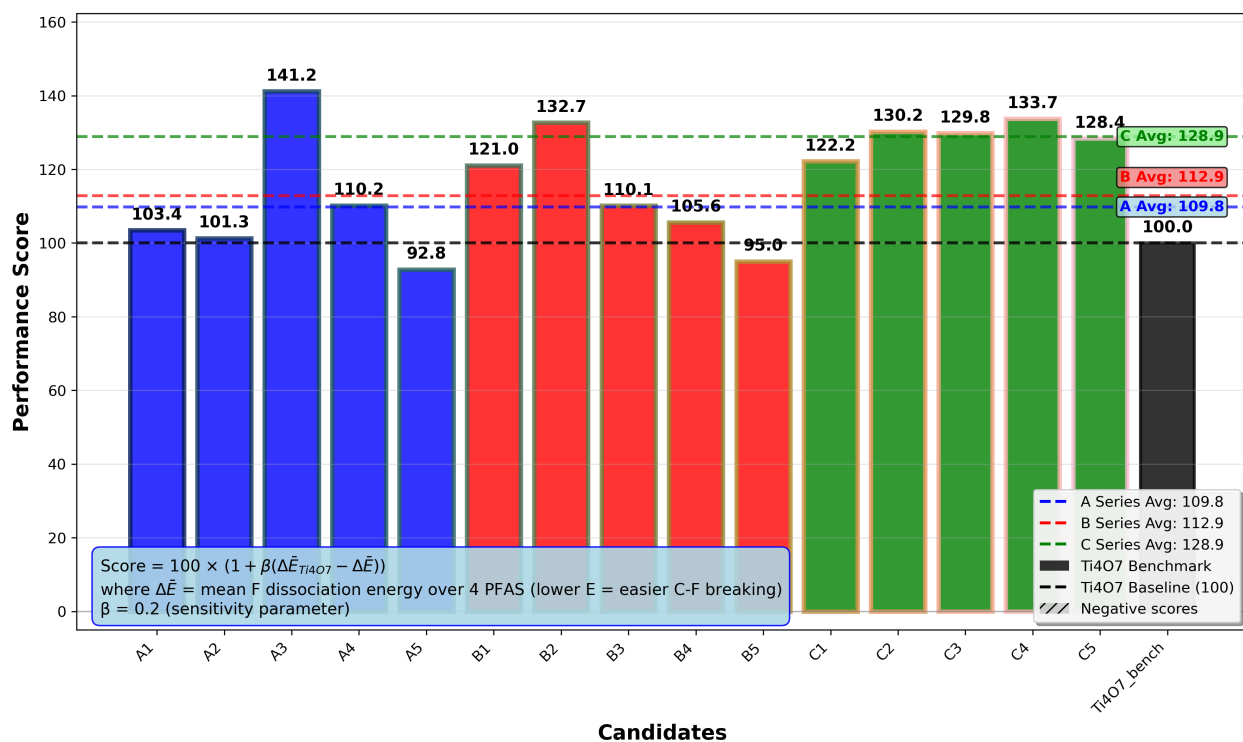


Figure S29: C–F bond activation scores for all candidate catalysts from static DFT calculations, normalized to Ti_4O_7 baseline (100). Scores are calculated using the linear metric with sensitivity parameter $\beta = 0.2$, where $\Delta \bar{E} = \bar{E}_{F-dis}$ represents the mean C–F dissociation energy averaged over four PFAS compounds. Higher scores indicate lower dissociation barriers and more favorable degradation potential.

AIMD Explicit Solvent: PFAS Degradation Binding Scores

Explicit water molecules, captures solvent reorganization effects

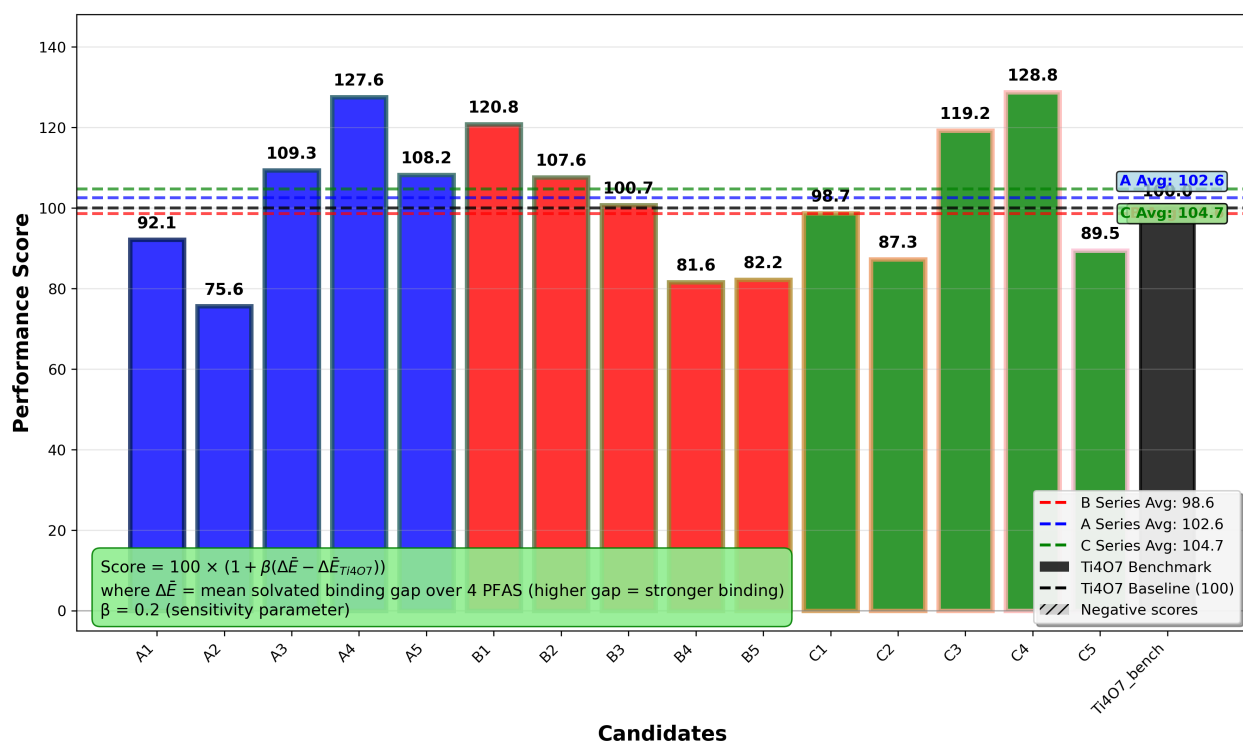


Figure S30: PFAS binding scores for all candidate catalysts from explicit-solvent AIMD simulations, normalized to Ti_4O_7 baseline (100). The scoring methodology remains identical to static DFT, with $\Delta\bar{E}$ representing the mean ΔE_{pot}^{ES} values averaged over four PFAS compounds from the 3 ps production period.

F.4 Battery Binder

F.4.1 LIB_Advanced_Binders

For the third application: Battery Binder. The query as shown in C is:

Which advanced binder technologies are being developed to improve the performance and longevity of lithium-ion batteries?

The best commercial solution is: **ChatGPT_o4_mini_high_DR**.

The best local non gpt-oss solution is: **DToR_qwq32B_local500**.

The best local gpt-oss solution is: **DToR_gpt-oss120B_local500**.

The expert based on the two reports, provided 4 commercial DR report derived candidates (A1-A4), and 4 local non gpt-oss DR report derived candidates (B1-B4), and 4 local gpt-oss DR report derived candidates (C1-C4), visualized in Fig. S31:

NCM811 cathode description In order to create a test bench for lithium ion battery binder, we modeled a (104)-terminated slab of layered $\text{LiNi}_{0.8}\text{Co}_{0.1}\text{Mn}_{0.1}\text{O}_2$ (NCM811) cathode in a periodic cell with $a = 27.67 \text{ \AA}$, $b = 25.55 \text{ \AA}$, $c = 49.47 \text{ \AA}$ and $\alpha = \beta = 90^\circ$, $\gamma = 72.51^\circ$ (P1). The atomic slab spans $\approx 12.1 \text{ \AA}$ along the surface normal, leaving $\approx 37.4 \text{ \AA}$ of vacuum to suppress spurious interactions; the model contains 732 atoms ($\text{Li}_{174} \text{Ni}_{129} \text{Co}_{21} \text{Mn}_{21} \text{O}_{387}$). For structural relaxations, we used a large in-plane surface cell (tripled along b) and constrained the bottom $\approx 1/3$ of atoms to mimic bulk termination.

PVDF benchmark binder For the benchmark binder, we built an all-trans PVDF 10-mer $(-\text{CH}_2-\text{CF}_2-)_{10}$, end-capped with H/F, pre-relaxed in vacuo, and then laid it flat on the pre-relaxed NCM811 (104) slab, constructed and constrained following our surface-build script. In the configuration, the chain backbone lies approximately parallel to the surface ($\sim 30^\circ$ off the b -axis), with a closest polymer-surface contact of $\sim 2.0 \text{ \AA}$, an in-plane backbone span of $\approx 23 \text{ \AA}$, and a projected convex-hull footprint of $\approx 125 \text{ \AA}^2$; the polymer fragment contributes $\text{C}_{20}\text{H}_{21}\text{F}_{21}$, bringing the full model to 794 atoms.

A1 — PVPA (after binder adsorbed) A poly(vinyl-phosphonic acid) 10-mer ($\text{C}_{20}\text{H}_{32}\text{O}_{30}\text{P}_{10}$) was adsorbed on the NCM811 (104) slab, using the same surface-build constraints as our base slab. The slab portion is 12.58 \AA thick, leaving 36.88 \AA of vacuum; the full system contains 824 atoms (slab = 732; polymer = 92). The PVPA backbone lies nearly parallel to the surface ($\approx 34^\circ$ off the b -axis), spans 20.59 \AA in-plane, and covers a projected convex-hull footprint of 115.09 \AA^2 . Phosphonate O atoms approach surface cations with a shortest O-Li contact of 2 \AA , alongside O-O hydrogen-bond contacts to surface oxygen of $2.5\text{--}2.9 \text{ \AA}$.

A2 — Alg-Ca (after binder adsorbed) A Ca^{2+} -cross-linked alginate 5-mer (G-M blocks; carboxylates protonated except those coordinating Ca^{2+}) was laid approximately parallel to the NCM811(104) surface with the bottom oxide layers fixed. The combined model has 834 atoms (slab = 732; binder = 102, $\approx \text{C}_{30}\text{H}_{40}\text{O}_{31}\text{Ca}$). The slab portion is 12.20 \AA thick with 37.27 \AA vacuum. The polymer backbone aligns quasi-parallel to the surface (24.62° off b), spans 17.71 \AA in-plane, and presents a convex-hull footprint of 92.64 \AA^2 . Interfacial contacts are dominated by non-specific physisorption (nearest heavy-atom approach 3.23 \AA ; $\text{O}_{\text{binder}}\text{-O}_{\text{slab}}$ $3.31\text{--}4.17 \text{ \AA}$), while Ca^{2+} remains intrachain-coordinated (closest $\text{Ca-O}_{\text{slab}}$ 7.13 \AA).

A3 — Sulfonyl-polyimide (S-PI) (after binder adsorbed) A tri-repeat S-PI fragment ($\text{C}_{42}\text{H}_{14}\text{N}_6\text{O}_{20}\text{S}_3$, 85 atoms) was constructed following the imide-dianhydride/diamino-sulfone motif and combined with the standard NCM811(104) slab (total 817 atoms; slab = 732, binder = 85). The polymer lies parallel to the surface, oriented 37.49° off the b -axis (principal in-plane span 25.71 \AA) with a projected convex-hull footprint of 152.10 \AA^2 . This configuration represents the separated reference: the nearest polymer heavy atom is 17.42 \AA above the top oxide layer (no interfacial contacts; shortest $\text{O}_{\text{binder}} \cdots \text{O}_{\text{slab}} = 19.17 \text{ \AA}$; $\text{O}_{\text{binder}} \cdots \text{Ni/Co/Mn} = 19.75 \text{ \AA}$).

A4 — PTFE $(-\text{CF}_2-\text{CF}_2-)_{10}$ (after binder adsorbed) A perfluoroethylene decamer ($\text{C}_{20}\text{F}_{42}$, 62 atoms) is laid flat on the NCM811(104) surface to provide a non-reactive binder baseline; the combined model has 794 atoms (slab = 732; polymer = 62). The slab portion is 12.20 \AA thick with 37.27 \AA vacuum. The chain axis lies 39.61° off b within the ab plane, with a principal in-plane span of 25.14 \AA and a projected convex-hull footprint of 80.55 \AA^2 . Interfacial contacts are dispersive: the nearest heavy-atom approach is 2.49 \AA (F-Li); the shortest F-O_{slab} and F-Ni contacts are 2.84 \AA and 3.43 \AA ,

respectively, while C-O_slab ≥ 3.63 Å and no metal-fluorine contact falls below 2.49 Å. These metrics set a PTFE benchmark for subsequent $\Delta E_{\text{ads}}/A$ comparisons.

B1 — Schiff-base polymer (imine-linked poly(aldehyde-amine)) (after binder adsorbed) An imine-linked poly(aldehyde-amine) fragment ($\text{C}_{40}\text{H}_{28}\text{N}_4$, 72 atoms) is adsorbed on the NCM811(104) slab; the combined model contains 804 atoms (slab = 732; binder = 72). The oxide portion is 13.07 Å thick with 36.39 Å vacuum. The polymer lies quasi-parallel to the surface, oriented 36.97° off **b** within the **ab** plane; its principal in-plane span is 34.60 Å, and the projected convex-hull footprint is 168.51 Å². Interfacial contacts show a nearest heavy-atom approach of 2.57 Å (C-Li); the imine N approaches surface oxygen at 2.35 Å, while separations to cation sites remain larger (N-Li 3.68 Å; N-Ni 4.29 Å; N-Co 4.57 Å; N-Mn 4.76 Å).

B2 — lignin + CNT (after binder adsorbed) A β -O-4 lignin dimer was positioned at the NCM811(104) interface and co-laid with an armchair (6,6) carbon nanotube segment (8 axial repeats; 192 C) oriented roughly parallel to the terrace; the tube’s in-plane principal axis is rotated 36.86° off **b** and spans 24.91 Å. The composite binder portion contains $\text{C}_{234}\text{H}_{80}\text{O}_{46}$. The oxide portion spans 11.05 Å in thickness along the surface normal with 38.42 Å of vacuum retained. Lignin’s phenolic/ether oxygens face the cation-terminated ridges, with the closest O-(Ni/Co/Mn) approach of 3.32 Å, consistent with physisorptive H-bond/ion-dipole contacts rather than direct chelation; the CNT lies flat to provide an extended π -contact, with a near-surface carbon convex-hull footprint of 84.71 Å². Together, this layout tests cooperative anchoring: localized polar adhesion from lignin complemented by broad dispersive contact from the nanotube across the NCM811 terrace.

B3 — Lignin-CMC hybrid (β -O-4 lignin dimer + CMC monomer, Na⁺ exchanged) (after binder adsorbed) The composite contains 876 atoms (slab = 732; binder = 144 with $\text{C}_{50}\text{H}_{69}\text{O}_{24}\text{Na}_1$) and uses the same NCM811(104) platform and assembly recipe (lignin dimer H-bonded to a CMC unit, carboxylate presented to the terrace). The organic complex lies quasi-parallel to the surface, its principal in-plane axis oriented 38.18° off **b**, with a 35.09 Å backbone span and a projected convex-hull footprint of 235.11 Å². The oxide portion is 11.09 Å thick with 38.38 Å of vacuum along **c**. Interfacial approach distances indicate mixed ionic/coordination contacts: nearest heavy-atom approach 2.25 Å (O_binder-Li), with O_binder-Ni = 2.99 Å, O_binder-Co = 4.09 Å, and O_binder-Mn = 4.29 Å; the exchanged Na⁺ sits remote from the terrace (Na-O_slab = 6.80 Å). During relaxations, the **bottom one-third of oxide atoms** are held fixed to emulate a semi-infinite substrate.

B4 — ZIF-8 face ($\text{Zn}_4(2\text{-mim})_8$ cluster) (after binder adsorbed) We approximate the MOF by a single sodalite-cage face—four Zn nodes bridged by eight 2-methylimidazoles—so the interface samples the correct local Zn-N₄/ μ_2 -imidazolate chemistry without imposing the artificial pore matching and long-range lattice constraints of a periodic ZIF on a finite oxide slab. The internal Zn-N network is kept near its intrinsic geometry via mild constraints, while only the interfacial coordinate is relaxed; one Zn is oriented toward a surface oxygen with an initial Zn-O set to ~ 2.10 Å to seed chemisorption and allow secondary N-Li/C-O_slab contacts to adjust around it. This charge-neutral ring thus captures the short-range bonding physics that governs adhesion at comparable cost to polymer fragments, enabling fair ranking by area-normalized adsorption energy $\Delta E_{\text{ads}}/A$ across all candidates.

C1 — Polyvinyl alcohol (PVA) oligomer Flexible, water-processable oligomer of repeating vinyl alcohol units ($-\text{CH}_2\text{CHOH}-$) with formula $\text{C}_{23}\text{H}_{48}\text{O}_{11}$ (~ 11 – 12 ethylene-glycol-like repeats; ~ 82 atoms). Dense pendant $-\text{OH}$ groups furnish multiple H-bond donors/acceptors and Lewis-basic oxygens capable of coordinating metal cations (e.g., Li⁺), delivering strong film formation and polar-surface adhesion while maintaining mechanical flexibility from partial crystallinity and amorphous chain mobility.

C2 — CMC + waterborne polyurethane (WBPU) hybrid Aqueous, interpenetrating network of a carboxymethyl cellulose oligomer blended with a WBPU soft-segment fragment (no covalent linking). Representative composition: $\text{C}_{33}\text{H}_{58}\text{Li}_5\text{N}_4\text{O}_{23}$ (123 atoms). CMC supplies anionic $-\text{COO}^-$ sites (neutralized by Li⁺) and hydroxyl-rich backbone for polar adhesion; WBPU contributes urethane $-\text{NH}-\text{CO}-\text{O}-$ H-bond donors and ductile segments for toughness and crack resistance. The hybrid is solvent-free (water-based) and mechanically robust via H-bonding and electrostatic interactions.

C3 — Lithiated cellulose nanofiber (LCNF) oligomer Partially lithiated cellulose fragment, $C_{42}H_{62}Li_8O_{41}$ (153 atoms), approximating ~ 7 glucose repeats with selective deprotonation to form $-O^-Li^+$ sites (~ 1 Li per glucose). Lithiation introduces single-ion-conducting motifs while retaining some $-OH$ H-bonding for mechanical integrity. The $-O^-Li^+$ network supports Li^+ coordination/hopping along the polysaccharide, potentially lowering interfacial impedance.

C4 — Polyethylene glycol (PEG) oligomer Linear polyether $HO-[CH_2CH_2O]_{12}-H$ ($C_{24}H_{50}O_{12}$; 86 atoms). Ether oxygens provide Lewis-basic coordination to Li^+ ; low T_g and high segmental mobility enable compliance and ion solvating/plasticizing behavior. PEG is miscible with carbonate electrolytes and offers broad electrochemical compatibility, acting as a flexible, coordinating binder/plasticizer at the interface.

F.4.2 Battery Binder Adhesion Performance

The mechanical integrity of lithium-ion battery cathodes critically depends on binder adhesion strength, particularly under the chemically aggressive conditions of liquid electrolyte environments. To evaluate candidate binder materials proposed by the DR agents (Figure S31), we employed the same computational framework described for PFAS sensors, with binding energies normalized by the interfacial contact area A to account for varying polymer-cathode interaction footprints. The contact area was determined through convex hull analysis of atoms within 3.5 \AA of the NCM811 surface, enabling direct comparison of adhesion strength per unit interfacial area. Static DFT calculations reveal favorable adhesion for all candidates, with areal-normalized binding energies ranging from 0.015 to 0.111 eV/\AA^2 (Figure S32). These values, equivalent to 0.24 – 1.78 J/m^2 , align well with established benchmarks for dry interface adhesion, such as graphene on SiO_2 ($\sim 0.45 \text{ J/m}^2$) and metal-oxide contacts ($\sim 2 \text{ J/m}^2$). Candidates B4 and B1 demonstrate the strongest adhesion, while the benchmark PVDF falls in the mid-range, suggesting potential improvements over current commercial binders. However, the introduction of explicit battery electrolyte (EC:EMC:LiPF₆ = 9:9:2:2 at 1.25 g/cm^3) through AIMD simulations dramatically alters the adhesion landscape (Figures S33 and S34). Following the same protocol of 2 ps equilibration and 3 ps production runs, most candidates exhibit negative $\Delta E_{\text{pot}}^{\text{ES}}/A$ values, indicating that the separated, electrolyte-wetted interface becomes energetically favorable over the bound state. This solvent-induced adhesion reversal reflects competitive adsorption of electrolyte molecules at the binder-cathode interface, disrupting direct polymer-surface interactions. Four exceptions stand out in this trend: candidates A3 (sulfonyl-polyimide), B2 (lignin + CNT), C1 (PVA), and C2 (CMC + WBPU) maintain positive $\Delta E_{\text{pot}}^{\text{ES}}/A$ even in explicit electrolyte, indicating robust wet adhesion despite first-layer solvent and ion crowding. Mechanistically, S-PI (A3) presents dense imide carbonyl and sulfone dipoles that support Li^+ -bridged, multidentate contacts while its aromatic backbone provides broad dispersive π contact; the lignin+CNT composite (B2) couples phenolic/ether O donors (ion-dipole/H-bonding) with a large-area CNT π interface that helps offset solvent-displacement penalties; PVA (C1) contributes a high density of hydroxyl groups enabling multidentate H-bonding and Li^+ -mediated coordination to surface sites with sufficient chain flexibility to maintain conformal contact; and the CMC+WBPU hybrid (C2) combines inner-sphere/ion-paired adhesion from CMC carboxylates ($O \cdots Li/TM$) with urethane H-bonding and local solvent exclusion by the WBPU soft segments. The performance scoring normalized to the PVDF baseline (Figures S35 and S36) quantifies this wet-interface reordering: candidates optimized for dry adhesion may underperform under operating electrolyte conditions, whereas others show unexpected compatibility. These results underscore the need for explicit-solvent, potential-controlled calculations in binder screening, since interfacial energetics in liquid electrolytes are governed by solvent layering, ion crowding, and potential-dependent desolvation that vacuum or implicit-solvent models cannot capture.

Battery Binder Materials on NCM811 Cathode

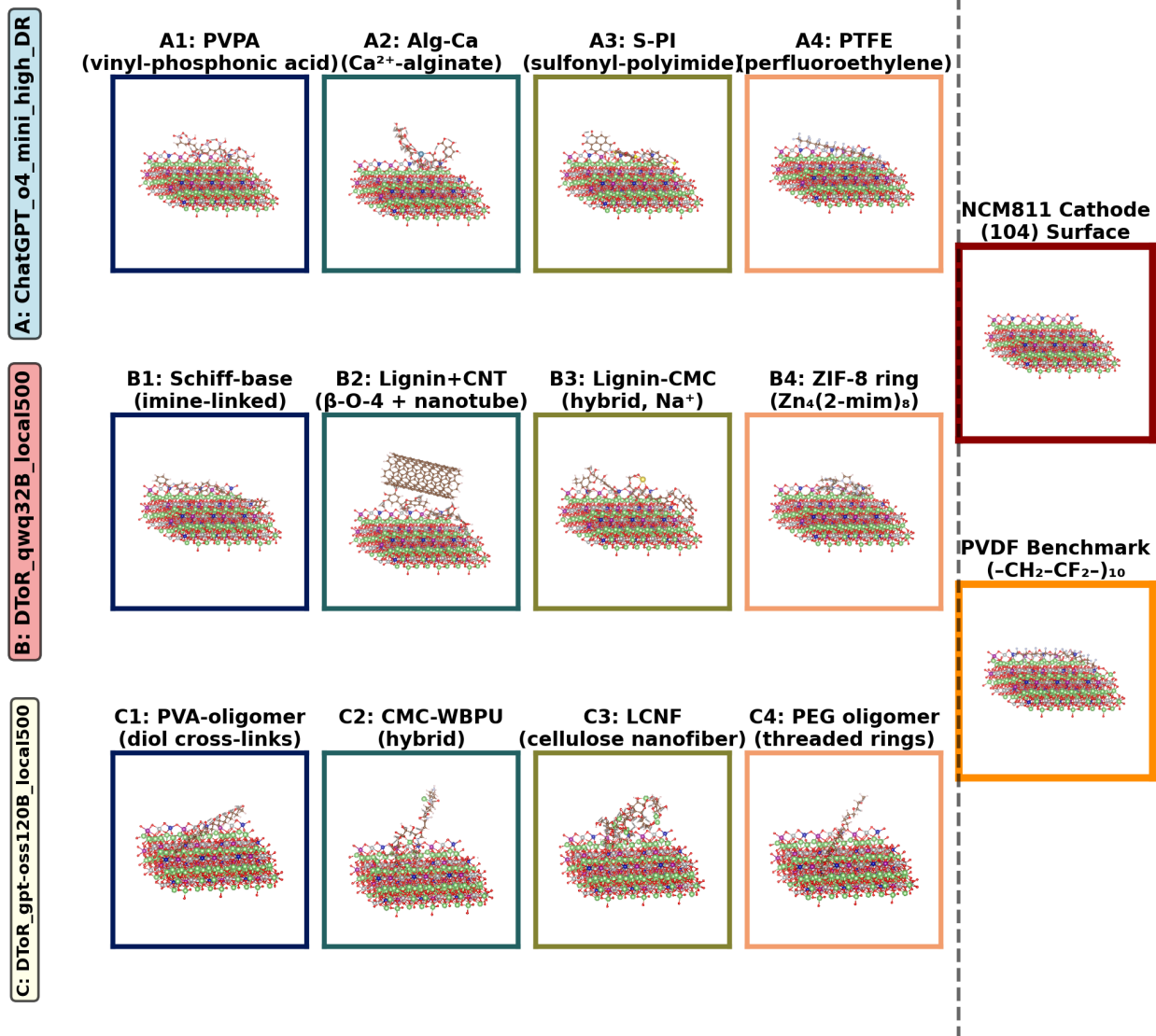


Figure S31: Structural configurations of battery binder candidates proposed by DR agents, with PVDF [28] included as the domain benchmark reference. Optimized adsorption configurations on the NCM811 cathode surface are shown for each candidate system.

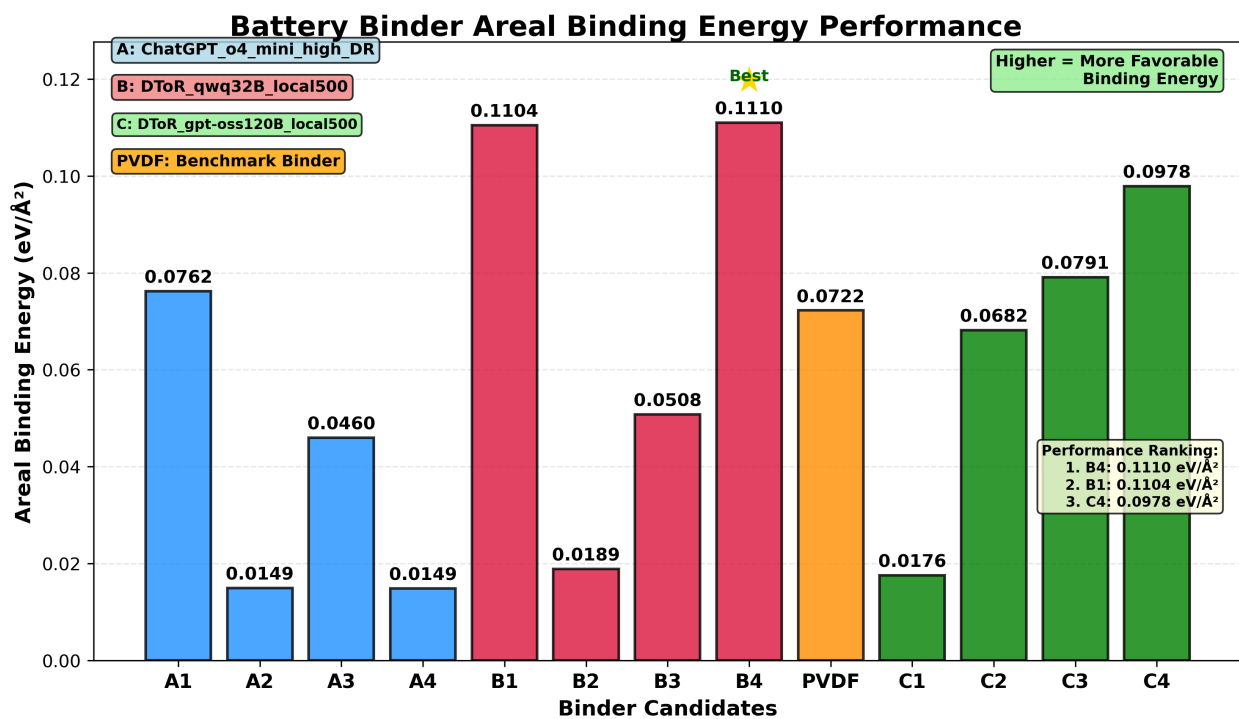


Figure S32: Comparison of areal-normalized binding energies ($\Delta E_{\text{bind}}/A$) from static DFT calculations. Values are expressed in eV/Å², where A represents the interfacial contact area determined by convex hull analysis of atoms within 3.5 Å of the NCM811 surface.

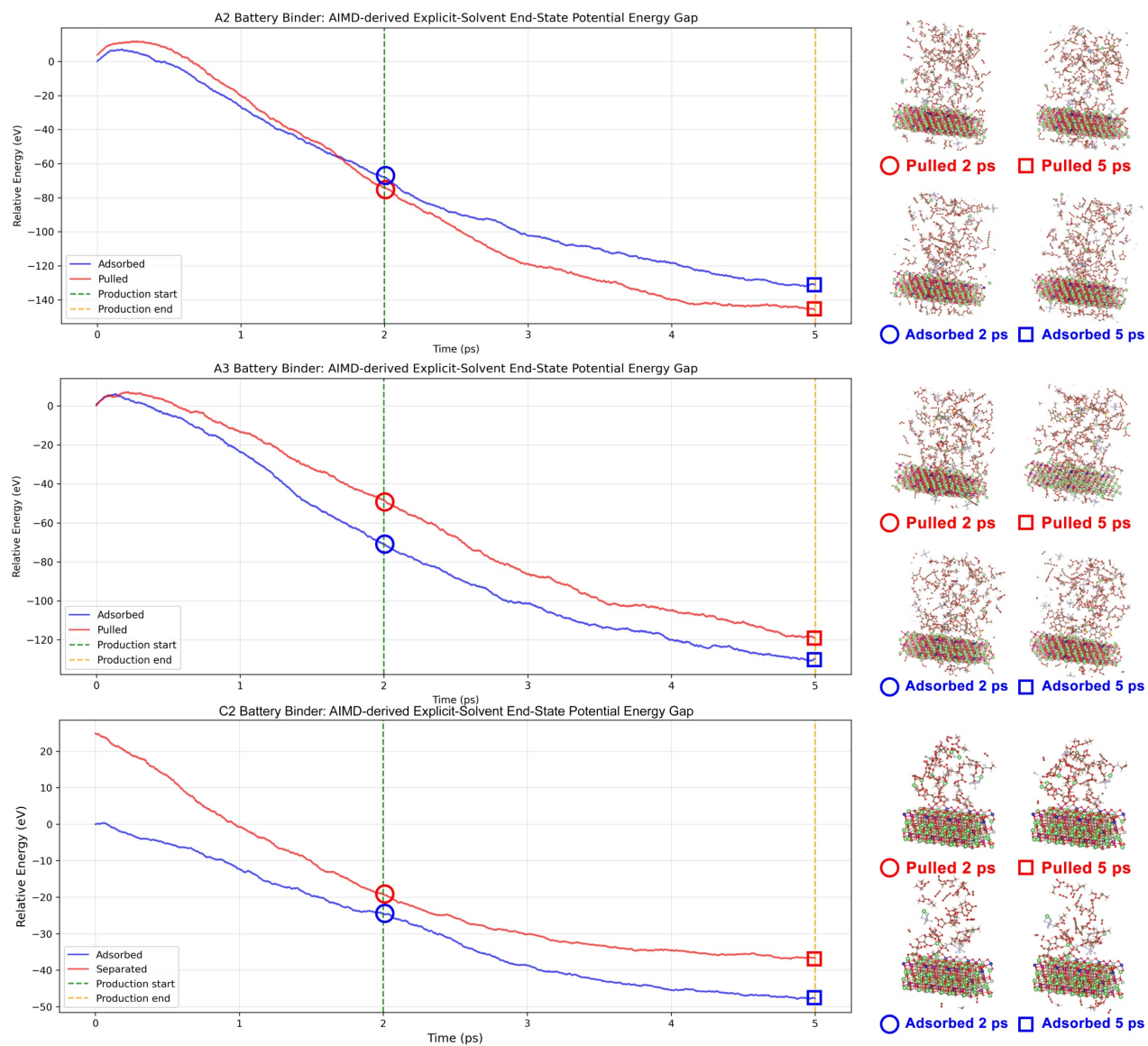


Figure S33: Representative AIMD trajectory showing system energy evolution in explicit battery electrolyte (EC:EMC:LiPF₆ = 9:9:2:2). The green dashed line denotes the 2 ps equilibration period. Right panels display system configurations at highlighted time points along the 3 ps production trajectory.

AIMD-derived Explicit-Solvent End-State Potential Energy Gap (eV) for Contact Areal Binding

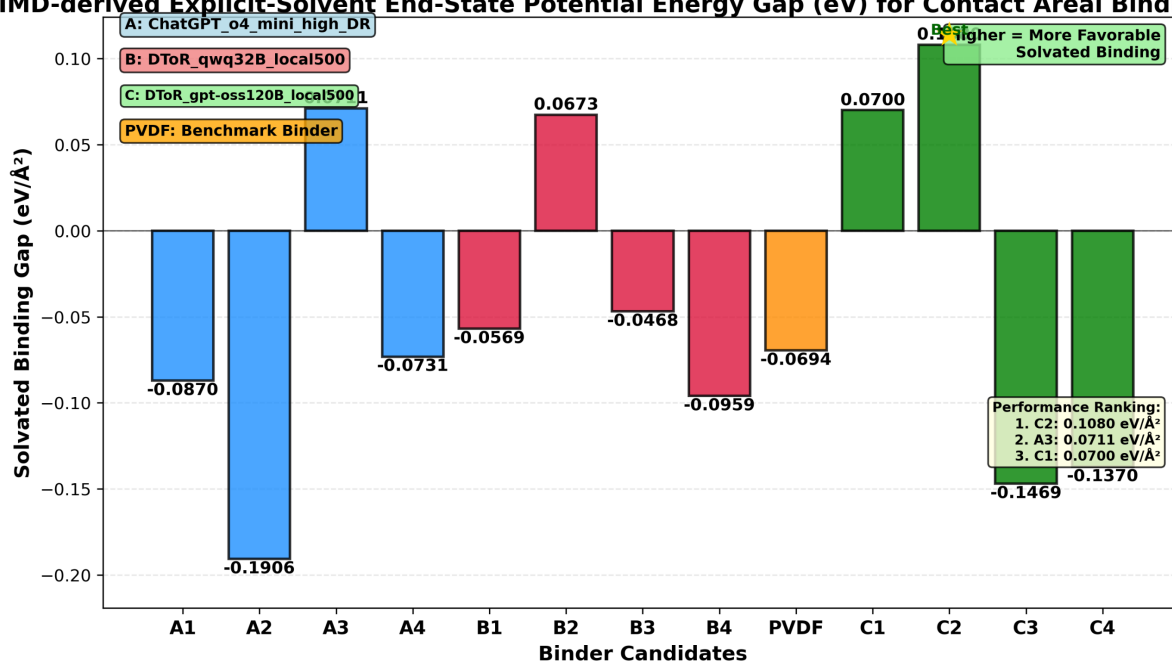


Figure S34: Areal-normalized explicit-solvent end-state potential energy gaps ($\Delta E_{\text{pot}}^{\text{ES}}/A$) from AIMD simulations. Negative values indicate unfavorable adhesion in the presence of electrolyte (Pulled state in explicit solvation stabilizes the pulled state), reflecting competitive solvent adsorption at the binder–cathode interface.

DFT Static: Battery Binder Adhesion Performance Scores

Contact Areal Binding Energy (eV/Å²), static optimization

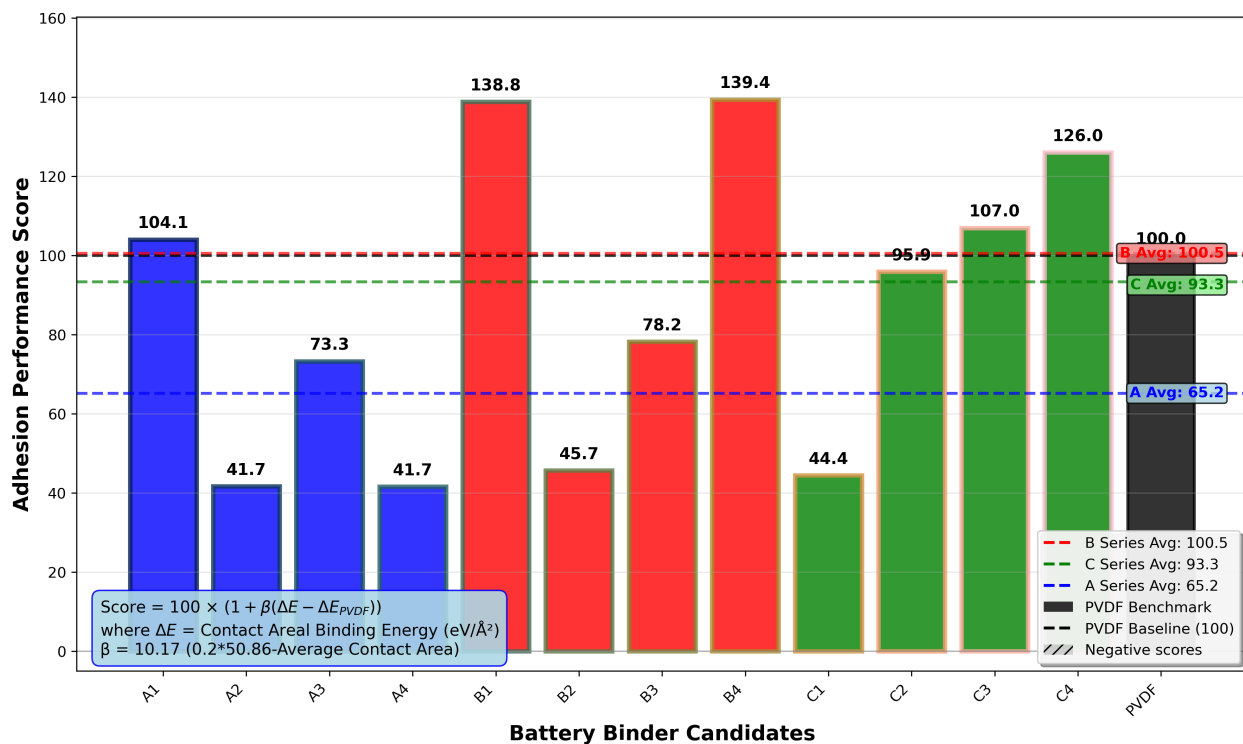


Figure S35: Adhesion performance scores for all binder candidates from static DFT calculations, normalized to PVDF baseline (100). Scores are calculated using the linear scaling metric with sensitivity parameter $\beta = 10.17$, applied to areal-normalized binding energies.

AIMD Solvated Binding Gap: Battery Binder Adhesion Performance Scores

AIMD-derived Explicit-Solvent End-State Potential Energy Gap (eV) for Contact Areal Binding

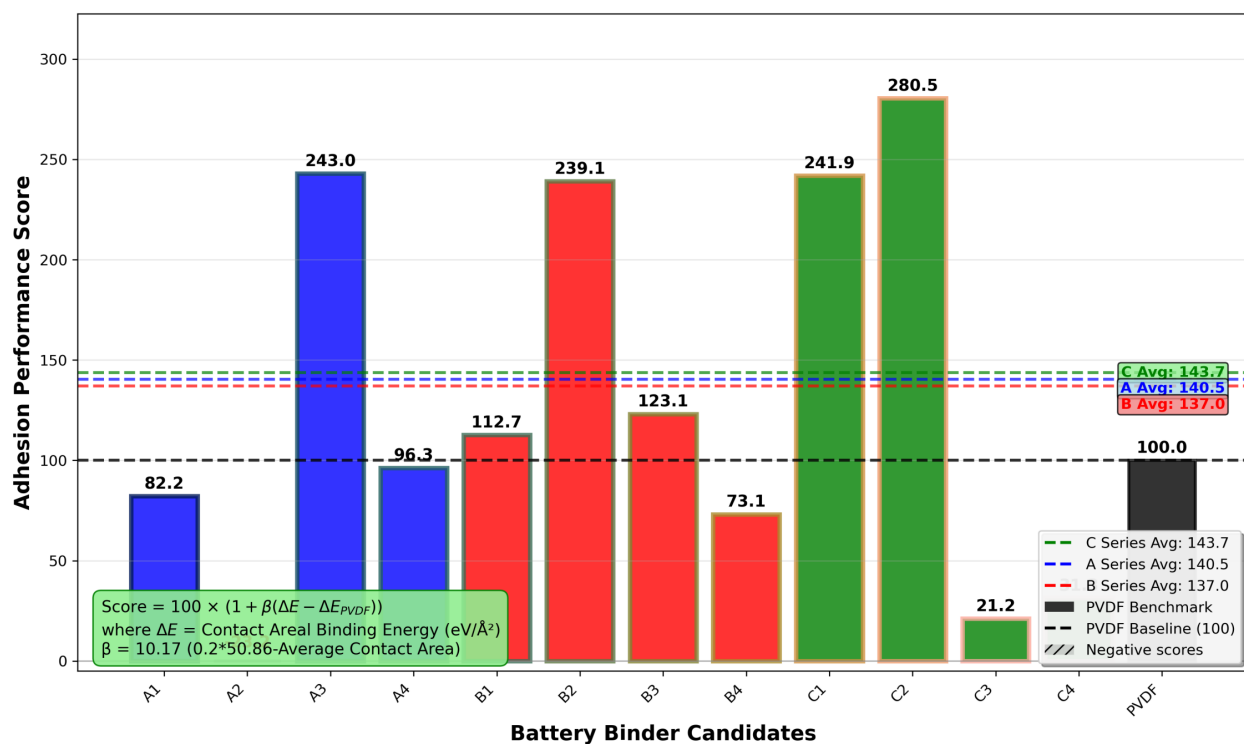


Figure S36: Adhesion performance scores for all binder candidates from explicit-electrolyte AIMD simulations, normalized to PVDF baseline (100). The scoring methodology remains identical to static DFT, with $\Delta E_{\text{bind}}/A$ replaced by time-averaged $\Delta E_{\text{pot}}^{\text{ES}}/A$ from the 3 ps production period.⁶

F.5 OER Stability

F.5.1 OER_Wastewater_Resistant_Cats

For the fourth application: OER Stability. The query as shown in C is:

Identify the top nanostructured electrocatalyst materials for driving the oxygen evolution reaction (OER) in complex wastewater matrices--such as high-chloride, high-organic-load, or multi-ion streams--, for each the material class/composition, comprehensively consider key performance metrics (overpotential at 10 mA cm⁻², Faradaic efficiency, stability), and the surface-engineering strategies that confer corrosion resistance and sustained activity in real effluent conditions.

The best commercial solution is: **Perplexity_DR**.

The best local non gpt-oss solution is: **DToR_qwq32B_local500**.

The best local gpt-oss solution is: **DToR_gpt-oss120B_local500**.

The expert based on the two reports, provided 4 commercial DR report derived candidates (A1-A4), and 4 local non gpt-oss DR report derived candidates (B1-B4), and 4 local gpt-oss DR report derived candidates (C1-C4), visualized in Fig. S37:

Benchmark 110 IrO₂ For benchmark material, we created most commonly seen, a stoichiometric rutile IrO₂ (110) slab built as a 6 × 3 in-plane supercell along × [1 $\bar{1}$ 0], with cell parameters **a = 19.06 Å**, **b = 19.11 Å**, **c = 45.18 Å**, $\alpha = \beta = \gamma = 90^\circ$ (**P1**), from which the underlying bulk metrics map to $a \approx 4.51$ Å and $c \approx 3.18$ Å. The slab comprises **five O–Ir–O trilayers** (thickness ≈ 15.18 Å) separated by ≈ 30.0 Å of vacuum along c , yielding **symmetric, O-terminated (bridging-O) surfaces** that expose the conventional row motif used for OER modeling (adjacent Ir_{cus}/O_{br} sites). The model is **strictly stoichiometric (Ir:O = 1:2; 180 Ir and 360 O)** and thus suitable as a clean, non-polar benchmark surface for computational electrocatalysis studies.

A1 — Ni–Fe layered double hydroxide (LDH) slab (basal) A hexagonal brucite-derived Ni–Fe hydroxide (001) slab was constructed as a 6 × 6 in-plane supercell (basal lattice $a_0 \approx 3.126$ Å), with cell metrics **a = b = 18.7560 Å**, **c = 62.3777 Å**, $\alpha = \beta = 90^\circ$, $\gamma = 120^\circ$ (**P1**). The model contains **three brucite-like [M(OH)₆]** octahedral sheets stacked along c (36 cation sites per sheet), with a **Ni:Fe = 81:27** distribution (**25% Fe on the cation sublattice; 9 Fe per sheet**), and overall stoichiometry **Ni₈₁Fe₂₇O₂₁₆H₂₁₆ (540 atoms)**. Both basal surfaces are **symmetrically hydroxyl-terminated** (H atoms constitute the outermost layers), yielding a **stoichiometric, non-polar** slab of thickness ≈ 19.67 Å, separated by ≈ 42.71 Å of vacuum within the c dimension; the **inter-sheet metal-plane separations** are **7.87** and **7.81** Å, consistent with LDH-like basal spacing. This geometry provides equivalent top/bottom (001) terminations exposing M–OH motifs suitable for benchmarking OER intermediates on LDH surfaces.

A2 — phosphate-intercalated Ni–Fe LDH (001) Kept identical to **A1** in lattice and slab construction (6 × 6 hexagonal basal supercell; $a = b = 18.756$ Å, $\gamma = 120^\circ$, $c = 62.3777$ Å; P1) with symmetric hydroxyl-terminated basal surfaces, **A2 is derived from A1 by inserting protonated phosphate molecules (H₃PO₄)** into the interlayer galleries—**18 PO₄ units per supercell (9 per gallery)**, giving an overall composition **Ni₈₁Fe₂₇O₂₈₈H₂₇₀P₁₈** (684 atoms, Ni:Fe = 3:1). The intercalation shifts the metal-plane separations from $\sim 7.87/7.81$ Å (A1) to **8.89/8.90** Å, increasing the slab thickness to **22.22** Å and leaving ~ 40.16 Å of vacuum along c ; the phosphorus centroids sit near the mid-planes of each gallery.

A3 — Ni single atoms on Sb-doped SnO₂(110) A rutile SnO₂(110) slab was built as a 4 × 8 in-plane supercell along [1 $\bar{1}$ 0] × (cell **a = 26.8022 Å**, **b = 25.4960 Å**, **c = 57.0945 Å**; $\alpha = \beta = \gamma = 90^\circ$; **P1**), comprising **four O–Sn–O trilayers** (slab thickness ≈ 12.72 Å) and ≈ 44.37 Å of vacuum. **Eight Sb atoms** substitute Sn in the **subsurface cation plane (second layer from the top)**—**12.5 %** within that plane, **3.2 %** overall (**Sn₂₄₄Sb₈**). The **top (110) surface** carries **four isolated Ni adatoms** arranged in a 2 × 2 array (**coverage ≈ 0.585 Ni nm⁻²**), each adopting a **square-pyramidal NiO₅** environment with **four equatorial Ni–O = 1.922 Å** and **one apical Ni–O = 2.033 Å**; the **bottom surface** is left **clean and O-terminated**. The full supercell stoichiometry is **Sn₂₄₄Sb₈Ni₄O₅₀₈ (764 atoms)**.

A4 — Ce-doped, oxygen-deficient spinel NiCo₂O₄ slab (asymmetric OH termination) Modeled in P1 with an oblique in-plane cell ($\mathbf{a} = 19.807 \text{ \AA}$, $\mathbf{b} = 30.866 \text{ \AA}$, $\gamma = 108.715^\circ$; $\mathbf{c} = 41.150 \text{ \AA}$), giving an in-plane area of 579.05 \AA^2 (5.79 nm^2); the atomic slab spans 14.87 \AA along c and is separated by 26.28 \AA of vacuum. The supercell composition is $\text{Co}_{188}\text{Ce}_8\text{Ni}_{92}\text{O}_{376}\text{H}_{96}$ (**760 atoms**), i.e., $\text{Ni}:\text{Co} \approx 1:2.04$ with **Ce at 2.8 at.% of the cation sublattice**. Relative to the ideal AB_2O_4 stoichiometry for 288 cations, the model contains **8 lattice-oxygen vacancies** ($x \approx 0.021$ in $\text{NiCo}_2\text{O}_{4-x}$), corresponding—if evenly split between the two faces—to $\approx 0.69 \text{ vac nm}^{-2}$ per surface. **Ce dopants occupy two equivalent subsurface cation planes** (four Ce per plane), located $\sim 4.31 \text{ \AA}$ below the top and $\sim 5.32 \text{ \AA}$ above the bottom surface, preserving an overall centrosymmetric placement. The **top surface is Co-rich and partially hydroxylated** (within the outermost 2 \AA : **8 Co, 20 O, 28 H** $\rightarrow \approx 1.38 \text{ Co nm}^{-2}$ and $\approx 5.5 \text{ OH nm}^{-2}$), while the **bottom surface is more strongly hydroxyl-passivated** (**64 H** on that side overall, $\approx 11.1 \text{ OH nm}^{-2}$). No Ni appears within the outermost 2 \AA of the top surface (Ni resides in subsurface layers), yielding a **Co–O(H) termination** appropriate for probing OER pathways on spinel-type oxides.

B1 — graphene-capped Ni–Fe LDH (001) Retaining the A1 lattice and slab construction (6×6 hexagonal basal supercell; $a = b = 18.756 \text{ \AA}$, $\gamma = 120^\circ$, $c = 70.6707 \text{ \AA}$; P1), this model is derived from A1 by placing a **single-layer graphene overlayer (128 C)** above the top basal surface while keeping the LDH stoichiometry $\text{Ni}_{81}\text{Fe}_{27}\text{O}_{216}\text{H}_{216}$ unchanged. The LDH comprises **three brucite-like [M(OH)₆] sheets** ($\text{Ni}:\text{Fe} = 3:1$) with **metal-plane separations of 7.87 and 7.81 \AA**; both basal faces are hydroxyl-terminated, but only the **top face is covered by graphene**. The LDH portion spans 19.67 \AA along c ; including graphene, the occupied thickness is 24.67 \AA , leaving 46.00 \AA of vacuum. The graphene sheet is essentially planar (out-of-plane corrugation $\leq 0.001 \text{ \AA}$) and sits **5.00 \AA above the outermost hydroxyl-H layer (5.97 \AA above the topmost O layer)**, consistent with a physisorbed, non-perturbative interface that preserves the LDH surface structure; the **bottom layers are identical to A1** and remain exposed/hydroxylated for benchmarking.

B2 — graphene-capped hematite ($\alpha\text{-Fe}_2\text{O}_3$) (0001) with an aperture A hexagonal $\alpha\text{-Fe}_2\text{O}_3$ (0001) slab was modeled in P1 with $\mathbf{a} = \mathbf{b} = 20.152 \text{ \AA}$, $\gamma = 120^\circ$; $\mathbf{c} = 60.339 \text{ \AA}$ (in-plane area $351.70 \text{ \AA}^2 = 3.517 \text{ nm}^2$), giving an atomistic thickness of 32.20 \AA separated by 28.14 \AA of vacuum. The slab is **stoichiometric Fe₂O₃** in the interior ($\text{Fe}_{384}\text{O}_{576}$) with **both faces hydroxyl-terminated (H₉₂ total)** to render a non-polar model. A **single sp²-carbon overlayer (C₁₁₅)** caps only the **top face** and includes a **circular $\sim 6 \text{ \AA}$ “window”** (aperture) that leaves a patch of **exposed surface Fe sites** beneath the opening; elsewhere the carbon sheet remains graphene-like, with its centroid $\sim 2.84 \text{ \AA}$ above the outermost O plane ($\approx 2.04 \text{ \AA}$ above terminal H) and a small out-of-plane corrugation ($\Delta z \approx 0.91 \text{ \AA}$). The **bottom face** remains hydroxylated and exposed for benchmarking.

B3 — BaCo_{0.6}Fe_{0.4}O₃ perovskite (001), BO₂||BaO asymmetric slab In line with Branch B’s chloride-resilience goal, a stoichiometric Ba(B)O₃ slab with mixed B-site cations ($\text{Ba}_{180}\text{Co}_{108}\text{Fe}_{72}\text{O}_{540}$; 900 atoms) was modeled in P1 with $\mathbf{a} = \mathbf{b} = 23.820 \text{ \AA}$, $\mathbf{c} = 49.850 \text{ \AA}$, $\alpha = \beta = \gamma = 90^\circ$ (in-plane area $567.39 \text{ \AA}^2 = 5.674 \text{ nm}^2$). The atomic slab spans 19.31 \AA along c and is separated by 30.54 \AA of vacuum. Terminations are **asymmetric**: the **top face is a BO₂ layer that is Co-rich (Co:Fe = 27:9 \approx 3:1)**, while the **bottom face is BaO-terminated**; within $\pm 2 \text{ \AA}$ of the surfaces this corresponds to $\sim 6.35 \text{ B nm}^{-2}$ (with $\sim 12.69 \text{ O nm}^{-2}$) at the top and $\sim 6.35 \text{ Ba nm}^{-2}$ at the bottom. This construction furnishes a corrosion-tolerant, **bare BO₂ active surface** over a BaO support, consistent with the initial design brief to benchmark robust oxide surfaces against chloride attack.

B4 — coral-mimetic Ni–Fe LDH (001) Keeping the MXene/LDH base identical to A1/B1 (6×6 hex basal supercell; $a = b = 18.756 \text{ \AA}$, $\gamma = 120^\circ$, $c = 62.3777 \text{ \AA}$; P1), the “coral” morphology was introduced by excising a single cylindrical pore ($\sim 8 \text{ \AA}$ diameter) through the **top two hydroxide layers** and hydroxyl-passivating all newly exposed edges, as specified in the design note; both basal faces remain hydroxyl-terminated, with the **bottom face unchanged** from A1/B1. The resulting model is $\text{Ni}_{69}\text{Fe}_{25}\text{O}_{192}\text{H}_{216}$ (**502 atoms**), occupying 26.58 \AA along c with 35.79 \AA vacuum (in-plane area 304.66 \AA^2), yielding a non-polar, porous benchmark that preserves the original basal registry while exposing M–OH rim sites within the aperture.

C1 — FeNi–OOH/spinel nanoplate on N-doped carbon scaffold with amorphous Al–O/Ti–O overlayer Derived from B1 (Ni–Fe LDH on graphene), retaining the hexagonal $6 \times$

6 basal supercell ($\mathbf{a} = \mathbf{b} = 18.756 \text{ \AA}$, $\gamma = 120^\circ$; $\mathbf{c} \approx 70.6707 \text{ \AA}$; **P1**). The graphene support is **N-doped** by substituting **6 C** \rightarrow **N** ($\sim 4.7\%$ of 128 C) at distributed sites (pyridinic/pyrrolic character), while the LDH layer remains $\text{Ni}_{81}\text{Fe}_{27}\text{O}_{216}\text{H}_{216}$. The exposed LDH face is capped by **8 amorphous Al–O/Ti–O clusters** (4 small, 4–6 atoms; 4 medium, 6–9 atoms) at $\sim 25\text{--}30\%$ areal coverage; clusters sit $\sim 2.5 \text{ \AA}$ above the surface, are spaced $\geq 3.5 \text{ \AA}$ apart, and show $\text{Al–O} \sim 1.8 \text{ \AA}$ and $\text{Ti–O} \sim 1.9 \text{ \AA}$ with $\pm 15\%$ distortions (SALD-like islands that leave lateral windows/edge sites accessible). After relaxation the oxide islands form interfacial bonds to LDH hydroxyls while the N-doped graphene adjusts registry. Overall composition: **722 atoms** ($\text{C}_{122}\text{N}_6\text{Fe}_{27}\text{Ni}_{81}\text{O}_{251}\text{Al}_5\text{Ti}_{14}\text{H}_{216}$), a tractable model of nanoplate/carbon composites with selective SALD protection.

C2 — Fe single atom on Nb-doped anatase $\text{TiO}_2(101)$ with amorphous Al–O/Ti–O overlayer An anatase $\text{TiO}_2(101)$ slab was built as a 2×4 lateral supercell ($\mathbf{b} \approx 15.13 \text{ \AA}$ after doubling), comprising **5 trilayers** (slab thickness $\approx 17 \text{ \AA}$) and $\approx 15 \text{ \AA}$ vacuum (**P1**). **Four Ti** in the first subsurface cation plane are replaced by **Nb** ($\sim 2.5 \text{ at.}\%$); a **surface bridging-O vacancy** is created $\sim 1.08 \text{ \AA}$ from the nearest subsurface Nb. A **single Fe adatom** anchors at this vacancy (fivefold/bridge motif). The surface is capped by **7 amorphous Al–O/Ti–O clusters** (4 small, 4–6 atoms; 3 medium, 6–9 atoms) at $\sim 25\text{--}30\%$ coverage, each $\sim 2.5 \text{ \AA}$ above the surface and $\geq 3.5 \text{ \AA}$ apart, with $\text{Al–O} \sim 1.8 \text{ \AA}$ and $\text{Ti–O} \sim 1.9 \text{ \AA}$ ($\pm 15\%$ distortions). Clusters maintain $\geq 4 \text{ \AA}$ lateral clearance to the Fe site to preserve accessibility; relaxation yields interfacial Al–O–Ti linkages while the Fe coordination adapts to the vacancy environment.

C3 — Ru single atom on W-doped anatase $\text{TiO}_2(101)$ with amorphous Al–O/Ti–O overlayer Constructed analogously to **C2**: anatase $\text{TiO}_2(101)$ 2×4 lateral supercell ($\mathbf{b} \approx 15.13 \text{ \AA}$), **5 trilayers** ($\approx 17 \text{ \AA}$ thick) and $\approx 15 \text{ \AA}$ vacuum (**P1**). **Four Ti** in the first subsurface cation plane are replaced by **W** ($\sim 2.5 \text{ at.}\%$); a **surface bridging-O vacancy** is placed $\sim 1.08 \text{ \AA}$ from the nearest subsurface W. A **single Ru adatom** anchors at the vacancy. The surface carries **8 amorphous Al–O/Ti–O clusters** (4 small, 4–6 atoms; 4 medium, 6–9 atoms) at $\sim 25\text{--}30\%$ coverage, each $\sim 2.5 \text{ \AA}$ above and $\geq 3.5 \text{ \AA}$ apart, with $\text{Al–O} \sim 1.8 \text{ \AA}$ and $\text{Ti–O} \sim 1.9 \text{ \AA}$ ($\pm 15\%$ distortions) and $\geq 4 \text{ \AA}$ lateral clearance to the Ru site. Relaxation forms interfacial Al–O–Ti bonds while preserving accessibility of the **Ru single-atom** OER site.

C4 — Gradient-doped NiCo_2O_4 spinel (111) with amorphous Al–O/Ti–O overlayer Based on the **A4** spinel slab, modeled along (111) with in-plane metrics $\sim 20 \text{ \AA}$ and $\mathbf{c} \approx 41 \text{ \AA}$ ($\sim 15 \text{ \AA}$ vacuum; **P1**). The **Ce dopants** in A4 are replaced by a **gradient dopant distribution**: **2 Cr** near the surface ($z \approx 11.76 \text{ \AA}$), **4 Ti** in mid-subsurface (two at $z \approx 11.76 \text{ \AA}$, two at $z \approx 6.97 \text{ \AA}$), and **2 Mg** deeper ($z \approx 6.97 \text{ \AA}$)— $\sim 1\%$ combined dopants in the **760-atom** base, enriching the **BO-rich** surface for corrosion tolerance; existing **lattice O-vacancies** from A4 are retained. The surface is capped by **8 amorphous Al–O/Ti–O clusters** (4 small, 4–6 atoms; 4 medium, 6–9 atoms) at $\sim 25\text{--}30\%$ coverage, each $\sim 2.5 \text{ \AA}$ above and $\geq 3.5 \text{ \AA}$ apart, with $\text{Al–O} \sim 1.8 \text{ \AA}$ and $\text{Ti–O} \sim 1.9 \text{ \AA}$ ($\pm 15\%$ distortions), representing a 3–5 nm nanolaminate protection motif. After relaxation, clusters form Al–O–(Co,Ni) linkages while the dopant gradient accommodates lattice/electronic modulation. Final composition: **814 atoms** ($\text{Co}_{188}\text{Ni}_{92}\text{Cr}_2\text{Mg}_2\text{Ti}_{18}\text{O}_{411}\text{Al}_5\text{H}_{96}$); the (111) surface itself provides the primary OER sites, with the gradient and ALD layer furnishing complementary stability.

Metal Site Choices Considering the complexity of each slab created based on DR report, we decide to select from each slab only representative sites for further study:

IrO₂ On $\text{IrO}_2(110)$ we target the canonical fivefold Ir terrace site (Ir_{5c}) on the top surface cation row. Its local geometry is square-pyramidal, with four coplanar surface O neighbors at 2.00 \AA and a single subsurface apical O at 1.97 \AA ; the missing apical ligand points toward vacuum. Situated in the outermost O–Ir–O trilayer, this terrace Ir is the standard benchmark adsorption site on rutile-type oxides and is chosen to probe intrinsic, defect-free reactivity under well-defined coordination.

A1 On A1 we probe two "regular" terrace cations on the **top basal (001) surface**—one Fe and one Ni located in the central, step-free region. Both exhibit near-ideal octahedral $\text{M}(\text{OH})_6$ coordination with a 3-up/3-down O arrangement; their mean M–O distances are **2.09 \AA (Fe)** and **2.07 \AA (Ni)**, and the in-plane metal–metal spacing reflects the basal lattice at $\sim 3.13 \text{ \AA}$. The Fe site sits in a Ni-rich cation shell (isolated Fe amid Ni), whereas the Ni site has a typical mixed neighborhood ($\sim 4 \text{ Ni}$, 2 Fe), consistent with the $\sim 3:1$ Ni:Fe layer composition. These terrace positions were chosen as **representative, bulk-like**

references—well coordinated and far from edges or defects—providing robust baselines for adsorption benchmarking on LDH surfaces.

A2 In **A2** we focus on two regular first-layer cations on the **top basal (001) surface**—one Fe and one Ni—above the phosphate-filled interlayer. Both sites are octahedral with **3 O above / 3 O below**; the Fe exhibits **Fe–O \approx 2.06/2.01 Å** (above/below) and the Ni **Ni–O \approx 2.10/2.07 Å**. Relative to the subsurface phosphate, the Fe sits **nearly on-axis** over a PO₄ unit ($\Delta z \approx 4.30$ Å, lateral offset ≈ 0.71 Å), whereas the Ni is **laterally off-axis** from the nearest PO₄ ($\Delta z \approx 4.54$ Å, lateral ≈ 2.95 Å). These two surface metals are chosen as representative, symmetry-inequivalent terrace sites that sample **distinct interlayer electrostatic environments** (aligned vs off-axis to PO₄) while avoiding edges/defects—providing a solid, structure-based rationale for benchmarking metal-identity and phosphate-proximity effects.

A3 For A3, on the top SnO₂(110) terrace, the representative site comprises a single Ni atom anchored above a bridging-O row, adopting a square-pyramidal NiO₅ geometry with four surface O_{br} ligands in the equatorial plane (Ni–O ≈ 1.92 Å) and one apical O beneath (Ni–O ≈ 2.03 Å); the Ni sits ~ 0.19 Å below the O_{br} plane and ~ 2.03 Å above the apical O. The two nearest subsurface Sn cations on adjacent cation rows are each connected to the adatom via a Sn–O_{br}–Ni bridge (Sn–O ≈ 2.07 Å; Ni–Sn ≈ 3.12 Å). Situated on the upper, flat terrace away from step edges, this motif matches your original "Ni single-atom adjacent to Sn via bridging O" note and is selected as a representative active site because it captures the canonical O_{br}–M_{cus} environment of rutile(110) while providing quantitatively well-defined, low-coverage coordination ideal for benchmarking OER intermediates.

A4 For A4, we have chosen a total of 6 Co/Ni atoms. On the top Co–O(H)-terminated face of the Ce-doped, oxygen-deficient NiCo₂O₄ slab, we consider two Ce-proximal motifs and one Ce-remote control set. Ce-proximal: (i) a two-fold-coordinated Co sitting at the rim of a surface O-vacancy directly above the subsurface Ce layer, and (ii) a three-fold Co one O row back on the same terrace; alongside these, a three-fold Ni in the same Co-rich layer but still within the Ce-perturbed field captures the B-site identity contrast. Ce-remote (terrace center, far from dopants/vacancies): (iii) a two-/three-fold Co pair representative of the intact hydroxylated terrace, and (iv) a two-fold Ni surrounded by a largely unreconstructed O sublattice. Together these five local environments span coordination (2 vs. 3), cation identity (Co vs. Ni), and dopant/vacancy proximity (near-Ce vs. terrace-center) consistent with the A4 design (Ce in subsurface planes + engineered surface O-vacancies with hydroxyl passivation). This reflects the selection logic: Ce-adjacent rims/near-rim terrace sites plus Ce-remote terrace controls with 2- and 3-coordinate Co/Ni.

B1 On **B1 (graphene-capped NiFe-LDH (001))**, the representative **first-layer surface Fe and Ni** are the outermost cations in the top brucite-like sheet directly beneath the graphene overlayer. Each sits in a **regular M(OH)₆ octahedron** with nearly isotropic M–O bonds (Fe: **2.09 Å** apical/**2.09 Å** apical; equatorial **2.09 \pm 0.00 Å**; Ni: **2.08 Å** apical/**2.08 Å** apical; equatorial **2.07 \pm 0.00 Å**; octahedral distortion ≈ 0.11 %), positioned **1.03 Å** below the topmost O plane and **2.00 Å** below terminal OH, with the graphene sheet **7.00 Å** above the metal plane (**5.97 Å** above the surface O layer). The chosen Fe lies near the in-plane center (**> 8.09 Å** from periodic edges) and the Ni is also well inside the terrace (≈ 5.45 Å from edges), i.e., **regular terrace sites** rather than step/edge motifs—matching the "regular first-layer" description in the earlier manual note. These sites were selected to provide **clean, defensible benchmarks** for OER under Branch-B1's design goal (probing LDH activity beneath a protective graphene barrier): they are far from defects and intercalants, exhibit bulk-like octahedral geometry, and experience only **physisorbed** graphene influence, thus isolating intrinsic Fe/Ni–OH reactivity at the **top basal surface**.

B2 on B2, On the top (0001) face beneath the graphene aperture, four representative surface Fe sites were selected: two **rim** Fe located along the edge of the ~ 6 Å window where the sp² rim approaches the oxide, each making Fe–C contact (shortest Fe–C ≈ 2.17 Å), with under-coordination (Fe–O CN ≈ 3) and a slight outward relaxation (≈ 1.33 Å above the terminal O plane); and two **center-of-window** Fe positioned near the middle of the opening, far from the carbon edge (nearest C ≥ 5.24 Å), retaining octahedral-like coordination (Fe–O CN ≈ 6) and sitting ≈ 1.19 Å below the top O/H plane. These two site families—carbon-contacted rim vs carbon-free aperture interior—follow the original design intent and provide a physically motivated contrast to quantify how the graphene shell perturbs intrinsic hematite reactivity.

B3 On the BO_2 -terminated top surface of B3 we sample four terrace cations: (i) one **Fe** and (ii) one **Co** sitting at the rim of a deliberate surface O-vacancy, each **three-coordinated** to lattice O (vacancy-edge sites, no apical O) with shortened in-plane M–O distances of $\sim 1.90\text{--}1.97$ Å; and, as references, (iii) one **Fe** and (iv) one **Co** on the same terrace but **far from any defect** (≥ 10.00 Å lateral separation), retaining the regular **square-pyramidal BO_5** environment (four equatorial M–O $\approx 1.95\text{--}2.02$ Å, one apical $\approx 2.05\text{--}2.10$ Å). This choice—consistent with the original notes—targets the most contrastive local motifs (vacancy-edge undercoordination vs pristine terrace; Fe vs Co identity) while keeping all sites in the **outermost BO_2 plane** above the BaO underlayer.

B4 In B4’s coral-type aperture, we target four representative rim sites: a Fe and a Ni in the **top metal plane** at the pore edge, and the corresponding **second-plane** Fe and Ni located directly beneath the rim (as in the earlier manual note). The two top-layer cations sit 1.88 Å (**Fe**) and 1.55 Å (**Ni**) below the outermost O plane and lie within $0.10\text{--}0.23$ Å of the top-plane centroid; their in-plane separation is 3.21 Å. At the rim, **Fe remains near-octahedral** ($6 \text{ O} \leq 2.30$ Å; $\langle d_{\text{M-O}} \rangle = 2.13$ Å), whereas **Ni is under-coordinated** ($4 \text{ O} \leq 2.30$ Å; $\langle d_{\text{M-O}} \rangle = 2.12$ Å). The second-layer pair occupies the ring immediately below the aperture edge, $13.53\text{--}13.43$ Å beneath the top O plane and within $0.09\text{--}0.02$ Å of the second-plane centroid; both are **under-coordinated** ($4 \text{ O} \leq 2.30$ Å; $\langle d_{\text{M-O}} \rangle = 2.12$ Å (**Ni**), 2.06 Å (**Fe**)), with an in-plane separation of 3.21 Å. These sites were chosen to systematically span **cation identity (Fe vs Ni)**, **depth (surface vs subsurface)**, and **coordination state at the pore edge**, i.e., the structural factors most likely to govern *OH/*O/*OOH binding and chloride tolerance in the coral design.

C1 On **C1 (Ni–Fe LDH on 5% N-doped graphene with partial SALD Al–O/Ti–O coverage)**, we sample **two terrace metals** on the **top basal (001) sheet (Fe and Ni)** and one **subsurface Fe** to probe depth effects under the overlayer. The **surface Fe** sits in a near-ideal Fe(OH)_6 octahedron ($\text{Fe–O} \approx 2.09$ Å), the **surface Ni** in a matching Ni(OH)_6 environment ($\text{Ni–O} \approx 2.07$ Å), both placed in the **central, step-free terrace** beneath regions **not capped** by amorphous clusters. The **subsurface Fe** resides one hydroxide layer down ($\Delta z \approx 7.8$ Å relative to the top Fe) with octahedral $\text{Fe–O} \approx 2.10$ Å. These **Fe/Ni surface vs Fe subsurface** choices span **metal identity** and **depth**, enabling paired benchmarks of dissolution propensity and local lattice oxygen stability in the composite LDH/carbon/SALD architecture. For VO tests we target the **lowest-coordination** O neighbors of each metal (CN 1–3 within $2.0\text{--}2.10$ Å) to provide a consistent, edge-biased vacancy protocol.

C2 On **C2 (Fe single atom on Nb-doped anatase $\text{TiO}_2(101)$ with amorphous ALD clusters)**, we select the **Fe adatom** anchored at a surface **O-vacancy** (square-pyramidal, bridging-O motif) as the **core active site**, then pair it with **two subsurface Nb dopants**: a **near Nb** directly beneath Fe in the first cation plane ($\Delta z \approx 1.9$ Å; nearly on-axis), and a **far Nb** in the same plane but ~ 4.25 Å laterally displaced. This triad isolates **active-site stability** (Fe) and **dopant anchoring/retention** (Nb near vs far) under the partially passivated surface. For VO we remove the **least-coordinated** O within ≤ 3.0 Å of each target (CN ≈ 2 ; **Fe** neighbor at ~ 2.46 Å, **Nb** neighbors at ~ 1.94 Å) to assess oxygen-lattice integrity in proximity-contrasted environments.

C3 On **C3 (Ru single atom on W-doped anatase $\text{TiO}_2(101)$ with amorphous ALD clusters)**, we mirror the C2 schema: the **Ru adatom** at a surface **O-vacancy** (square-pyramidal, bridging-O motif) serves as the **primary site**, coupled to **two first-subsurface W dopants**—one **near/on-axis** ($\Delta z \approx 1.9$ Å beneath Ru) and one **laterally offset** by ~ 4.25 Å. This comparison quantifies the **noble-metal advantage** (Ru vs Fe) and the effect of **higher-valent dopant** (W^{6+} vs Nb^{5+}) on both **active-site** and **dopant** stability. VO tests again remove the **lowest-CN** O within ≤ 3.0 Å (CN ≈ 2 ; neighbors at ~ 2.46 Å for Ru and ~ 1.94 Å for W) to benchmark vacancy energetics across the proximity series.

C4 On **C4 (gradient-doped NiCo_2O_4 spinel with amorphous ALD protection)**, we probe **three cations** spanning the designed gradient: a **surface-enriched Cr** dopant in the upper octahedral layer ($z \approx 25.3$ Å), a **Co** octahedral site **near Cr** ($\text{Cr–Co} \approx 2.86$ Å; same region), and a **Co** octahedral **far from all Cr** (~ 23 Å away) as the baseline. This set interrogates whether **aliovalent Cr** resists leaching and whether **Cr proximity** stabilizes neighboring **Co–O** bonding relative to **Cr-remote** Co in the spinel framework. For VO we remove under-coordinated O neighbors (e.g., $\sim 1.91\text{--}1.93$ Å to Cr/Co; CN 2–4) to consistently stress the lattice at the most vulnerable positions across **Cr-near** and **Cr-far** environments.

F.5.2 OER Catalyst Stability Assessment

Discussion of OER stability. While recent advances in transition metal layered double hydroxides (LDH) and related materials have achieved excellent oxygen evolution reaction (OER) activity approaching theoretical limits, catalyst stability remains the critical bottleneck preventing commercial deployment of water splitting technologies. Operating potentials exceeding 1.5 V vs. RHE in alkaline conditions create thermodynamically favorable pathways for both metal dissolution and lattice oxygen loss, leading to rapid catalyst degradation. To address this fundamental challenge, we evaluated candidate catalysts proposed by the DR agents (Figure S37) using two complementary stability descriptors following established protocols from our previous work [29]: dissolution potential (U_{diss}) and oxygen vacancy formation energy (V_{O}).

Stability Descriptors and Physical Interpretation

The dissolution potential U_{diss} quantifies the thermodynamic driving force for metal atom leaching from the catalyst surface, calculated as:

$$U_{\text{diss}}(M@\text{slab}) = U_{\text{diss,bulk}}^{\circ}(M^{z+}/M) + \frac{E_{\text{slab-vac}}(M) + \mu_{\text{bulk}}(M) - E_{\text{slab}}}{ne} \quad (6)$$

where E_{slab} and $E_{\text{slab-vac}}(M)$ represent the DFT energies of the intact and metal-vacancy surfaces, respectively (Figure S38), $\mu_{\text{bulk}}(M)$ is the bulk metal chemical potential, $U_{\text{diss,bulk}}^{\circ}$ is the standard reduction potential, and n is the number of electrons transferred. Higher U_{diss} values indicate greater resistance to metal dissolution, with positive values suggesting thermodynamic stability under standard conditions. The oxygen vacancy formation energy V_{O} captures the structural integrity of the oxide lattice during OER cycling. We following the following protocol for picking lattice oxygen atom to remove, oxygen atoms are identified within 3.0 Å of active metal sites and removed based on coordination number, with under-coordinated oxygen atoms preferentially selected (Figure S38). Higher V_{O} values indicate stronger metal–oxygen bonds and reduced susceptibility to lattice oxygen participation in the OER mechanism, which can lead to irreversible structural degradation. **Comparative Stability Analysis**

Evaluation across representative surface sites (Figure S39) reveals significant variation in stability metrics among candidate catalysts. The dissolution potentials span from approximately -0.4 V to $+1.2$ V vs. SHE (Figure S40). Oxygen vacancy formation energies similarly exhibit broad distribution. In general, higher V_{O} suggests enhanced lattice stability potentially arising from stronger metal–oxygen covalency or favorable coordination environments that stabilize the oxide framework. **Correlation Between Stability Metrics**

A positive correlation emerges between U_{diss} and V_{O} across all 39 evaluated metal sites (Figure S42), indicating that resistance to metal dissolution and oxygen vacancy formation are intrinsically linked. This correlation suggests a unified electronic origin for both stability mechanisms: catalysts with stronger metal–oxygen bonds resist both metal leaching and oxygen loss. The observed relationship validates the use of either metric as a reasonable proxy for overall stability, though evaluating both provides more comprehensive assessment. **Normalized Stability Scoring**

To enable quantitative comparison, we similarly applied the linear scoring framework with IrO_2 as the baseline reference (Score = 100), using sensitivity parameter $\beta = 0.2$ consistent with other applications. The U_{diss} -based scores are shown in Figure S43. The V_{O} -based scores (Figure S44) show similar trends but not quite exactly the same rankings, highlighting the value of assessing both metrics. The divergence between U_{diss} and V_{O} rankings for specific candidates reflects different stability-limiting mechanisms: some materials may excel at preventing metal dissolution while remaining vulnerable to oxygen loss, or vice versa. This complementary information guides rational catalyst design—for instance, candidates with high U_{diss} but moderate V_{O} might benefit from strategies to strengthen metal–oxygen bonds, while those with the opposite profile could require enhanced metal site anchoring.

OER Catalyst Structures

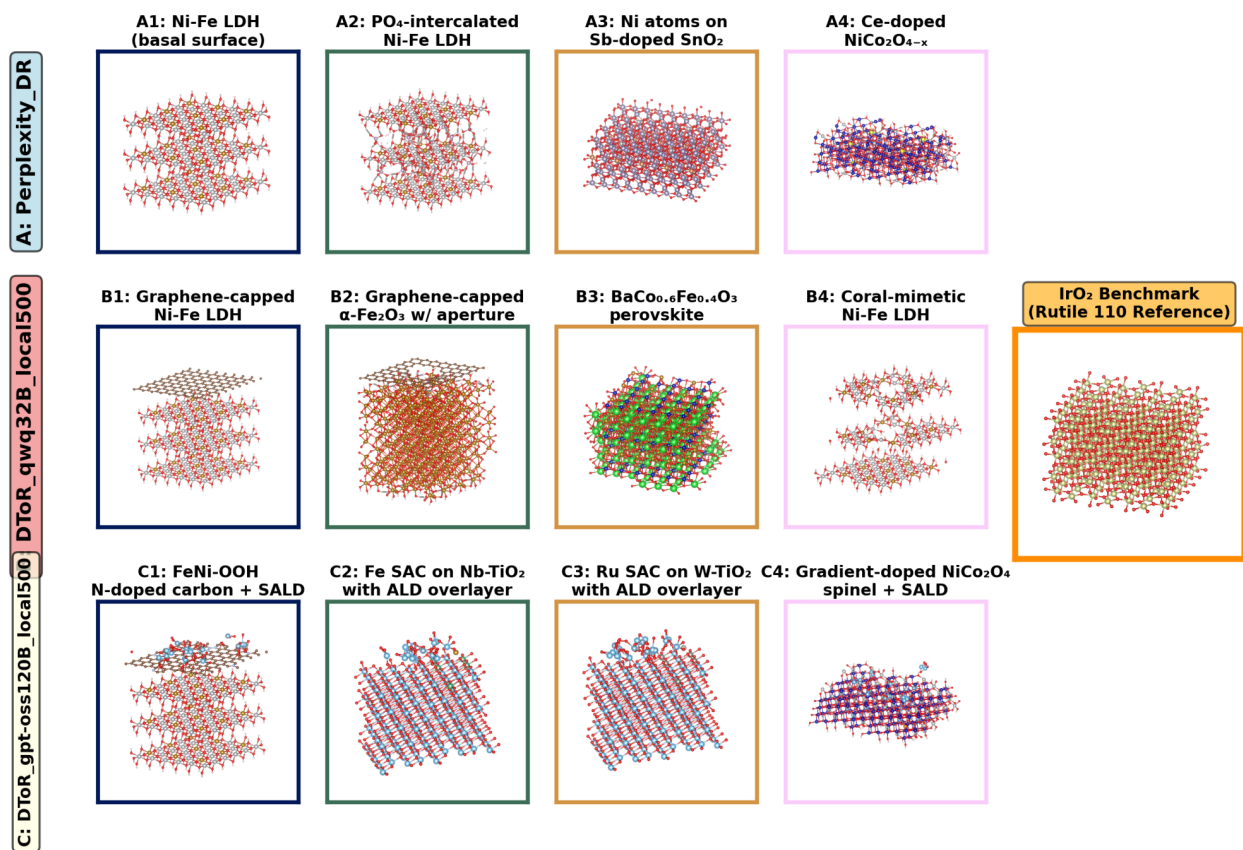


Figure S37: Structural configurations of OER catalyst candidates proposed by DR agents, with IrO₂ (110) included as the domain benchmark reference for stability assessment.

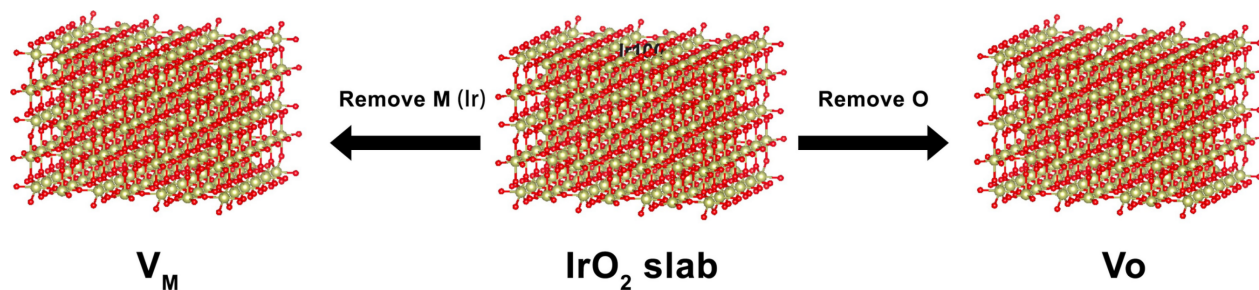


Figure S38: Schematic illustration of vacancy creation on the IrO_2 rutile (110) surface. Left: Metal vacancy (V_M) created by removing a surface metal atom for dissolution potential (U_{diss}) calculation. Right: Oxygen vacancy (V_O) created by removing a surface oxygen atom for vacancy formation energy calculation.

OER Catalyst Site Choices

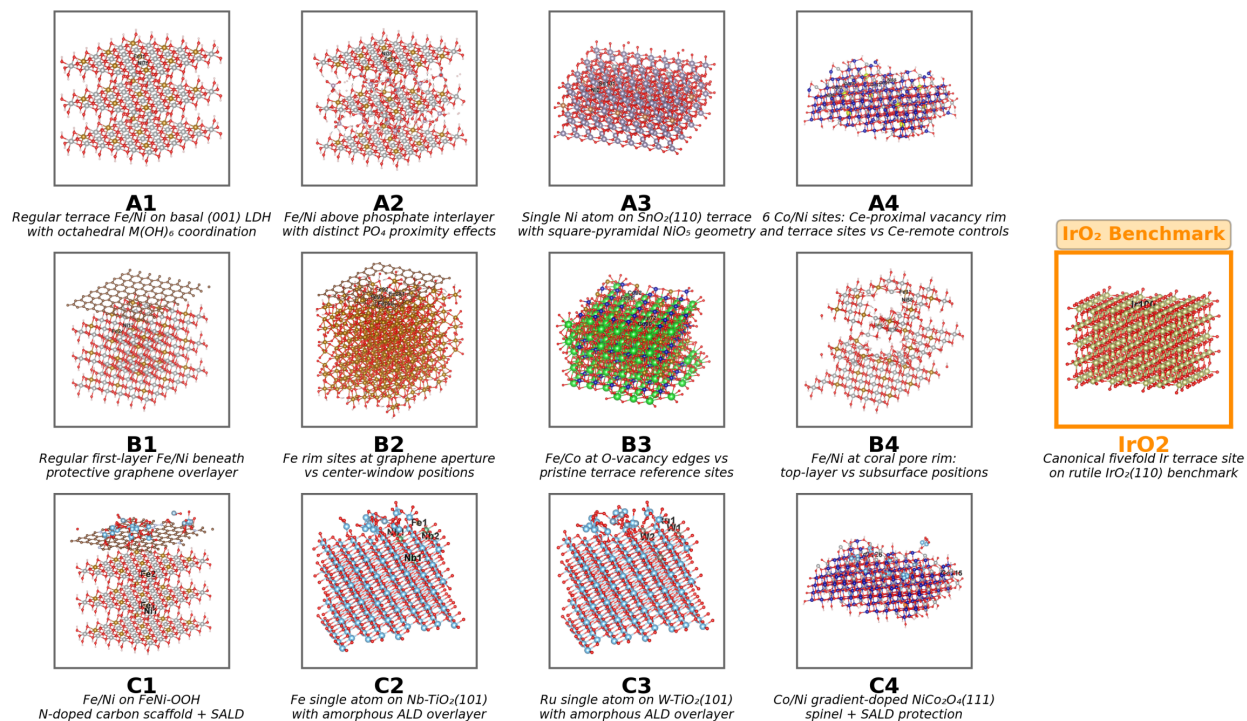


Figure S39: Matrix representation of selected metal sites for stability assessment across A-series (A1–A4) and B-series (B1–B4) catalyst candidates. Representative surface metal atoms are highlighted for dissolution and vacancy formation calculations.

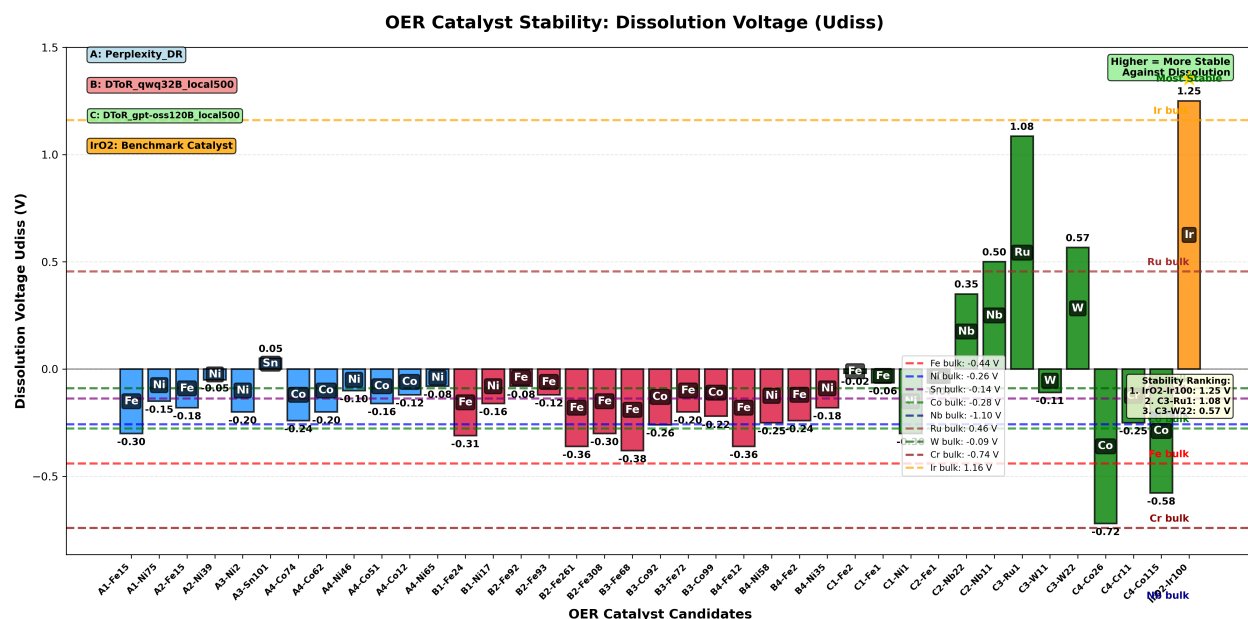


Figure S40: Dissolution potentials (U_{diss}) for all candidate catalysts at representative surface sites. Higher values indicate greater resistance to metal dissolution. Dashed horizontal lines denote standard bulk dissolution potentials for reference metals (Fe: -0.44 V, Co: -0.277 V, Ni: -0.257 V, Ir: +1.16 V vs. SHE).

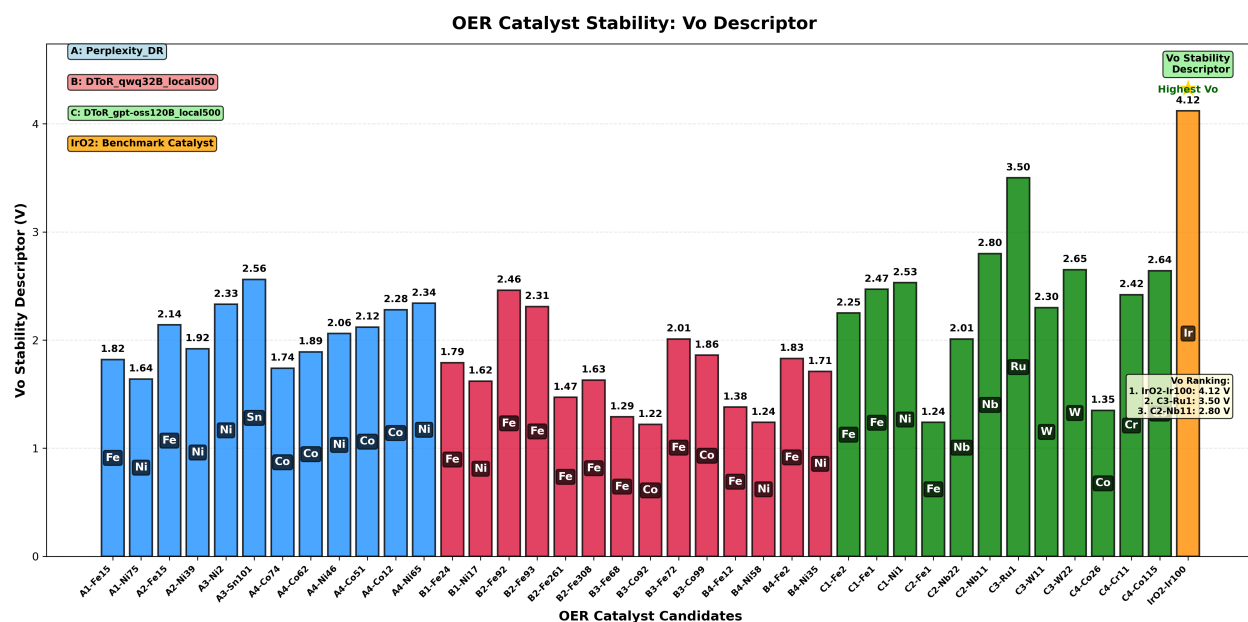


Figure S41: Oxygen vacancy formation energies (V_o) for all candidate catalysts at representative surface sites. Higher formation energies indicate greater structural stability and resistance to oxygen loss during OER operation.

OER Catalyst Stability: Dissolution Potential (U_{diss}) Scores

Higher U_{diss} indicates better stability (dissolution resistance)

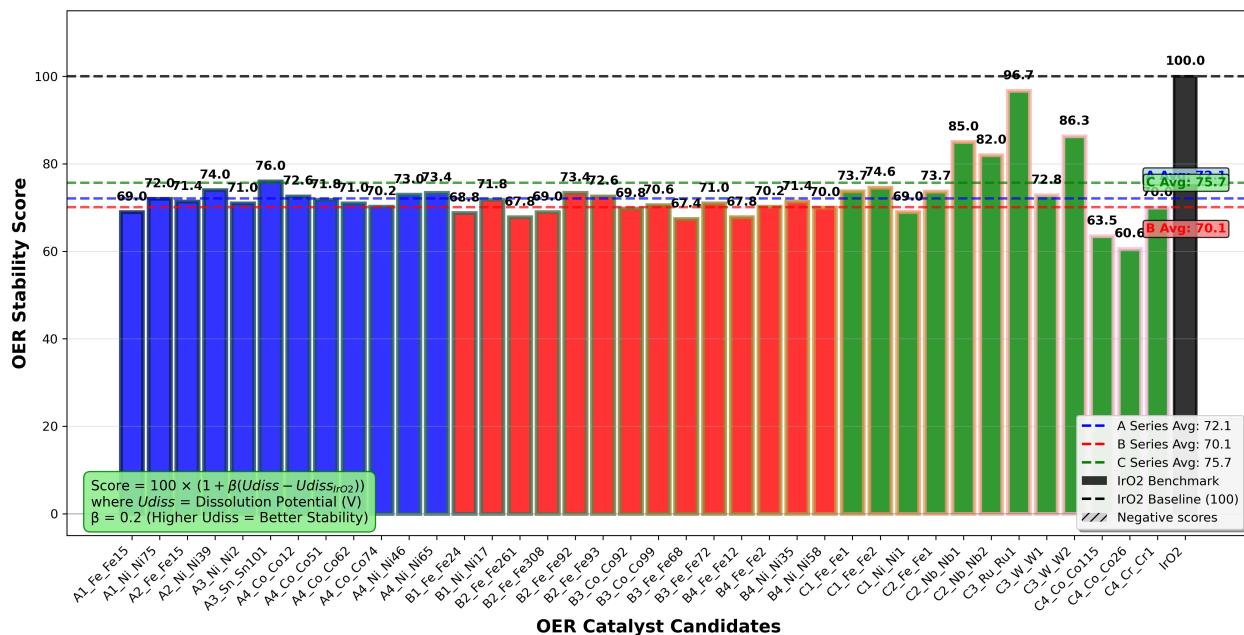


Figure S43: Stability scores based on dissolution potential (U_{diss}), normalized to IrO_2 baseline (100). Scores are calculated using the linear metric with sensitivity parameter $\beta = 0.2$, where higher U_{diss} values yield higher scores.

OER Catalyst Stability: Oxygen Vacancy Formation Energy (V_o) Scores

Lower V_o indicates better OER activity (easier oxygen vacancy formation)

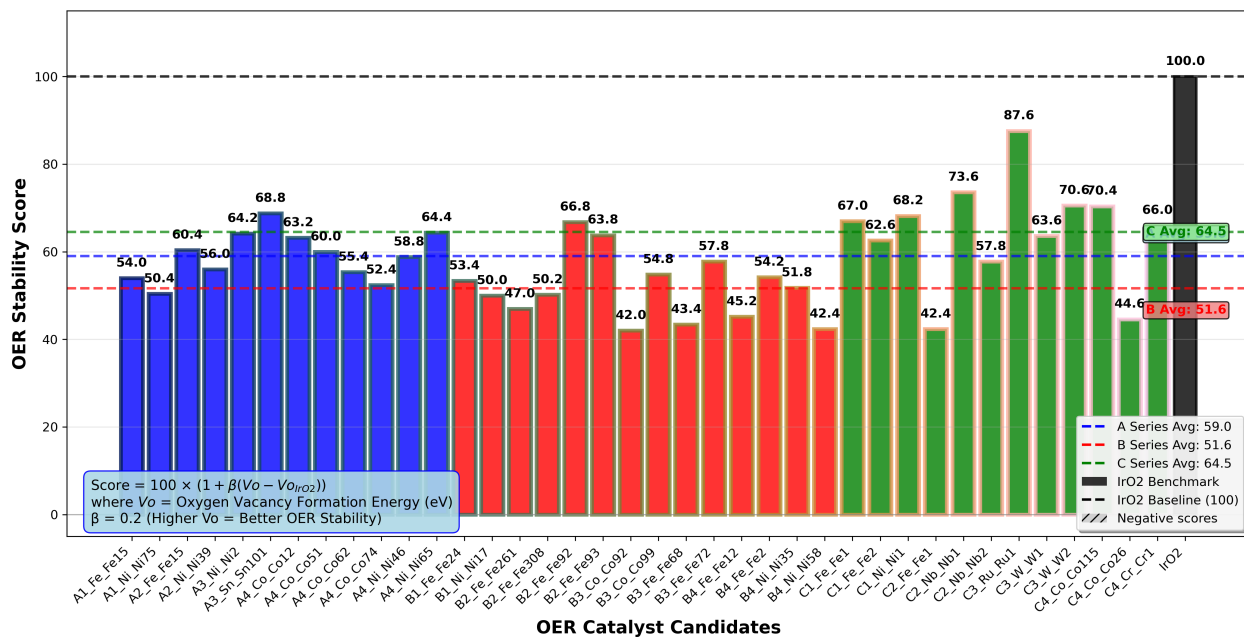


Figure S44: Stability scores based on oxygen vacancy formation energy (V_o), normalized to IrO_2 baseline (100). The scoring methodology employs the same linear scaling ($\beta = 0.2$), with higher V_o values indicating superior stability.

F.6 CO₂ Sensor Probe

F.6.1 CO₂_Sensing_2D_Materials

For the fifth application: CO₂ Sensor Probe. The query as shown in C is:

```
Which two-dimensional materials--such as graphene derivatives, transition metal
dichalcogenides, or MXenes--offer the highest CO2 sensing performance in complex gas
or aqueous environments, and how do they compare in terms of detection limit (ppm),
selectivity against common interferents (e.g., O2, H2O), response/recovery time, and
long-term stability, including any functionalization or structural
modifications that enhance these metrics? Think of novel candidates.
```

The best commercial solution is: **GlideLogic_DR**.

The best local non gpt-oss solution is: **DToR_qwq32B_local500**.

The best local gpt-oss solution is: **Single_gpt-oss120B_local500**.

The expert based on the two reports, provided 4 commercial DR report derived candidates (A1-A4), and 4 local non gpt-oss DR report derived candidates (B1-B4), and 4 local gpt-oss DR report derived candidates (C1-C4), visualized in Fig. S45:

g-C₃N₄ description For CO₂ binding, the benchmark substrate is a monolayer graphitic carbon nitride (g-C₃N₄) built as a 7×7 in-plane supercell of the primitive sheet (49 formula units; C₁₄₇N₁₉₆) in a hexagonal cell with a = b = 33.50 Å, γ = 120°, and c = 35.0 Å. All atoms lie in a single atomic plane at z ≈ 5.0 Å, leaving ~30 Å of vacuum to the next periodic image along c, i.e., no interlayer interactions. The in-plane network is a fully conjugated sp² C–N lattice: each C is three-coordinate, N sites are predominantly two- to three-coordinate ((CN) ≈ 2.25), and nearest-neighbor C–N distances cluster at 1.37 ± 0.06 Å. No heteroatoms, defects, terminations, or adsorbates are present (P1 by construction). This clean, stoichiometric, and strictly planar C₃N₄ slab (areal density ≈ 5.05 formula units nm⁻²) serves as our reference surface for CO₂ binding.

A1 (rGO–PEI) Hexagonal P1 slab with a = b = 36.90 Å, γ = 120.00°, c = 45.00 Å (α = β = 90.00°). The model contains 605 atoms (C₄₆₁H₈₀O₅₄N₁₀). Atomic z positions span 4.63–16.63 Å, giving a slab thickness of 12.01 Å and 32.99 Å of vacuum along c. The in-plane area is 11.79 nm², yielding areal number densities of C 39.09 nm⁻², H 6.78 nm⁻², O 4.58 nm⁻², and N 0.85 nm⁻². Carbon heights resolve a dominant rGO basal plane centered at z ≈ 7.39 ± 0.64 Å (441 C) and a minor upper carbon domain at 12.09–15.35 Å (20 C). All N atoms reside in the upper domain (11.23–16.53 Å; ⟨z⟩ = 13.03 Å), consistent with an amine-rich polyethylenimine (PEI) branch moiety tethered above the rGO sheet; O atoms are concentrated below 10.65 Å, consistent with residual rGO oxygen functionalities. This rGO–PEI slab, isolated by ample vacuum, provides a structurally well-defined platform for site-specific CO₂ binding calculations.

A2 (phosphorene | Al₂O₃ cap with drilled through-pore) Orthorhombic P1 cell (a = 26.36 Å, b = 27.26 Å, c = 27.08 Å; α = β = γ = 90.00°) comprising a phosphorene sublayer (P₁₉₂) beneath an alumina cap (Al₁₄₆O₂₂₀). Atomic z spans 3.95–17.44 Å, giving a slab thickness of 13.49 Å and 13.59 Å of vacuum. Phosphorene occupies z = 3.95–8.12 Å (thickness 4.17 Å; top P plane at 8.12 Å), while the cap exhibits O/Al = 1.51 (≈Al₂O₃) with the Al framework at z = 8.83–15.83 Å (7.00 Å) and the O network extending 8.05–17.44 Å (9.39 Å), slightly overlapping the top P plane (Δz = 0.07 Å) to form an interfacial contact. The in-plane area is 718.57 Å² (7.19 nm²). A single through-pore pierces the cap near (f_x, f_y) = (0.51, 0.50): the top aperture has radius 6.27 Å (∅ 12.54 Å), narrows to a bottleneck radius 5.11 Å (∅ 10.22 Å; section 82.02 Å², 11.42% of the surface), and re-expands near the interface to radius 5.22 Å (∅ 10.44 Å). The pore rim at the bottleneck is O-rich (~7 O : 2 Al) distributed over z = 9.53–12.66 Å, yielding an oxygen-lined channel above phosphorene that enables CO₂ access both to alumina terminations and to interfacial sites.

A3 (MoS₂ monolayer with vacancies) P1 cell with a = 27.58 Å, b = 22.29 Å, c = 28.13 Å (α = β = γ = 90.00°). The slab contains 200 atoms (Mo₆₄S₁₃₆; S/Mo = 2.13) and occupies z = 4.83–8.50 Å (thickness 3.67 Å) with 24.46 Å of vacuum along c. The in-plane area is 6.15 nm², giving areal number densities of Mo 10.41 nm⁻² and S 22.13 nm⁻². Layering is a single S–Mo–S tri-layer: the Mo plane is centered at z = 6.56 Å (spread 0.31 Å), bracketed by S planes at z = 5.01 Å and 8.12 Å, yielding an average S–S separation of 3.11 Å and Mo–S vertical offsets of 1.54 Å (bottom) and 1.57 Å (top). No heteroatoms,

functional groups, or adsorbates are present. Five Mo atoms are removed to create Mo vacancies. This monolayer MoS₂ slab provides a simple, well-isolated reference for CO₂ adsorption benchmarks.

A4 (Ti₃C₂T_x, mixed terminations) Hexagonal P1 slab with $a = b = 30.67 \text{ \AA}$, $\gamma = 120.00^\circ$, $c = 51.70 \text{ \AA}$ ($\alpha = \beta = 90.00^\circ$); in-plane area 8.15 nm^2 . The model contains Ti₃₀₀C₂₀₀O₁₇₅F₂₅H₂₅, i.e., 100 Ti₃C₂ formula units with 200 surface sites. Terminations are asymmetric: the top face comprises 50.00% *O, 25.00% *OH, and 25.00% *F (100 sites), whereas the bottom face is 100.00% *O (100 sites), giving an overall distribution of 75.00% *O, 12.50% *OH, and 12.50% *F. Atomic heights span $z = 5.01\text{--}13.29 \text{ \AA}$ (thickness 8.29 \AA) with 43.41 \AA of vacuum; the carbide core lies at $z = 7.22\text{--}9.90 \text{ \AA}$ (2.68 \AA). Mean vertical offsets from the surface Ti planes are 0.96 \AA for top *O, 1.06 \AA for top *F, 2.06 \AA for H in *OH, and 0.89 \AA for bottom *O; the corresponding site density is 12.28 nm^{-2} per face. This slab provides a well-defined mixed-termination MXene surface for probing site-specific CO₂ adsorption.

B1 (rGO–NH₂; same rGO basal slab as A1) This model reuses the rGO lattice from A1 without change ($a = b = 36.90 \text{ \AA}$, $\gamma = 120.00^\circ$, $c = 45.00 \text{ \AA}$; in-plane area 11.79 nm^2), retaining the 441-C rippled basal plane centered at $z = 7.29 \pm 0.67 \text{ \AA}$. The slab contains 585 atoms (C₄₄₁H₇₀O₅₄N₂₀) with heights spanning $4.36\text{--}11.16 \text{ \AA}$ (thickness 6.80 \AA) and 38.20 \AA of vacuum. Oxygen functionalities lie over $4.36\text{--}10.64 \text{ \AA}$, while primary amines are grafted exclusively on the upper face (N $8.37\text{--}10.38 \text{ \AA}$, $\langle z \rangle = 9.40 \pm 0.63 \text{ \AA}$; H up to 11.16 \AA), giving an –NH₂ areal density of 1.70 nm^{-2} . Areal number densities are C 37.40 nm^{-2} , O 4.58 nm^{-2} , N 1.70 nm^{-2} , and H 5.94 nm^{-2} . With lattice vectors and basal carbon topology identical to A1, this slab isolates the effect of replacing the PEI overlayer with discrete –NH₂ terminations for CO₂ binding studies.

B2 (Ti₃C₂F₂, fully F-terminated; same construction protocol as A4) Hexagonal P1 slab with $a = b = 30.67 \text{ \AA}$, $\gamma = 120.00^\circ$, $c = 51.70 \text{ \AA}$ ($\alpha = \beta = 90.00^\circ$); in-plane area 8.15 nm^2 . The CIF contains Ti₃₀₀C₂₀₀F₂₀₀ (100 Ti₃C₂ formula units; 200 surface sites), i.e., both faces are 100.00% *F with no *O or *OH terminations. Atomic heights span $z = 4.85\text{--}12.14 \text{ \AA}$, giving a slab thickness of 7.29 \AA and 44.41 \AA of vacuum. The carbide core (Ti/C) lies at $z = 6.11\text{--}10.87 \text{ \AA}$ (4.76 \AA); terminal F layers sit symmetrically at offsets of 1.27 \AA above the top Ti plane and 1.27 \AA below the bottom Ti plane. The termination site density is 12.28 nm^{-2} per face (100 sites over 8.15 nm^2). This symmetric, fully fluorinated MXene provides a clean counterpoint to the mixed-termination Ti₃C₂T_x model (A4) for isolating the effect of *F terminations on CO₂ adsorption.

B3 (graphene | Ti₃C₂O₂ heterojunction; same MXene cell as As A4/B2) Hexagonal P1 slab with $a = b = 30.67 \text{ \AA}$, $\gamma = 120.00^\circ$, $c = 51.70 \text{ \AA}$ (in-plane area 8.15 nm^2). The MXene sub-slab matches the A4/B2 Ti₃C₂ lattice and is fully *O-terminated on both faces (Ti₃₀₀C₂₀₀O₂₀₀; 100 *O per face, $12.28 \text{ sites nm}^{-2}$). A single-layer graphene sheet (C₃₃₈) is appended on the bottom side, giving a total composition Ti₃₀₀C₅₃₈O₂₀₀. Atomic heights span $z = 7.31\text{--}19.41 \text{ \AA}$ (thickness 12.10 \AA) with 39.60 \AA of vacuum along c. The graphene forms a narrow plane at $z = 7.79 \pm 0.31 \text{ \AA}$ ($7.31\text{--}8.45 \text{ \AA}$), the bottom *O plane is at $z = 12.40 \text{ \AA}$ and the top *O plane at $z = 19.41 \text{ \AA}$; the graphene–MXene van der Waals gap is 4.61 \AA (center-to-plane; minimum 3.95 \AA to *O), and the graphene–bottom Ti plane separation is 6.78 \AA . The result is a well-isolated graphene|Ti₃C₂O₂ heterojunction with symmetric *O terminations and a dense graphene areal carbon density of 41.49 nm^{-2} .

B4 (Cu-inserted MoS₂; same MoS₂ host as A3) Orthorhombic P1 cell with $a = 27.58 \text{ \AA}$, $b = 22.29 \text{ \AA}$, $c = 28.13 \text{ \AA}$ ($\alpha = \beta = \gamma = 90.00^\circ$); in-plane area 6.15 nm^2). The slab contains Mo₆₄Cu₅S₁₃₆ and occupies $z = 4.80\text{--}8.32 \text{ \AA}$ (thickness 3.51 \AA) with 24.61 \AA of vacuum. The host S–Mo–S tri-layer is preserved ($\langle z \rangle$: S(bottom) = 5.03 \AA , Mo = 6.59 \AA , S(top) = 8.15 \AA ; S–S spacing 3.12 \AA ; Mo–S offsets $1.55/1.56 \text{ \AA}$), as in A3. At A3’s Mo vacancies, five Cu centers lie within the chalcogen sandwich at $z = 6.55\text{--}6.89 \text{ \AA}$ ($\langle z \rangle = 6.70 \text{ \AA}$), i.e., $\sim 0.11 \text{ \AA}$ above the Mo plane and biased toward the top S layer; the areal Cu density is 0.81 nm^{-2} . Local coordination around Cu is consistent with insertion at chalcogen-vacancy-like sites: each Cu shows $\sim 4\text{--}5$ short Cu–S contacts at $2.28\text{--}2.38 \text{ \AA}$ (mean of first shell $\approx 2.31 \text{ \AA}$) with the next S neighbors near $2.95\text{--}3.06 \text{ \AA}$, and $\sim 2\text{--}3$ Cu–Mo contacts at $2.78\text{--}3.26 \text{ \AA}$. This configuration provides a well-defined model to probe how subsurface/embedded Cu at vacancy motifs modulates CO₂ binding relative to the pristine A3 monolayer.

C1 (Mo₂C T_x MXene with hydrophobic silane + PEI) Orthorhombic P1 slab with $a = 34.64 \text{ \AA}$, $b = 30.00 \text{ \AA}$, $c = 65.36 \text{ \AA}$ ($\alpha = \beta = \gamma = 90.00^\circ$). The model contains 1006 atoms

(Mo₂₈₈C₂₂₀O₂₉₄N₂₀H₁₈₂Si₂). Atomic z positions span 22.50–42.86 Å, giving a slab thickness of 20.36 Å and 45.00 Å of vacuum along c . The in-plane area is 10.39 nm², yielding areal number densities of Mo 27.72 nm⁻², C 21.17 nm⁻², O 28.30 nm⁻², N 1.92 nm⁻², Si 0.19 nm⁻², and H 17.52 nm⁻². The Mo₂CO₂ MXene base forms a 6×6 supercell (2×2 expansion of the 3×3 primitive cell) with Mo atoms occupying $z = 23.70$ – 26.56 Å ($\langle z \rangle = 25.13$ Å; thickness 2.86 Å), bracketed by symmetric oxygen terminations at $z = 22.50$ – 30.15 Å, consistent with O-terminated MXene surfaces. Above the substrate, three surface-adsorbed components lie ~ 2.5 Å above the top Mo plane: one branched polyethylenimine (PEI) cluster centered at fractional coordinates (0.20, 0.50) with N distributed across $z = 24.42$ – 41.98 Å ($\langle z \rangle = 32.42$ Å; 20 amine sites at 1.92 nm⁻²), and two trimethoxycaprylsilane molecules at (0.95, 0.50) and (0.45, 0.50) with Si at $z = 29.18$ Å, forming a hydrophobic coating to resist humidity. Organic-layer C spans 25.13–40.94 Å, with H up to 42.86 Å, defining the top surface. Laterally, the PEI cluster occupies the left region while the silanes are separated across the middle/right, maintaining exposed MXene for electrical conduction. This Mo₂C T_x slab with patchy amine functionalization and hydrophobic silane capping, isolated by ample vacuum, provides a structurally well-defined platform for CO₂ sensing simulations targeting sub-ppm detection with enhanced humidity resistance.

C2 (Mo₂C T_x MXene | 2-D MOF UiO-66-NH₂) Orthorhombic P1 slab with $a = 34.64$ Å, $b = 30.00$ Å, $c = 66.75$ Å ($\alpha = \beta = \gamma = 90.00^\circ$). The model contains 1002 atoms (Mo₂₈₈C₂₄₀O₃₆₀N₁₂H₉₆Zr₆). Atomic z positions span 22.50–44.25 Å, giving a slab thickness of 21.75 Å and 45.00 Å of vacuum. The in-plane area is 10.39 nm², yielding areal number densities of Mo 27.72 nm⁻², C 23.10 nm⁻², O 34.65 nm⁻², N 1.15 nm⁻², Zr 0.58 nm⁻², and H 9.24 nm⁻². The Mo₂CO₂ MXene base forms a 6×6 supercell with Mo at $z = 23.70$ – 26.56 Å ($\langle z \rangle = 25.13$ Å; thickness 2.86 Å) bracketed by symmetric O terminations. Above the substrate, a single UiO-66-NH₂ MOF cage is positioned ~ 10.0 Å above the top Mo plane at (0.20, 0.50), offset to leave exposed MXene for transduction. The cage comprises a Zr₆ node coordinated by aminoterephthalate linkers (C₉₆H₉₆N₁₂O₇₂), providing 12 –NH₂ sites (1.15 nm⁻²) for CO₂ capture; the Zr₆ node imparts stability and Lewis acidity, while –NH₂ groups offer basic binding sites. The topmost atoms reach $z = 44.25$ Å, ensuring separation from the MXene base. This Mo₂C T_x | UiO-66-NH₂ hybrid, isolated by ample vacuum, provides a well-defined platform for CO₂ sensing simulations targeting sub-0.3 ppm detection with fast response and minimal drift via synergistic MXene conductivity and MOF selectivity.

C3 (Mo₂C T_x MXene with ZnO nano-grain cluster) Orthorhombic P1 cell with $a = 34.64$ Å, $b = 30.00$ Å, $c = 61.06$ Å ($\alpha = \beta = \gamma = 90.00^\circ$). The slab contains 829 atoms (Mo₂₈₈C₁₄₄O₃₄₂Zn₅₅). Atomic z spans 22.50–38.56 Å (thickness 16.06 Å) with 45.00 Å of vacuum. The in-plane area is 10.39 nm², giving areal densities of Mo 27.72 nm⁻², C 13.86 nm⁻², O 32.92 nm⁻² (MXene + ZnO), and Zn 5.29 nm⁻². The Mo₂CO₂ MXene base forms a 6×6 supercell with Mo at $z = 23.70$ – 26.56 Å ($\langle z \rangle = 25.13$ Å; 2.86 Å thick) and symmetric O terminations. Above the substrate, an octahedral ZnO nano-grain (Zn₅₅O₅₄; 109 atoms) is placed ~ 7.0 Å above the top Mo plane at (0.13, 0.50), spanning $z = 28.56$ – 38.56 Å (~ 10.0 Å vertical extent). The cluster, constructed with ASE, exhibits uniform (111)-type facets; surface Zn provide coordinatively unsaturated sites for CO₂ interaction, while surface O offer basic sites for hydrogen bonding/dipole interactions. The moderate 7.0 Å clearance balances electronic coupling with structural independence, enabling efficient transduction via the conductive MXene. This Mo₂C T_x | ZnO hybrid slab, isolated by ample vacuum, offers a well-defined platform for CO₂ sensing simulations targeting sub-0.25 ppm detection and >15:1 selectivity via synergistic conductivity and uniformly distributed ZnO capture sites.

C4 (Janus Ti₂C T_x MXene + PEI interlayer) Hexagonal P1 slab with $a = 18.18$ Å, $b = 15.74$ Å, $c = 64.57$ Å ($\alpha = \beta = 90.00^\circ$, $\gamma = 120.00^\circ$). The model contains 384 atoms (Ti₇₂C₃₆O₇₂ + PEI C₅₄H₁₃₀N₂₀; total Ti₇₂C₉₀O₇₂H₁₃₀N₂₀). Atomic z positions span 22.50–42.07 Å, giving a slab thickness of 19.57 Å and 45.00 Å of vacuum. The in-plane area is 2.86 nm², yielding areal densities of Ti 25.17 nm⁻², C 31.47 nm⁻² (12.59 nm⁻² from MXene; 18.88 nm⁻² from PEI), O 25.17 nm⁻², N 6.99 nm⁻², and H 45.45 nm⁻². The Ti₂CO₂ MXene base (validated 3×3 primitive reused and expanded to 6×6) has Ti at $z = 23.74$ – 26.26 Å ($\langle z \rangle = 25.00$ Å; 2.52 Å thick) with symmetric O terminations at ~ 22.50 Å (bottom) and 27.74 Å (top), Ti–O ≈ 1.95 Å. Above the substrate, a branched PEI interlayer cluster (C₅₄H₁₃₀N₂₀; 9 repeat units, 20 amine sites) sits 5.0 Å above the top Ti plane at (0.50, 0.50), spanning $z = 29.39$ – 42.07 Å (~ 12.7 Å vertical extent). The amine density is 6.99 N nm⁻² (≥ 3 nm⁻² target), supporting reversible amine–CO₂ chemistry (R–NH₂ + CO₂ → R–NH₂⁺–COO⁻) that modulates MXene conductivity; central placement ensures symmetric coverage while preserving peripheral MXene for contacts. This Ti₂C T_x | PEI hybrid, isolated by ample vacuum, provides a well-defined platform for CO₂ sensing simulations

targeting sub-0.25 ppm detection and >15:1 selectivity via metallic conductivity, O-termination stability, and high-density amine capture sites.

F.6.2 CO₂ Sensor Performance Evaluation

The development of sensitive and selective CO₂ sensors addresses critical needs in environmental monitoring, industrial process control, and indoor air quality management. To evaluate the CO₂ sensing capabilities of candidates proposed by the DR agents (Figure S45), we quantified binding energies using a systematic grid-based sampling approach that captures the heterogeneity of surface adsorption sites, with g-C₃N₄ serving as the established benchmark reference [30]. The comprehensive sampling methodology employed a 5×5 grid across each surface unit cell, positioning CO₂ molecules at 25 distinct initial configurations to explore the complete adsorption landscape (Figure S46). At each grid point, CO₂ molecules were placed 1.8 Å above the highest surface atom within a 3.0 Å search radius, with initial linear configurations parallel to the surface. This systematic approach ensures unbiased sampling of potential binding sites, including atop atoms, bridge sites, hollow sites, and defect locations, providing statistically robust binding energy distributions rather than single-point estimates. The resulting binding energy distributions reveal significant variability both within and between candidate systems (Figure S47). The violin plots demonstrate that surface heterogeneity plays a crucial role in CO₂ adsorption, with some candidates exhibiting narrow distributions indicating uniform binding sites, while others show broad distributions suggesting diverse adsorption environments. Mean binding energies range from approximately 0.15 to 0.90 eV across the evaluated systems, with A-series candidates generally demonstrating stronger CO₂ interactions compared to B-series materials. Performance scoring using the linear transformation framework with sensitivity parameter $\beta = 0.2$ (Figure S48) quantifies the relative sensing capabilities normalized to the g-C₃N₄ baseline. The distribution of scores reveals that commercial DR agent successfully identified materials spanning a range of binding strengths, from weak physisorption suitable for rapid-response sensors to stronger chemisorption appropriate for CO₂ capture applications. The systematic evaluation highlights the importance of comprehensive surface sampling in sensor material assessment. Candidates with both high mean binding energies and narrow distributions, such as B4, represent ideal sensor materials offering consistent response across the entire surface. Conversely, materials with broad binding energy distributions may exhibit non-uniform sensor responses, potentially complicating calibration and reducing reliability. These findings underscore that effective CO₂ sensor design requires not only optimizing average binding strength but also minimizing surface heterogeneity to ensure reproducible sensing performance.

CO₂ Sensor Material Structures

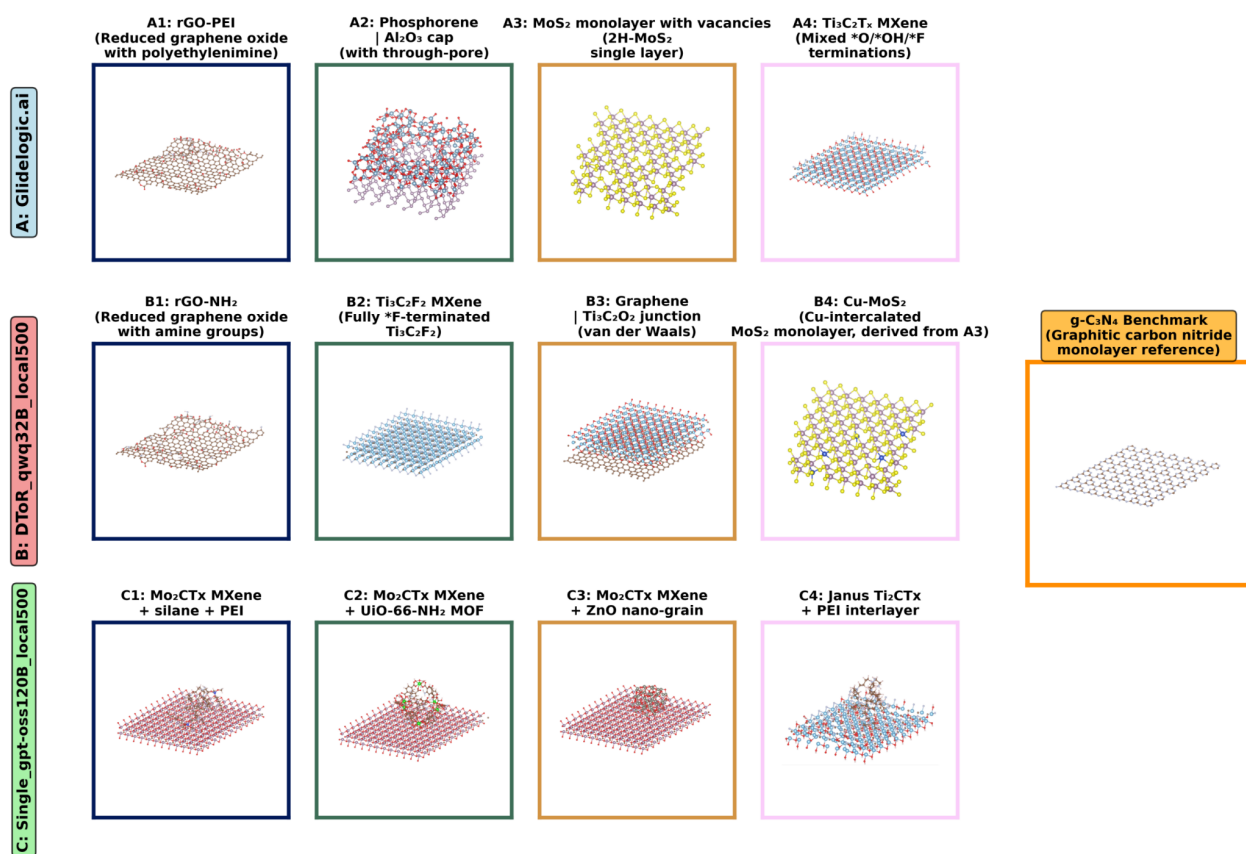


Figure S45: Structural configurations of CO₂ sensor candidates proposed by DR agents, with g-C₃N₄ [30] included as the domain benchmark reference.



Figure S46: Top-view representation of the 5×5 grid sampling approach for CO_2 adsorption sites. Relaxed configurations show CO_2 molecules at 25 distinct initial positions on candidate A2, demonstrating comprehensive exploration of the binding landscape.

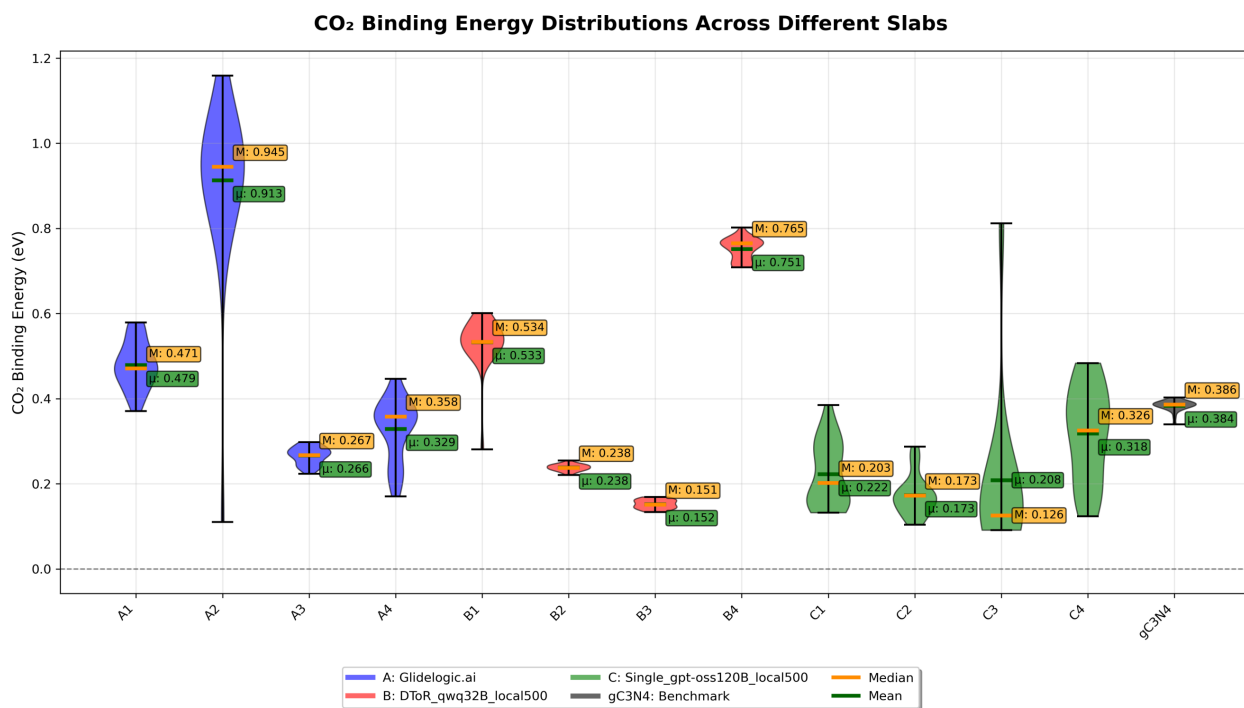


Figure S47: Distribution of CO₂ binding energies across all candidate systems visualized as violin plots. Mean (solid line) and median (dashed line) values are shown for each candidate, derived from 25 configurations per surface using the 5×5 grid sampling methodology.

CO₂ Sensor: Binding Energy Scores

Higher binding energy indicates better CO₂ sensing performance

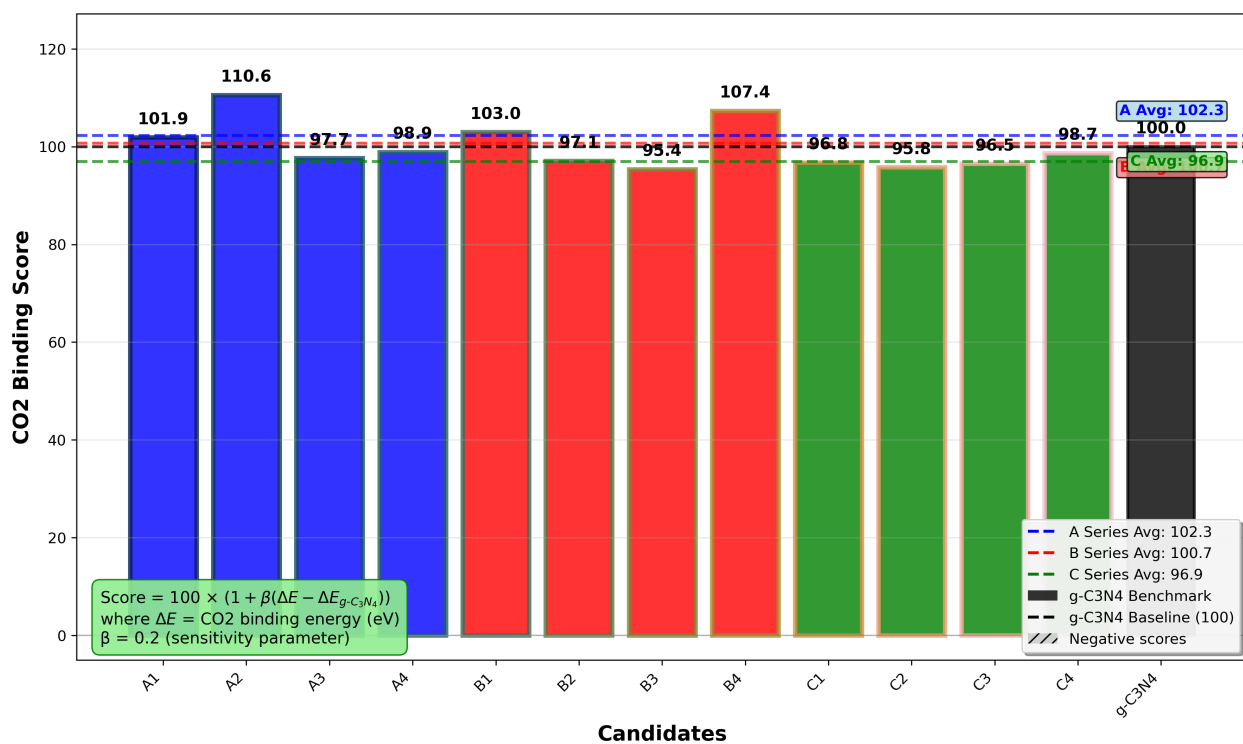


Figure S48: CO₂ sensing performance scores for all candidate systems from static DFT calculations, normalized to g-C₃N₄ baseline (100). Scores are calculated using the linear transformation with sensitivity parameter $\beta = 0.2$, where higher binding energies yield higher scores.

F.7 Candidate Feasibility Discussions

In PFAS sensing, our "good" versus "bad" judgments were anchored in well-established supramolecular and materials design principles rather than subjective preferences. A1 (rGO + β -CD) and B1 (MXene + methacrylic-acid MIP cavity) closely mirror experimentally validated motifs. β -CD polymers and β -CD-based molecularly imprinted layers are now recognized PFAS sorbents and sensing elements: their ~ 0.7 – 0.8 nm hydrophobic cavity matches the cross-section of perfluoroalkyl tails and can concentrate PFOA/PFOS while excluding bulkier natural organic matter[69, 70, 71, 72, 73, 26]. Besides, methacrylic-acid-based MIP have also been experimentally demonstrated for highly selective electrochemical detection of PFOA and related PFAS in complex matrices, further supporting the plausibility of methacrylic-acid-based MIP cavity[73]. Anchoring such cavities on conductive 2D supports (rGO or $\text{Ti}_3\text{C}_2\text{T}_x$ MXene) is also experimentally routine; MXene- and graphene-based electrochemical/FET sensors already exploit their high carrier density, hydrophilic terminations and solution processability for chemical detection. By contrast, C3 deliberately stacks a hydrophobic fluorosilane brush (C12-PFOTS), hydrophilic and chemically fragile MXene, metallic Ag nanoparticles, and acidic PEDOT:PSS. Fluorosilanes such as PFOTS/POTS are designed to form superhydrophobic, electrolyte-repelling coatings on oxide or silica surfaces, with water contact angles above 150° and strong exclusion of aqueous electrolytes[74, 75]. PEDOT:PSS, in turn, is well-known to be strongly acidic; its PSS component can corrode underlying oxides/metallic layers and compromise stability unless neutralized or buffered[31]. MXenes such as $\text{Ti}_3\text{C}_2\text{T}_x$ are chemically sensitive to oxidative and harsh aqueous environments, with reviews emphasizing pH and oxidant control to mitigate degradation[32]. Putting all of these in a single wet-processed stack raises obvious risks of phase separation (fluorosilane domains de-wetting hydrophilic PEDOT:PSS/MXene), acid-induced MXene/Ag degradation, and loss of stable ionic conduction paths—failure modes that are invisible to purely structural dry lab scoring but very familiar to experimental device builders.

An analogous pattern appears in PFAS degradation. Our dry-lab "winners" cluster around Ti_4O_7 -based electrodes (A3) and defect-engineered spinel oxides such as ZnFe_2O_4 (C4), both of which have strong literature support as cost-effective, robust platforms for oxidative degradation. Magnéli-phase Ti_4O_7 anodes are now among the most widely studied PFAS electro-oxidation catalysts, combining high conductivity, electrochemical stability, and near-complete defluorination/mineralization under realistic cell conditions [76, 77]. ZnFe_2O_4 composites, especially those with oxygen-vacancy-rich or doped structures, have been repeatedly shown to provide strong adsorption and efficient ROS generation for degradation of dyes and pharmaceuticals while remaining structurally robust and inexpensive[78]. In contrast, C5 proposes a triple heterostructure (MXene/g- C_3N_4 /atomic layer deposition:ALD-grown Al_2O_3) that is difficult to justify from either a synthesis or a charge-transport perspective. State-of-the-art MXene/g- C_3N_4 catalysts emphasize intimate 2D/2D contact and carefully tuned band alignment to promote interfacial charge separation; even in those carefully engineered systems, charge-transfer efficiency is highly sensitive to interface quality and layer thickness[33]. Adding a conformal ALD Al_2O_3 overlayer on top further increases interfacial complexity and typically introduces an additional insulating barrier that suppresses electron transfer to solution unless its thickness and coverage are exquisitely controlled[34, 79]. Practically, ALD processing on a solution-processed MXene/g- C_3N_4 stack also imposes thermal and chemical constraints that risk degrading MXene or passivating catalytically active sites without clear performance gains. When combined with emerging evidence that current LLMs struggle with complex, interconnected materials constraints and can generate plausible but impractical designs without explicit domain priors or tool-based validation, these examples illustrate a characteristic "inverse-design hallucination"[35, 36]: agents tend to assume that stacking more functional components is always beneficial, even when well-established electrochemical and colloidal considerations make such architectures unlikely to be buildable or stable in the wet lab.

Appendix G Targeted Component Ablations

G.1 Experimental setup

To address reviewer concerns without changing our code or indices, we performed a minimal-cost sensitivity study on three representative topics—*LIB_Fluoroether_Anion_Receptor*, *Microplastics_Sensing_2D*, and *PFAS_2D_FET_Probes*—under the same LLM-as-jury evaluation protocol and budget as the main paper. We compare against our local baseline `DToR_gpt-oss120B_local1500` (local-first, gap-triggered web complement, default Tree-of-Thought orchestration and per-node reflection). We introduce three families of deliberately “degraded” variants: (1) **Limited-Scale** variants that constrain orchestration and local retrieval while keeping the architecture intact: `weak_ToT` reduces the number of initial perspectives and the maximum tree depth from 3→2; `low_source_counts` limits the local RAG fetch to `paper_results_count = 1` instead of the default 5 (approaching the *local0* regime in the main text); `low_iterate_counts` disables all reflection loops per DR node (default = 3). (2) **No-Web-Search** variants that remove complementary web evidence: `local_only` restricts retrieval to the 500-volume local corpus; `LLM_only` disables both local and web retrieval, i.e., generation from the LLM alone. (3) **ChatGPT-API-driven** variants that keep the exact same framework but swap the local backbone for OpenAI gpt-5-mini or gpt-5-nano (*gpt_5_mini_driven*, *gpt_5_nano_driven*). All variants were evaluated with the same five-dimension rubric used in the paper and via anonymous A/B duels against `DToR_gpt-oss120B_local1500`; we additionally tracked the token footprint of API runs ($\approx 38\text{M}$ tokens, $\approx \$15$ per our OpenAI Console), which is materially higher than the cost of our local deployment. Finally, all ablation runs held the evaluation protocol and default budgets constant (depth/branches/top-k/iterations and the same five judges), varying only the indicated knobs so differences can be attributed to the ablated factors.

G.2 Results and interpretation

Across all three topics and both evaluation modes, every variant underperforms the local baseline on the five-dimension rubric (Fig. S6). The degradation follows a consistent gradient: No-Web-Search < Limited-Scale, with `LLM_only` the strongest negative control (unsurprisingly, report-level usefulness collapses without any retrieval). Within Limited-Scale, `low_iterate_counts` harms quality more than `low_source_counts`, indicating that **per-node reflection is more consequential than retrieval minutiae** at fixed budgets. `local_only` trails the full system, confirming that gap-triggered web complement adds measurable value beyond local evidence. In A/B duels, `DToR_gpt-oss120B_local1500` achieves $\sim 60\text{--}80\%$ average win-rates versus each residual variant (Fig. S7); among the ablated models, the gpt-5-mini/nano-driven versions are the least degraded (they narrow the duel margins) but at the cost of significantly higher token spend and operational expense. Importantly, when we drive the framework with small API models (mini/nano) across the same three topics, the relative ordering of variants persists, demonstrating that the DToR orchestration policy is robust to model scale and to the particular RAG instantiation. Inter LLM-judger and experimental trial consistency analysis similar to previous ones in Fig. S8 also support the reliability of our conclusions. These outcomes reinforce our positioning: we do not claim “better retrieval accuracy” in the IR sense; rather, **under a fixed resource budget, the local-first gap-triggered fusion with DToR branching makes reports more usable** (coverage \times depth \times coherence), while preserving on-prem deployment, data compliance, and markedly lower cost/energy. Ablation study presented in Fig. 2b reveal that reducing local RAG corpus size from 500 to 100 volumes only marginally impacts scores (drop $< 0.2/10$) in comparison, suggesting DToR’s efficiency regardless of local RAG on corpus. Also, notably, even the gpt-oss20B model under DToR outperforms all commercial baselines as shown in Fig. 2a, confirming that orchestration—not just model scale—drives performance. Combined with our dry-lab simulations/computations, which turn textual suggestions into actionable candidates and reproducible scripts, this is the kind of system-level utility the materials/chemistry community actually values.

Appendix H Topic Analysis

Computation methodology: We evaluate each research topic along two complementary axes using the full matrix of results from 41 agents across all trials and critic LLMs. Topic difficulty is defined as the mean performance across all agents for that topic; lower means indicate harder topics. To compute it, we aggregate all available scores per topic (over trials and critics), average per agent, then average across agents to obtain a single topic mean; topics are then ordered from easiest to hardest by this mean for display. Topic discrimination power is defined as the standard deviation (σ) of the per-agent mean scores within a topic; higher σ means the topic separates strong and weak agents more clearly. Discrimination is intentionally analyzed independently of difficulty because both easy and hard topics can show either high or low separation. For visualization, we present a Topic \times Agent heatmap (rows = topics ordered by difficulty, columns = agents ordered by overall performance) and a Topic Difficulty Ranking bar chart that shows mean \pm SEM per topic and overlays dashed vertical lines at the overall means of six reference agents to contextualize the global difficulty scale.

Result observations: The analysis reveals a clear difficulty spectrum (Fig. S49): the hard end is anchored by LIB_Fluoroether_Anion_Receptor ($\mu \approx 6.9$), LIB_Advanced_Binders ($\mu \approx 6.9$), and CO2_Sensing_2D_Materials ($\mu \approx 7.0$), while the easy end features InSitu_Liquid_TEM_MoS2_Sensing ($\mu \approx 7.7$), Printed_FET_Array_Process_Window ($\mu \approx 7.6$), and ML_e_Tongue_for_Water ($\mu \approx 7.5$); this ranking aligns with the row ordering in the heatmap (Fig. S50). Importantly, discrimination power (Fig. S51) is decoupled from difficulty: LIB_Fluoroether_Anion_Receptor exhibits the largest spread ($\sigma \approx 1.24$), sharply separating agents despite its high difficulty, whereas Microplastics_Sensing_2D has low σ (≈ 0.69) with mid-pack difficulty, indicating limited benchmarking sensitivity; easy topics such as InSitu_Liquid_TEM_MoS2_Sensing still show moderate σ , underscoring the independence. For benchmark design, topics with mid-range difficulty ($\mu \approx 7.2$ – 7.4) and elevated σ give the best sensitivity—e.g., PFAS_Electro_Degradation ($\sigma \approx 1.07$), Ambient_Pressure_Diamond_Growth ($\sigma \approx 1.12$), and Mixed_Dimensional_Low_Noise_Transducers ($\sigma \approx 1.10$)—while low- σ topics (e.g., Microplastics_Sensing_2D, Solar_Evap_Wastewater_Phothermal) add little discriminatory signal. Agent capability patterns follow the column ordering: stronger agents (left) show consistently higher bands, DToR configurations dominate the high-score region yet still dip on the hardest LIB chemistry topics, and commercial baselines (ChatGPT_o3, ChatGPT_o4_mini_high) sit mid-pack—no agent family is universally strong. However, the advantages of local DToR agents over commercial solutions are still obvious based on the statistics by in-pair dueling (Fig. S52). Domain-specific challenges cluster in battery/electrolyte design, pointing to persistent electrochemistry gaps; sensing/detection topics occupy the middle with modest discrimination (shared failure modes), and materials processing topics like Ambient_Pressure_Diamond_Growth and NextGen_Solar_Unconventional couple mid difficulty with high σ , suggesting nuanced trade-offs that expose architectural differences. Collectively, we recommend selecting topics with $\sigma > 1.0$ and mean 6.5–7.5 for future benchmarks; we interpret low- σ topics as signaling systematic weaknesses shared across approaches, and the difficulty–discrimination decoupling as evidence that agents face both “universally hard” challenges and “high-variance” generalization tests.

Taken together, the topic analysis indicates that our evaluation is both reliable and discriminative. The difficulty spectrum aligns with domain intuition (electrochemistry hardest; sensing mid-band), while discrimination (σ) is decoupled from difficulty and isolates topics that genuinely separate systems rather than amplifying noise. The resulting agent orderings are stable across topics and mirror our minimal-sensitivity ablations (LLM_only weakest, weak_ToT degraded, local_only below gap-triggered fusion), suggesting that the benchmark captures real capability differences instead of prompt or dataset artifacts. Practically, this lens identifies where progress is most needed and confirms that our orchestration-centric design delivers benefits that persist across model scales and RAG choices. We therefore regard the evaluation as a fair, actionable basis for future comparisons.

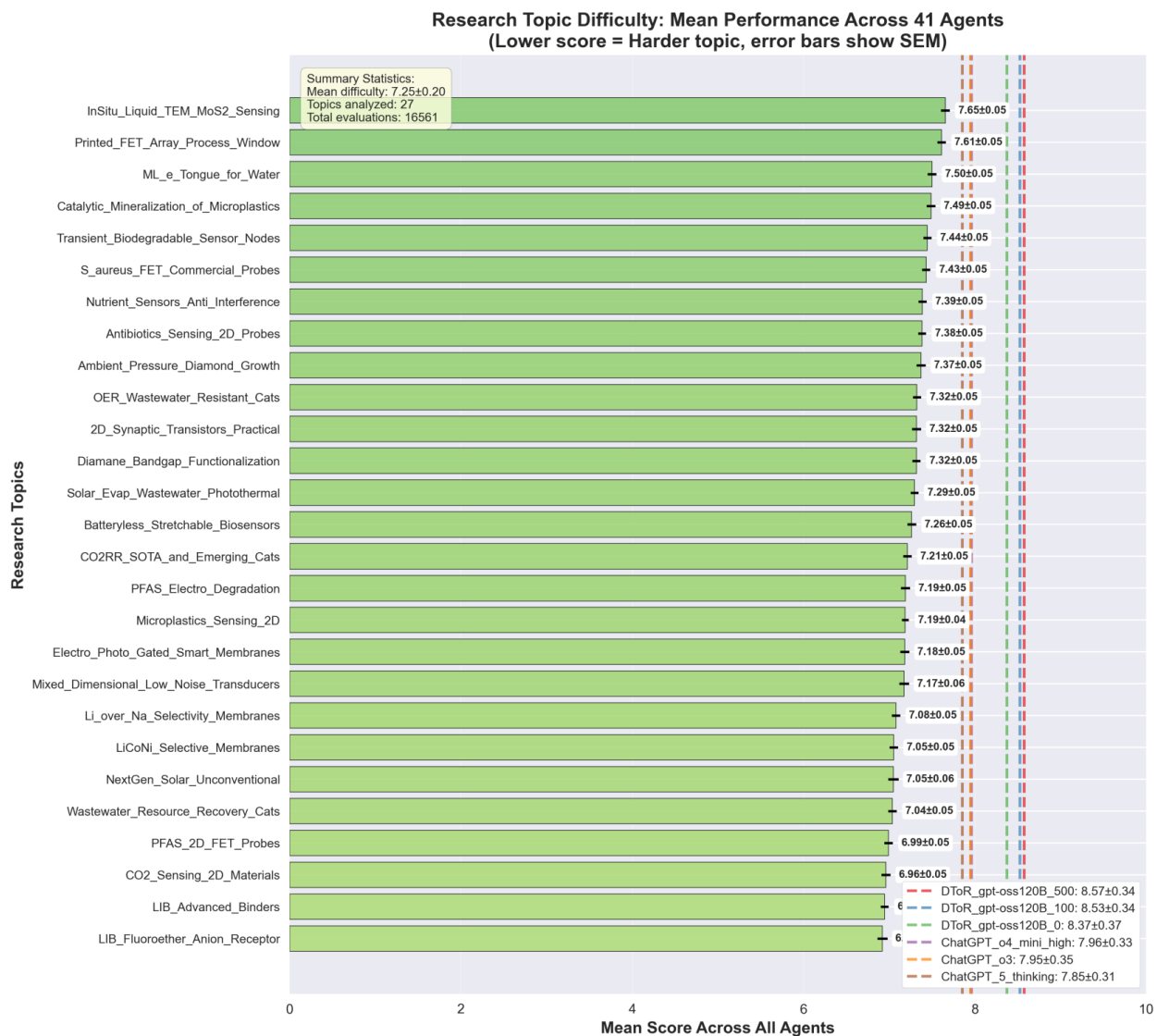


Figure S49: Bar chart summarizing mean performance (\pm SEM) across all agents for each topic. Bars are sorted from hardest (left, lower mean) to easiest (right, higher mean), with dashed vertical lines marking the six reference agents' overall means. This view highlights where topics sit on the global difficulty spectrum.

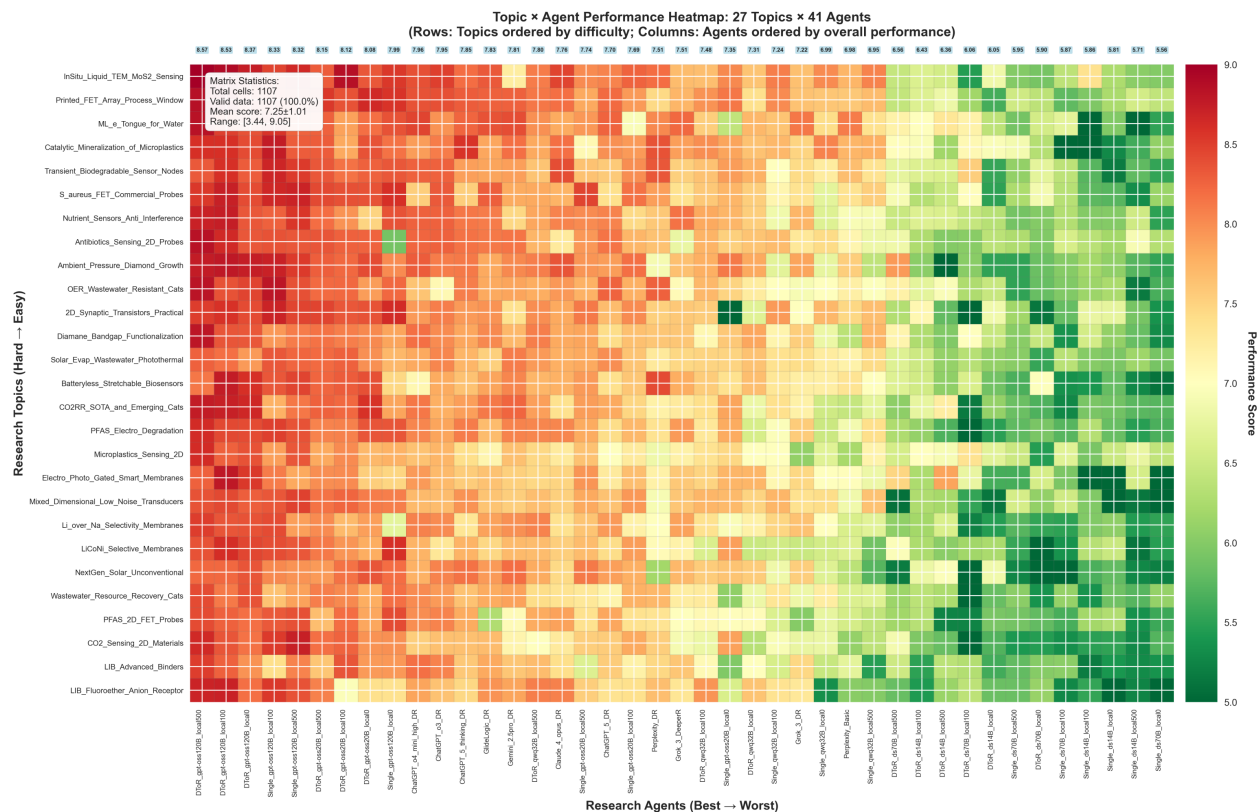


Figure S50: Performance matrix showing 27 research topics (rows, ordered by difficulty: easy→hard) and 41 agents (columns, ordered by overall performance: strong→weak). Because the colormap is reversed (RdYlGn_r), deeper reds indicate higher scores while greens mark lower scores. The layout reveals topic-specific challenges and agent-specific strengths directly on the matrix.

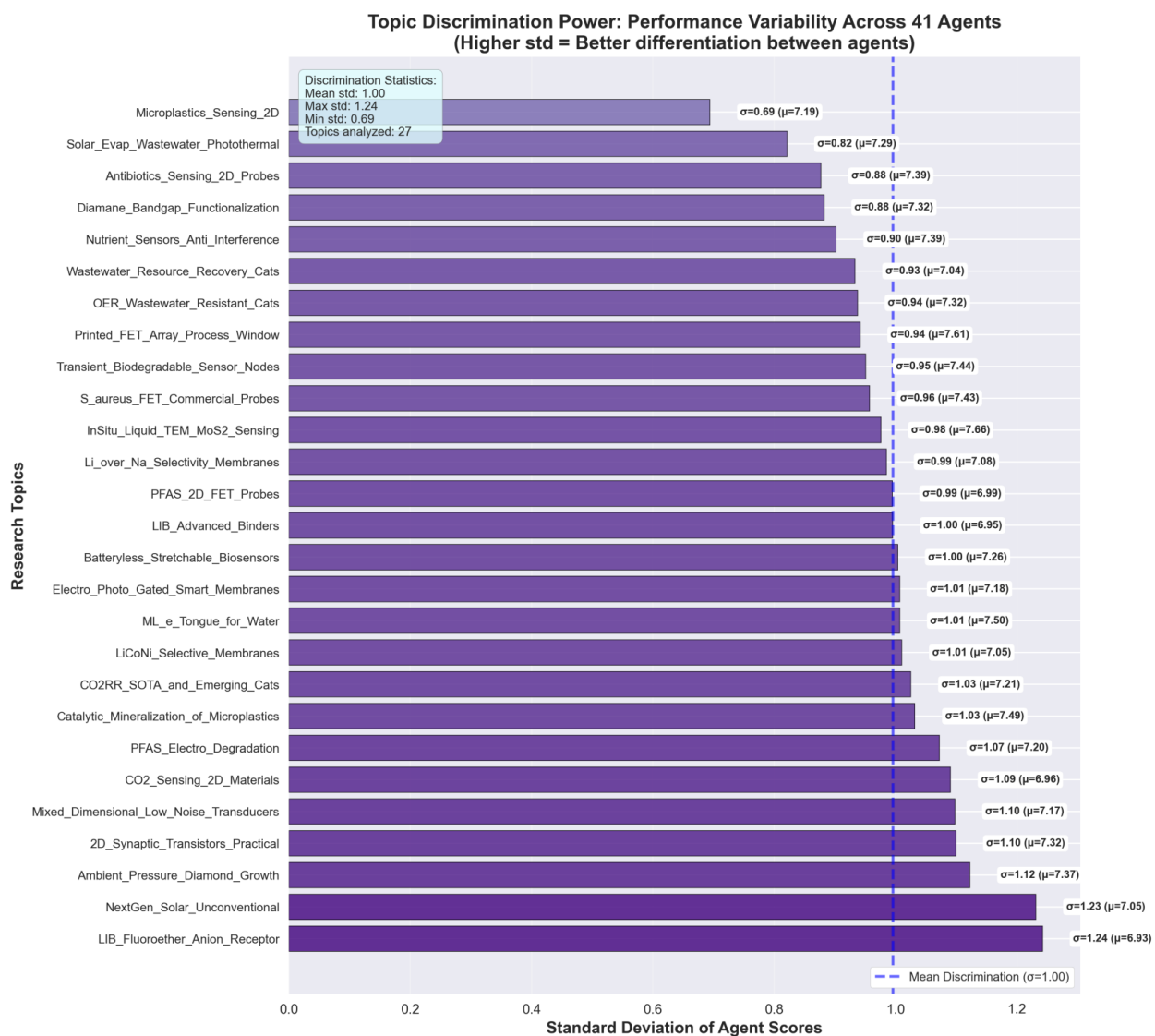


Figure S51: Standard deviation of agent scores for each topic, measuring how effectively each topic differentiates between strong and weak agents. Higher values indicate topics that create larger performance gaps across the agent spectrum, making them more suitable for benchmark evaluation.

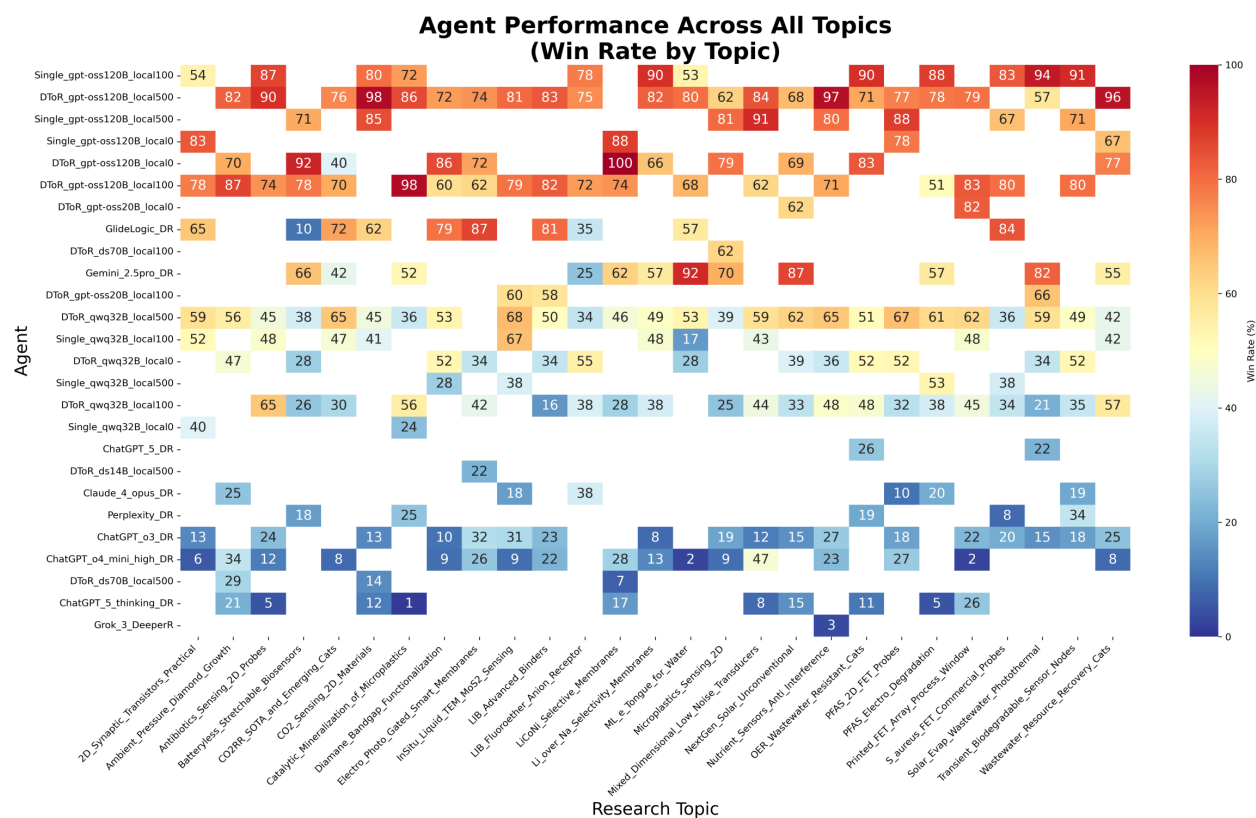


Figure S52: Win-rate heatmap across 27 research topics (columns) for every evaluated agent (rows); DTOR variants dominate the warm/red cells, while weaker single and commercial baselines cluster in the cool/blue range, revealing topic-specific strengths and gaps

Appendix I Power Consumption Estimation

I.1 Power estimation and LLM/RAG time decomposition.

We convert runtime to energy using a calibrated two-level power model on our workstation (4×NVIDIA RTX A5500, Ubuntu). System power was monitored continuously during experiments using `nvidia-smi` for GPU power draw and `powertop` for system-level consumption. We acknowledge that our power measurement methodology is relatively basic; however, the core contribution of this work lies in demonstrating the feasibility of edge-device deployment, which already showcases significant democratization and decentralization advantages over commercial subscription-based solutions. The quantitative power estimates provided here serve primarily as reference points for relative comparisons rather than definitive consumption benchmarks. Across runs we *observed* a typical baseline draw during retrieval/IO of $P_{\text{base}} \approx 76 \pm 3$ W (CPU, memory, disks, and idle GPUs). When the LLM generates tokens the GPU adds a model-dependent draw reported by `nvidia-smi`:

$$\begin{aligned}\Delta P_{\text{GPU}}(\text{ds14B}) &= 282 \pm 4 \text{ W}, & \Delta P_{\text{GPU}}(\text{ds70B}) &= 310 \pm 5 \text{ W}, \\ \Delta P_{\text{GPU}}(\text{qwq32B}) &= 301 \pm 4 \text{ W}, & \Delta P_{\text{GPU}}(\text{gpt-oss20B}) &= 320 \pm 5 \text{ W}, \\ \Delta P_{\text{GPU}}(\text{gpt-oss120B}) &= 360 \pm 6 \text{ W}.\end{aligned}$$

Hence $P_{\text{LLM}}(\text{model}) = P_{\text{base}} + \Delta P_{\text{GPU}}(\text{model})$ is 358 W (ds14B), 386 W (ds70B), 377 W (qwq32B), 396 W (gpt-oss20B), and 436 W (gpt-oss120B). During RAG (vector search over the local store, parsing, and file IO) the GPU utilization remained near-idle, so we bill RAG at $P_{\text{RAG}} = P_{\text{base}} \approx 76$ W.⁷

I.2 Empirical split of runtime into LLM vs. RAG.

Let $\bar{t}_{\text{tot}}(s, m, k)$ be the mean wall-clock time for strategy $s \in \{\text{Single, DToR}\}$, model $m \in \{\text{ds14B, ds70B, qwq32B, gpt-oss20B, gpt-oss120B}\}$ and local-RAG size $k \in \{0, 100, 500\}$. For $k = 0$ (no local vector store) we roughly estimated that all time is attributable to LLM generation:

$$t_{\text{LLM}}(s, m, 0) = \bar{t}_{\text{tot}}(s, m, 0), \quad t_{\text{RAG}}(s, m, 0) = 0.$$

For $k > 0$ we roughly split $\bar{t}_{\text{tot}}(s, m, k)$ into LLM and RAG by scaling the $k = 0$ LLM time to reflect the additional LLM passes used in local-knowledge summarization and complementary-query generation. The scale factors were estimated from repeated single-node micro-benchmarks (profiling isolated summarization and query-generation calls with coarse-grained timing) and calibrated against observed aggregate runtime patterns across full runs. Given measurement noise and workload variability, we report representative values that *differed by both strategy and model size*:

$$\begin{array}{l} \text{Single: } \alpha_{\text{ds14B}}^{\text{Single}} \approx 1.05, \quad \alpha_{\text{ds70B}}^{\text{Single}} \approx 1.07, \quad \alpha_{\text{qwq32B}}^{\text{Single}} \approx 1.09, \quad \alpha_{\text{gpt-oss20B}}^{\text{Single}} \approx 1.11, \quad \alpha_{\text{gpt-oss120B}}^{\text{Single}} \approx 1.13; \\ \text{DToR: } \alpha_{\text{ds14B}}^{\text{DToR}} \approx 1.10, \quad \alpha_{\text{ds70B}}^{\text{DToR}} \approx 1.20, \quad \alpha_{\text{qwq32B}}^{\text{DToR}} \approx 1.35, \quad \alpha_{\text{gpt-oss20B}}^{\text{DToR}} \approx 1.25, \quad \alpha_{\text{gpt-oss120B}}^{\text{DToR}} \approx 1.35. \end{array}$$

We then compute

$$t_{\text{LLM}}(s, m, k) = \alpha_m^s \bar{t}_{\text{tot}}(s, m, 0), \quad t_{\text{RAG}}(s, m, k) = \bar{t}_{\text{tot}}(s, m, k) - t_{\text{LLM}}(s, m, k) \quad (\text{clipped at } \geq 0).$$

Two empirical patterns are worth noting. (i) In **Single** mode the increase in t_{LLM} from $k = 0$ to $k > 0$ is modest (ranging from +5% to +13% across models, with larger models showing slightly higher overheads), and t_{RAG} exhibits a smaller difference than theoretically expected between $k = 100$ and $k = 500$ within measurement tolerance. (ii) In **DToR** mode, multi-hour runs accumulate more local-knowledge summarization and complementary-query steps; correspondingly t_{LLM} shows larger scaling (ranging from 1.10× to 1.35× as above, with overhead correlating with model complexity), and t_{RAG} increases with k due to heavier vector-store traffic and post-processing over longer context. When attribution is ambiguous we conservatively charge time to the LLM bucket. We emphasize that this decomposition serves as a *coarse approximation* for comparative analysis rather than exact per-component accounting.

⁷Short web fetches last seconds relative to multi-hour runs and are neglected.

I.3 Energy calculation.

Per-report energy is the sum of LLM and RAG contributions:

$$\begin{aligned} E_{\text{LLM}}(s, m, k) &= \frac{P_{\text{LLM}}(m) t_{\text{LLM}}(s, m, k)}{1000} \quad (\text{kWh}), \\ E_{\text{RAG}}(s, m, k) &= \frac{P_{\text{RAG}} t_{\text{RAG}}(s, m, k)}{1000} \quad (\text{kWh}), \\ E_{\text{tot}}(s, m, k) &= E_{\text{LLM}}(s, m, k) + E_{\text{RAG}}(s, m, k). \end{aligned}$$

All results in Fig. 6 use $P_{\text{base}} \approx 76$ W, $\Delta P_{\text{GPU}} \approx \{282, 310, 301, 320, 360\}$ W (ds14B, ds70B, qwq32B, gpt-oss20B, gpt-oss120B), and the strategy- and model-specific α values above (measurement uncertainties for power values range $\pm 3 - \pm 6$ W). For example, substituting the estimated $\{t_{\text{LLM}}, t_{\text{RAG}}\}$ of DToR_gpt-oss120B_local500 yields $E_{\text{tot}} \approx 4.37$ kWh per completed report⁸; configuration-wise LLM/RAG splits are provided alongside runtime heatmaps in the Appendix.

⁸For context, 4.37 kWh/report is comparable to running a household refrigerator for 1.5 days or training a small CNN on ImageNet once—orders of magnitude below the carbon footprint of cloud-based DR APIs over repeated use.